Solar fuels production from thermochemical gasification and reforming of carbonaceous feedstocks

Srirat Chuayboon

THÈSE

Pour obtenir le grade de

Docteur

Délivré par

UNIVERSITE DE PERPIGNAN VIA DOMITIA

Préparée au sein de l'école doctorale

Énergie et Environnement ED 305

Et de l'unité de recherche

PROMES-CNRS UPR 8521

Spécialité :

Sciences de l'ingénieur

Présentée par

Srirat CHUAYBOON

Solar fuels production from thermochemical gasification and reforming of carbonaceous feedstocks

Soutenue le 29 Novembre 2019 devant le jury composé de

M. Sylvain SALVADOR, Professeur, École des Mines d'Albi-Carmaux	Rapporteur
M. Doan PHAM MINH, Maître de Conférences, École des Mines d'Albi-Carmaux	Rapporteur
M. Laurent VAN DE STEENE, Directeur de Recherche, CIRAD, Montpellier	Examinateur
M. Juan ADÁNEZ ELORZA, Professeur, ICB-CSIC, Zaragoza	Examinateur
M. Stéphane ABANADES, Directeur de Recherche, PROMES-CNRS	Directeur de thèse
M. Sylvain RODAT, Ingénieur-Chercheur, CEA-LITEN	Co-Directeur de thèse

Acknowledgements

Throughout the three years of Ph.D. study at PROMES-CNRS Laboratory, Odeillo, France, I have received a great deal of support and assistance.

First of all, I would like to gratefully acknowledge King Mongkut' s Institute of Technology Ladkrabang (KMITL), Thailand and Campus France, Thailand for Ph.D. scholarship funding, and PROMES-CNRS Laboratory for experimental support.

I would like to acknowledge my advisor, Dr. Stéphane ABANADES, who cannot be thanked enough for giving me a good opportunity to be his Ph.D. student and for his endless guidance. Over three years, you have daily advised, intensively taught, and supported me not only on my dissertation but also my real life. It has been my greatest honor to work with you.

I would like to acknowledge my co-advisor at CEA, Dr. Sylvain RODAT, who has regularly given me valuable recommendations and professional assistance on my thesis over three years.

I also would like to thank my friends, colleagues, and team especially at PROMES-CNRS laboratory for their wonderful collaboration. You have greatly supported me and have always been willing to help me. I would particularly like to thank Joya ZEITOUNY and Lucile BARKA for your unending helps and friendship.

Finally, I would like to gratefully thank my parents and sister, who have done so much in their life to support me to accomplish my Ph.D. goals. You are always there for me with wonderful care without conditions.

Table of Contents

List of Tables

List of Figures

Nomenclature

Abbreviations

DNI	Direct Normal Irradiance
CSP	Concentrated solar power
CLR	Chemical looping reforming
CLRM	Chemical looping reforming of methane
CLG	Chemical looping gasification
CTR	Carbothermal reduction
MTR	Methanothermal reduction
FESEM	Field emission scanning electron microscopy
XRD	X-ray powder diffraction

Latin letters

ΔG	Gibbs free energy (J)
ΔH	Enthalpy change of reaction (J/mol)
T	Temperature (℃, K)
ΔS	Entropy change (J/K)
Q_{solar}	Solar power input (W)
$Q_{aperture}$	Solar power captured by the aperture area (W)
$A_{aperture}$	Area of aperture (m^2)
$\tilde{C}$	mean concentration ratio (-)
I	Intensity of solar radiation (W/sr)
U	Energy upgrade factor (-)
X_{CH_4}	Methane conversion (-)
S_{H_2}	Hydrogen selectivity (-)
S_{CO}	Carbon monoxide selectivity (-)
$\dot{m}_{feedstock}$	Biomass feeding rate (g/min)
LHV	Lower heating value (J/kg)
M	Global mass balance (-)
X_C	Carbon conversion (-)
X_{ZnO}	ZnO conversion (-)
X_{MgO}	MgO conversion (-)

Greek letters

τ	Mean gas residence time (s)
α_{eff}	Absorptance solar cavity receiver
ε_{eff}	Emittance of solar cavity receiver
η	Efficiency
$\eta_{\text{solar-to-fuel}}$	Solar-to-fuel energy conversion efficiency
$\eta_{reactor}$	Thermochemical reactor efficiency
$\eta_{solar\ fraction}$	Solar energy storage fraction
σ	Stefan-Boltzmann constant ($W/m^2\text{-}K^4$); $\sigma = 5.670373.10^{-8}$ $W/m^2\text{-}K^4$
δ	Bed-averaged oxygen non-stoichiometry

Introduction

One of the most serious concerns in the near future is the depletion of fossil fuels associated with increasing greenhouse gases emissions. According to the strategical review of world energy 2019, energy demand worldwide increased at its fastest rate since 2010: world energy consumption grew by 2.9% in 2018 with fossil fuels meeting nearly 70% of the rise in energy consumption, almost double of its 10-year average of 1.5% per year [1]. This led to an unprecedented increase in the global energy-related carbon dioxide (CO_2) emissions by 1.7% in 2018 [1], thereby contributing to hastened global climate change. Consequently, it is extremely important to develop environmentally friendly routes for alternative fuel production such as synthesis gas (syngas), supplied by sustainable renewable energy sources such as biomass, biogas, and solar energy. Syngas can be used as an interesting energy carrier for a multitude of chemical synthesis processes. Moreover, it can be burned directly in internal combustion engines, furnaces, boilers and stoves, utilized to produce methanol and hydrogen, or further converted into synthetic liquid fuels via the Fisher-Tropsch method [2].

Solar thermochemical fuel production processes involve the thermochemical conversion of solid and gaseous carbonaceous feedstocks as well as metal oxides (M_xO_y) into syngas and metals utilizing concentrated solar energy to drive endothermic chemical reactions. In particular, the use of solar energy as the source of process heat for supplying such solar thermochemical processes has several advantages:

(i) eliminate the need for fossil fuels combustion as heat source, which in turn reduces the total world fossil fuels energy consumption,
(ii) avoid producing CO_2, which seriously affects climate change and global warming,
(iii) store intermittent solar energy within the chemical products through the endothermic reactions,
(iv) produce clean and transportable chemical fuels and materials commodities,
(v) provide very high temperatures, dependent on the magnitude of solar concentration, which may exceed those supplied by combustion-based heat sources.

The physical state of carbonaceous feedstocks can be used to categorize the solar thermochemical processes into two main groups according to Fig. 1. Regarding gaseous feedstocks, natural gas, methane (CH_4), and biogas can be converted to syngas via cracking, steam/dry reforming, or chemical looping reforming (CLR) or to syngas and metals via methano-thermal reduction (MTR), representing an attractive approach for the short-term solar process implementation. In addition, the gaseous H_2O/CO_2 feedstock can also be converted to H_2/CO via direct thermolysis or two-step H_2O/CO_2 splitting, but requires higher temperatures, thus representing an attractive option for the long-term sustainable fuel production. Concerning solid feedstocks, pet coke, coal, biomass, or waste can be converted to syngas via pyrolysis/gasification or chemical looping gasification (CLG). In addition, they can be used as a chemical reducing agent to separate oxygen from metals oxides, thereby generating elemental metals concomitantly with carbon monoxide (CO) or syngas. This process is known as carbothermal reduction (CTR). As shown in Fig. 1, the solar thermochemical processes offer different pathways to produce solar fuels, and each one has its own advantages and drawbacks. In this study, CLR and gasification are considered as attractive means to convert gaseous and

solid feedstocks, respectively, into syngas, while CTR is considered as an attractive avenue to produce metals according to Fig. 2.

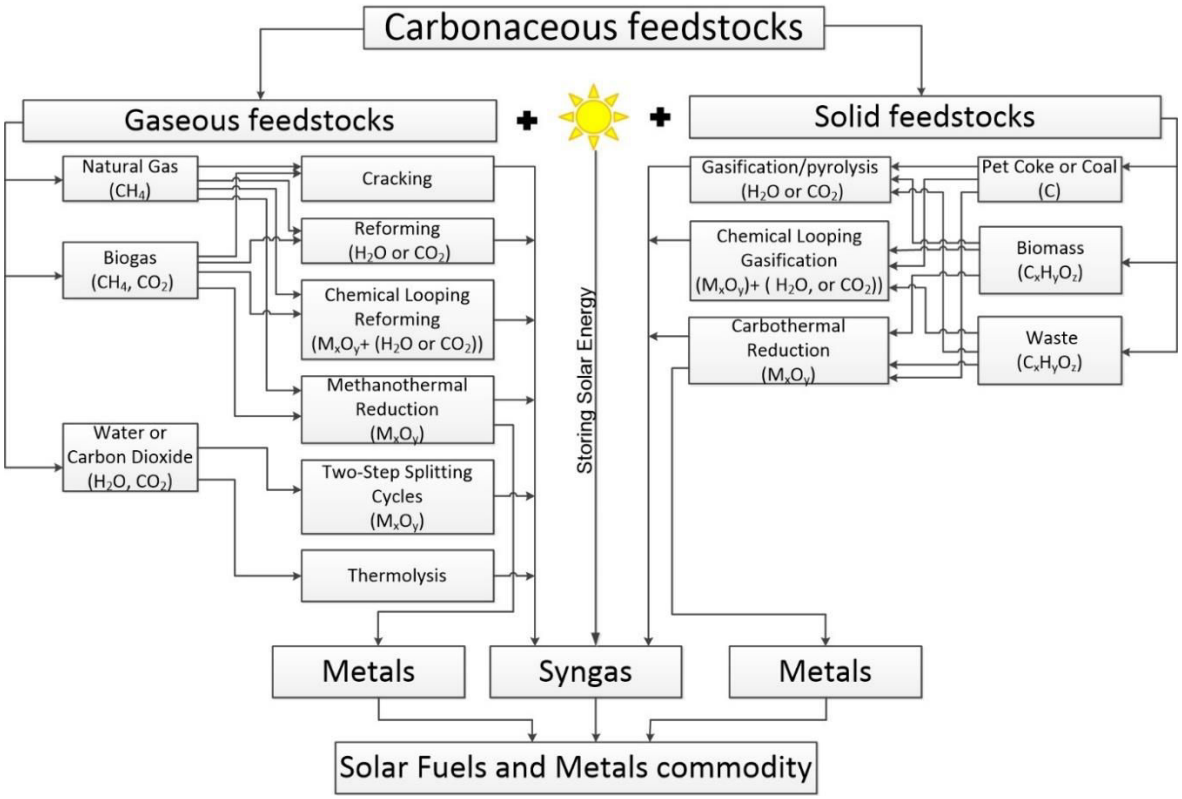

Figure 1. Diagram of the conversion routes of carbonaceous feedstocks for solar thermochemical processes.

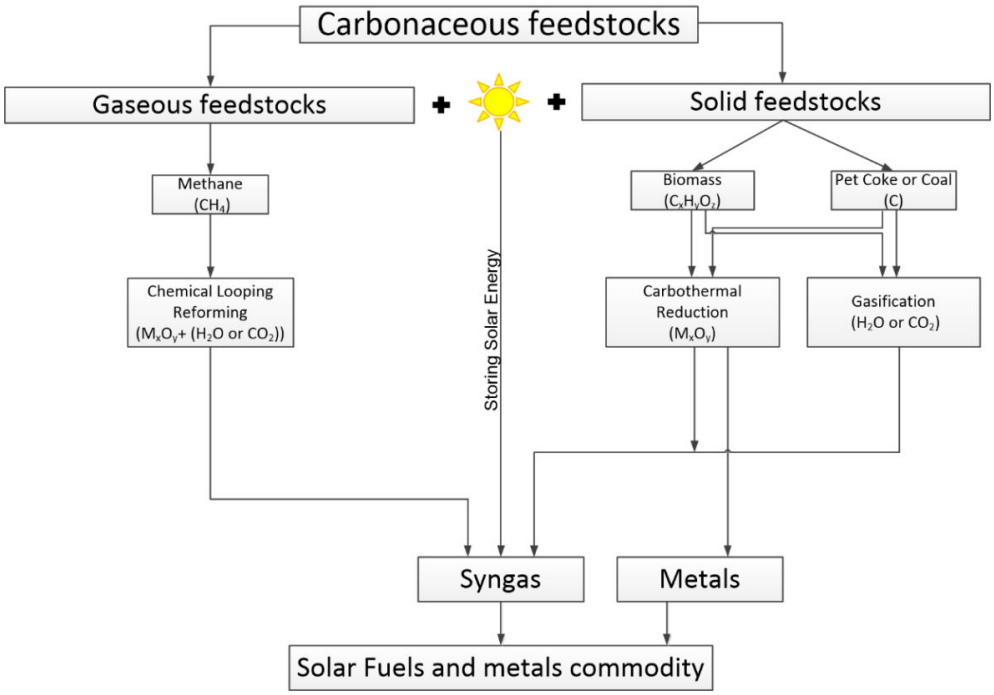

Figure 2. Diagram of the three considered conversion routes of carbonaceous feedstocks for solar thermochemical processes.

Research objectives

The main goal of this work is to convert gaseous (methane) and solid feedstocks (wood biomass) into syngas via solar chemical looping reforming and solar gasification, respectively, and to produce metals from metal oxides (ZnO and MgO) via solar carbothermal reduction. The conventional processes of reforming, gasification, and metallurgy have demonstrated several serious major drawbacks regarding the need for fossil fuels as heat source, partial combustion of feedstocks, CO_2 emissions, products contamination by combustion by-products, and catalyst requirement. This also provides incentives in this present study to overcome the conventional processes. The objective is to experimentally investigate such considered processes and demonstrate a variety of solar thermochemical processes capability in both converting gaseous and solid carbonaceous feedstocks to syngas and producing metals in new solar thermochemical reactors operated flexibly in batch and continuous modes under vacuum and atmospheric conditions during on-sun testing.

Scope of the study

The work is performed by conducting thermodynamic studies and experimental investigations of solar CLR, biomass gasification, and CTR processes in 1.5 kW_{th} prototype solar chemical reactors during on-sun operation. Methane and H_2O/CO_2 are considered as gaseous feedstocks while wood biomass and solid carbon (charcoal/carbon black) are considered as solid feedstocks. Four metal oxides materials regarding two non-volatile oxides (ceria and iron oxides) and two volatile oxides (ZnO and MgO) are considered as oxygen carriers or oxidants. The results for each considered solar thermochemical process are compared. Insights into the influence of operating parameters on conversion, yield, and reactor performance are emphasized. The feasibility and reliability of the considered processes are demonstrated.

Thesis outline

This work aims to experimentally investigate various solar thermochemical processes to convert both gaseous and solid carbonaceous feedstocks to syngas and to produce metals, using 1.5 kW_{th} prototype solar chemical reactors during continuous on-sun operation.

Chapter 1 describes the background involving principles of solar concentrating technologies, followed by thermodynamics of solar thermochemical conversion, solar fuel thermochemical processes, metal oxide redox pairs, and solar reactors, which are detailed and reviewed to identify the scientific research gaps leading to the investigation of solar CLR, solar gasification, and solar CTR.

Chapter 2 presents an experimental investigation of the chemical looping reforming of methane (CLRM) using non-volatile materials including ceria and iron oxides with different morphologies in a 1.5 kW_{th} solar reactor driven by real high-flux concentrated sunlight. Fifty-five on-sun experiments with eight different ceria and iron oxides samples were performed isothermally in the solar reactor in the temperature range 900-1150 °C. The effect of different ceria and iron oxides morphologies (reticulated porous foam, packed-bed powder, and blend of metal oxides powder mixed with inert Al_2O_3 particles), CH_4 flow-rate, reduction

temperature, and sintering temperature on the bed-averaged oxygen non-stoichiometry (δ), methane conversion, syngas production yield, cycle stability, and reactor performance was experimentally investigated and evaluated.

Chapter 3 focuses on the experimental study of continuous solar gasification of biomass with sixty-four on-sun tests in a 1.5 kW_{th} prototype spouted-bed reactor at 1100-1300 °C. A comprehensive parametric study considering the influence of different lignocellulosic biomass feedstocks (wood type), biomass feeding rates, steam/biomass molar ratios, carrier gas flow rates, and reaction temperatures was conducted to optimize the syngas production capacity and evaluate the gasification performances. An optimization in the syngas yield through the study of biomass feeding rate influence is highlighted.

Chapter 4 addresses a novel metallurgical process via the solar CTR of volatile metal oxides. Two metal oxide candidates (ZnO and MgO) were decomposed with different solid reducing agents in a new ceramic cavity solar reactor at temperatures depending on the metal oxide (950-1350 °C for ZnO and 1400-1650 °C for MgO). This reactor was designed to be flexible for operation at temperatures up to above 1600 °C under 1.5 kW_{th} solar power input. Twenty-six on-sun experiments were carried out by varying different operating parameters such as solid reducing agents (activated charcoal, carbon black, graphite, and beech wood biomass) and reactant molar ratio in batch or continuous modes under vacuum and atmospheric pressures. High conversion of ZnO and MgO to Zn and Mg is highlighted.

Chapter 5 demonstrates the feasibility of the combination of biomass gasification and CTR of ZnO to produce both Zn and syngas in a single process. The combined process was operated in continuous mode utilizing the same solar reactor, which was used in the gasification process, in the temperature range 1050-1300 °C through sixteen runs. The influence of temperature and reactant molar ratio on syngas production was studied and compared to the case of a pyrolysis process (without any oxidant). The advantages and reliability of such a combined process for co-production of syngas and metallic Zn are highlighted.

General conclusion presents the thesis with a summary of the results and perspectives for future work.

Chapter 1: Background on solar thermochemical processes

1.1 Solar energy

Solar energy is radiant light and derived heat from the sun. This radiant energy is generally measured and reported as the solar irradiance. In fact, the total amount of solar energy incident on Earth is largely in excess of the anticipated energy requirements; however, its intensity is quite low. If harnessed, this energy source has the high potential to meet global energy demands without the concomitant production of greenhouse gases [3]. Fig. 1-1 shows the potential of solar energy in terms of the average daily/year sum of direct normal irradiation (DNI). The colors on the map represent the local solar irradiance averaged from 1994/1999/2007 to 2015, calculated by the Solargis model from atmospheric and satellite data [4]. The area close to the equator exhibits the greatest amount of solar radiation, and the regions with the highest potential are Australia, China, India, France, Spain, Morocco, Sub-Saharan Africa, South Africa, and Latin America and Caribbean, which are capable for producing heat to supply chemical reactions or electricity generation process.

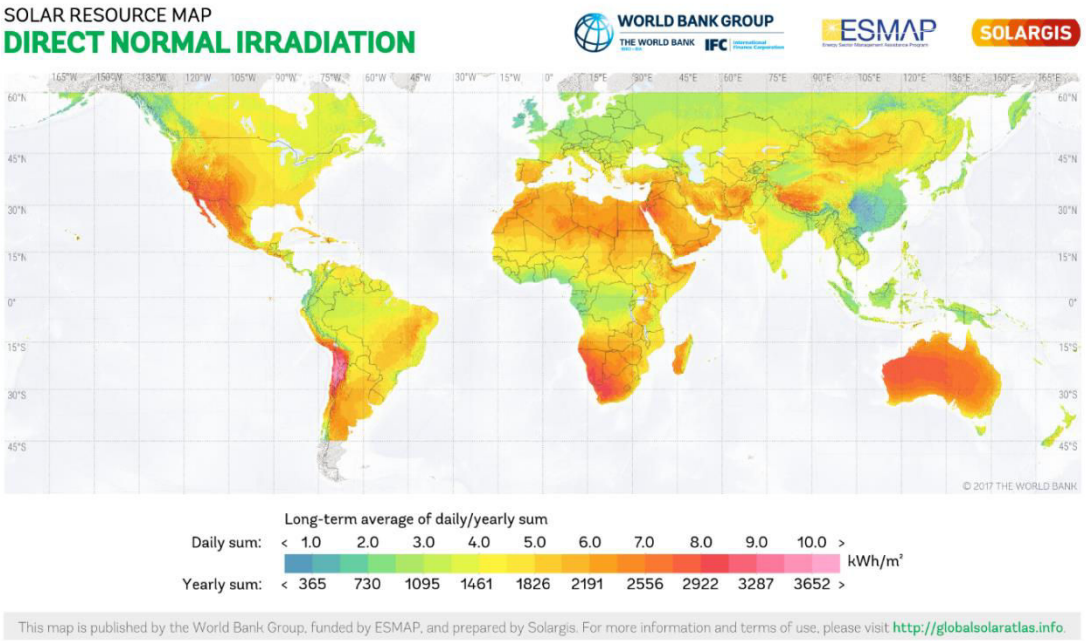

Figure 1-1. Global distribution of solar radiation intensity [4].

1.2 Principles of solar concentration

Among the different ever-evolving technologies for harnessing solar energy, solar concentrating power systems utilize lens or mirrors and tracking systems to focus a large area of sunlight into a small beam. These technologies mainly consist of parabolic troughs and concentrating linear Fresnel reflectors, solar dishes, solar power tower, double reflection solar furnace, and solar simulator.

1.2.1 Parabolic trough and linear Fresnel systems

Parabolic troughs are the oldest solar thermal technology for concentrated solar power (CSP) plants [5]. The concentrating systems utilize parabolic-shaped collectors made of reflecting material, according to Fig. 1-2. The mirrors reflect the incident solar radiation onto a focal line, where receivers are placed to be heated. Parabolic trough reflectors can concentrate sunlight between 60 and 100 times [6], which is sufficient to raise the temperature of the heat transfer fluid to as much as 550 ℃.

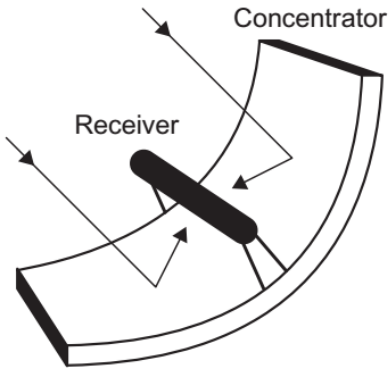

Figure 1-2. Schematic of a solar trough [5].

Another system, which is similar to the parabolic troughs, is the linear Fresnel reflector system (Fig. 1-3). Flat plane mirrors are split into multiple parts to track sunlight that is reflected onto the secondary reflector and absorber tube.

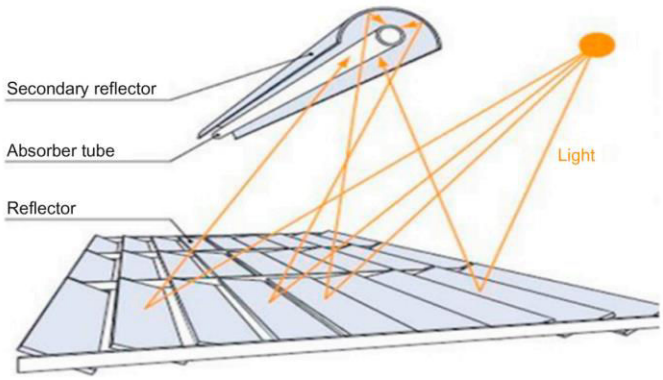

Figure 1-3. Linear Fresnel reflector system [7].

1.2.2 Solar dishes

Fig. 1-4 shows a parabolic-dish solar concentrator. Sunlight is concentrated and reflected by a parabolic dish toward the thermal receiver positioned on the focal point of the dish collector. The operating temperature is above 1000 °C with a concentration ratio in the range of 1000-5000 [5]. This technology is limited by the size of the dish and can be equipped with “dish-Stirling” engines.

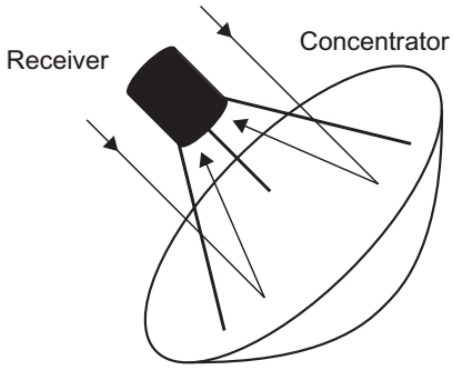

Figure 1-4. Parabolic-Dish solar concentrator [5].

1.2.3 Solar towers

The solar tower system includes a massive heliostat field focusing on a single solar receiver mounted on a tall tower positioned at its center, according to Fig 1-5. Each mirror tracks the sun independently, making the solar collection system relatively more expensive than for a solar trough plant. The benefit is that a higher temperature can be achieved with this plant type. A concentration factor of between 600 to 1000 times is possible, reaching temperature in the range 800-1000 °C [8].

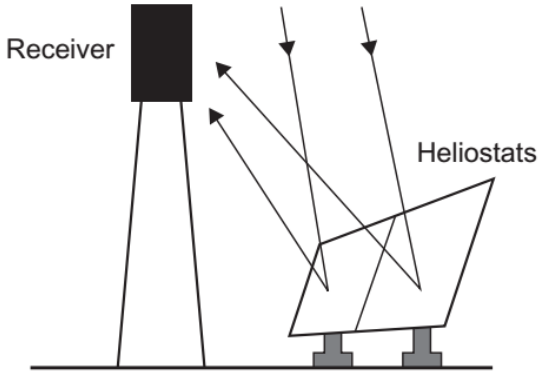

Figure 1-5. Solar tower system [5].

1.2.4 Double reflection solar furnace

The concentrating system uses one or several heliostats like solar towers. In place of a tower with a central receiver, a parabolic mirror is employed as a secondary optical component to concentrate the sunlight at the focal point with a concentration ratio up to 20,000 times. Several parabolic mirrors can be joined because a single mirror is restricted in size. The largest system is the solar furnace in Odeillo, which is 54 m high and 48 m wide, including 63 heliostats. The thermal power capacity is 1 MW with a maximum temperature above 3500 °C (Fig. 1-6).

Figure 1-6. Solar furnace in Odeillo, France [9].

1.2.5 Solar simulator

The solar simulator is a device delivering illumination approximating natural sunlight, and it can generally be categorized into two types: those that utilize a pointing source of simulated solar radiation positioned away from the collector and those that have a large area of multiple lamps positioned close to the collector. The objective of the solar simulator is to provide a controllable indoor test facility under laboratory conditions without the issues of unstable natural solar irradiation. The world's biggest solar simulator is located at the DLR facility in Jülich, Germany (Fig. 1-7). The 149 high-performance Xenon short-arc lamps generate artificial sun [10].

Figure 1-7. 149 xenon short-arc lamps that are employed to simulate solar irradiation at DLR in Jülich, Germany [10].

1.3 Thermodynamics of solar thermochemical conversion

Solar thermochemical processes use the concept of the conversion of solar energy to chemical energy carriers. Therefore, two fundamental thermodynamic laws regarding the 1st and 2nd principle laws are nescessary to analyze solar thermochemical processes. To estimate the feasibility of chemical reactions, Gibbs free energy (ΔG) of system needs to be verified:

$$\Delta G=\Delta H-T\Delta S<0 \quad (1\text{-}1)$$

Where: ΔG is Gibbs free energy, ΔH is the enthalpy change of reaction, T is temperature, and ΔS is the entropy change.

Fig. 1-8 shows variations of ΔH, $T\Delta S$, ΔG as a function of temperature. For solar thermochemical processes, the total required energy to transform reactants to products is equal to the enthalpy change of reactions (ΔH), while the amount of energy supplied by solar energy as process heat to complete reversible process is equivalent to $T\Delta S$. ΔG decreases with increasing temperature. If ΔG is negative, the reaction can proceed spontaneously and is thermodynamically favorable.

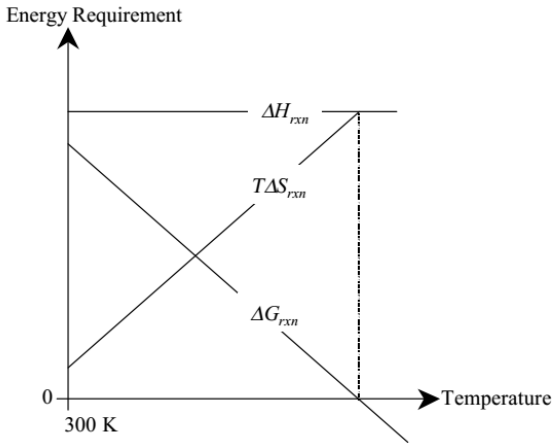

Figure 1-8. Variations of ΔH, TΔS, ΔG as a function of temperature [11].

The performance indicator of CSP plant is the solar energy absorption efficiency of the receiver ($\eta_{absorption}$). It is the ratio of the net rate of absorbed energy to the solar power input from the concentrator. Unless accounting for the conduction and convection losses, the absorption efficiency is given by [11,12]:

$$\eta_{absorption} = \frac{(\alpha_{eff} \cdot Q_{aperture}) - (\varepsilon_{eff} \cdot A_{aperture} \cdot \sigma \cdot T^4)}{Q_{solar}} \quad (1\text{-}2)$$

Where: Q_{solar} is the total solar power input, $\cdot Q_{aperture}$ is the amount of solar power captured by the aperture area ($A_{aperture}$), α_{eff} and ε_{eff} are the absorptance and emittance of the solar cavity receiver, respectively, T is the nominal cavity receiver temperature, σ is the Stefan-Boltzmann constant.

The ability of the collector to concentrate solar energy is represented by the mean concentration ratio ($\tilde{C}$) over the aperture as follows:

$$\tilde{C} = \frac{Q_{aperture}}{I A_{aperture}} \quad (1\text{-}3)$$

Where I is the intensity of solar radiation

Assuming that all incoming solar energy can be ideally captured, i.e. $Q_{aperture}$=Q_{solar}, and the cavity receiver is a perfectly insulated blackbody (no heat losses except radiative heat losses), with $\alpha_{eff} = \varepsilon_{eff}$=1, $\eta_{absorption}$ can be simplified as:

$$\eta_{absorption} = 1 - \left(\frac{\sigma T^4}{I\tilde{C}}\right) \tag{1-4}$$

The absorbed solar power drives the endothermic chemical reaction; therefore, the conversion of solar energy to chemical form is quantified as the exergy efficiency:

$$\eta_{exergy} = \frac{-\dot{n}\Delta G_{rxn}}{Q_{solar}} \tag{1-5}$$

Where $\dot{n}$ is the molar flow rate of products, and $\Delta G_{rxn}$is the maximum amount of work that may be obtained from the products when converted back to the reactants at 298K. Thus, the 2nd law is employed to calculate the maximum exergy efficiency ($\eta_{exergy,ideal}$).

Because the conversion of the solar process heat to chemical energy is limited by both solar absorption and Carnot efficiency, the $\eta_{exergy,ideal}$ is given by:

$$\eta_{exergy,ideal} = \eta_{absorption} \cdot \eta_{Carnot} = \left(1 - \frac{\sigma T^4}{I\tilde{C}}\right) \cdot \left(1 - \frac{T_L}{T}\right) \tag{1-6}$$

where T_L is ambient temperature.

Fig. 1-9 shows the ideal exergy efficiency ($\eta_{exergy,ideal}$) as a function of temperature (T) for different concentration ratios. It is also compared with Carnot efficiency. An increase in temperature and concentration ratio increases the $\eta_{exergy,ideal}$. For example, at 1100 K the maximum $\eta_{exergy,ideal}$ of 65–72% can be obtained for concentration ratios of 1000–10,000 respectively. In addition, the optimal operating temperatures that maximize $\eta_{exergy,ideal}$ can be calculated [11]. Therefore, maximizing the actual solar-to-chemical energy efficiency as close as possible to the ideal efficiency in solar thermochemical endothermic processes operated at 1100-1800K is a key challenge for solar thermochemical research.

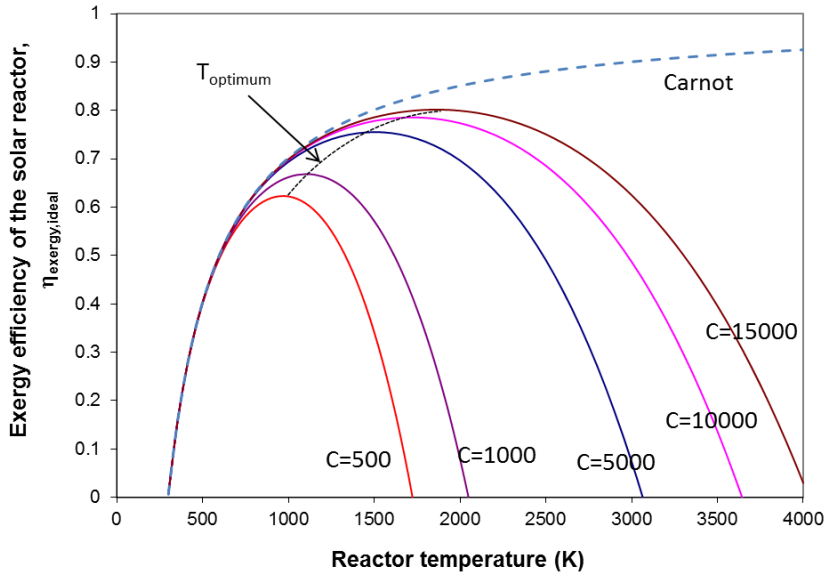

Figure 1-9. $\eta_{exergy\ ideal}$ as a function of operating temperature at different solar concentration ratios for a blackbody cavity receiver [11].

1.4 Solar fuel thermochemical processes

Solar fuel thermochemical processes use solar energy to drive endothermic chemical reactions for the conversion of either gaseous/solid feedstocks or metal oxides to storable and transportable fuels or chemical commodities. They can be divided into two groups based on the feedstocks (Fig. 1-10). On the one hand, H_2O/CO_2 splitting, which consists of thermolysis (or electrolysis) and two-step cycles, represents a long-term ultimate goal for sustainable fuel production. On the other hand, decarbonization, which consists of reforming/chemical looping reforming (CLR), cracking, gasification/chemical looping gasification (CLG), and carbothermal/methanothermal reduction, should be promising for the short-term solar process implementation. It consists of the conversion of solid/gaseous carbonaceous feedstocks to syngas that can be combined with the conversion of metal oxides to metals. The details of each solar thermochemical process are reviewed and discussed in the following.

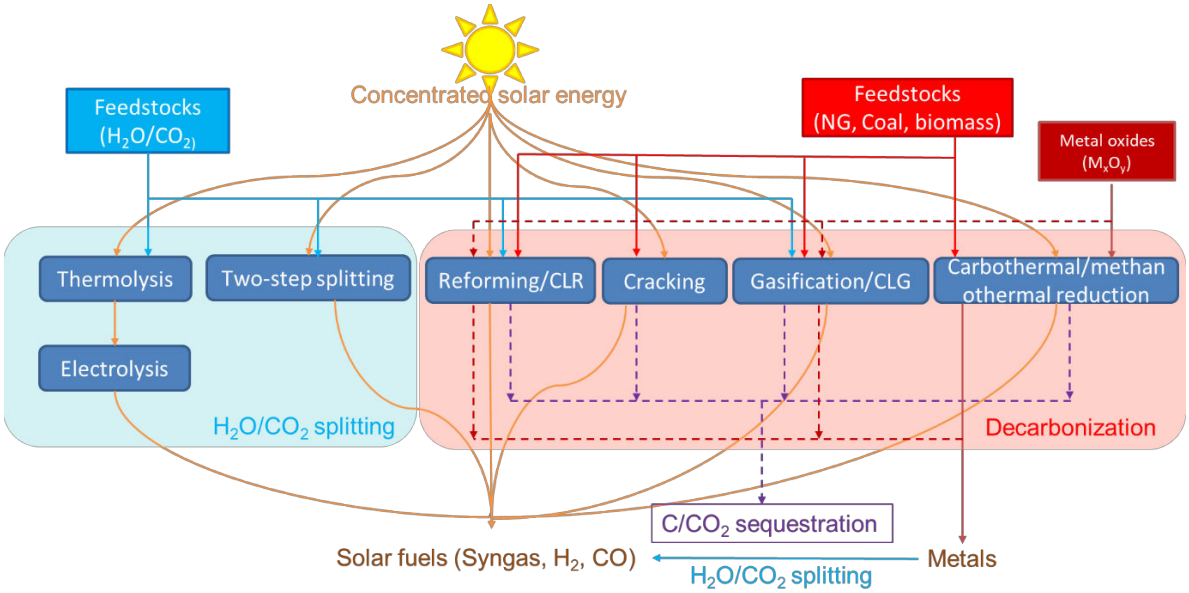

Figure 1-10. Thermochemical routes for solar fuel production using concentrated solar energy.

1.4.1 H_2O/CO_2 splitting

The H_2O/CO_2 splitting processes use only H_2O or CO_2 as feedstocks to produce H_2/CO. They consist of thermolysis/electrolysis and two-step splitting cycles.

1.4.1.1 Solar thermolysis of water

Direct thermal water splitting is the simplest pathway for solar thermochemical hydrogen production from H_2O, according to Eq. 1-7.

$$H_2O \rightarrow H_2 + \frac{1}{2}O_2 \tag{1-7}$$

Nevertheless, this process is hardly practical due to both very high temperatures needed as evidenced by the ΔG equal to zero at 4300 K for 1 bar (Fig. 1-11) [13], and difficulty in effectively separating/quenching H_2 and O_2 to avoid recombination and explosive mixtures. High solar flux concentration is thus required to reach the reduction temperature of H_2O,

thereby adversely resulting in issues regarding solar reactor materials thermal stability, costs, and heat losses.

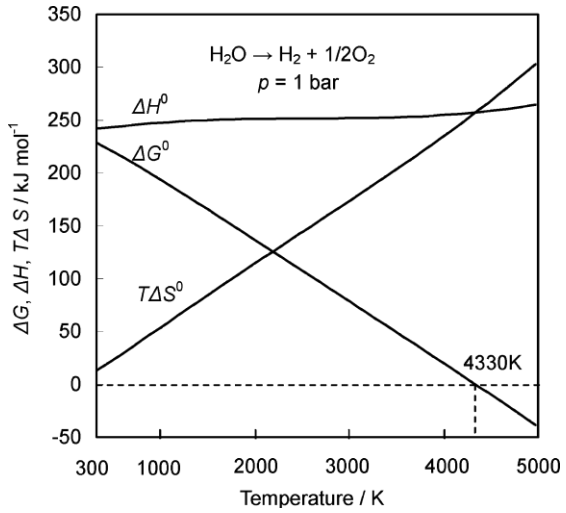

Figure 1-11. ΔH°, $T\Delta S^{\circ}$, and ΔG° as a function of temperature for direct thermal water splitting at 1 bar [14].

1.4.1.2 Two-step splitting cycles

Two-step thermochemical cycles are a series of consecutive chemical reactions. In this pathway, metal oxides (either non-volatile or volatile metal oxides) are employed as initial oxygen carrier materials that need to be reduced to release oxygen in the first step (endothermic) and recycled via oxidation with H_2O or CO_2 in the second step (exothermic); therefore, the process temperatures strongly depend on the applied metal oxides. Moreover, the reduction step requires reaction temperature lower than that of the thermolysis of water (single step), thereby allowing operation at moderately high temperatures. Likewise, the separation issue can be avoided as two-step thermochemical cycles produce H_2/CO and O_2 separately. The two-step thermochemical cycles using metal oxide redox pairs are shown in Eqs. 1-8 and 1-9:

1^{st} step endothermic reaction (Solar) : $M_xO_y \rightarrow xM + \frac{y}{2}O_2$ (1-8)

2^{nd} step exothermic reaction (non-solar) : $xM + yH_2O(CO_2) \rightarrow M_xO_y + yH_2(CO)$ (1-9)

Nakamura [15] originally proposed a simple two-step water-splitting cycle using Fe_3O_4/FeO redox pair:

$$Fe_3O_4 \rightarrow 3FeO + \frac{1}{2}O_2 \quad (1\text{-}10)$$

$$3FeO + H_2O \rightarrow Fe_3O_4 + H_2 \quad (1\text{-}11)$$

Fig. 1-12 shows the variations of ΔG as a function of temperature for the reduction of Fe_3O_4, Mn_3O_4, and Co_3O_4 metal oxides theoretically favored at above 2500 K, 2000 K, and 1000 K, respectively.

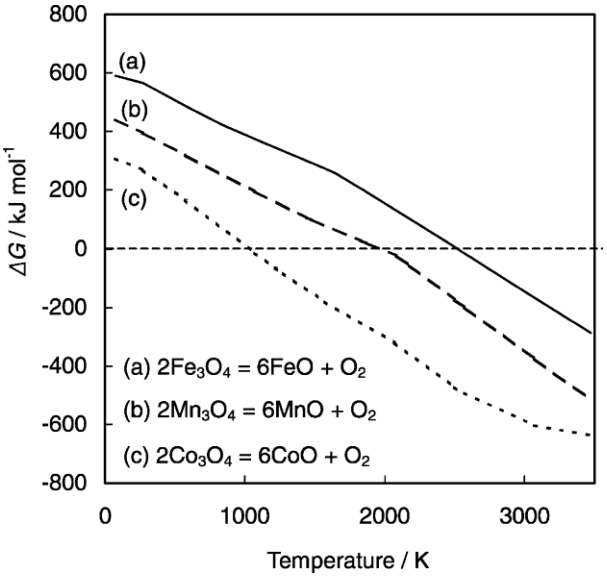

Figure 1-12. Variations of ΔG for the thermal reduction of (a) Fe_3O_4, (b) Mn_3O_4 and (c) Co_3O_4 as a function of temperature at 1 bar [14].

In contrast, the oxidation of MnO and CoO with water to produce hydrogen is not thermodynamically favorable as evidenced by ΔG above zero [16], whereas FeO oxidation is possible below ~1000K according to Fig. 1-13.

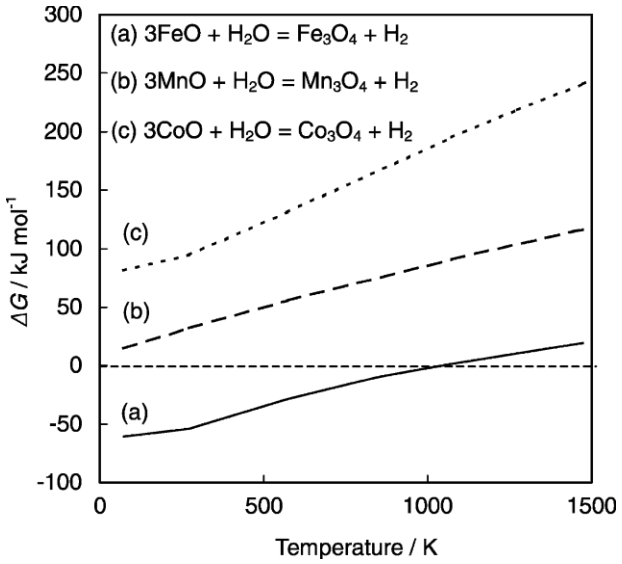

Figure 1-13. Variations of ΔG for the oxidation of (a) FeO, (b) MnO, and (c) CoO with water as a function of temperature at 1 bar [14].

From these observations, the ease of reduction and oxidation of any metal oxide needs to be thermodynamically evaluated for two-step thermochemical cycles.

1.4.2 Decarbonization processes

Decarbonization of hydrocarbon species consists of the conversion of solid/gaseous carbonaceous feedstocks to syngas. It can be combined with the conversion of metal oxides to metals using such feedstocks as reducing agents.

1.4.2.1 Solar cracking

The solar cracking involves the thermochemical decomposition of fossil fuels (pyrolysis) including natural gases, oil, and other hydrocarbons. The simplified net reaction is given in Eq. 1-12.

$$C_xH_y \rightarrow xC(s) + \frac{y}{2}H_2 \quad (1\text{-}12)$$

The products of the solar cracking process mainly consist of a carbon-rich condensed phase and hydrogen-rich gas phase. However, other components may occur depending on the composition of starting materials and reaction kinetics. The solid carbonaceous product can be used as a reducing agent for carbothermal reduction processes or valorized as it.

1.4.2.2 Solar reforming and solar chemical looping reforming (CLR)

The conventional steam/dry reforming method utilized in the chemical industry to produce syngas uses both fossil fuels as the source of process heat and catalysts to catalyze the endothermic chemical reactions. This results in both CO_2 emissions contributing to global warming and catalysts deactivation. Gaseous carbonaceous feedstocks such as methane (CH_4) are oxidized utilizing H_2O/CO_2 as oxidizing agents to syngas, and the reaction temperature is usually 1000 K at 1 atm. The simplified net reaction of steam reforming is given according to Eq. 1-13. Alternatively, the heat required for such an endothermic reaction can be supplied by solar energy using concentrating solar technologies, thereby storing solar energy into transportable and storable chemical fuels [13–15].

$$C_xH_y + xH_2O \rightarrow \left(\frac{y}{2} + x\right)H_2 + xCO \quad (1\text{-}13)$$

In contrast to the conventional method, solar chemical looping reforming of methane (CLRM) employs solid metal oxides as oxygen carriers in place of pure oxygen as the oxidant. For chemical looping scheme, in the endothermic step gaseous CH_4 is partially oxidized with the metal oxides to produce syngas while the metal oxide is reduced. The reduced metal oxide is subsequently oxidized in the exothermic step with H_2O/CO_2 to generate H_2/CO. The solid metal oxide oxygen carrier is then circulated between these two steps. The simplified net reaction of CLRM corresponds to Eqs. 1-14 and 1-15:

Endothermic partial oxidation of methane: $CH_4 + \frac{1}{\Delta\delta}MO_{x-\delta_{ox}} \rightarrow \frac{1}{\Delta\delta}MO_{x-\delta_{red}} + 2H_2 + CO$ (1-14)

Exothermic step: $\alpha H_2O + (1-\alpha)CO_2 + \frac{1}{\Delta\delta}MO_{x-\delta_{red}} \rightarrow \frac{1}{\Delta\delta}MO_{x-\delta_{ox}} + \alpha H_2 + (1-\alpha)CO$ (1-15)

The net products of chemical looping reforming equal those of steam and dry reforming for fractions of α= 1 and α= 0, respectively [17].

Compared to the first step in two-step redox cycles, the methane-induced reduction of metal oxides significantly lowers the reduction temperature [16] due to the CH_4 reducing agent. Since the metal oxide reduction with CH_4 and H_2O/CO_2 splitting steps can proceed at similar

temperatures, isothermal cycle operation is possible, thereby reducing the constrains imposed to reactor materials as well as thermal radiation losses [18].

The advantages of the CLRM are: (i) the discharge of pollutants is avoided, as the required heat is provided by solar energy [19–22], (ii) the utilization of CH_4 in the reduction step allows for isothermal operation between first and second steps, thereby avoiding sensible heat losses taking place during temperature-swing cycles and eliminating the need for heat recovery, (iii) solid oxide is used in place of gaseous oxygen which eliminates the need for oxygen production from air, (iv) reduced metal oxide can be subsequently oxidized with H_2O/CO_2 in the oxidation step to produce additional syngas and complete the cycle, (v) deposited carbon on metal oxide structures can be concomitantly gasified and removed during the oxidation step, thus avoiding material deactivation and eliminating the requirement for expensive catalysts.

The feasibility of utilizing metal oxides (either non-volatile or volatile metals) as oxygen carriers for CH_4 partial oxidation has been experimentally reported e.g. for ceria (CeO_2) [18], cerium-based oxides [23], iron oxide [24], tungsten oxide [21], and zinc oxide [25].

1.4.2.3 Solar gasification and solar chemical looping gasification (CLG)

Conventional gasification of solid carbonaceous feedstocks requires a significant portion of feedstocks (up to 30-45%) being subjected to combustion with air or oxygen to drive endothermic gasification reactions [26], in turn discharging a large amount of CO_2 [27]. Moreover, a purification of the produced syngas may be needed, thereby consuming additional energy for gas separation requirement [8-9]. Either solid fossil fuels (coal and pet coke) or renewable fuels (biomass) can be employed as feedstocks for the gasification. Additionally, when biomass is used as the feedstock, the process is carbon neutral. A novel approach for converting such solid carbonaceous feedstocks to syngas without CO_2 emissions is solar thermochemical gasification [10-15]. In this approach, two sustainable energy sources regarding solar energy and biomass can be combined in a single process to convert both biomass and intermittent solar energy into high-quality syngas [31,32]. The ideal stoichiometric steam-based gasification reaction of solid carbonaceous materials to syngas can be written by the simplified overall reaction as:

$$C_xH_yO_z + (x-z)H_2O \rightarrow \left(\frac{y}{2} + x - z\right)H_2 + xCO \quad (1\text{-}16)$$

When employing biomass as feedstock, the thermochemical gasification reactions are very complex because of the variability of starting biomass compositions in accordance with the variant of carbonaceous feedstock, age, geographic location and period of the year [33]. However, it can mainly be divided into two sequential processes. First, a pyrolysis step occurs via the decomposition of solid hydrocarbons at temperatures from 300 ˚C to 1000 ºC. The biomass chiefly decomposes into char, tars, and incondensable gases, as represented in Eq. 1--17. During this step, both high temperatures and heat transfer rates favor the production of gas products over char and tars [14].

$$Biomass \rightarrow char(carbon) + CO + CO_2 + H_2 + CH_4 + Tars \quad (1\text{-}17)$$

Second, the produced char is gasified with an oxidizing agent (such as steam or CO_2), thereby yielding different possible reactions (Eqs. 1-18 to 1-22):

$$C+H_2O \rightarrow CO+H_2 \qquad \Delta H^\circ = 131.3 \text{ kJ/mol} \qquad (1\text{-}18)$$

$$C+2H_2 \rightarrow CH_4 \qquad \Delta H^\circ = -74.6 \text{ kJ/mol} \qquad (1\text{-}19)$$

$$C+CO_2 \rightarrow 2CO \qquad \Delta H^\circ = 172.4 \text{ kJ/mol} \qquad (1\text{-}20)$$

$$CO+H_2O \rightarrow CO_2+H_2 \qquad \Delta H^\circ = -42 \text{ kJ/mol} \qquad (1\text{-}21)$$

$$CH_4+H_2O \rightarrow CO+3H_2 \qquad \Delta H^\circ = 206 \text{ kJ/mol} \qquad (1\text{-}22)$$

Equilibrium gas compositions of carbon-steam and carbon-CO_2 systems as a function of temperature show that H_2 and CO are the main gas produced when the temperature exceeds 1000°C [14]. In contrast, CH_4 decreases considerably when increasing the temperature because both CH_4 formation is thermodynamically favored at lower temperatures (CH_4 is unstable above ~1000°C) and the kinetics of methane formation is too slow [14].

In comparison to the conventional process, the advantages of the solar gasification of biomass are: (i) the portion of biomass feedstock (in the range of 30-45%) combusted for process heat can be avoided [34], thus increasing syngas output per unit of feedstock and reducing CO_2 emissions [35]; (ii) the production of an energy-rich and high quality syngas that is not contaminated by the products of combustion; (iii) the calorific value of the feedstock is solar upgraded, resulting in the storage of intermittent solar energy into a storable and dispatchable chemical fuel; (iv) the requirement of additional energy consumption in downstream gas separation systems is circumvented [28,29]; (v) the discharge of pollutants to the environment is avoided [36]; (vi) the solar reactor can be operated at high temperatures (>1200°C), resulting in faster reaction kinetics, higher syngas quality, and thereby avoiding the presence of tars in the produced syngas [37,38]. To cope with the problem of intermittent solar energy, the concept of hybrid solar gasification has been investigated [39,40] with emphasis on the importance of operating systems around-the-clock.

Alternatively, another novel approach is solar chemical looping gasification (CLG). The operating principles for the CLG are similar to CLRM. The difference is just the use of solid carbonaceous feedstocks in place of the gaseous feedstocks. In this pathway, the solid carbonaceous feedstocks, which can be fossil fuels or biomass, are partially oxidized to generate syngas utilizing metal oxides as oxygen carriers, while the metal oxide is reduced as given by:

$$CH_aO_b + \frac{1-b}{\delta} MeO_x \rightarrow CO + \frac{a}{2} H_2 + \frac{1-b}{\delta} MeO_{x-\delta} \qquad (1\text{-}23)$$

When the reduced metal oxide is re-oxidized by H_2O or CO_2, the overall reaction is given by Eq. 1-15. The CLG lies in the advantages outperforming the solar steam gasification in both being able to avoid the use of pure oxygen or H_2O in the reaction (corrosion issue), and operating as chemical looping cycles.

1.4.2.4 Solar carbothermal and methano-thermal reduction

Solar carbothermal reduction (CTR) and methano-thermal reduction (MTR) is the reduction of metal oxides using solid and gaseous feedstocks, respectively, as a reducing agent and concentrated solar energy as the source of process heat. Such reductants can be either fossil sources such as coke [41,42], coal [43], methane [25] or renewable sources biomass or biogas [44]. When employing biomass feedstock, the chemical reactions become the combination of CTR and gasification. The objective of the CTR and MTR is to produce metals (metallurgical processes) by removing oxygen from metal oxides utilizing carbonaceous feedstocks, generating metals and CO/syngas. The CTR and MTR overall reactions can be written as Eqs. 1-24 and 1-25 respectively:

$$M_xO_y + yC \rightarrow xM + yCO \quad (1\text{-}24)$$

$$M_xO_y + yCH_4 \rightarrow xM + yCO + y2H_2 \quad (1\text{-}25)$$

Comparing to direct thermochemical dissociation of metal oxides, the carbothermal/methanothermal chemical reactions can be conducted at much lower temperatures thanks to the reducing agent. For example, the solar direct ZnO dissociation (ZnO(s) + solar heat → Zn(g) + ½ O_2) requires temperatures up to ~1975 °C at atmospheric pressure [45–51], while the CTR of ZnO can be performed at a reduction temperature as low as 950 °C, resulting in 1025 °C lower compared to direct dissociation of ZnO.

1.5 Metal oxides redox pairs for solar thermochemical processes

Several metal oxide redox pairs have been studied extensively for solar thermochemical processes (two-step splitting cycles, CLR, CLG, CTR, and MTR). They can be mainly classified into two groups based on their phase change regarding volatile oxides such as ZnO [52], SnO_2 [53], and MgO [54] and non-volatile oxides such as iron oxides (Fe_2O_3/Fe_3O_4, ferrites [55]), and ceria (CeO_2/Ce_2O_3) [56] perovskites ($La_{1-x}Sr_xMnO_{3-\delta}$) [57]. In this study, four attractive metal oxides candidates regarding two non-volatile oxides (ceria and iron oxides) and two volatile oxides (ZnO and MgO) are considered as oxygen carriers or oxidants due to their interesting chemical and physical properties.

1.5.1 Volatile oxides

When employing volatile metal oxides (stoichiometric materials), a solid-to-gas/liquid phase transition of the products (either gaseous (ZnO/Zn) [58,59], MgO/Mg or liquid (SnO_2/Sn)) occurs in the reduction step. The reduced product species are first vaporized/melted and then condensed in the form of fine solid particles when temperature decreases. Volatile metal oxides usually have high oxygen storage capacity and high entropy variation since they can be completely reduced to their metallic elements, thus enhancing fuel production capacity. However, they come at the expense of a recombination issue with oxygen (O_2) during thermal reduction. Two attractive volatile oxides candidates (ZnO and MgO) are reviewed in different thermochemical processes.

1.5.1.1 ZnO

ZnO is an attractive candidate for various thermochemical processes because of its physical properties (Table 1-1). Its decomposition temperature is not too high (1975 °C) compared to other volatile candidates [60]. In addition, zinc is highly reactive for oxidation with H_2O/CO_2 to generate high-purity H_2/CO [47] and needed for the applications of both corrosion-resistant zinc plating of iron and electrical batteries [61]. The direct thermal dissociation of ZnO is usually conducted at temperatures exceeding 1975 °C at atmospheric pressure [45–51] as mentioned before. This system has been extensively investigated experimentally and numerically by research teams (e.g. at PROMES CNRS-Odeillo in France and PSI in Switzerland). Abanades et al [45] experimented and simulated the direct thermal dissociation of ZnO involved in water-splitting thermochemical cycles for hydrogen production. They found that reaction completion was achieved for reactant temperature exceeding 2200 K for a 1 mm initial particle diameter, and the higher the particle surface area, the higher the conversion rate. Koepf et al. [51] tested a 100 kW_{th} scale reactor for ZnO dissociation. The solar reactor was operated for over 97 h and yielded ZnO dissociation rates as high as 28 g/min totaling over 28 kg of processed reactant during 13 full days of experimentation. However, the major drawback of the thermal dissociation of ZnO is attributed to its high reduction temperature as well as recombination of Zn product. Alternatively, utilizing gaseous [19,62,63]/solid carbon species [19,43] as reducing agents regarding a CTR/MTR approach for the reduction of ZnO can tremendously lower the reduction temperature to ~950 °C [64], generating Zn and CO/syngas according to Eqs 1-26 and 1-27.

Carbothermal reduction of ZnO: $ZnO+C \rightarrow Zn+CO$ (1-26)

Methano-thermal reduction of ZnO: $ZnO+CH_4 \rightarrow Zn+2H_2+CO$ (1-27)

Prior thermodynamic and experimental studies on ZnO in different solar thermochemical processes dealing with the utilization of solid/gaseous carbonaceous feedstocks have been conducted. Osinga et al. [41] experimentally investigated the CTR of ZnO using a two-cavity packed-bed reactor. Thermal efficiency up to 20% was achieved for batch tests but 20% of non-reacted ZnO remained and was assumed to diffuse into the insulation material. The influence of temperature, carbon source, and carrier gas composition on CTR of ZnO was later examined utilizing the same reactor to gain data for designing a scaled up reactor [42]. Wieckert et al. [65] tested a 300 kW packed-bed batch reactor for the CTR of ZnO in the temperature range 1300-1500 K, yielding 50 kg/h of 95%-purity Zn and 30% of thermal efficiency, and confirmed that ZnO condensation and rock crystal generally grew on cooled surface. Various works on thermodynamic and experimental analysis of MTR of ZnO were proposed [62,63,66–69]. For example, Steinfeld et al. [63] examined the combined solar thermal reduction of ZnO and reforming of CH_4 in a fluidized-bed tubular quartz reactor at 1200 K and 1 atm. They reported that the combined process offered the simultaneous production of Zn and syngas from ZnO and CH_4 without discharging greenhouse gases. Three years later, the same group [25] tested the same process in a gas-particle vortex flow under continuous operation in the temperature range 1000-1600 K, yielding up to 90% of Zn conversion. Koepf et al. [59] studied the CTR of ZnO with beech charcoal in a continuous

beam down, gravity-fed solar reactor, yielding 12.4% of thermal efficiency, 75% of Zn content, and 14% of reactant conversion; however, critical issues related to clogging and significant unreacted reactant were encountered. Recently, Brkic et al. [70] tested CTR of ZnO in a drop tube reactor at pressure between 1 and 960 hPa and found that the Zn production rate is maximal at ~100 hPa and significantly drops under vacuum because of insufficient residence time and limited particles heat up in the reaction zone. Besides, vacuum CTR of ZnO was proposed in order to enhance the reduction rate [58,71] and decrease products recombination reaction, according to Le Chatelier's principle. Leveque and Abanades [58] studied the influence of the total pressure and the oxygen partial pressure (dilution) for the CTR of different volatile oxides (ZnO, SnO_2, GeO_2, and MgO) via solar-driven vacuum thermogravimetry. They reported that when metal oxides were reduced by lowering pressure, the reaction rate was greatly enhanced, and the required temperature to achieve a given reduction rate was significantly lowered. A decrease in total pressure also lowered the need for a diluent gas.

1.5.1.2 MgO

MgO is also considered as an attractive candidate for solar thermochemical processes [58] towards Mg commodity. Mg product is commonly used as structural material involving magnesium-based alloys [72,73] and power generation in magnesium-based combustion engines, and it also shows high reactivity and stability for H_2O/CO_2 splitting [58]. The melting and boiling points of MgO are extremely high (2852 °C and 3600 °C, Table. 1-1), while those of Mg are 650 °C and 1091 °C, respectively. Mg is conventionally produced by Pidgeon, Magnetherm, and electrolytic methods. The Pidgeon and Magnetherm techniques require the reduction of calcined dolomite ore with ferrosilicon at high temperatures (1700 °C), while the electrolysis requires the reduction of molten magnesium chloride in the temperature range 680–720 °C [74]. They proceed with additional materials (silicothermic process) and need very high energy consumption from either electricity or fossil fuels to drive the endothermic reactions, thereby raising serious environmental concerns. For these reasons, solar thermochemical reduction of MgO becomes an alternative attractive approach towards a CO_2-free Mg economy. Nevertheless, solar direct reduction of MgO ($MgO(s) + \text{solar heat} \rightarrow Mg(g) + 1/2O_2$) is not practical because of its extremely high dissociation temperature (3600 °C). Hence, carbothermal ($MgO + C \rightarrow Mg + CO$) and methano-thermal ($MgO + CH_4 \rightarrow Mg + CO + 2H_2$) reduction can be alternatively considered to be a better option for producing Mg. Previous studies mainly focused on the kinetics of the CTR of MgO with the utilization of various solid carbonaceous materials such as graphite [75–78] and charcoal [75] via thermogravimetry analysis (TGA). A two-step thermochemical process based on MgO/Mg with charcoal and petcoke for syngas production was thermodynamically and experimentally examined via TGA under atmospheric pressure [54], and the steam-hydrolysis of Mg was also studied in the temperature range 350–550 °C. The reactions kinetics were also studied and compared (the E_a values of MgO reduction with charcoal, 468.4 kJ/mol and petcoke, 419.1 kJ/mol were higher than those reported in previous studies [76]). The methano-thermal reduction of MgO was hardly found in literature [54].

Despite employing carbonaceous materials for decreasing the reduction temperature, the CTR of MgO still requires high temperatures above 1600 °C at atmospheric pressure for

complete conversion [76,78]. Two main approaches can be considered to avoid gaseous products recombination and allow metal product recovery: rapid quenching of the vapor and dissolving the magnesium directly in a suitable metal solvent before reversion can occur [79]. Alternatively, decreasing CO partial pressure also improves Mg yield [80]. Vacuum operation has been studied theoretically and experimentally with the MgO carbothermal reduction to lower the temperature [58,71,75,81–87]. This concept offers possibilities not only to alleviate heat losses and reactor materials issues but also to increase MgO reduction rate and conversion, at the expense of pumping energy requirement. Chubukov et al. [75] studied pressure dependent kinetics of MgO carbothermal reduction with carbon black in the temperature range 1350-1650 °C and pressure range 0.1–100 kPa in a graphite furnace. They found that the rate of MgO carbothermal reduction increased inversely with pressure, and a transition between conversions of 20–35% occurred after the reaction rate was maximal at 10 kPa. Recently, the same group [81] studied the kinetic enhancement of MgO carbothermal reduction with petroleum coke by the means of catalysis, milling, and vacuum operation in the same furnace.

Table 1-1. Physical and chemical properties of ZnO and MgO.

Property	Zinc oxide	Magnesium oxide
Chemical formula	ZnO	MgO
Molar mass	81.38 g/mol	40.3044 g/mol
Appearance	White solid	White powder
Density	5.606 g/cm^3	3.58 g/cm^3
Melting point	1,975 °C	2,852 °C
Boiling point	1,975 °C	3,600 °C
Solubility in water	0.0004% (17.8°C)	0.0086 g/100 mL (30 °C)
Refractive index (n_D)	2.0041	1.7355
Flash point	1,436 °C	Non-flammable
Specific heat capacity (C_p)	-	37.8 J/mol K
Std molar entropy (S^o298)	43.9 J·K^{-1}mol^{-1}	26.9 J·mol^{-1}·K^{-1}
Std enthalpy of formation (Δ_fH^o298)	-348.0 kJ/mol	-601.8 kJ·mol^{-1}
Gibbs free energy (Δ_fG°)	-	-596.6 kJ/mol
Crystal structure	Wurtzite	Halite (cubic)

1.5.2 Non-volatile oxides

In contrast to volatile oxides, non-volatile oxides remain in the solid state over the thermochemical process; therefore, only oxygen is released from their structure, thereby bypassing the recombination issue and suitably matching with CLRM and CLG pathways in terms of process operation in a single reactor. However, non-volatile oxides exhibit issues of both non-stoichiometric reaction (case of ceria), which results in lower oxygen storage/release capacity leading to low fuel productivity and sintering (case of iron oxides). For these reasons, physicochemical characteristics regarding specific surface area, particle porosity, particle size, and thermal stability become important factors for non-volatile oxides. Ferrites and ceria are reviewed for different solar thermochemical processes.

1.5.2.1 Ferrites

Ferrites are usually ferromagnetic ceramic compounds developed from iron oxides, e.g. magnetite (Fe_3O_4). Iron oxide is a promising candidate due to abundant source, low cost, and

easy handling. They exhibit large oxygen releasing ability compared to other candidates thanks to stoichiometric materials but may encounter sintering issues, contributing to low cycling stability [24,88]. Over the past four decades, Nakamura first assessed the two-step cycle of iron oxide (Fe_3O_4/FeO). The reduction reaction of Fe_3O_4 proceeds at temperature of 2500 K, and the subsequent hydrolysis reaction proceeds at 450 K. The melting points of Fe_3O_4 and FeO are 1870 K and 1650 K, respectively (Table 1-2). Thus, Fe_3O_4 is thermally reduced to liquid FeO in the first step. In the second step, solid FeO reacts with steam to generate hydrogen and solid Fe_3O_4. Steinfeld and Fletcher [89] conducted the CTR of Fe_2O_3 with graphite in the temperature range 1300-2390 K using solar energy. They found that the iron yields were extremely low when the reaction temperature was below its melting point due to slow reaction kinetics and diffusion limitation; moreover, the highest iron yields were obtained in a higher temperature range 1850-2390 K, demonstrating a relatively strong effect of the reactor temperature and the cooling and/or heating rate. The same research group proposed the solar Fe_3O_4+4CH_4 system [66,90,91] and reported that the chemical equilibrium species consist of metallic iron in the solid phase and a mixture of 67% H_2 and 33% CO in the gaseous phase (at 1 bar and 1027 °C), while showing experimentally that the reduction of Fe_3O_4 with CH_4 is strongly dependent on temperature and residence time. Lu et al. [24] investigated the reactivity of magnetite (Fe_3O_4) via CH_4 reforming and H_2O splitting in a continuous prototype. The reduction kinetics was also studied with both fresh and recycled magnetite. The hydrogen yields from the original and calcinated magnetite after successive cycling were 4.94 and 5.25 mmol/g, respectively, and the activation energy for the reduction was 93 kJ/mol. In addition, Bleeker et al. [88] studied the deactivation of iron oxide used in the steam-iron process to produce hydrogen and reported that the main drawback of using iron oxide is the inherent structural changes that take place during oxygen loading and unloading, leading to severe deactivation due to loss of specific surface area. In addition, doped iron oxides were examined thermodynamically and experimentally to improve their reactivity and stability [55,92–97], e.g. $Ni_{0.39}Fe_{2.61}O_4/ZrO_2$. Kodama et al. [55] evaluated $M_{0.39}Fe_{2.61}O_4$ with M = Ni, Zn, Co. The Ni-ferrite achieved the highest conversion and selectivity (X_{CH4} = 31%, S_{H2} = 75%, S_{CO} = 72%), and supporting on ZrO_2 reduced sintering and improved reactivity.

1.5.2.2 Ceria

Currently, ceria is considered as an attractive non-volatile redox candidate for both two-step H_2O/CO_2 splitting and CLRM. It exhibits crystallographic stability through extensive thermal cycling [98,99], oxygen release and storage capacities, fast oxygen exchange rates, and reversible shift between Ce^{4+} and Ce^{3+} oxidation states [100,101]. Ceria retains a stable cubic fluorite structure during large variations in oxidation state [102–104] and demonstrates rapid kinetics during thermochemical cycles as compared to other non-volatile metal oxides such as ferrites [55,105,106]. The physical properties of Ce(III) and Ce(IV) oxide are shown in Table 1-2. Ceria has been widely investigated as a redox material for thermochemical two-step H_2O/CO_2 splitting cycles in which reduction is conducted in an inert sweep gas or at sub-atmospheric pressures. The two-step solar-driven water-splitting cycle based on cerium oxides was first demonstrated by Abanades and Flamant [107]. The ceria is first partially reduced to

nonstoichiometric state at above 1400 °C [103]. Then, the reduced ceria ($CeO_{2-\delta}$) is re-oxidized completely with H_2O/CO_2 to form H_2/CO with fast reaction kinetic at lower temperature.

Alternatively, utilizing ceria as oxygen carriers for CLRM is also particularly attractive. Prior experimental studies considering the partial oxidation of CH_4 using the redox properties of ceria was first reported by Otsuka et al. [108], without the utilization of solar energy. They demonstrated that the conversion of methane into syngas with a H_2/CO ratio of two was possible, and the reduced ceria could be re-oxidized with CO_2 to produce CO. Then, both thermodynamic and experimental studies with the combination of concentrated solar energy were considered [109]. Krenzke and Davidson [109] studied the thermodynamics of the ceria cycle with methane. They indicated that coupling the reduction of ceria with the partial oxidation of methane enables isothermal cycling at 950 °C with high-quality syngas produced during the reduction step and maximum predicted solar-to-fuel efficiency of 40%. Welte et al. [22] experimentally investigated the methane reforming over ceria in a particle-transport reactor. This reactor achieved a bed-averaged oxygen non-stoichiometry (δ) as high as 0.25 at the expense of unreacted ceria particle being entrained by the produced syngas. Otsuka et al.[108,110,111] reported that carbon accumulation tends to occur when more than 80% of the available oxygen from the oxygen carrier material has been consumed. The ceria macrostructure plays a significant role on the performance of the combined two-step process in terms of conductive and radiative heat transfer across the material and reactivity. Various metal oxide structures such as porous foams [98,103,112–114], textured plates [113], vertical pins [113], powder [115], powder mixed with inert material [100], multi-channeled honeycombs [13,116], felts [104] and three-dimensionally ordered macroporous (3DOM) ceramics [13,104,114–117] have been studied for two-step thermochemical H_2O/CO_2 splitting cycles in order to provide an effective interface for uniform concentrated solar energy absorption and sufficient surface area for supporting rapid chemical reactions. The powder bed structure or powder mixed with inert promoter [100] exhibited rapid oxidation rates; however at the expense of high radiative opacity, which may lead to undesired temperature gradients across the bed. Such a barrier can be tackled by using porous foam structures with high specific surface area [117], although heat transfer limitation may arise from their high optical thickness. Such reactive structures could therefore be applied advantageously to the solar-driven isothermal chemical looping reforming process with CH_4 and oxidant gas (H_2O or CO_2) alternately flowing through the oxide structure.

Table 1-2. Physical properties of cerium and iron oxides.

Property	Cerium (III) oxide	Cerium (IV) oxide	Hematite	Magnetite
Chemical formula	Ce_2O_3	CeO_2	Fe_2O_3	Fe_3O_4
Molar mass	328.24 g/mol	172.115 g/mol	159.687 g/mol	231.533 g/mol
Appearance	Yellow-green dust	White or light pale yellow solid	Red-brown solid	Solid black powder
Density	6.2 g/cm^3	7.215 g/cm^3 (24 °C)	5.25 g/cm^3	5.00 g/cm^3
Melting point	2,177 °C	2,400 °C	1539 °C	1597°C
Boiling point	3,730 °C	3,500 °C	-	2623 °C
Solubility in water	Insoluble	Insoluble	Soluble in diluted acid	-
Crystal structure	Hexagonal, hP5	Cubic (fluorite)	Rhombohedral, hR30(α-form)	-

1.6 Reactors for solar thermochemical processes

The design of solar reactors for solar thermochemical processes remains one of the most significant challenges to improve process efficiency. Concentrated solar power input, chemical reactants, heat and mass transfer, chemical thermodynamics, residence time, reaction kinetics as well as operating temperature are important parameters for reactor design that must consider reactor type, geometry/size, materials of construction, and modes of operation. The reactors may be classified according to either reactor operation mode (batch and continuous reactors) or solar irradiation pathway (indirectly and directly irradiated reactors). For the directly-irradiated reactors, the chemical reactants are directly exposed to concentrated solar radiation, thereby providing efficient radiative heat transfer directly to the reaction site, at the expense of the need for a transparent window, which remains a critical and troublesome component at large scale and, particularly, under industrially-preferred high pressures [118]. The indirectly-irradiated reactors offer radiative heat transfer to the reaction site via an opaque absorbing wall, eliminating the need for a transparent window at the expense of limitations imposed by the absorbing materials such as maximum operating temperature, thermal conductivity, radiative absorptance, inertness, and resistance to thermal shocks. The different solar reactors are reviewed according to their operation with volatile oxides (such as ZnO and MgO), non-volatile oxides (such as ceria and ferrites), and biomass.

1.6.1 Solar reactors for volatile metal oxide processes

A large number of solar reactors have been designed, developed, and tested for direct dissociation, CTR, and MTR of ZnO. In this case, solar reactors can be classified regarding batch and continuous operation. On the one hand, packed-bed reactors, whether directly or indirectly irradiated are usually operated in a batch mode [41,42,65,119]. These reactor concepts demonstrate high extent of reaction as a result of the relatively large exposed reactant surface area able to absorb upcoming solar radiation and long residence time [65]; however, they exhibit temperature gradient issues [42], and unreacted reactant remaining [119]. For example, packed-beds at 5 kW_{th} lab-scale [41] (Fig. 1-14, left) and 300 kW_{th} pilot-scale [65] (Fig 1-14, right) were developed featuring two-cavity indirectly-irradiated solar reactors for the CTR of ZnO. They consist of two cavities in which the upper one acts as the solar absorber and the lower one acts as the reaction chamber. With this concept, the upper cavity can protect the window against products deposition and condensable gases coming from the reaction chamber.

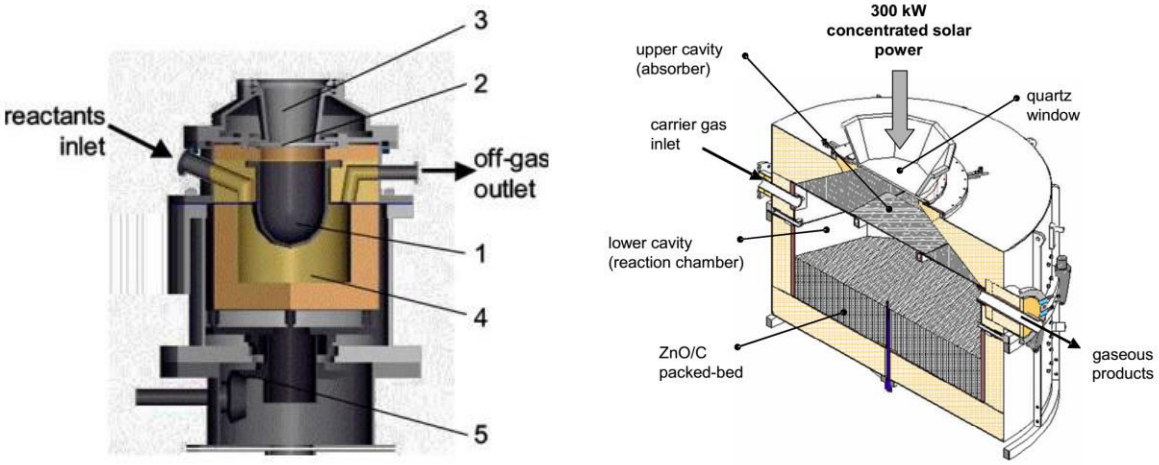

Figure 1-14. Two-cavity solar reactors: 5 kW_{th} [41] (left) and 300 kW_{th} [65] (right).

On the other hand, entrained particle flow [45,48,51,61], moving-front [50], gravity-fed [120,121], drop tube [70], vortex flow[25], and spouted-bed [122]solar reactors were operated in a continuous mode. These reactors achieve rapid conversion rates, but the reactant feeding rate must match well the reaction rate to avoid a reactant accumulation issue, and heat and mass transfer limitations must be taken into account [49]. The continuous system may also require large amounts of carrier gas for maintaining particle entrainment. When compared to batch operation, reactants conversion efficiencies may be lower, as residence time is shorter, and solid reactant can escape from the reactor with carrier gases. For example, continuous particle-fed [50] and pellet-fed solar reactors [45] for the direct dissociation of ZnO under controlled atmosphere are presented in Fig. 1-15 and 1-16, respectively. The former reactor was mounted on a horizontal axis solar furnace, and ZnO particles were fed by a screw feeder in a rotary cavity, while the latter one was installed at the focus of a vertical axis solar furnace and ZnO pellets were injected by a pushing rod. Both reactors were heated by real concentrated sunlight delivered by a sun-tracking heliostat and a 2 m diameter parabolic concentrator.

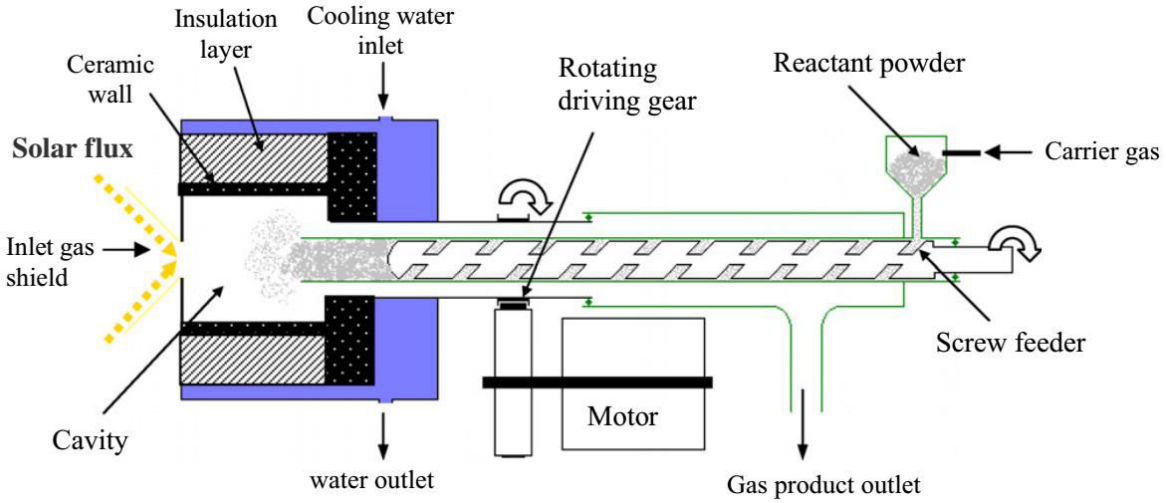

Figure 1-15. Particle-fed rotating solar reactor for continuous dissociation of ZnO [50].

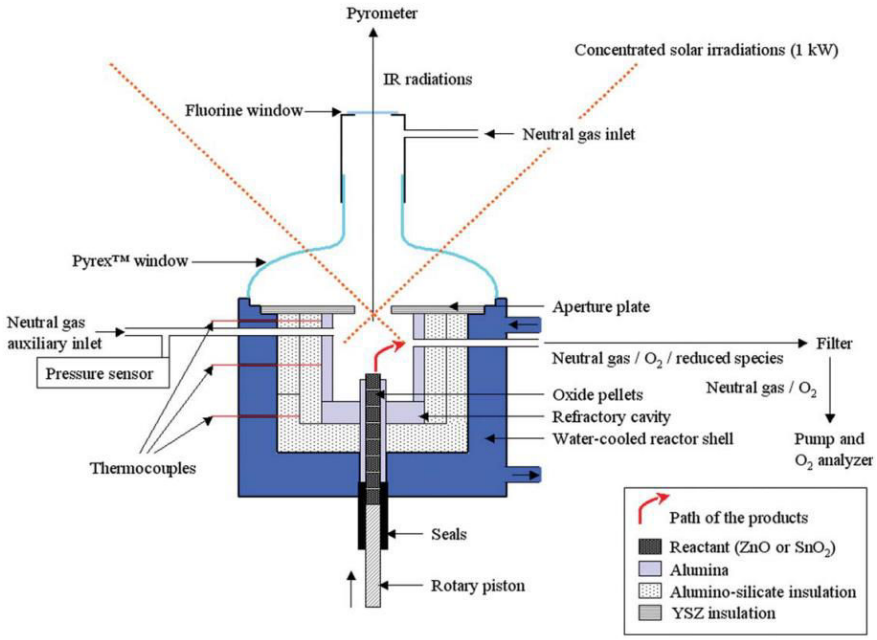

Figure 1-16. Pellet-fed moving-front solar reactor for continuous thermal dissociation of ZnO [45].

Two other directly-irradiated reactors designed for the solar thermal dissociation of ZnO operated in a semi-continuous mode in the temperature range of 2000-2300 K are depicted in Fig. 1-17. Their concept features a windowed rotating cavity-receiver lined with ZnO particles and exposed directly to high-flux solar irradiation [48,61].

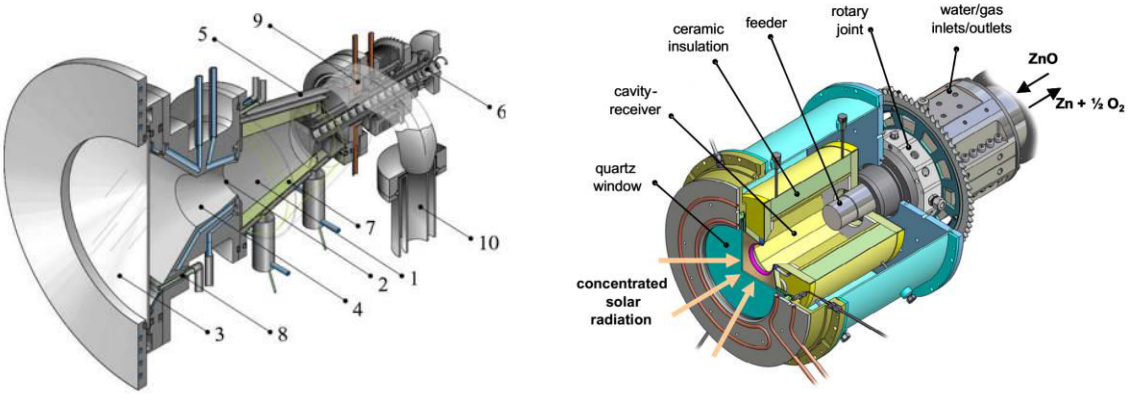

Figure 1-17. Scheme of the windowed rotating cavity-receiver solar reactor configurations for thermal dissociation of ZnO [48,61].

A vortex-flow solar reactor concept for the continuous combined ZnO reduction and CH_4 reforming at 1300 K is shown in Fig. 1-18. It includes a cylindrical cavity containing a windowed aperture to capture concentrated solar energy. A mixture of ZnO particles and CH_4 was continuously fed into the cavity receiver via a tangential inlet port while the chemical products regarding Zn vapor and syngas exited the cavity via a tangential outlet port.

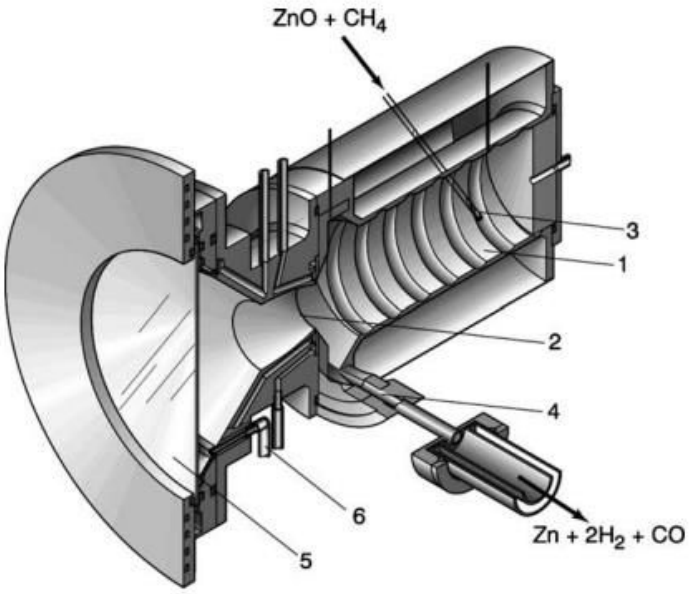

Figure 1-18. Vortex-flow solar reactor concept for the combined ZnO reduction and CH_4 reforming [25].

1.6.2 Solar reactors for non-volatile metal oxide processes

Similar to the solar reactors developed for volatile metal oxides, solar reactor concepts are generally fixed bed and fluidized bed reactors. Regarding fixed bed reactors, Marxer et al. [103] studied the two-step solar thermochemical CO_2 splitting cycle using a reticulated porous structure made of ceria. A schematic of the directly-irradiated solar configuration is shown in Fig. 1-19. It consists of a windowed cavity-receiver including a reticulated porous ceramic (RPC) foam-type structure directly exposed to high-flux solar irradiation provided by a solar simulator. The maximum conversion of 83% for CO_2 and solar-to-fuel energy efficiency of 5.25% were achieved.

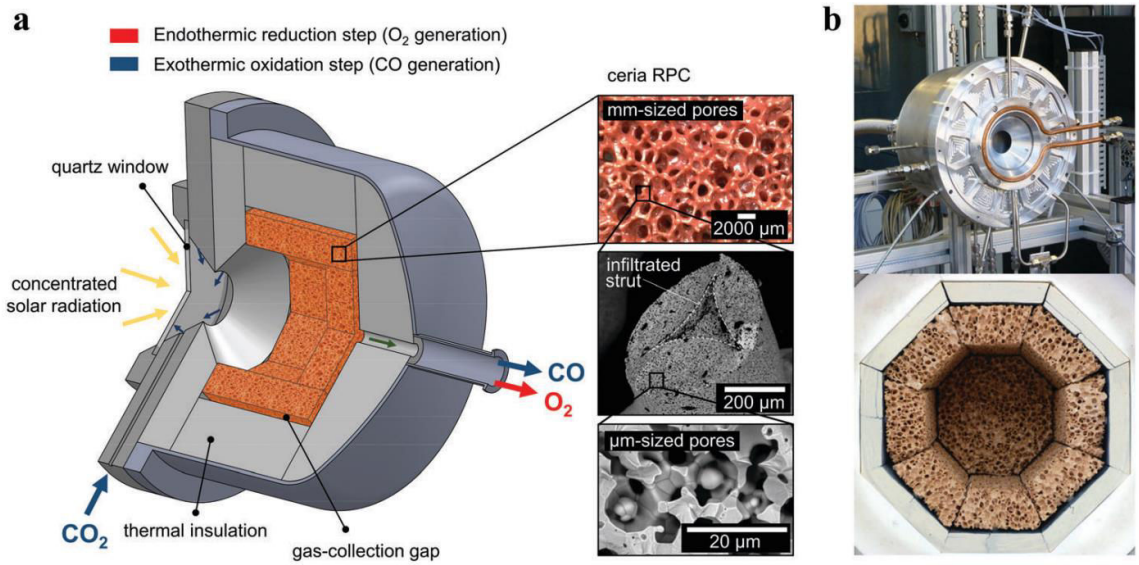

Figure 1-19. Schematic of the solar reactor configuration for CO_2 splitting via a two-step thermochemical redox cycle [103].

Another example of solar fixed bed concept is an indirectly-irradiated tubular reactor (Fig. 1-20) [100]. This reactor was tested for both ceria redox cycle and CLRM using ceria particles as oxygen carrier and H_2O/CO_2 as oxidants in second exothermic oxidation step. It comprises a cavity receiver with the aperture (15 mm diameter) placed at the focal point of a horizontal axis solar furnace. The cavity made of graphite is lined with a surrounding insulation layer and separated from the atmosphere using a glass window. High reduction rate and bed-averaged oxygen non-stoichiometry (δ) up to 0.431 during reduction with CH_4 at 1000 °C were achieved.

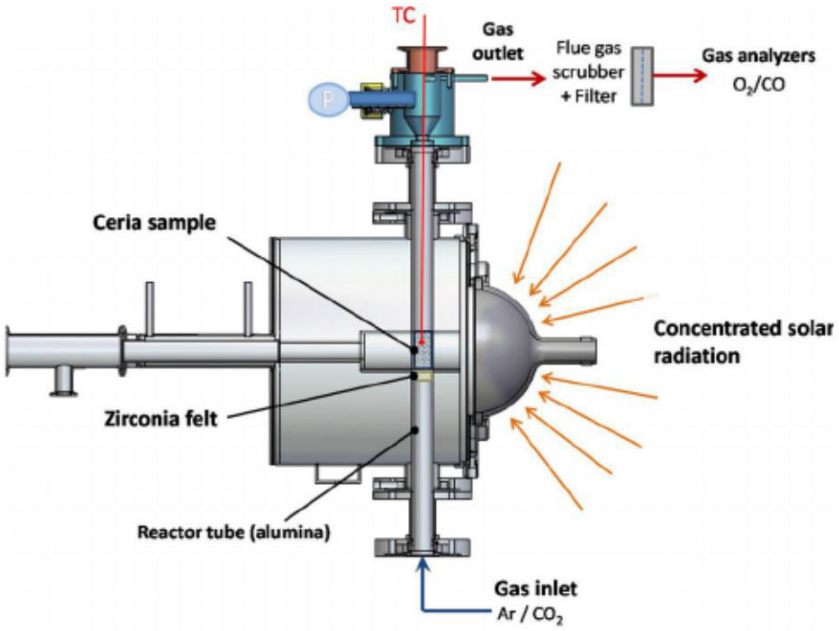

Figure 1-20. Schematic of the indirectly-irradiated tubular reactor for solar-driven CeO_2 redox cycles [114].

To enhance heat and mass transfer, fluidized-bed solar reactors were proposed in which reactants are continuously stirred with inert particles by a neutral gas and/or oxidizing agent. Gokon et al. [123] tested the two-step water splitting for hydrogen production by using a single reactor consisting of an internally-circulating fluidized bed of $NiFe_2O_4$ or ceriaparticles at a temperature up to 1600 ℃ (Fig. 1-21 left). A metal foam distributor of porous stainless-steel was fixed at the bottom of the fluidized bed region of the reactor. The circulating fluidized bed was subjected to simulated solar light from Xe lamps with an input power in the range 1.6–2.6 kW_{th}. As a result, hydrogen productivity reached about 1000 Ncm^3 for successive reactions of thermal-reduction and water-decomposition, while ferrite conversion was in the range 5–35%. However, the major drawbacks of fluidized bed reactors are the reactive particle size limitation and the difficult operation in continuous mode. In addition, Welte et al. [22] examined the continuous combined ceria reduction and methane reforming in a 2 kW_{th} particle-transport solar reactor utilizing a vertical Al_2O_3 tube receiver including a downward gravity-driven particle flow of ceria particles (Fig. 1-21 right). Ceria particles were delivered to the alumina tube in either co-current or counter-current to a CH_4 flow. Methane conversion was up to 89% at 1300 °C for residence times under 1 s and the maximum reduction extent (δ) was 0.25.

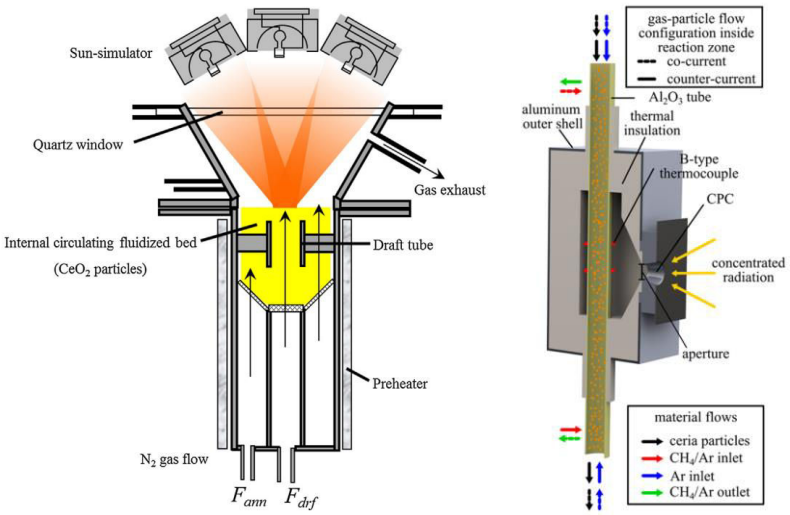

Figure 1-21. Schematic of the fluidized bed solar reactor for two-step H_2O splitting using metal oxides particles (left) [123] and solar particle-transport reactor for continuous combined ceria reduction and methane reforming (right) [22].

1.6.3 Solar reactors for gasification

The solar reactor concepts for solar gasification of solid carbonaceous materials are similar as compared to those for volatile and non-volatile oxides. For example, Piatkowski et al. [124,125] conducted steam-gasification of coal, biomass, and carbonaceous waste feedstocks for syngas production in 5 kW and 150 kW [126] indirectly irradiated packed-bed reactors operated in a batch mode. Such reactors feature two cavity receivers with an emitter plate between them (Fig. 1-22 left). They achieved high solar-to-chemical energy conversion efficiencies varying between 17.3% and 29% but exhibited issues with liquid tars in the product gas stream and incomplete conversion because of non-homogeneous heating. The gasification of carbonaceous materials with fluidized-bed reactor was also investigated. The reactor uses oxidative gas to stir solid feedstocks within the cavity receiver (Fig. 1-22 right). This reactor can especially overcome the limitations of heat and mass transfer, enhance solid residence times, and reduce ash buildup [127–129], however at the expense of limitation of allowable feedstock size (<1 mm) and operation usually in batch mode.

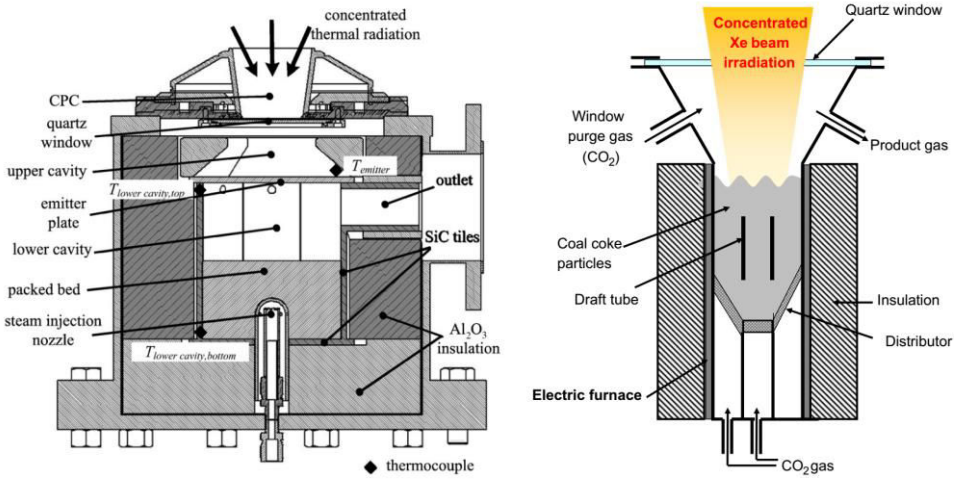

Figure 1-22. Section view of the packed-bed solar reactor, featuring two cavities separated by an emitter plate (left) [124] and internally circulating fluidized bed reactor (right) [129].

Additional design and development of solar-driven gasification reactors include the utilization of molten salts that offer the advantages of improved heat transfer, catalysis of gasification, reduced production of tars as well as thermal stability (inertia) for transient solar power input [130]. Hathaway and Davidson [131] demonstrated a 2.2 kW prototype molten salt solar gasification reactor in a continuous process, Fig.1-23. This reactor yielded a solar-to-fuel thermochemical efficiency of up to 30% and converted 47% of the carbon at 945 °C. However, the problems of unreacted char release and salt leakage were pointed out. In addition, entrained flow reactors have been developed for improving heat and mass transfer and for operating in a continuous process; nevertheless, the drawback of such reactors is an excessively short residence time, and rather small particles (<1 mm) are required [132]. In order to increase the residence time that significantly affects the extent of reaction, drop-tube and vortex flow reactors have been proposed; however, the particle sizes of feedstocks are quite limited for these reactors. Bellouard et al. [30] developed and tested a high-temperature tubular solar reactor (1 kW_{th}) combining drop tube and packed-bed concepts for continuous solar-driven gasification of biomass, according to Fig. 1-20. This reactor yielded an energy upgrade factor of 1.21 and a solar-to-fuel thermochemical efficiency up to 28% at 1400 °C. Müller et al. [118] demonstrated a 3 kW indirectly-irradiated (windowless, Fig. 1-24a) vortex flow solar reactor for the thermochemical gasification of carbonaceous particles at high pressures (1–6 bars). The reactor performances were studied and compared with a directly-irradiated (windowed, Fig 1-24b) vortex flow reactor. The calorific value of the feedstock was upgraded from 16% to 35% and a peak solar-to-fuel energy conversion efficiency of 20% was achieved. Higher reaction extents, solar-to-fuel energy conversion efficiencies and calorific upgrade factors were demonstrated with the indirectly-irradiated solar reactor than with the directly-irradiated configuration.

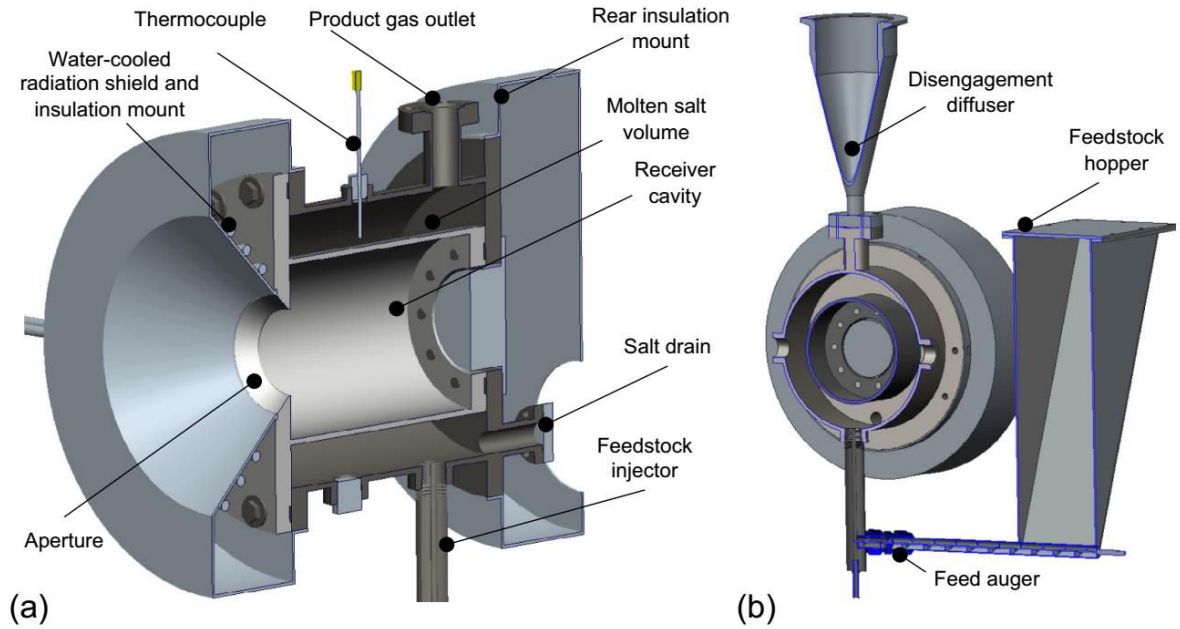

Figure 1-23. Schematic the molten salt gasification reactor with (a) side-cutaway to reveal key internal features and (b) axial-cutaway at the injector plane to illustrate feed delivery system and exit disengagement diffuser [131].

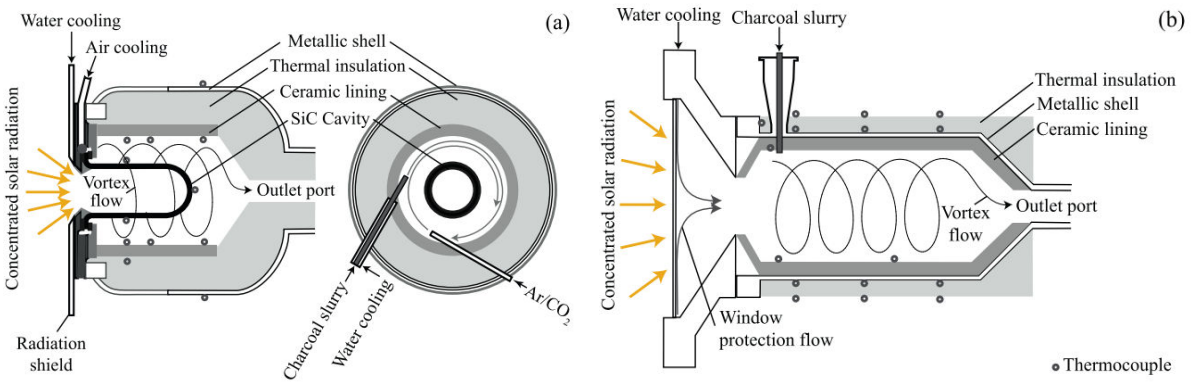

Figure 1-24. Schematic of: (a) the indirectly-irradiated solar reactor and (b) the directly-irradiated solar reactor [118].

1.7 Conclusions

Solar thermochemical processes offer promising pathways to convert gaseous and solid carbonaceous feedstocks to solar fuels and further allow production of metals from their corresponding metal oxides. These energy-demanding processes use solar energy to drive endothermic chemical reactions, concomitantly storing intermittent solar energy into transportable and storable energy carriers. Cracking, reforming/chemical looping reforming, gasification/chemical looping gasification, and carbothermal/methanothermal reduction represent attractive approaches for short-term solar process implementation, while direct thermolysis and two-step H_2O/CO_2 splitting represent a promising option for long-term sustainable fuel production. In this work, three main solar thermochemical conversion approaches regarding solar chemical looping reforming (CLR), solar carbothermal reduction (CTR), and solar gasification (Fig. 1-25) were experimentally investigated to demonstrate their feasibility, reliability and robustness in converting both gaseous and solid carbonaceous feedstocks to syngas and producing metals in solar reactors. On-sun experiments were performed to gain understanding on the involved phenomena, reaction mechanisms and reactor performance under solar irradiation conditions. They were carried out in 1.5 kW_{th} prototype solar chemical reactors utilizing highly concentrated sunlight provided by a solar concentrating system. On the one hand, the spouted bed solar reactor with continuous particle injection was employed for investigating solar gasification of biomass and combined gasification/CTR of ZnO with biomass, which was demonstrated for the first time, and it was further adapted for studying the CLRM process (Fig. 1-25). On the other hand, the high-temperature cavity-type solar reactor was developed for the CTR of both ZnO and MgO in batch and continuous operation under vacuum and atmospheric pressures. Concerning metal oxides, ceria and iron oxides were considered as oxygen carriers for the CLRM process, while ZnO and MgO were considered for the CTR process because they represent attractive metal oxides candidates as previously described in the review parts. Regarding feedstocks, methane and H_2O/CO_2 were considered as gaseous feedstocks for the CLRM process while wood biomass and solid carbon (charcoal/carbon black/graphite) were considered as either solid feedstocks for gasification or reducing agents for CTR, Fig. 1-25.

Insights into the influence of operating parameters on conversion, yield, and reactor performance metrics are emphasized during experimental investigations. The feasibility and

reliability of the considered processes are demonstrated, and research findings can be applied in next future works.

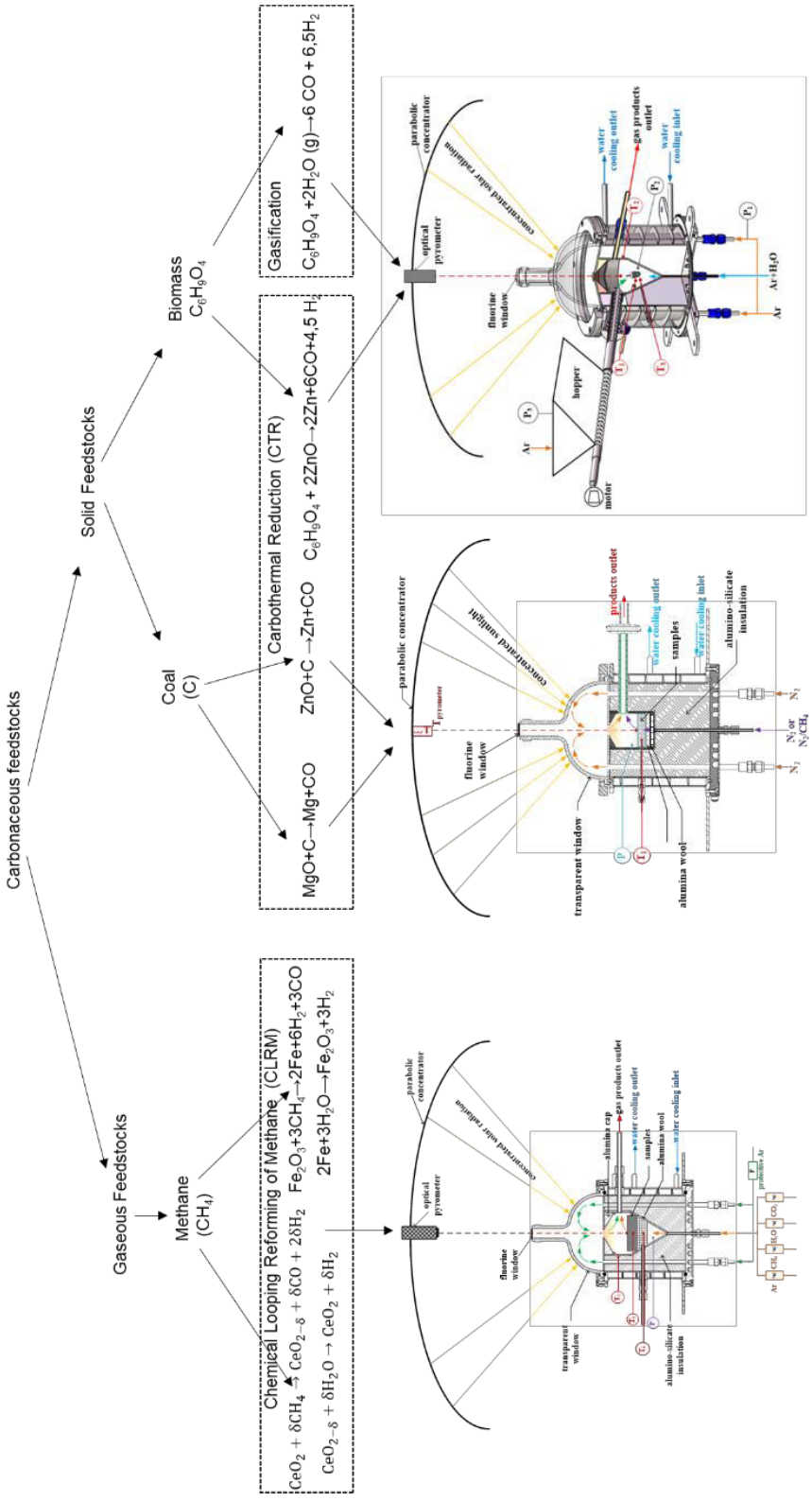

Figure 1-25. Summary of the experimental routes investigated regarding the three considered solar thermochemical processes in different solar reactors.

Chapter 2: Solar chemical looping reforming of methane through iron and cerium oxides[1]

2.1 Introduction

Methane reforming is the conventional method for producing synthesis gas (syngas). Steam [133] and dry reforming [134–137] are two possible routes for methane reforming:

$$\text{Steam reforming: } CH_4+H_2O\rightarrow 3H_2+CO \quad \Delta H^0=+206 \text{ kJ/mol} \tag{2-1}$$

$$\text{Dry reforming: } CH_4+CO_2\rightarrow 2H_2+2CO \quad \Delta H^0=+247 \text{ kJ/mol} \tag{2-2}$$

Both reactions are highly endothermic, and the required energy to drive these reactions is generally supplied by the combustion of fossil fuels, resulting in methane feedstock consumption and greenhouse gas emissions, especially CO_2 responsible for climate change and global warming. Using solar energy in place of fossil fuels for supplying process heat thus represents a suitable option to alleviate these issues. Alternatively, a promising modern pathway to produce clean syngas is the utilization of metal oxide redox pairs for partial oxidation of methane (namely, chemical looping reforming of methane, CLRM) using concentrated solar energy to drive endothermic reactions [18,56,138]. Such a process usually encompasses two steps: (1) partial oxidation of methane along with metal oxide reduction, and (2) re-oxidation of the oxide with steam (or CO_2) to produce pure H_2 (or CO). The net products of CLRM are the same as those of steam (Eq. 2-1) and dry reforming (Eq.2-2).

The additional advantages of solar CLRM with metal oxides when compared to the conventional methane reforming process are: (i) produced syngas has a H_2:CO ratio of 2:1, suitable for methanol synthesis, (ii) an excess in oxidizer is not necessary while conventional process needs to be operated with excess oxidizer (H_2O:$CH_4\geq 3$), which rises energy requirements and reduces process efficiency [139].

Cerium and iron oxides are particularly attractive because of their different beneficial physical and chemical properties [140]. Ceria keeps a stable cubic fluorite structure during large changes in oxygen non-stoichiometries (reduction extents), and exhibits rapid oxygen storage/release through lattice transfer [100,101,112,141]. On the other hand, iron oxide (Fe_2O_3) is abundant and low cost, and exhibits large oxygen releasing ability compared to CeO_2 and other candidates, but it may encounter sintering issues, leading to low cycling stability [24,88]. The main motivation of using iron oxide for CLRM is thus related to process cost reduction because of large material availability, compared to cerium oxide. Moreover, the sintering issue of iron oxide may be counterbalanced by its superior fuel production capability

[1] Details of this chapter consist of three peer-reviewed articles:

- S. Chuayboon, S. Abanades, S. Rodat, *Energy Technol*. -(2019) 1900415.
- S. Chuayboon, S. Abanades, S. Rodat, *J. Energy Chem*. 41 (2020) 60–72.
- S. Chuayboon, S. Abanades, S. Rodat, *Chem. Eng. J*. 356 (2019) 756–770.

due to reactions involving multivalent iron species (Fe, FeO, Fe_3O_4), thus potentially leading to higher amounts of oxygen transferred during redox reactions. Conversely, the exchanged oxygen and fuel productivity from ceria are determined by the reduction extent corresponding to the achieved non-stoichiometry (amount of oxygen vacancies in $CeO_{2-\delta}$, which is always lower than δ_{max}=0.5 mol_O/mol_{CeO2} corresponding to complete reduction of Ce(IV) to Ce(III)). Thus, evaluation and comparison of the materials reactivity for fuel production upon cycling under real solar irradiation conditions is necessary to identify the most suitable one.

In this chapter, the CLRM process is experimentally investigated in a directly-irradiated volumetric lab-scale solar reactor utilizing iron and cerium oxides with different structures (packed-bed powder, blend of metal oxide mixed with inert Al_2O_3 particles, and reticulated porous foam). The work mainly focuses on cerium oxide candidate while iron oxide was studied for comparison purpose. The relevant performance metrics of the process are quantified including metal oxide structures influence, lattice oxygen transfer (n_O) and average oxygen non-stoichiometry (δ), methane conversion (X_{CH_4}), syngas yield, sintering temperature, and thermochemical cycling stability. A comprehensive experimental analysis of the solar process performance outputs was performed, encompassing quantification of gas yields produced during each step and by each side reaction, amounts of oxygen transferred during the redox process as well as energy conversion efficiency. In addition, the demonstration of the whole two-step solar process in a solar reactor operated with a real solar concentrating system is presented with determination of the fuel production capacity during both steps.

2.2 Thermodynamics

2.2.1 Iron oxide

The endothermic reduction reaction of iron oxide (Fe_2O_3) with CH_4 is composed of successive steps:

$$Fe_2O_3+1/3CH_4 \longrightarrow 2/3Fe_3O_4+2/3H_2+1/3CO \quad (2\text{-}3)$$
$$2/3Fe_3O_4+2/3CH_4 \longrightarrow 2FeO+4/3H_2+2/3CO \quad (2\text{-}4)$$
$$2FeO+2CH_4 \longrightarrow 2Fe+4H_2+2CO \quad (2\text{-}5)$$

The summation of the above reactions corresponds to:

$$Fe_2O_3+3CH_4 \rightarrow 2Fe+6H_2+3CO \qquad \Delta H^0 = 715\ kJ/mol \quad (2\text{-}6)$$

The enthalpy of CLRM with Fe_2O_3 (Eq. 2-6) is three times higher than those of conventional reforming (Eqs. 2-1 and 2-2); thus, the use of solar energy as energy source of process heat is appropriate to drive the chemical reaction of CLRM.

Possible side reactions related to methane cracking and direct reaction of Fe_2O_3 with carbon may also occur during iron oxide reduction with methane:

$$CH_4 \longrightarrow C+2H_2 \quad (2\text{-}7)$$
$$Fe_2O_3+3C \rightarrow 2Fe+3CO \quad (2\text{-}8)$$

The exothermic oxidation reaction of metallic iron with H_2O is represented as:

$$3Fe+4H_2O \longrightarrow Fe_3O_4+4H_2 \qquad \Delta H^0 = -151 \text{ kJ/mol} \tag{2-9}$$

Fe_3O_4 re-oxidation to Fe_2O_3 with H_2O is not thermodynamically possible.
Possible side reactions during oxidation step are carbon deposition gasification with H_2O:

$$C+H_2O \longrightarrow CO+H_2 \tag{2-10}$$
$$C+2H_2O \longrightarrow CO_2+2H_2 \tag{2-11}$$

The thermodynamic feasibility of chemical reactions involving iron oxide species reduction with methane can be assessed from the Gibbs free enthalpy change (ΔG°) (Fig. 2-1). The ΔG° values decrease with temperature (ΔG° equals zero at 400 °C for $3Fe_2O_3+CH_4$, and at above 600 °C for the other reactions), which means that all the reduction reactions are thermodynamically favorable when increasing the temperature.

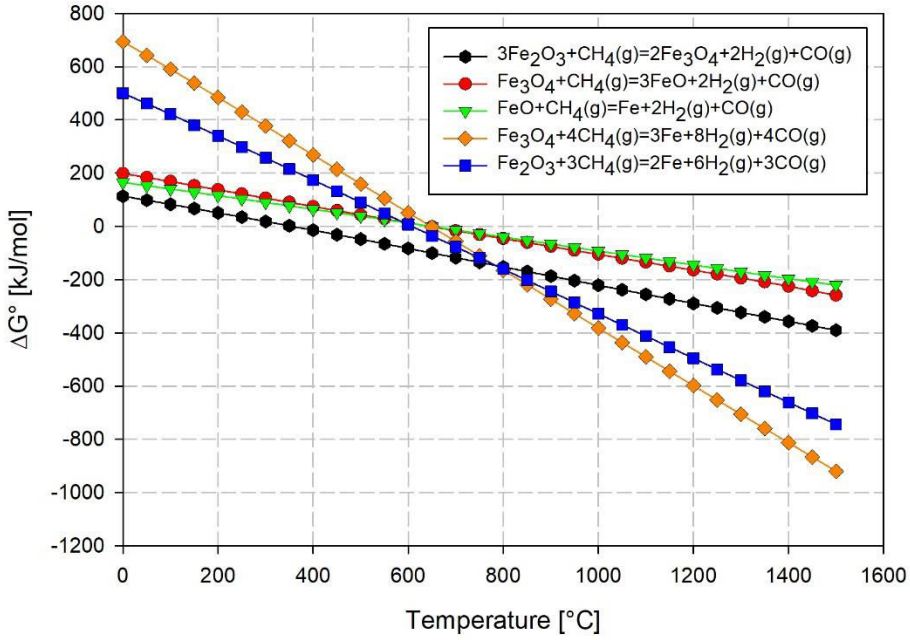

Figure 2-1. ΔG° variations for iron oxides reduction with methane as a function of temperature.

Regarding the possible side reactions (Fig. 2-2), the direct reductions of Fe_3O_4 with C and H_2 are thermodynamically favorable (Fe_3O_4+2C and Fe_3O_4+4C proceed spontaneously at above 700 °C, and $Fe_3O_4+4H_2$ proceeds at above 1100 °C). In contrast, the direct reduction of Fe_3O_4 with CO is not thermodynamically possible.

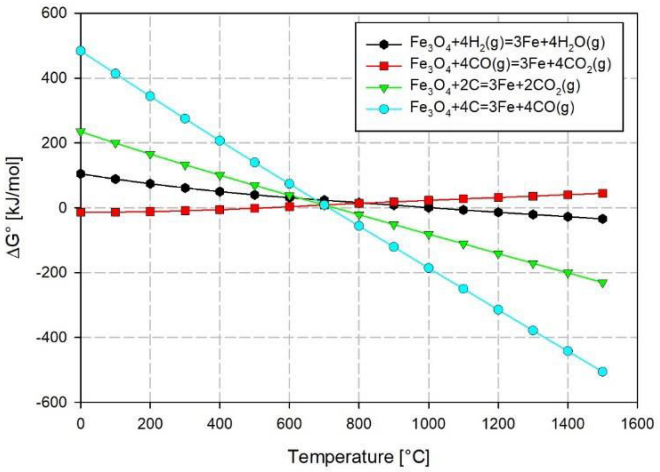

Figure 2-2. Variations for the reactions of Fe_3O_4 with H_2, CO, and C as a function of temperature.

The thermodynamic equilibrium composition was calculated with HSC Chemistry software to appraise the species distribution and system composition as a function of temperature. It provides a realistic overview of the chemical product species and the most favorable conditions for carrying out the reduction reaction with CH_4 and for reaching completion. The main assumptions of the method must be reminded, including closed system approach without any gas flow and available thermodynamic properties for any chemical species to represent the system as closely as possible.

The equilibrium species composition of Fe_2O_3+3CH_4 at 1 bar as a function of temperature is shown in Fig. 2-3 (and in Fig. A-1 for Fe_3O_4+4CH_4 in Appendix A). Fe_2O_3 is first reduced to Fe_3O_4 while methane is decomposed to C and H_2 when the temperature exceeds 400 °C. Then, Fe_3O_4 is reduced to FeO, along with intermediate non-stoichiometric species ($Fe_{0.945}O$, $Fe_{0.947}O$, and $FeO_{1.056}$) while H_2, C, and H_2O(g) become the main product components. Above 400 °C, FeO starts reducing into Fe, along with CO and CO_2 formation. Complete reduction to Fe is reached above 700 °C, while C, H_2O, and CO_2 decrease constantly. Finally, the main products are both H_2 and CO with H_2/CO ratio approaching two, and Fe above 1000 °C.

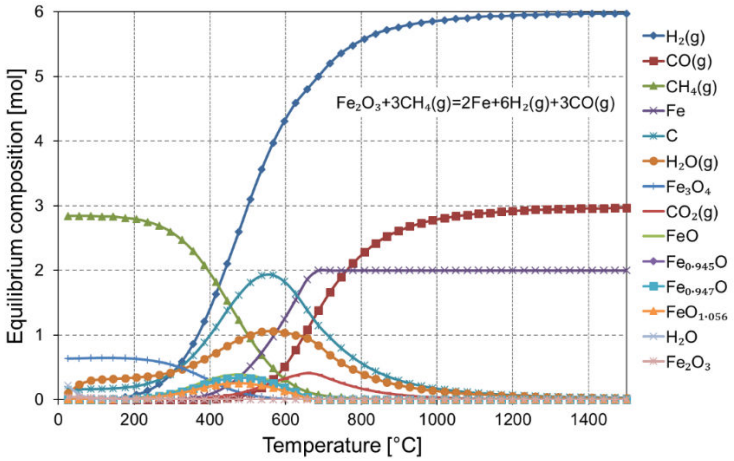

Figure 2-3. Thermodynamic equilibrium composition of methane reforming over Fe_2O_3 as a function of temperature at 1 bar.

Regarding carbothermal reduction of Fe_2O_3 in Fig. 2-4 (and in Fig. A-2 for Fe_3O_4+4C), Fe_2O_3 is first reduced to Fe_3O_4 along with the formation of CO_2 above 200 °C. Subsequently, Fe_3O_4 is reduced to FeO and non-stoichiometric compounds ($Fe_{0.945}O$, $Fe_{0.947}O$, and $FeO_{1.056}$) above 400 °C, and FeO is finally reduced to Fe along with CO formation above 500 °C. Reduction to Fe reaches completion at above 800 °C, while CO_2 declines continuously. The global reaction approaches completion at above 1000 °C, yielding Fe and CO.

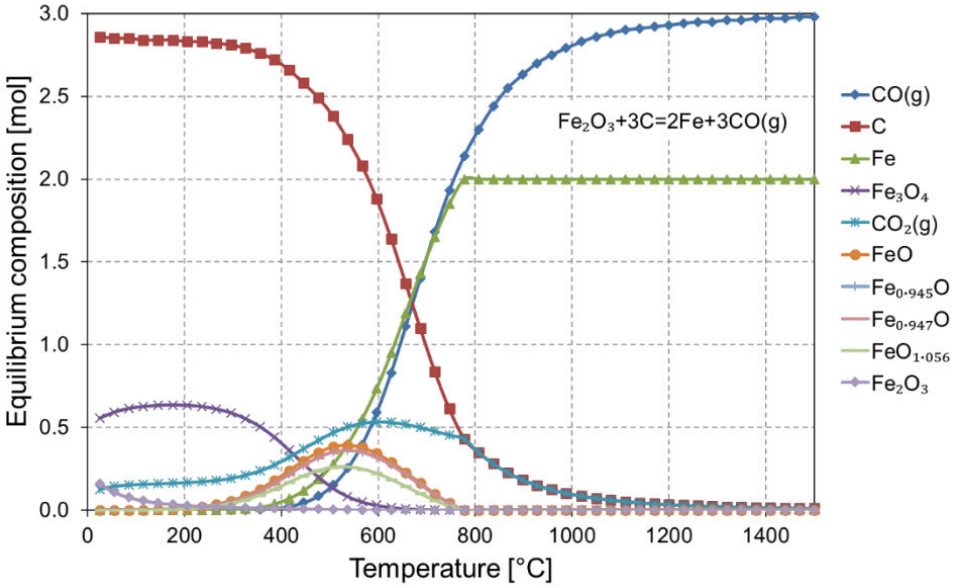

Figure 2-4. Thermodynamic equilibrium composition of Fe_2O_3 carbothermal reduction as a function of temperature at 1 bar.

2.2.2 Cerium oxide

Solar CLRM based on non-stoichiometric cerium oxide is represented as:

$$\text{Reduction step: } CeO_2 + \delta CH_4 \longrightarrow CeO_{2-\delta} + \delta CO + 2\delta H_2 \quad (2\text{-}12)$$

$$\text{Oxidation step: } CeO_{2-\delta} + \delta H_2O(\delta CO_2) \longrightarrow CeO_2 + \delta H_2(\delta CO) \quad (2\text{-}13)$$

The thermodynamic equilibrium composition for the reduction step (Fig. 2-5) shows that CH_4 first starts thermally decomposing into both solid carbon and H_2(g), while the reduction of CeO_2 proceeds with the formation of $CeO_{1.81}$ and $CeO_{1.78}$. Meanwhile, small amounts of both H_2O(g) and CO_2(g) are formed at the beginning of reaction. Subsequently, C deposition starts reacting with oxygen released from ceria resulting in CO formation at above 500 °C. Non-stoichiometric compounds ($CeO_{1.72}$ and $CeO_{1.83}$ mainly, and $CeO_{1.67}$ in negligible amount) are formed as intermediate species, which provide a good representation of the overall reduction mechanism during Ce(IV) reduction into Ce(III) species. The reaction reaches completion at above 1000 °C, yielding Ce_2O_3 and H_2/CO mixture (with H_2/CO ratio approaching two).

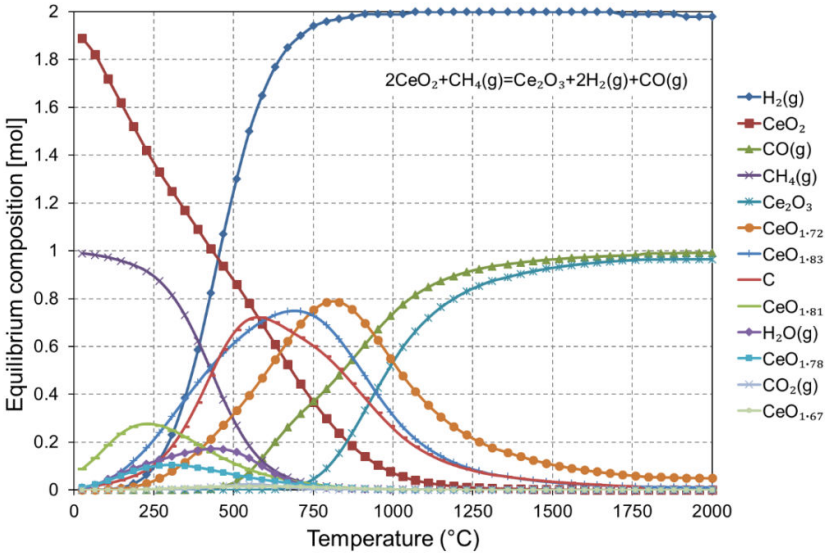

Figure 2-5. Thermodynamic equilibrium composition of methane reforming over ceria as a function of temperature at 1 bar.

2.3 Experimental section

2.3.1 Material synthesis

Iron and cerium oxides were employed as oxygen carrier for solar-driven CLRM using two structures including powder and porous foam. For powder preparation, both cerium and iron oxide powders were mechanically grinded with a mortar and then loaded into the cavity receiver as shown in Fig. 2-6a and Fig. 2-6d. For ceria powder mixed with Al_2O_3, the Al_2O_3 particles (1.2 mm size and 1.72 g/cm^3 apparent density) were calcined at 1000 °C for 2 h under air to ensure their structural and chemical stability and to eliminate their moisture content. Then, the calcined Al_2O_3 particles and ceria powder with a mass ratio of 2.2:1 were mixed homogeneously (61.54 vol% of alumina) before performing the tests as presented in Fig. 2-6b. The Al_2O_3 particles with large particle sizes were used to favor the dispersion of ceria powder bed and improve the gas flow through the reactive bed (at the expense of a higher bed volume: 56.79 cm^3 for CeO_2-Al_2O_3 blend compared to 24.16 cm^3 for CeO_2 without Al_2O_3). For foam structure, both cerium and iron oxides were synthesized via a replication technique and further subjected to thermal stabilization. Regarding the ceria reticulated porous foam, a slurry of cerium oxide powder (Sigma Aldrich, particle size < 5µm, 99.9% purity, 1.12 g/cm^3 apparent density) was prepared. To increase the micro-scale porosity, solid carbon particles (graphite purchased from TIMCAL, particle size 5-10 µm) were added as pore-forming agent in a ratio 50 vol% of ceria. The mixture of the ceria slurry and solid carbon particles was achieved by magnetic stirring under heating at 60 °C. The organic polyurethane template with a cylindrical shape (5 pores/inch) was completely and repeatedly immersed into the ceria slurry. After 20 min drying at ambient temperature, the coated foams were fired in a furnace (Nabertherm, model: L9/12/C6) under air at 1000 °C for 6 h to totally burn the carbon particles, organic binder, and organic polyurethane matrix. The ceria foams annealed at 1000 °C are designated as ST-1000. Finally, one ceria foam was annealed again in a small furnace (Nabertherm, model: LTH 02/16) for 2 h at 1400 °C in air to further sinter the structure and it is designated as ST-1400. In case of iron reticulated porous foam, the applied method was the same. Fig. 2-6c and

Fig. 2-6e show photographs of the cerium and iron oxide porous foams loaded in the solar cavity receiver.

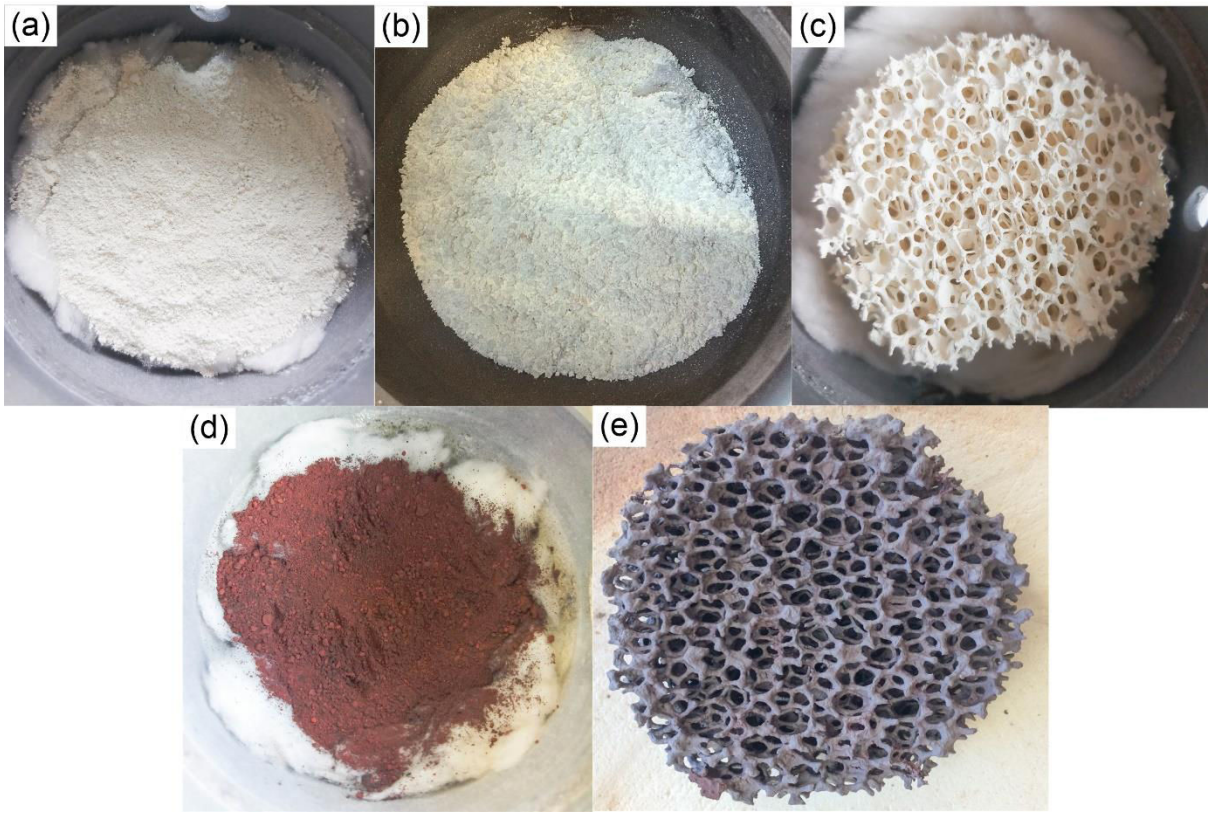

Figure 2-6. Photographs of (a) ceria powder, (b) ceria powder mixed with calcined Al_2O_3 particles, (c) ceria porous foam, (d) iron oxide powder, and (e) iron oxide porous foam.

2.3.2 Solar reactor configuration and experimental method

The solar reactor concept is schematically shown in Fig. 2-7. The solar reactor consists of a cylindrical metallic cavity receiver with a conical part (60° angle) at its bottom (volume: 0.299 L and total height: 115 mm), wrapped by a 30 mm-thick alumino-silicate insulation layer. The insulated cavity receiver is vertically placed in a water-cooled cylindrical stainless-steel shell and then closed by an alumina cap with a 20 mm-diameter aperture for the access of concentrated sunlight. A protective graphite plate (2 mm-thick) with a 15 mm-diameter aperture is positioned on top of the alumina cap to protect it. A hemispherical transparent glass window equipped with a small fluorine window is lastly attached to the front flange edge of the reactor shell. A 2-m diameter parabolic mirror with a solar concentration ratio above 10000 suns (peak flux density of ~10.5 MW/m^2 at the focal plane for a DNI of 1 kW/m^2) is employed to concentrate sunlight to the focal point where the reactor aperture is positioned.

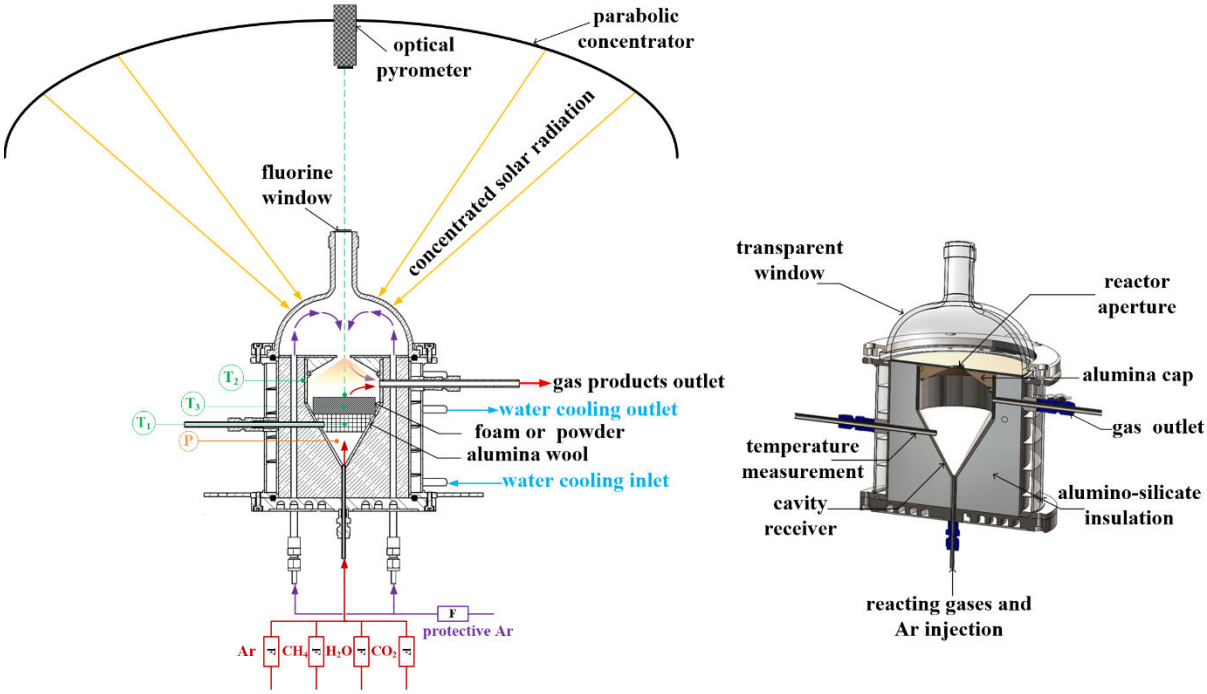

Figure 2-7. Schematic of the 1.5 kW_{th} directly-irradiated solar reactor and external components (left) and 3D cross section of the solar reactor (right).

Three temperatures are measured by B-type thermocouples inside the alumina wool supporting the reactive material (T_1), at the external cavity wall surface (T_2), and in the middle of samples (T_3); and an optical pyrometer (operating at 4.8-5.2 µm in a H_2O absorption band) also measures the temperature at the uppermost sample surface ($T_{pyrometer}$) through the fluorine window. In addition, the operating pressure (P) inside the cavity receiver is measured by a pressure transducer. CH_4 and Ar (gases purity of 99.999%) flow-rates are controlled by electronic Mass Flow Controllers (MFC, Brooks Instruments model SLA5850S, range 0-5 Nl/min ±0.2% of full scale), while liquid water (H_2O) flow-rate is also regulated by a MFC (range 0-30 g/h ±1% of full scale).

A given amount of cerium or iron oxide is loaded within the cavity receiver directly subjected to concentrated sunlight. Three types of materials structures for each oxide (powders, powders mixed with inert particles, and porous foams) were assessed to compare their thermochemical reactivity. Since the objective is to conduct the thermochemical reactions in a solar reactor, efficient solar radiation absorption and high heat and mass transfer rates are necessary to warrant homogeneous material heating and reaction in the whole structure for utilization of the entire reactant mass. Therefore, using reticulated porous foam may be an attractive option for volumetric solar radiative absorption while offering a large available interface for gas species access and solid/gas reactions. Reactive gases (CH_4 or H_2O/CO_2) and Ar carrier gas are fed via the single inlet port at the bottom of the cavity receiver. Prior to gas analysis, product gases flow through a gas scrubber composed of both bubbler and gas filtering unit (two micro filters with 0.1 µm pore diameter) to remove moisture and entrained solid carbon particles. The gas composition is then analyzed by an on-line syngas analyzer (GEIT 3100, uncertainty <±0.1% of full scale), and all the measured data are recorded by an automated data acquisition system (BECKHOFF).

The reactor cavity was initially flushed by Ar and sucked by a Venturi pump to eliminate residual air from the system. Ar protective gas (2.0 Nl/min) was also provided to the window area to prevent the hot gas contact with the transparent window. Subsequently, the reactor was gradually heated by concentrated sunlight to the desired temperature (referred by T_3) under Ar. The solar power input was regulated by means of shutter opening to stabilize T_3.

Figs. A-3, A-4, and A-5 represent the evolution of temperatures and cavity pressure in the directly irradiated solar reactor during heating phase, ceria reduction with methane, and subsequent oxidation with H_2O at different operating cycle temperatures. While the cavity pressure remained stable at 0.86 bar (P_{atm}= ~0.85 bar at site elevation 1,500 m above sea level), the temperature increased gradually from the ambient temperature to the targeted temperature (1000 °C) for 35 min. It then changed in relation to endothermic and exothermic reactions and nominal operating cycle temperature defined, while the cavity pressure was constant (~0.9 bar) all over the cycles. According to Fig. A-3, the homogeneous temperature inside the ceria foam as well as the reactor cavity receiver was confirmed by narrow gaps between T_1 (below the foam), T_3 (inside the foam), and $T_{pyrometer}$ (upper surface of the foam) while the external cavity wall temperature (T_2) was ~150 °C lower than those temperatures.

Once T_3 was at steady-state, a CH_4/Ar gas mixture (50% CH_4 concentration) was delivered to the reaction zone to drive the reduction reaction. After finishing reduction, reflected by H_2 and CO concentrations approaching zero, CH_4 flow was stopped and only Ar flow was fed to remove residual CH_4. Subsequently, oxidation was performed by injecting the reacting gases (either H_2O or CO_2) at the same temperature. The reacting gases flow was stopped when H_2 or CO evolution ceased. The pressure was maintained at ~0.9 bar for both steps.

During partial oxidation of methane with metal oxides, the formation of both H_2O and CO_2 is also possible according to Eq. 2-14:

$$4M_xO_y + \delta CH_4 \longrightarrow 4M_xO_{y-\delta} + \delta CO_2 + 2\delta H_2O \quad (2\text{-}14)$$

Therefore, oxygen released from the oxide structure is recovered in the forms of CO, CO_2, and H_2O (twice the amount of CO_2). The global amount of oxygen released from the oxide structure ($n_{O,red}$) is therefore determined by:

$$n_{O,red} = n_{CO} + 2n_{CO_2} + n_{H_2O} \quad (2\text{-}15)$$

where n_i are the mole amounts of species i.

The replenished amount of oxygen ($n_{O,ox}$) during oxidation with H_2O (Eq. 2-9 and Eq. 2-13) can be calculated from oxygen mass balance (equal to total amount of produced H_2 minus amounts produced from carbon gasification with H_2O according to Eq. 2-10 and Eq. 2-11):

$$n_{O,ox} = n_{H_2} - n_{CO} - 2n_{CO_2} \quad (2\text{-}16)$$

Contrary to iron oxide (Fe_3O_4 cannot be reversibly oxidized with H_2O to Fe_2O_3), the partially-reduced ceria ($CeO_{2-\delta}$) can be completely re-oxidized to CeO_2. The oxygen non-stoichiometry during reduction (δ_{red}) can be defined by:

$$\delta_{red} = \frac{n_{O,red}}{n_{CeO_2}} \tag{2-17}$$

The replenished oxygen (δ_{ox}) during ceria oxidation with H_2O (Eq. 2-13) can be calculated as follows:

$$\delta_{ox} = \frac{n_{O,ox}}{n_{CeO_2}} \tag{2-18}$$

When using CO_2 as oxidant (Eq. 2-13), the replenished oxygen (δ_{ox}) is calculated by the mass balance of oxygen:

$$\delta_{ox} = \frac{2n_{CO_2,in} - n_{CO,out} - 2n_{CO_2,out}}{n_{CeO_2}} \tag{2-19}$$

For reduction, the CH_4 conversion is defined by:

$$X_{CH_4} = 1 - \frac{\dot{m}_{unreacted\ CH_4}}{\dot{m}_{CH_4}} \tag{2-20}$$

where $\dot{m}_{unreacted\ CH_4}$ is the mass flow rate of unreacted CH_4, and $\dot{m}_{CH_4}$ is the mass flow rate of injected CH_4.

Moreover, the quality of products is assessed from the selectivity of H_2 (S_{H2}) and CO (S_{CO}) towards syngas products:

$$S_{H_2} = \frac{n_{H_2}}{n_{H_2} + n_{H_2O}} \tag{2-21}$$

$$S_{CO} = \frac{n_{CO}}{n_{CO} + n_{CO_2}} \tag{2-22}$$

where n_{H_2} and n_{CO} are the total moles of produced H_2 and CO during oxidation and reduction steps, n_{H_2O} and n_{CO_2} are the moles of produced H_2O (equal to twice the mole of CO_2) and CO_2 during reduction step.

The performance metrics of the solar reactor for the chemical-looping process are encompassing methane conversion, solar-to-fuel energy conversion efficiency, and energy upgrade factor.

The solar-to-fuel energy conversion efficiency ($\eta_{\text{solar-to-fuel}}$) is defined as the ratio of the total chemical energy content of the produced syngas to the total energy input (including solar power input in both the reduction and oxidation steps and heating value of the converted methane):

$$\eta_{\text{solar-to-fuel}} = \frac{\left(\dot{m}_{H_2} \cdot \text{LHV}_{H_2} + \dot{m}_{CO} \cdot \text{LHV}_{CO}\right)_{\text{cycle}}}{\dot{P}_{\text{solar}} + \left(X_{CH_4} \cdot \dot{m}_{CH_4} \cdot \text{LHV}_{CH_4}\right)} \tag{2-23}$$

where LHV represents the Lower Heating Value (J/kg), $\dot{m}_{H_2}$ and $\dot{m}_{CO}$ are the mass flow rates of H_2 and CO produced in the cycle (kg/s), $\dot{m}_{CH_4}$ is the mass flow rate of injected methane, $\dot{P}_{\text{solar}}$ is the total solar power input in the cycle (W), and X_{CH_4} is the methane conversion.

The energy upgrade factor (U) is obtained by the ratio of the energy contained in the outlet gas species to the energy content of the inlet flow:

$$U = \frac{\left(\dot{m}_{H_2} \cdot LHV_{H_2} + \dot{m}_{CO} \cdot LHV_{CO}\right)_{cycle} + \left((1 - X_{CH_4}) \cdot \dot{m}_{CH_4} \cdot \mathrm{LHV}_{CH_4}\right)}{\left(\dot{m}_{CH_4} \cdot \mathrm{LHV}_{CH_4}\right)} \quad (2\text{-}24)$$

All the operating conditions and experimental results for 55 runs with 8 different ceria and irons oxide samples performed in the solar reactor are summarized in Appendix A (Table A-1).

2.4 Result and discussion

2.4.1 Methane reforming over iron oxide

Pure raw Fe_2O_3 powder (total mass: 20.52 g) (Figure 2-6d) was employed as an oxygen carrier material for the solar CLRM test. Experiments were conducted with 4 cycles at 950-1100 °C. Both CH_4 and Ar carrier gas flow-rates were injected at 0.2 Nl/min for reduction step (50% inlet CH_4 mole fraction), while H_2O flow-rate was fed at 200 mg/min along with Ar carrier gas (0.2 Nl/min) for subsequent oxidation step, yielding 55% steam mole fraction at inlet.

The transient syngas production rates along with nominal reactor temperature (T_3) during iron oxide powder reduction with methane and during reduced iron oxidation with H_2O for four consecutive cycles are plotted for the respective temperatures of 1000, 1100, 950, and 1000 °C (Fig. 2-8). During reduction step, the maximum CO_2 production rate (0.09 Nl/min) was noticed at the initial stage of the reaction at cycle #1 (Fig. 2-8a); moreover, its amount was higher than those of CO and H_2. Actually, H_2O was also formed simultaneously in accordance with thermodynamic analysis; however, it cannot be detected from gas analysis. The CO_2 production rate was observed again at cycle #2 (but it was lower than cycle #1) when increasing the temperature to 1100 °C (Fig. 2-8c), and after initial stage its trend remained stable along with H_2 and CO production rates. The peak H_2 and CO production rates (0.07 and 0.04 Nl/min) were found at the highest reduction temperature (1100 °C, Fig. 2-8c). After cycle #2, the syngas (H_2, CO, and CO_2) production rates during reduction were found in negligible amounts (Fig. 2-8e and Fig. 2-8g). During oxidation step, the peak of H_2 production rate (0.077 Nl/min) was also found at the same temperature (1100 °C, Fig. 2-8d), followed by 1000 °C (0.052 Nl/min, Fig. 2-8b) and 950 °C (0.035 Nl/min, Fig. 2-8f), while extremely small evolution of CO and CO_2 was noticed for any oxidation temperatures. Thus, the negligible impact of carbon deposition from methane cracking was demonstrated for the CLRM over iron oxide. Noticeably, the methane reforming over iron oxide required long duration to reach completion (because of strong oxide sintering during reduction and low available specific surface area) and strongly depended on the reduction temperature as evidenced in Fig. 2-8c (the required reduction temperature was higher than the one for CH_4 reforming over ceria). First, the reduction of fresh Fe_2O_3 to Fe_3O_4 in cycle #1 resulted in a large amount of oxygen released ($n_{O,red}$=0.095 vs. $n_{O,ox}$=0.012, Fig. 2-9) in the form of CO_2. Then, during the oxidation step of cycle #1, re-oxidation to Fe_2O_3 is not possible (only Fe_3O_4 can be formed, Eq. 2-9)[142], as evidenced by $n_{O,ox}$ much lower than $n_{O,red}$ (Fig. 2-9). The material was deactivated after cycle #2 because operation at 1100 °C resulted in strong sintering despite achieving high reduction rate, as reflected by increased CO and H_2 production rates and maximum X_{CH_4} (33.8%).

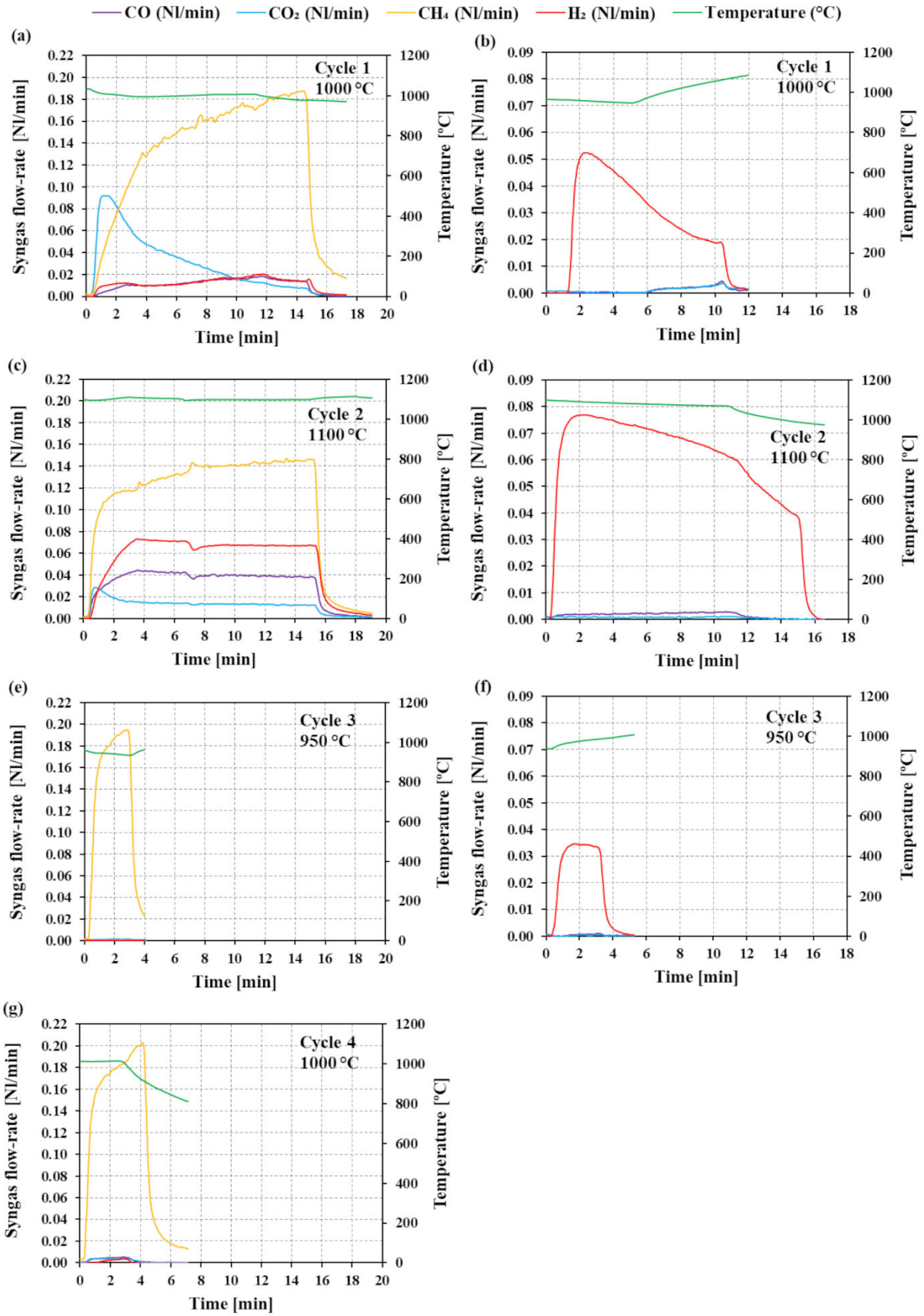

Figure 2-8. Evolution of the production rates of H_2, CO, CO_2, and CH_4 in the syngas along with nominal reactor temperature for reduction with CH_4 (a, c, e, and g) and oxidation with H_2O (b, d, and f) of iron oxide powder cycled isothermally at 1000, 1100, 950, and 1000°C.

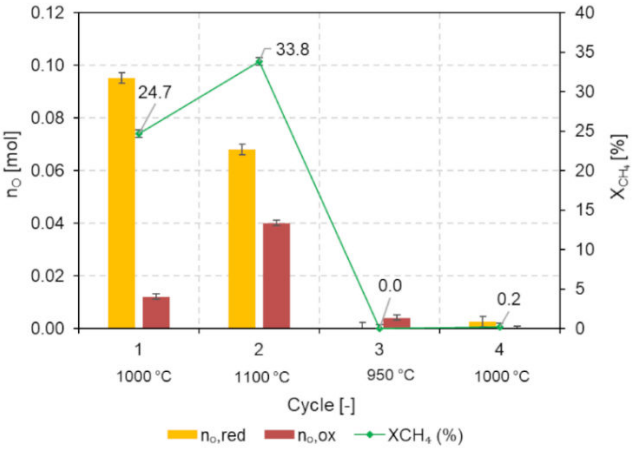

Figure 2-9. Comparison of $n_{O,red}$ and $n_{O,ox}$ along with CH_4 conversion during four consecutive redox cycles with iron oxide powder performed at 950-1100 °C.

Fig. 2-10 shows the syngas yields quantified from the integration of the measured syngas production rates (Fig. 2-8) during reduction and oxidation steps. As expected, the highest CO_2 yield (1.06 mmol/$g_{Fe_2O_3}$) was found in cycle #1, followed by cycle #2 (0.5 mmol/ $g_{Fe_2O_3}$) while the maximum total syngas yield (4.0 mmol/$g_{Fe_2O_3}$) was produced in cycle #2 (Fig. 2-10a), and no effect of CH_4 cracking reaction (Eq. 2-7) was observed as evidenced by a zero amount of H_2 (CH_4 cracking). Note that the amount of H_2 (CH_4 cracking) was quantified by the total H_2 yield measured by gas analysis minus the H_2 yield produced by the main reaction of iron oxide with methane (Eq. 2-6), which is equivalent to twice the quantity of produced CO. In addition, no syngas production was observed in cycle #3 (the reduction reaction was negligible as evidenced by X_{CH_4}=0%, Fig. 2-9), and a negligible syngas yield was found in cycle #4. These are because of a dramatic decrease in available surface area resulting from high sintering/coarsening and densification of the new-formed metallic iron particles after being reduced at high temperature (1100 °C, cycle #2), thereby leading to material deactivation and negligible re-oxidation. For these reasons, its powder structure cannot be backed to the initial stage despite passing re-oxidation step, thus adversely influencing the CLRM process in cycles #3 and #4 and thereby leading to negligible amounts of syngas produced. This was confirmed by the high sintering of iron powder structure observed after 4 cycles (Fig. A-6).

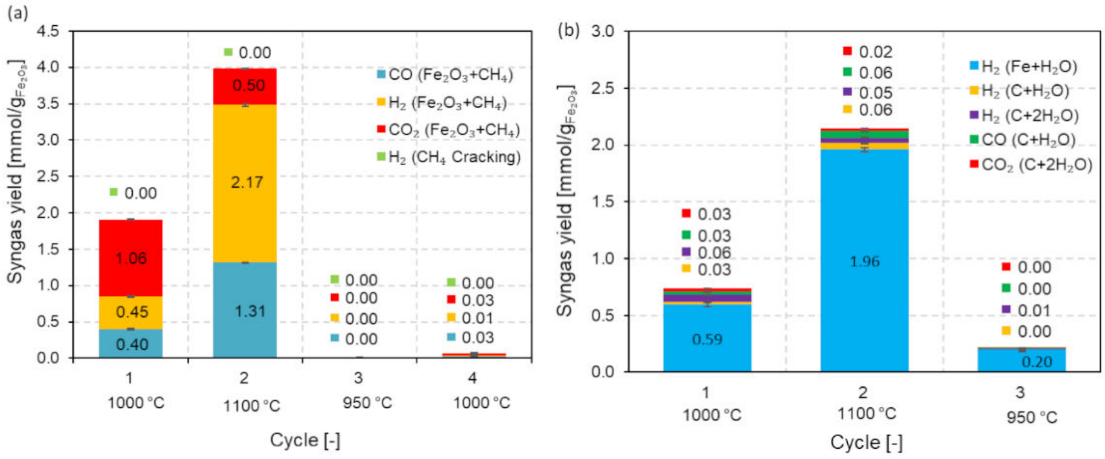

Figure 2-10. Syngas yields for (a) iron oxide powder reduction with CH_4 and (b) oxidation with H_2O during isothermal cycles at temperatures in the range 950-1100 °C.

Fig. 2-10b shows that most of the produced syngas yields during oxidation step was coming from H_2 associated with the main reaction (Eq. 2-9), and the maximum total syngas yield (2.15 mmol/$g_{Fe_2O_3}$) was found in cycle #2 in accordance with high syngas production rate in the reduction step. Moreover, negligible CO ($C+H_2O$), CO_2 ($C+2H_2O$), H_2 ($C+H_2O$), and H_2 ($C+2H_2O$) yields formed by side reactions (Eq. 2-10 and Eq. 2-11) were noticed, confirming that methane cracking reaction over iron oxide is not favored at 950-1100 °C. In addition, the H_2 (Eq. 2-21) and CO (Eq. 2-22) selectivity (Table A-1) rose sharply during cycling (e.g. from 28.6 and 34.8% at cycle #1 to 59.2 and 96.6% at cycle #3, respectively), because of the drop of H_2O and CO_2 yields. The reduced iron oxide after reduction step in cycle #4 was not re-oxidized, as it was kept for X-ray diffraction (XRD) analysis to characterize its phase composition (Fig. A-7). Phase identification shows the presence of mainly FeO, followed by traces of Fe_3O_4 and Fe. Thus, most of the iron oxide powder did not completely reduce to Fe despite already passing the reduction step with methane, thereby confirming material deactivation.

In order to confirm experimental repeatability and compare the results, another iron oxide structure (reticulated porous foam, total Fe_2O_3 mass: 13.91 g) was prepared (Fig. 2-6e) via a replication technique [98] and subsequently employed as an oxygen carrier material for the solar-driven CLRM. Experiments were conducted with seven consecutive cycles at different reduction temperatures in the range 1000-1150 °C, while the flow rates of CH_4, H_2O, and Ar were the same as the previous tests with iron oxide powder (CH_4: 0.2 Nl/min, H_2O: 200 mg/min, and total Ar: 2.2 Nl/min).

During reduction step, the peak rates of CO_2 production decreased, while the peak of H_2 and CO remained stable with cycles repetition from cycle #1 to cycle #3 at 1000 °C (Fig. 2-11). For example, the peak rates of CO_2, H_2, and CO production are 0.11, 0.02, and 0.02 Nl/min at cycle #1 compared to 0.01, 0.02, and 0.02 Nl/min at cycle #3. During oxidation step, the peak rate of H_2 production seemed to decrease slightly (0.07 Nl/min at cycle #1 compared to 0.06 Nl/min at cycle #3) while no CO and CO_2 production was evidenced. X_{CH_4} decreased dramatically from 24.9% at cycle #1 to 3.7% at cycle #3 (Fig. 2-12) arising from the sharp decline in oxygen release during reduction steps of cycles #2 ($n_{O,red}$=0.012) and #3 ($n_{O,red}$=0.009) compared to cycle #1 ($n_{O,red}$=0.059), caused by non-reversible Fe_2O_3 reduction to Fe_3O_4, in agreement with thermodynamic analysis (Fig. 2-3).

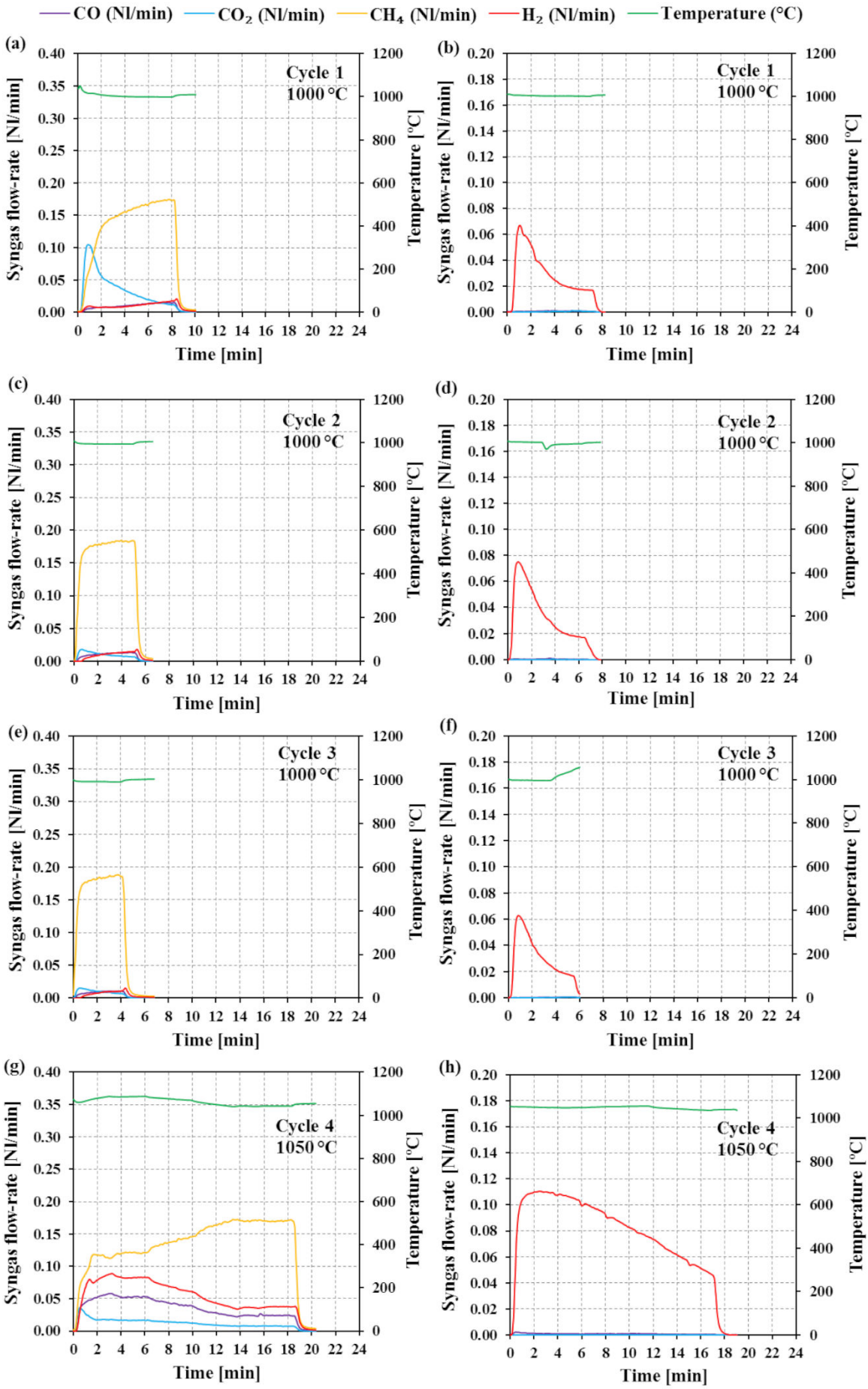
CO (Nl/min)
CO2 (Nl/min)
CH4 (Nl/min)
H2 (Nl/min)
Temperature (°C)
(a)
Cycle 1
1000 °C
(b)
Cycle 1
1000 °C
(c)
Cycle 2
1000 °C
(d)
Cycle 2
1000 °C
(e)
Cycle 3
1000 °C
(f)
Cycle 3
1000 °C
(g)
Cycle 4
1050 °C
(h)
Cycle 4
1050 °C
Syngas flow-rate [Nl/min]
Temperature [°C]
Time [min]

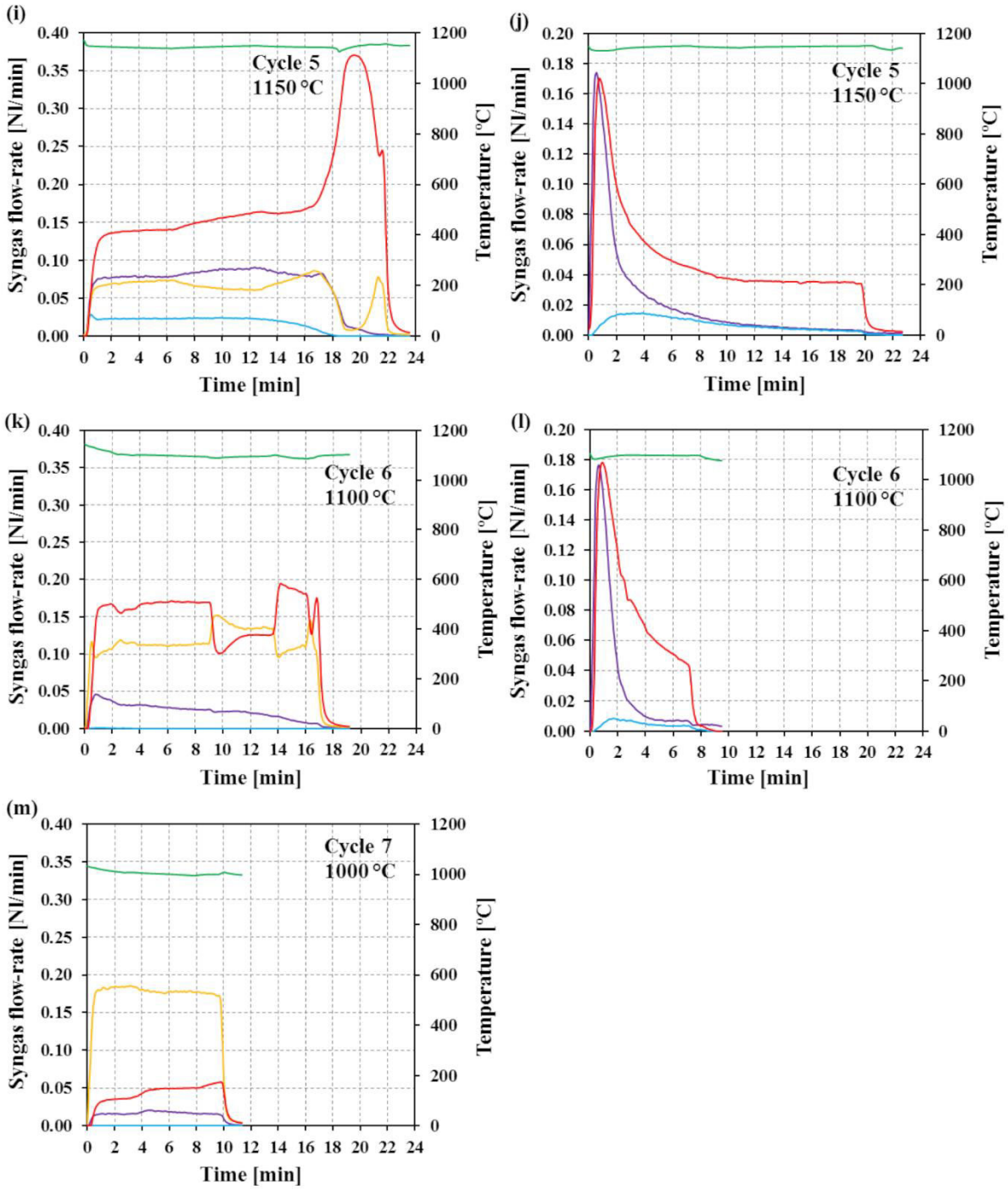

Figure 2-11. Evolution of the production rates of H_2, CO, CO_2, and CH_4 in the syngas along with nominal reactor temperature for reduction with CH_4 (a, c, e, and g) and oxidation with H_2O (b, d, and f) of iron oxide reticulated porous foam cycled isothermally for 7 consecutive cycles at 1000-1150 °C.

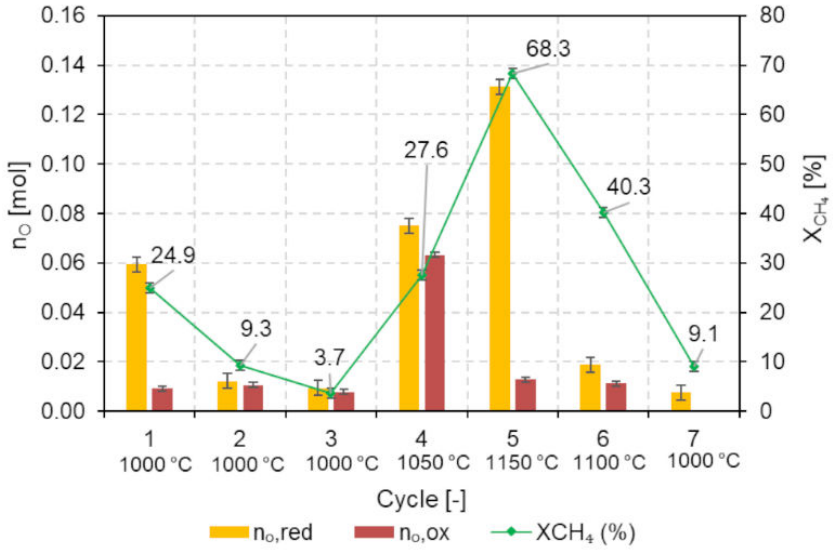

Figure 2-12. Comparison of $n_{O,red}$ and $n_{O,ox}$ along with CH_4 conversion during seven consecutive redox cycles with iron oxide foam performed at 1000-1150 °C.

Similar to previous tests with iron oxide powder, the kinetics of methane reforming with iron oxide porous foam were too slow at 1000 °C to allow reaching completion (CH_4 injection was therefore stopped before H_2 and CO approached zero (cycles #1-3, Fig. 2-11a, 2-11c, and 2-11e)). The reaction rates were enhanced when increasing the temperature to 1050 °C according to Fig. 2-11g and Fig. 2-11h. For example, the peak rates of H_2 and CO production were 0.09 and 0.05 Nl/min during reduction step (Fig. 2-11g), while the peak rate of H_2 production was 0.11 Nl/min during oxidation step at 1050 °C, and negligible CO and CO_2 production rates were observed (Fig. 2-11h), confirming the absence of carbon formation during reduction step.

The temperature was increased to 1150 °C in cycle #5 (Fig. 2-11i and Fig. 2-11j) to further hasten the kinetic rate of reduction. As a result, the syngas evolution profile (Fig. 2-11i) increased considerably; however, the effect of methane cracking reaction was detected as reflected by the peak of H_2 after 18 min with the maximum X_{CH_4} (68.3%, Fig. 2-12) while CO approached zero (thus indicating the end of iron oxide reduction). Note that the formed carbon can also act as reducing agent (Fe_3O_4 reduction) according to thermodynamics (Fig. 2-4 and Fig. A-2), and the cracking reaction may also be catalyzed by the newly formed metallic iron [90]. During oxidation with H_2O, both a sharp growth in CO (consistent with the H_2 evolution profile) and a significant increase in CO_2 were noticed (Fig. 2-11j), arising from the reaction of deposited C with H_2O and confirming that 1150 °C is favorable for CH_4 cracking reaction in this cycle. When the rate of oxide reduction is lower than the rate of methane decomposition, chemisorbed carbon may accumulate at the surface. This occurs when the rate of bulk lattice oxygen diffusion to the surface becomes lower than the CH_4 supply rate. In other words, when a lack of oxygen at the surface occurs, carbon deposition is fastened, which is increasingly favored as oxygen is being depleted during the iron oxide reduction progress.

The temperature was then decreased by 50 °C in cycle #6 to alleviate the adverse impact of CH_4 cracking reaction; nevertheless, the resulting syngas associated with CH_4 decomposition remained high as reflected by a stable H_2 evolution profile in the reduction step

even if CO approached zero (Fig. 2-11k) and a steep increase of the CO along with H_2 in the oxidation step (Fig. 2-11l). This may possibly be also due to the carbon accumulation from the previous cycle.

The cycling experiment was completed with the reduction step performed at 1000 °C (cycle #7, Fig. 2-11m). It was found that no CO_2 production was evolved; in contrast, the peak H_2 production rate was higher (0.06 Nl/min) while the peak CO production rate remained the same (0.02 Nl/min) as compared to those obtained from cycles #1-3. This suggests that the amount of excess available oxygen at the iron oxide surface was restrained in this last cycle, explaining the preferential formation of CO rather than CO_2 (and H_2O). Indeed, CO_2 and H_2O formation is favored when an excess amount of surface oxygen is available, thus occurring during the first cycle because the pristine oxide is Fe_2O_3. In the subsequent cycles, the participating oxide during reduction is either FeO or Fe_3O_4 (because re-oxidation to Fe_2O_3 is not thermodynamically possible when using H_2O as oxidant) with less available oxygen for the reduction step. Moreover, selectivity increased from 23.2% to 99.7% (H_2) and 33.5% to 99.9% (CO), in agreement with the decline in CO_2 and H_2O formation during cycling.

Once again, the time integration of the measured syngas production rates in Fig. 2-13 during reduction and oxidation steps was used to calculate the syngas yields according to Fig. 2-11. Note that the reduced iron after reduction in the last cycle (cycle #7) was not re-oxidized, as it was kept for analyzing its phase composition via XRD. Therefore, no syngas yield during oxidation at cycle #7 was presented.

During reduction step (Fig. 2-13a), as expected a large amount of CO_2 was observed during the first reduction (1.00 mmol/$g_{Fe_2O_3}$) arising from Fe_2O_3 reduction to Fe_3O_4 (0.059 mole of oxygen released, Fig. 2-12), and total syngas yield decreased with cycles repetition (cycles #1-3). The syngas yields (especially H_2 and CO) grew with increasing reduction temperature (cycles #4-6), thereby confirming that the partial oxidation of CH_4 over iron oxide strongly depends on the reduction temperature, and temperatures higher than 1000 °C were required to favor reactions. However, a remarkable amount of H_2 associated with CH_4 cracking (3.01-5.57 mmol/$g_{Fe_2O_3}$) was inherently measured at cycles #5-6 because of higher reduction temperatures (1100-1150 °C). Noticeably, CO_2 yield decreased with cycles repetition (except in cycle #5 at which the amount of CO_2 was higher than that obtained from cycle #1 as a result of the exacerbated temperature effect at 1150 °C), and it was not observed during the last cycle (cycle #7). This is because a large amount of the oxygen contained in the iron oxide lattice structure was released during the previous cycles favoring CO_2 formation. In fact, Fe_3O_4 reduction takes place into two stages: first the reduction from Fe_3O_4 to FeO (Eq. 2-4) and then FeO to Fe (Eq. 2-5). The first stage is faster than the second one presumably as a result of produced H_2 that reacts with Fe_3O_4 (Fig. 2-2) but not with FeO [90]. The slower second reaction stage is caused by the material surface reduction resulting from sintering [90]. These variations may explain the decrease of CO_2 with cycles repetition (as evidenced in cycles #1-7) since the iron oxide structure does not completely return to the initial state despite passing the oxidation step (as proved by $n_{O,ox}$ values always lower than $n_{O,red}$, Fig. 2-12), thereby leading to lower available oxygen for the subsequent reduction reaction.

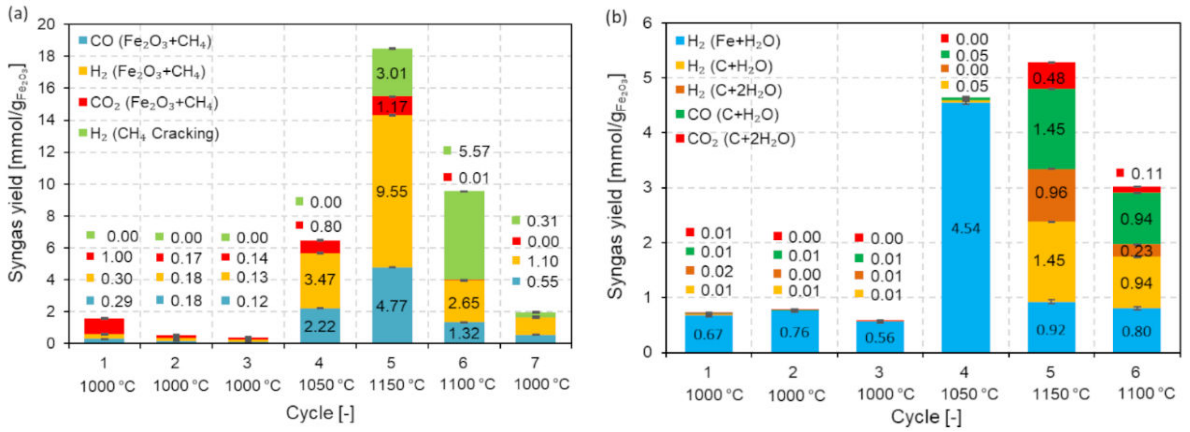

Figure 2-13. Syngas yields for (a) iron oxide reticulated porous foam reduction with CH_4 and (b) oxidation with H_2O cycled isothermally at temperatures in the range 1000-1150 °C.

During oxidation step (Fig. 2-13b), most of the produced syngas yield at cycles #1-4 was ascribed to the production of H_2 formed by Eq. 2-9. The CO ($C+H_2O$), CO_2 ($C+2H_2O$), H_2 ($C+H_2O$), and H_2 ($C+2H_2O$) yields formed by side reactions (Eq. 2-10 and Eq. 2-11) were negligible, implying negligible amount of carbon deposition. In contrast, they were found in significant amounts in cycles #5-6, suggesting important impact of carbon deposition on syngas yields at 1100-1150 °C. Likewise, the reduced iron oxide composition after reduction in cycle #7 was characterized by XRD. Its phase identification is presented in Fig. A-8.

The material is mainly composed of Fe, followed by traces of FeO, in agreement with the hard structure of iron in Fig. A-9. Most of the iron oxide foam was converted to metallic Fe. It can be assumed that the iron oxide porous foam structure might be lastingly converted to metallic iron coarsened structure after being reduced at 1150 °C (cycle #5), and that the process is not reversible due to extremely high sintering entailing low re-oxidation ability, as observed in Fig. A-9b. This assumption can be evidenced by a sharp drop of H_2 ($Fe+H_2O$) yield associated with the oxidation reaction in cycles #5-6 (ranging between 0.80-0.92 mmol/$g_{Fe_2O_3}$, Fig. 2-13b) with extremely low oxygen uptake (0.013 mole for cycle #5 and 0.011 mole for cycle #6, Fig. 2-12).

In conclusion, the CLRM over both iron oxide powder and foam dramatically suffers from morphological instability (high sintering), slow reaction kinetics, and unfavorable oxidation because of strong material coarsening and densification, thus strongly altering the oxygen exchange reversibility. Then, the oxygen uptake during oxidation is always lower than the oxygen released during reduction because of low material thermal stability. For these reasons, iron oxide is not suitable for CLRM process and would require stabilization for high-temperature processing (e.g. using inert ceramic support for improving material stability). Alternatively, iron oxide reduction using CH_4 is suitable for producing both metallic iron and syngas in a solar metallurgical process.

2.4.2 Influence of sintering temperature for ceria foams

In order to experimentally study the effect of calcination temperature during ceria foam elaboration on the evolved syngas yield, two ceria reticulated porous foams were prepared and subsequently annealed under air at 1000 °C (for 6 h) and one of them was further sintered at

1400 °C for 2 h for densifying the structure. Thus, the obtained sintered foams were labeled as ST-1000 and ST-1400, respectively. The initial volumes of ST-1000 and ST-1400 were 46.76 and 83.13 cm^3 (after ceria coating process), and they were shrunk to 30.88 cm^3 (Fig. A-10a, ST-1000) and 31.10 cm^3 (Fig. A-10b, ST-1400) after heat treatment, representing a decrease of 34% and 63% of their initial volume, respectively. The final properties of the ceria foams are: porosity: 91.8% and 89.1%, mean cell size: 3.5 and 2.5 mm, and apparent density: 0.595 and 0.780 g/cm^3 for ST-1000 and ST-1400, respectively. Both ceria foams were cycled in the temperature range 900–1050 °C to experimentally study the influence of temperature on syngas evolution as well as reactor performance. Fig. A-11 shows the syngas production rate along with nominal reactor temperature during ceria foam (ST-1400) reduction in the range 900-1050 °C (CH_4 flow-rate: 0.2 NL/min, Ar flow rate: 0.2 NL/min, 50% CH_4 mole fraction). It was followed by subsequent ceria oxidation with H_2O carried out at the same temperature (H_2O: 200 mg/min, Ar: 0.2 NL/min, 55% steam mole fraction at inlet).

During reduction step, CO_2 production rate was maximal at the initial stage of the reaction, and it increased with temperature. In fact, H_2O was also formed simultaneously [108]; however, it cannot be detected from gas analysis. An increase in the operating cycle temperature promoted both the syngas production rate (especially H_2 and CO) and ceria reduction rate (as evidenced by a shortened reaction duration). The peak rates of CO and H_2 produced were 0.02 and 0.04 Nl/min at 900 °C compared to 0.11 and 0.24 Nl/min at 1050 °C, and the operating duration was 25.4 min at 900 °C compared to 18.4 min at 1050 °C. It is interesting to note that the H_2/CO mole ratio is constantly ~2 for any reduction temperatures [108]. Moreover, the significant H_2 evolution still continuing after 12 min (Fig. A-11e) was the result of the methane cracking reaction that is thermodynamically favorable at high temperature (>1000 °C) [100].

During oxidation step, the H_2 production rate increased with temperature while the CO and CO_2 production rates were negligible over the considered temperature range, thus demonstrating negligible impact of carbon formation associated with methane cracking for ST-1400.

Fig. 2-14 compares the H_2, CO, and CO_2 production rates (both reduction and oxidation steps) of ceria foam ST-1400 to those of ST-1000 at an operating cycle temperature of 1000 °C. During reduction step (Fig. 2-14a), increasing the sintering temperature (ST-1400) decreased syngas production rates while increasing the operating duration. This is because the high densification of the structure (at high sintering temperature of 1400 °C) leads to a decline of the porosity and hinders the access of the reacting gas to the solid surface and hollow struts of the foam. Likewise, higher sintering temperature (ST-1400) also led to lower reaction rates during oxidation step (Fig. 2-14b). Decreasing the sintering temperature (ST-1000) favored the oxidation rate and the formation of CO/CO_2 (because the formation of carbon during the reduction step was also favored).

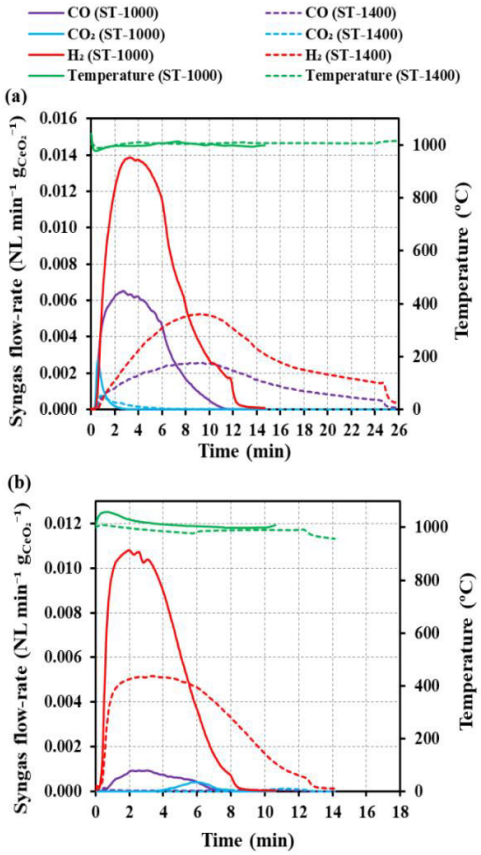

Figure 2-14. Influence of sintering temperature on H_2 and CO production rates during both reduction and oxidation of ceria foam at 1000 °C: (a) CH_4 was utilized as reducing agent and (b) H_2O was utilized as oxidizing agent.

Figure 2-15 presents the comparison of syngas yields (calculated by time-integration of the measured syngas production rates) produced per gram of CeO_2 (mmol/g_{CeO_2}) between ST-1000 and ST-1400 at the operating cycle temperature of 1000 and 1050 °C during ceria reduction with CH_4 (Fig. 2-15a) and oxidation with H_2O (Fig. 2-15b). The syngas yields ascribed to the main reactions (Eqs. (2-12) and (2-13)) and side reactions (methane cracking during reduction step: $CH_4 \longrightarrow C+2H_2$ (Eq. 2-7), and carbon gasification during oxidation step: $C+H_2O \longrightarrow CO+H_2$ (Eq. 2-10) and $C+2H_2O \longrightarrow CO_2+2H_2$ (Eq. 2-11)) are presented separately.

Fig. 2-15a shows that the syngas yields produced during reduction step decreased significantly with sintering temperature at the operating cycle temperatures of 1000 and 1050 °C, thus leading to a decline in δ_{red} (e.g., from 0.36 for ST-1000 to 0.34 for ST-1400 at 1000 °C). Furthermore, the H_2 yield produced from CH_4 cracking reaction (quantified by the total H_2 yield measured by gas analysis minus the H_2 yield produced by the reaction of ceria with methane, which is equivalent to twice the quantity of produced CO, according to Eq. 2-12) decreased considerably when increasing the sintering temperature (e.g. from 0.67 mmol/g_{CeO_2} for ST-1000 to 0.07 mmol/g_{CeO_2} for ST-1400 at 1000 °C). This can be explained by the fact that increasing the sintering temperature lowers the available geometrical surface area for the heterogeneous reaction, which declines the surface concentration of adsorbed methane and alleviates the methane cracking reaction.

Likewise, Fig. 2-15b confirms that the methane cracking reaction is not favored for the sintered ceria foam (ST-1400), as evidenced by a sharp drop in the quantities of CO ($C+H_2O$), CO_2 ($C+2H_2O$), H_2 ($C+H_2O$), and H_2 ($C+2H_2O$) formed by the side reactions (carbon deposit gasification with H_2O). Note that the H_2 ($C+H_2O$) yield is equal to the CO yield measured by gas analysis ($C+H_2O \longrightarrow CO+H_2$), while the H_2 ($C+2H_2O$) yield is equal to twice the CO_2 yield measured by gas analysis ($C+2H_2O \longrightarrow CO_2+2H_2$). In addition, an increase in the sintering temperature decreased the H_2 ($CeO_{2-\delta}+H_2O$) yield (e.g., from 2.04 mmol/g_{CeO_2} for ST-1000 to 1.84 mmol/g_{CeO_2} for ST-1400 at 1000 °C, then resulting in a decrease of δ_{ox} from 0.35 to 0.32). Noticeably, δ_{red} matched well δ_{ox} values at both cycle temperatures of 1000 and 1050 °C, thereby confirming complete re-oxidation.

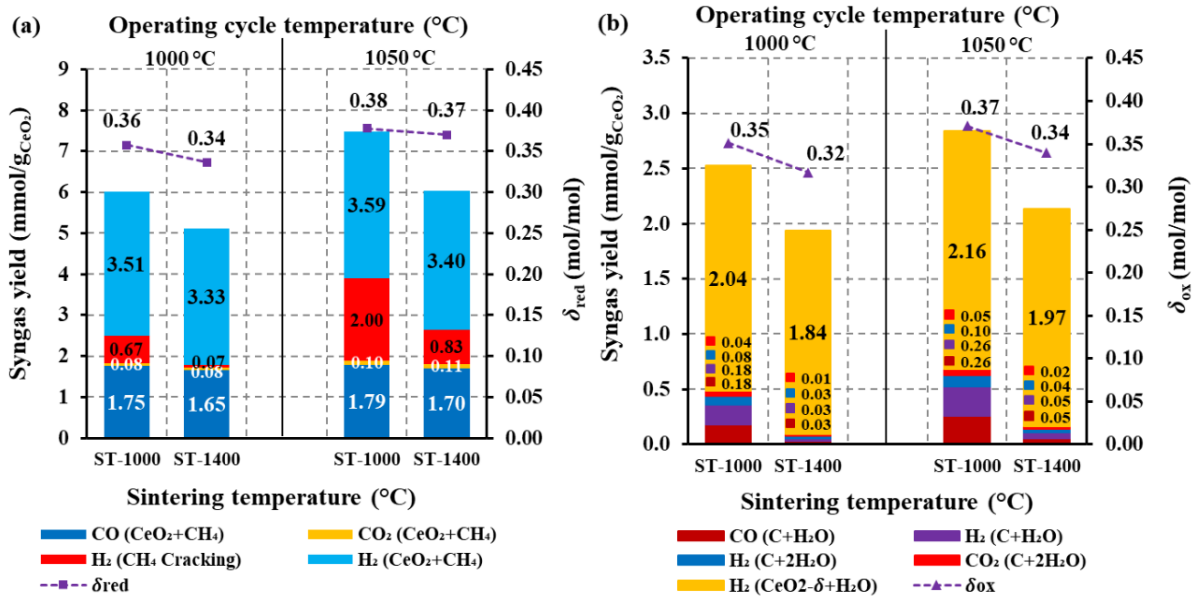

Figure 2-15. Effect of sintering temperature and cycle operating temperatures on syngas yields, δ_{red}, and δ_{ox} for (a) reduction and (b) oxidation of ceria foam cycled isothermally at a CH_4 flow-rate of 0.2 NL/min.

According to Fig. 2-16a, the reduction yield ($X_{red}=\delta_{red}/\delta_{max}$ where $\delta_{max}=0.5$ for complete reduction of Ce^{4+} into Ce^{3+}), oxidation yield ($X_{ox}=\delta_{ox}/\delta_{red}$), methane conversion ($X_{CH_4}$) and solar-to fuel energy conversion efficiency ($\eta_{solar\text{-}to\text{-}fuel}$) were decreased when increasing the sintering temperature (e.g., X_{red}, X_{ox}, X_{CH4}, and $\eta_{solar\text{-}to\text{-}fuel}$ ranging from 71.5%, 98.3%, 46.9%, and 3.8% for ST-1000 to 67.3%, 94.2%, 23.0%, and 2.8% for ST-1400, respectively, during cycling at 1000 °C). In addition, an increase in operating cycle temperature enhanced X_{red}, X_{CH_4}, and $\eta_{solar\text{-}to\text{-}fuel}$.

Fig. 2-16b compares the total syngas yields obtained for both reduction and oxidation steps of ceria foams (ST-1000 compared to ST-1400) during cycling at 1000 and 1050 °C. Increasing sintering temperature considerably decreased total H_2 and CO yields (from 6.48 and 1.93 mmol/g_{CeO_2} for ST-1000 to 5.29 and 1.68 mmol/g_{CeO_2} for ST-1400, respectively, at 1000 °C); however, the CO_2 and H_2O yields tended to decrease slightly. A growth in the energy upgrade factor (U) with increasing sintering temperature was observed (e.g., from 1.03 for ST-

1000 to 1.08 for ST-1400). This is because a high sintering of the ceria foam lowers the gaseous reactant access to the reactive surface and the ceria bulk reduction, thus increasing the unreacted CH_4 (much lower X_{CH_4} for ST-1400, Fig. 2-16a) and thereby leading to an increase in U. From these observations, it can be summarized that decreasing sintering temperature enhanced syngas production; however, at the expense of weakened structure, with reduced thermo-mechanical resistance.

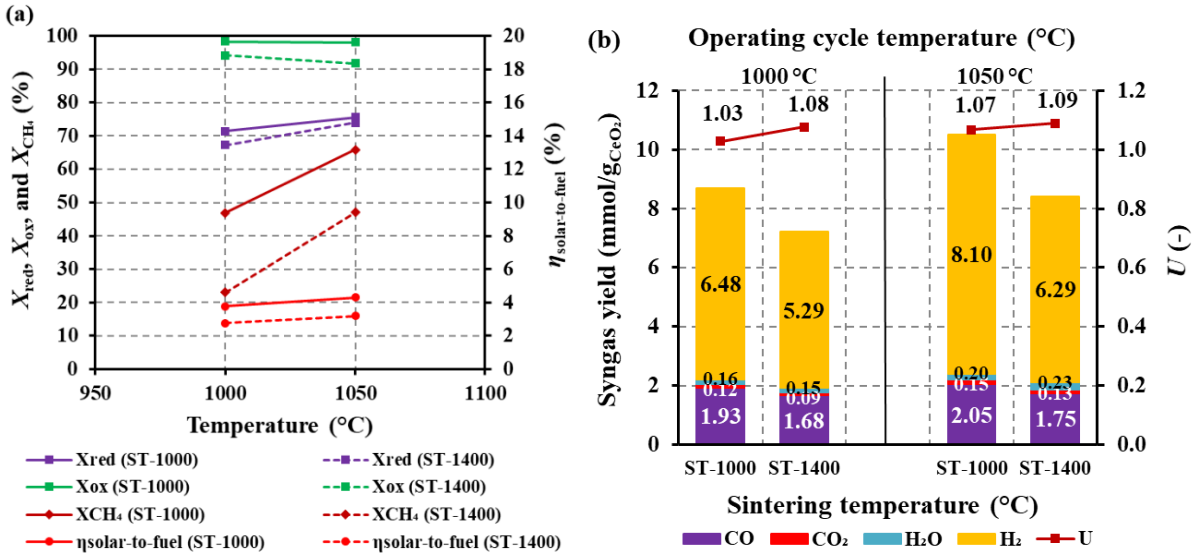

Figure 2-16. Effect of sintering temperature and cycle operating temperatures on (a) ceria reduction yield, ceria oxidation yield, methane conversion, and solar-to-fuel energy conversion efficiency, and (b) energy upgrade factor and total syngas yields obtained from both reduction and oxidation steps.

2.4.3 Influence of methane flow-rate and ceria macrostructure on syngas yield

The impact of methane flow-rate on syngas yields was experimentally studied with different ceria structures. Three ceria structures consisting of pure ceria powder (25.0052 g, bulk density: 1.12 g/cm^3, loose bed porosity: 84.5%), ceria powder (27.0605 g) mixed with inert Al_2O_3 promoter (bulk mixture density: 1.53 g/cm^3, loose bed porosity: 69.1%), and ceria reticulated foam (18.3705 g, ST-1000, bulk density: 0.595 g/cm^3, porosity: 91.8%) were employed to investigate the influence of ceria structure and reactive bed layout on syngas yield and reactor performance. During ceria reduction step, the CH_4 flow-rate was injected at 0.1, 0.2, 0.3, and 0.4 NL/min (with constant Ar carrier flow of 0.2 NL/min) at 1000 °C. In the oxidation step performed at the same temperature (1000 °C), H_2O was delivered at a constant flow-rate of 200 mg/min (with Ar carrier gas flow of 0.2 NL/min).

Fig. 2-17 shows the influence of CH_4 flow rate on syngas yields for each ceria structure. According to Fig. 2-17a, the H_2 and CO yields first increased significantly within a CH_4 flow-rate range of 0.1-0.2 NL/min and then tended to grow minimally at above 0.2 NL/min. For example, the H_2 and CO yields for ceria foam rose from 3.25 and 1.66 mmol/g_{CeO_2} at 0.1 NL/min to 3.64 and 1.82 mmol/g_{CeO_2} at 0.2 NL/min, and 3.78 and 1.89 mmol/g_{CeO_2} at 0.4 NL/min. The CO_2 yields for each ceria structure remained stable in negligible amounts (0.05-0.10 mmol/g_{CeO_2} within the considered range). A plateau in the H_2 and CO (at CH_4 above 0.2

NL/min) indicates that the final state completion of ceria reduction for each ceria structure is being approached, thereby leading to an excess in CH_4 flow-rate supply, which in turn favors CH_4 cracking reaction. Note that if the rate of ceria reduction is lower than the rate of methane decomposition, chemisorbed carbon may accumulate at the surface. This occurs when the rate of bulk lattice oxygen diffusion to the surface becomes lower than the CH_4 supply rate. In other words, when a lack of oxygen at the surface occurs, then carbon deposition is fastened, which is increasingly favored as oxygen is being depleted during the ceria reduction progress. It is interesting to highlight that when accounting for H_2 produced by CH_4 cracking reaction (Fig. 2-17b), the H_2 yield increased steeply (3. 25- 6.54 mmol/g_{CeO_2} for ceria foam) over the considered range, thus confirming that the CH_4 cracking reaction is favored when increasing CH_4 flow-rate, and leading to a sharp increase in H_2 yield along with carbon deposition.

The CO and H_2 productions for each ceria structure were not significantly different, although a slightly higher H_2 and CO production was noticed for ceria powder (presumably due to non-uniform heating of the bed ($T_{pyrometer}>T_3$) as evidenced by Fig. A-4 for ceria powder and Fig. A-5 for ceria powder mixed with inert Al_2O_3 promoter). This advantageously confirms that the shaping of ceria as foam does not downgrade the reactivity.

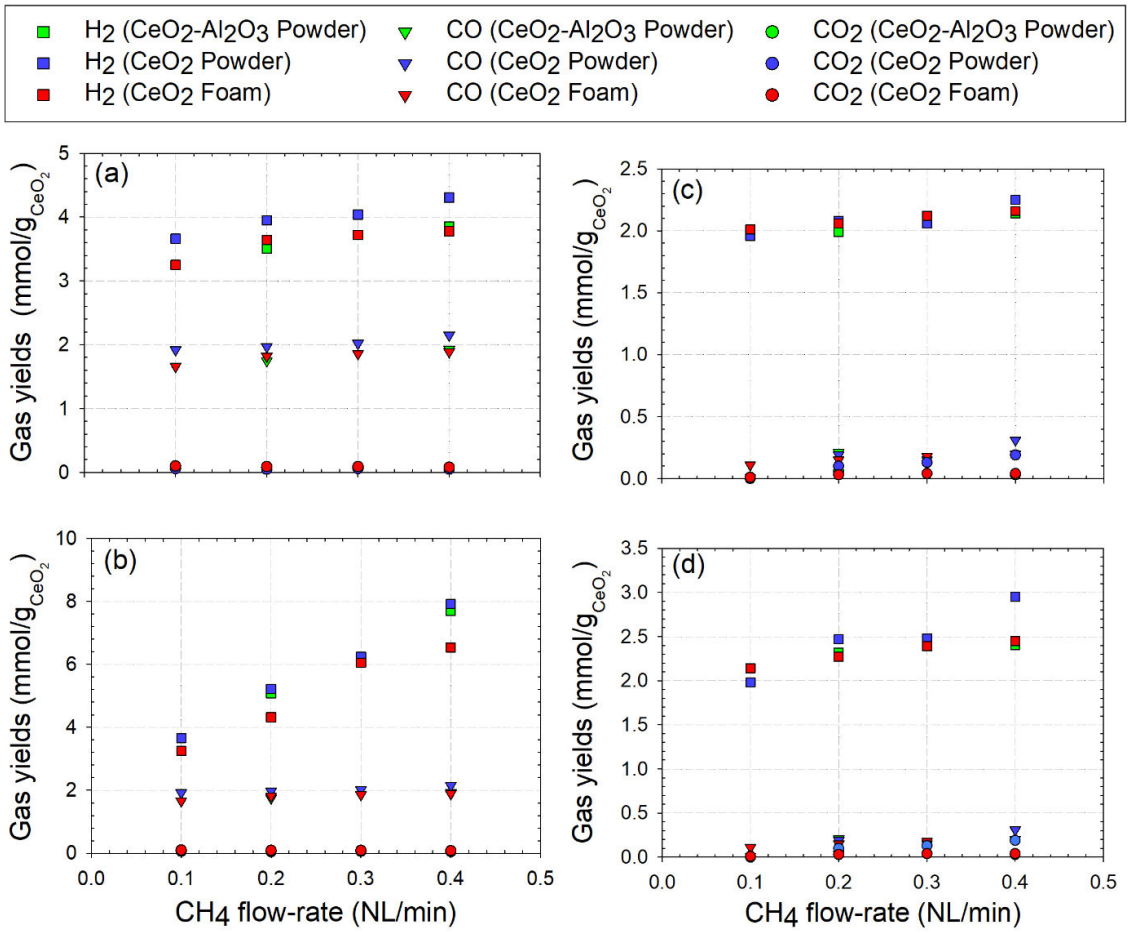

Figure 2-17. Effect of CH_4 flow-rate on H_2, CO, and CO_2 yields during (a,b) reduction of different ceria structures at 1000 °C: (a) not accounting and (b) accounting for H_2 produced by CH_4 cracking reaction; and during (c,d) oxidation of different ceria structures with H_2O at 1000 °C: (c) not accounting and (d) accounting for H_2 produced by carbon gasification reactions.

During subsequent ceria oxidation with H_2O at 1000 °C (Fig. 2-17c and 2-17d), H_2 yield (produced by Eq. 2-13) increased in accordance with an increase in CH_4 flow-rate during the reduction step, while the CO and CO_2 yields (produced by side reactions) also rose due to carbon deposition increase (Fig. 2-17c). For instance, the yields of H_2, CO, and CO_2 for ceria foam were 2.01, 0.11, and 0.01 mmol/g_{CeO_2} at 0.1 NL/min compared to 2.16, 0.20, and 0.04 mmol/g_{CeO_2} at 0.4 NL/min. Likewise, the H_2 yield increased sharper when including the amount of H_2 associated with carbon gasification (e.g. from 2.14 to 2.45 mmol/g_{CeO_2} at 0.1–0.4 NL/min for ceria foam), according to Fig. 2-17d. However, no significant effect of the ceria structure on H_2, CO, and CO_2 yields can be evidenced whether or not accounting for H_2 yields from carbon gasification reactions.

In order to emphasize the influence of CH_4 flow-rate on reactor performance, the evolution of the relevant metrics (δ_{red} and δ_{ox}, X_{red}, X_{ox}, X_{CH4}, U, and $\eta_{solar\text{-}to\text{-}fuel}$) is presented in Fig. 2-18. Both δ_{red} (Fig. 2-18a) and δ_{ox} (Fig. 2-18b) are enhanced with a CH_4 flow-rate increase (e.g., maximum δ_{red} and δ_{ox} of 0.41 and 0.39 at 0.4 NL/min, respectively, for ceria powder). Besides, the δ_{ox} values were consistent with δ_{red} for any ceria structures, thereby confirming complete ceria re-oxidation with H_2O. As expected, the δ_{red} (Fig. 2-18a) of ceria powder (0.37-0.41) was slightly higher than those of other materials, in agreement with the higher syngas yields during reduction (Fig. 2-17a). The δ_{ox} values were not different (Fig. 2-18b) (0.34-0.39 for ceria powder and 0.35-0.37 for ceria reticulated foam), in agreement with the similar syngas yields during oxidation (Fig. 2-17c). X_{red} grew with increasing CH_4 flow-rate (Fig. 2-18c), e.g. from 74.7% at 0.1 NL/min to 81.3% at 0.4 NL/min for ceria powder, and no significant influence of ceria structure on X_{red} can be observed. X_{ox} values were close to ~100% for any ceria structures, thereby demonstrating complete ceria re-oxidation. X_{CH_4} was reduced noticeably with increasing CH_4 flow-rate for each ceria structure (Fig. 2-18d) (e.g., from 76.4 to 43.0% at 0.1-0.4 NL/min, respectively, for ceria powder). The decrease in X_{CH_4} is attributable to the CH_4 supply rate that exceeds the rate of oxygen released by ceria, as noticed by a stable profile in X_{red} at 0.3-0.4 NL/min (Fig. 2-18c). U tended to decrease with CH_4 flow-rate (Fig. 2-18e). This variation is attributed to the carbon formation increase with CH_4 flow-rate, and partial entrainment out of the reactor cavity, as confirmed by the presence of carbon particles in the filtering unit (Fig. A-12), thus losing their heating value and lowering U. As expected, $\eta_{solar\text{-}to\text{-}fuel}$ rose with CH_4 flow-rate as a result of the substantial syngas yield improvement (Fig. 2-17), and the highest $\eta_{solar\text{-}to\text{-}fuel}$ was obtained for ceria foam (3.1%–5.6%), followed by CeO_2-Al_2O_3 blend (3.6%–5.0%), and CeO_2 powder (3.1%–3.6%), according to Fig. 2-18f. This can be explained by the different solar power inputs required for different ceria structures (1.06-1.14 kW for ceria powder, followed by 0.96-1.06 kW for CeO_2-Al_2O_3 blend, and 0.76-0.86 kW for ceria foam). Ceria foam thus requires lower solar power consumption than CeO_2-Al_2O_3 blend and CeO_2 powder. This is because the CeO_2-Al_2O_3 blend stands out from its high bed thickness (1.19 cm) and additional Al_2O_3 heating (Fig. A-13), while the CeO_2 powder layer (0.46 cm thickness) shows high opacity, which is not suitable for efficient radiative heat transfer in the whole volume. Both issues thus lead to temperature gradient, as evidenced in both Fig. A-4 (for CeO_2 powder) and Fig. A-5 (for CeO_2-Al_2O_3 blend), with a higher temperature at the bed uppermost surface ($T_{pyrometer}$>T_3). However, the CeO_2-Al_2O_3 blend offers a favored dispersion of ceria powder, which improves the gas flow through the reactive bed

and heat transfer and promotes the syngas yield (thereby leading to higher $\eta_{\text{solar-to-fuel}}$ than the one for ceria powder). The ceria foam consumed the lowest solar power input (thus enhancing $\eta_{\text{solar-to-fuel}}$), arising from the effective heat transfer through the semi-transparent medium and the uniform heating (as evidenced by the narrow temperature gap between ceria surface $T_{\text{pyrometer}}$ and T_3 in Fig. A-3). In summary, the ceria foam structure is the most efficient in term of heat transfer (as reflected by uniform heating with lower solar power consumption), thereby leading to higher $\eta_{\text{solar-to-fuel}}$, and it is thus the most suitable for the chemical-looping methane reforming.

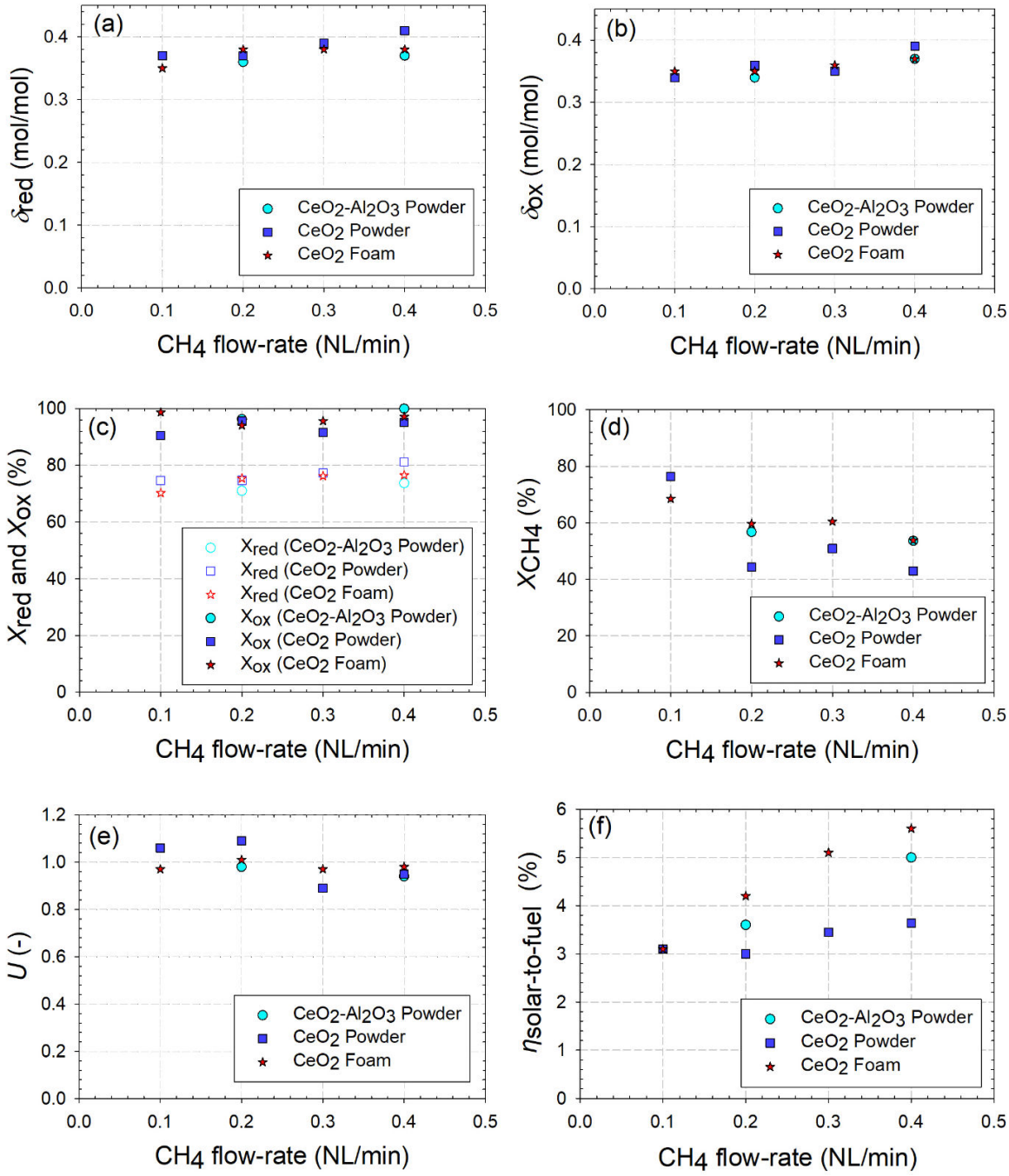

Figure 2-18. Effect of CH_4 flow-rate on (a) δ_{red}, (b) δ_{ox}, (c) reduction yield (X_{red}) and oxidation yield (X_{ox}), (d) CH_4 conversion (X_{CH_4}), (e) energy upgrade factor (U), and (d) solar-to-fuel energy conversion efficiency ($\eta_{\text{solar-to-fuel}}$) for different ceria structures at 1000 °C.

2.4.4 Influence of temperature on syngas yield

The influence of temperature on syngas yield was investigated for the different ceria structures at 900, 950, 1000, and 1050 °C (T_3 is the nominal-mentioned temperature for experiments).

Fig. 2-19a and Fig. 2-19b show the H_2, CO, and CO_2 yields obtained from ceria reduction with CH_4 as a function of reduction temperature. As expected, both H_2 and CO yields increased sharply, while CO_2 tended to rise minimally with temperature (Fig. 2-19a), regardless of the ceria structures. For example, H_2, CO, and CO_2 yields rose from 2.38, 1.21, and 0.05 mmol/g_{CeO_2} at 900 °C to 3.84, 1.92, and 0.09 mmol/g_{CeO_2} at 1050 °C, respectively, for CeO_2-Al_2O_3 blend. This is because increasing temperature accelerates the kinetic rate of ceria reduction with faster oxygen release, as evidenced by Arrhenius plot (Fig. A-14). The activation energy obtained for each ceria structure (92.8-114.2 kJ/mol for H_2 and 92.8-95.1 kJ/mol for CO, Table A-2) is consistent with previously reported data [100]. When accounting for the H_2 produced by CH_4 cracking reaction (Fig. 2-19b), the trends of H_2 became steeper, thus pointing out the significant influence of the reduction temperature on the H_2 formation from CH_4 cracking. Noticeably, the H_2 yield at 900 °C (CeO_2-Al_2O_3 blend) remained the same (2.38 mmol/g_{CeO_2}) whether or not accounting for H_2 produced by cracking reaction, thus indicating that CH_4 decomposition was negligible at 900 °C. In comparison, the ceria powder showed the highest H_2 and CO yields at 950-1000 °C, as a result of the higher bed surface temperature and lower bed height, as previously mentioned.

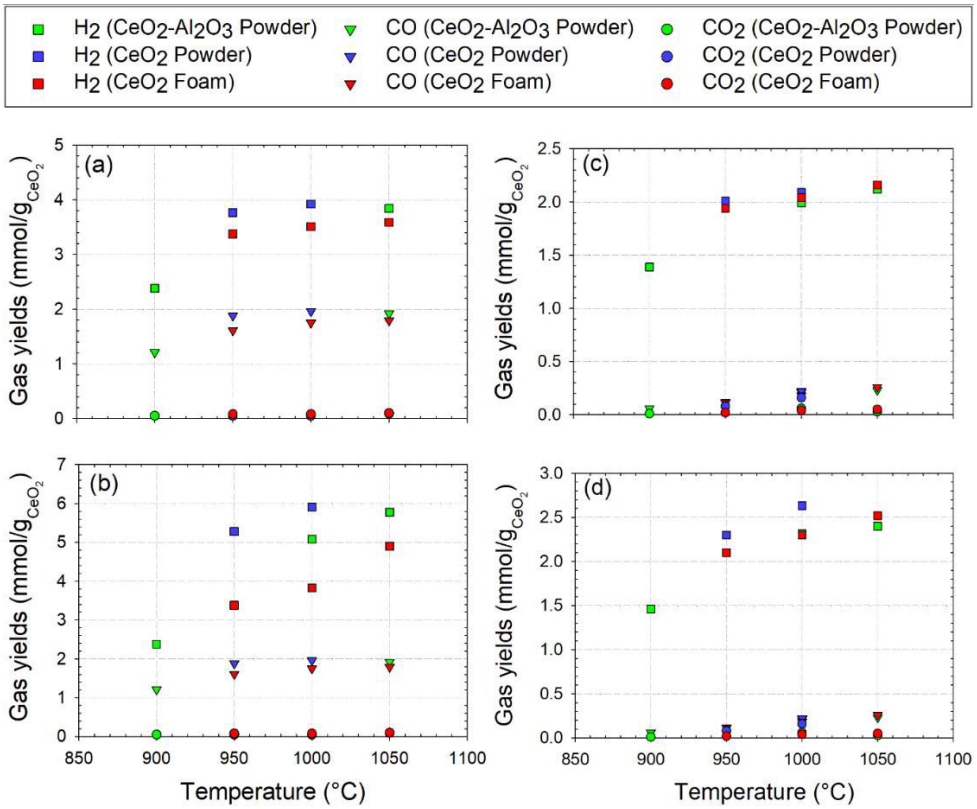

Figure 2-19. Effect of temperature on H_2, CO, and CO_2 yields during (a,b) ceria materials reduction with CH_4 (0.2 NL/min, inlet CH_4 mole fraction: 50%): (a) not accounting and (b) accounting for H_2 produced by CH_4 cracking reaction; and during (c,d) ceria materials oxidation with H_2O (200 mg/min, inlet steam mole fraction: 55%): (c) not accounting and (d) accounting for H_2 produced by carbon gasification reactions.

Fig. 2-19c and Fig.2-19d depict the H_2, CO, and CO_2 yields measured during ceria oxidation with H_2O as a function of temperature. The H_2 yields (from Eq. 2-13) rose significantly with temperature (1.39-2.12 mmol/g_{CeO_2} for CeO_2-Al_2O_3 blend), while a slight increase in CO and CO_2 yields was noticed (Fig. 2-19c). The presence of CO and CO_2 (e.g., ranging between 0.06-0.23 for CO and 0.01-0.03 mmol/g_{CeO_2} for CO_2 in the case of CeO_2-Al_2O_3 blend) is attributed to the side reactions of carbon gasification forming additional H_2, CO, and CO_2. These side reactions are beneficial to eliminate the deposited carbon on the surface of ceria structure, thereby avoiding deactivation. When including the H_2 produced by the carbon gasification (Fig. 2-19d), the H_2 yield for each ceria structure was higher (1.46-2.40 mmol/g_{CeO_2} for CeO_2-Al_2O_3 blend), thus confirming the growing effect of temperature on carbon formation.

Fig. 2-20 presents the evolution of δ_{red}, δ_{ox}, X_{red}, X_{ox}, X_{CH4}, U, and $\eta_{solar\text{-}to\text{-}fuel}$ as a function of temperature for each ceria structure. The temperature increase improved steadily the reduction extent of ceria δ_{red} (Fig. 2-20a), e.g. from 0.24 at 950 °C to 0.39 at 1050 °C for CeO_2-Al_2O_3 blend owing to a significant beneficial enhancement of the reduction kinetics (Fig. A-14). δ_{ox} also increased with temperature (ranging between 0.24-0.36 for CeO_2-Al_2O_3 blend, Fig. 2-20b) due to the oxygen vacancies consistently increasing with temperature. The impact of the considered ceria structures on both δ_{red} and δ_{ox} was not significant. δ_{ox} values were similar to δ_{red} values, thus validating complete ceria re-oxidation for any ceria structures. X_{red} rose considerably with temperature (e.g., in the range 48.8-78.0% for CeO_2-Al_2O_3 blend), while X_{ox} remained quite constant at ~100% for any ceria structures (Fig. 2-20c), thereby confirming complete ceria re-oxidation. X_{CH4} rose with temperature (Fig. 2-20d), and the highest X_{CH_4} was attained at 1050 °C (77.4% for CeO_2-Al_2O_3 blend). This is because the faster rate of oxygen release better matched the constant inlet flow of CH_4, which leads to X_{CH_4} increase. The X_{CH_4} for both ceria foam and CeO_2-Al_2O_3 blend was higher than that of ceria powder, presumably due to both better gas flow through the structure and solid/gas contact between ceria and CH_4. Moreover, U (Fig. 2-20e) first increased slightly within 900-950 °C and then decreased above 950 °C, as a result of carbon formation issue. Indeed, the carbon deposition increased with increasing temperature, and some particles escaped from the reactor cavity via gas flow, thus lowering U. This issue can be tackled by decreasing temperature to favor U at the expense of lower syngas yield. $\eta_{solar\text{-}to\text{-}fuel}$ (Fig. 2-20f) was improved by increasing temperature (e.g., in the range of 3.0-4.3% for ceria foam). The lowest $\eta_{solar\text{-}to\text{-}fuel}$ values were observed for ceria powder (2.75%–2.97% at 950-1000 °C) because of the higher solar power consumption (0.88-0.96 kW for ceria powder compared to 0.67-0.68 kW for ceria foam in the temperature range 950-1000 °C), confirming that ceria foam structure is the most suitable for the solar combined process.

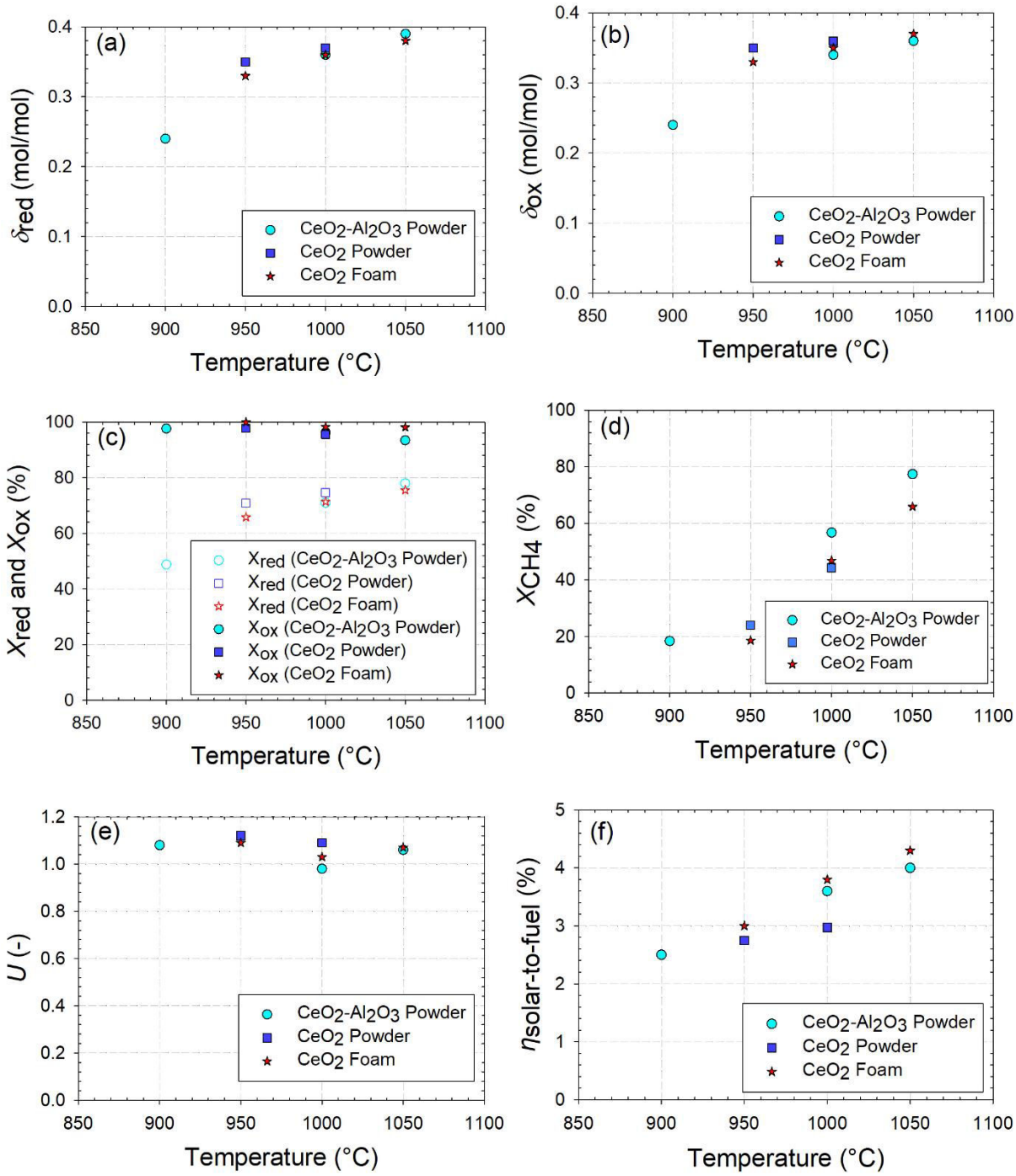

Figure 2-20. Effect of temperature on (a) δ_{red}, (b) δ_{ox}, (c) reduction yield (X_{red}) and oxidation yield (X_{ox}), (d) CH_4 conversion (X_{CH_4}), (e) energy upgrade factor (U), and (d) solar-to-fuel energy conversion efficiency ($\eta_{solar\text{-}to\text{-}fuel}$) for different ceria structures.

2.4.5 Oxidation step with CO_2 during ceria cycling

Another ceria powder (27.0892 g) mixed with Al_2O_3 (50 g) was employed to study the influence of temperature (950-1050 °C) on syngas yield and reactor performance during ceria oxidation with CO_2. This ceria was first reduced with a constant CH_4 flow-rate of 0.2 NL/min (50% CH_4 mole fraction at inlet) and subsequently re-oxidized with a constant CO_2 flow-rate of 0.2 NL/min (50% CO_2 mole fraction at inlet) at the same temperature.

Syngas production rates along with reactor temperature for both steps are presented in Fig. 2-21. During reduction step, the syngas production rates were higher at 1050 °C than at 1000 and 950 °C. For instance, the peak H_2 and CO production rates were 0.32 and 0.14 NL/min at 1050 °C compared to 0.21 and 0.10 NL/min at 950 °C. The reaction duration declined considerably with increasing temperature due to improved ceria reduction kinetics (from 24.4 min at 950 °C to 15.1 min at 1050 °C). During oxidation step, the peak CO production rate increased minimally from 0.14 to 0.16 NL/min while the oxidation duration decreased slightly (from 26 min at 950 °C to 22 min at 1050 °C). Therefore, the effect of temperature is not significant for the oxidation step with CO_2, which thus suggests low impact of kinetic reaction control for this step.

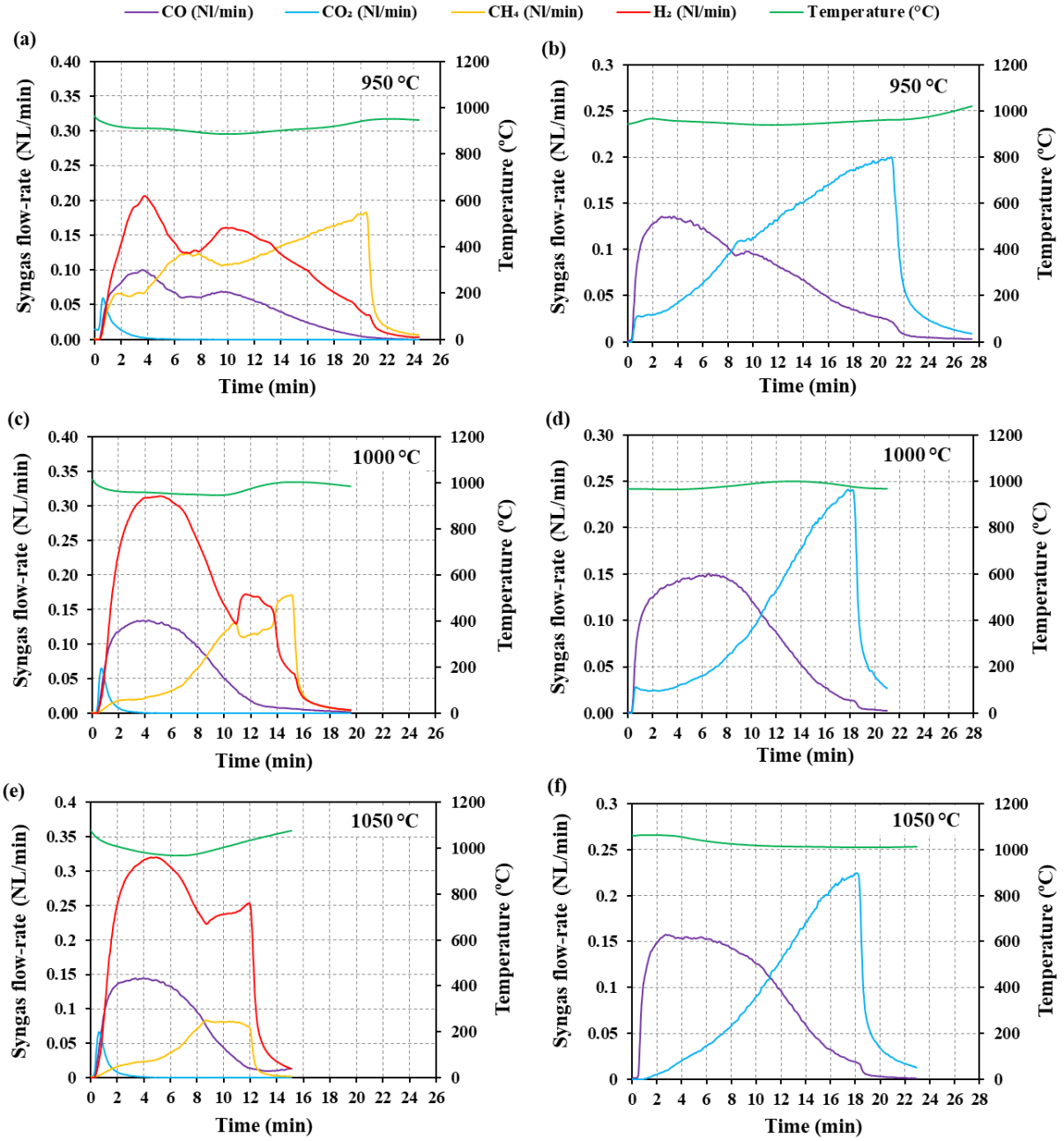

Figure 2-21. Evolution of the production rates of H_2, CO, CO_2, and CH_4 in the syngas along with nominal reactor temperature for reduction with CH_4 (a, c, and e) and oxidation with CO_2 (b, d, and f) of CeO_2-Al_2O_3 blend cycled isothermally at 950, 1000, and 1050 °C.

Fig. 2-22 shows the syngas yields quantified from the integration of the measured syngas production rates (Fig. 2-21) and reactor performance during reduction and oxidation steps. As expected, the CO (CeO_2+CH_4), H_2 (CeO_2+CH_4), H_2 (CH_4 cracking) yields, and δ_{red} increased with temperature, while the CO_2 (CeO_2+CH_4) yield remained the same (Fig. 2-22a). During oxidation step (Fig. 2-22b), an increase in the CO yield (2.89-3.12 mmol/g_{CeO_2}) was observed when increasing the temperature in the range of 950-1050 °C, thereby enhancing the δ_{ox} (0.37-0.40). The δ_{ox} values were similar to δ_{red}, thus confirming complete ceria re-oxidation with CO_2.

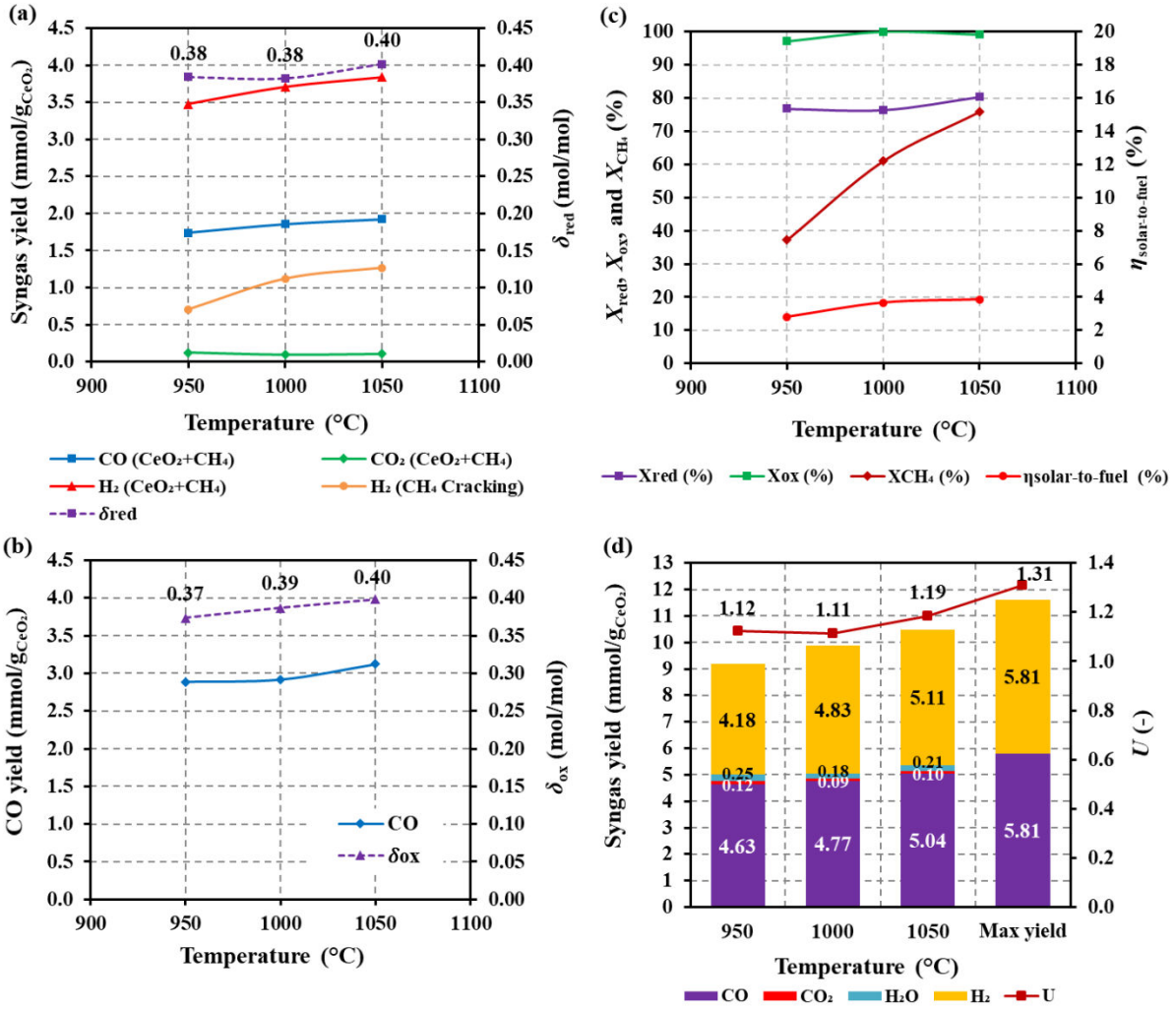

Figure 2-22. Effect of temperature on (a) syngas yields and δ_{red} for reduction with CH_4, (b) CO yield and δ_{ox} for oxidation with CO_2 of CeO_2-Al_2O_3 blend cycled isothermally (CH_4 and CO_2 flow-rate of 0.2 NL/min), (c) ceria reduction/oxidation yields (X_{red}, X_{ox}), methane conversion (X_{CH4}), and solar-to-fuel energy conversion efficiency ($\eta_{solar\text{-}to\text{-}fuel}$), and (d) energy upgrade factor (U) and total syngas yields obtained from both reduction and oxidation steps.

A temperature increase significantly enhanced the reactor performance (Fig. 2-22c), especially methane conversion (37.2%–75.8%). Fig. 2-22d compares the total syngas yield obtained from ceria cycles (sum of both steps) to the theoretical maximum yield (assuming that δ_{max}=0.5 in Eqs. 2-12 and 2-13, thereby yielding both 1 mol CO and 1 mole H_2 per mole CeO_2). Increasing temperature promoted the overall H_2 and CO yields with maximum measured values

of 5.11 and 5.04 mmol/g_{CeO_2} at 1050 °C, respectively, while the maximum theoretical H_2 and CO yields that can be expected with CO_2 are 5.81 mmol/g_{CeO_2}. Note that the amounts of both H_2 and CO produced by side reactions (CH_4 cracking: $CH_4 \rightarrow C+2H_2$ and carbon gasification: $C+CO_2 \rightarrow 2CO$) in both steps were taken into account in Fig. 2-22d). The CO yield was close to the H_2 yield throughout the range. In addition, U was in the range 1.11-1.19 (vs. 1.31 for a stoichiometric reaction with δ_{max}=0.5).

2.4.6 Comparison of oxidation with H_2O and CO_2

Fig. 2-23 compares the syngas production rates during exothermic ceria foam oxidation with H_2O (Fig. 2-23a) and with CO_2 (Fig. 2-23b) at 1000 °C, using the same operating conditions during reduction step (cycle 12 compared to cycle 15 for a ceria foam with 18.3057 g, ST-1000).

Using CO_2 as an oxidant resulted in longer oxidation duration (13.6 min for CO_2 vs. 10.6 min for H_2O) to reach completion, thereby denoting slower oxidation kinetics with CO_2 compared to H_2O. The slower syngas production rate during oxidation with CO_2 could also be due to reduced thermodynamic driving force and kinetics to gasify the deposited carbon via the Boudouard reaction compared to steam gasification and not due to the kinetics of ceria oxidation. The total CO yield with CO_2 as oxidant was higher when compared with the H_2 yield obtained with H_2O as oxidant (Table 2-1). This is because carbon from methane decomposition reacts with CO_2 ($C+CO_2 \rightarrow 2CO$), thus forming an additional amount of CO. However, the CO yield from $CeO_{2-\delta}+CO_2$ reaction was very similar to the H_2 yield from $CeO_{2-\delta}+H_2O$ (Eq. 2-13), thus confirming data consistency. For this reason, δ_{ox} and δ_{red} were also similar either using CO_2 or H_2O during ceria oxidation (Table 2-1).

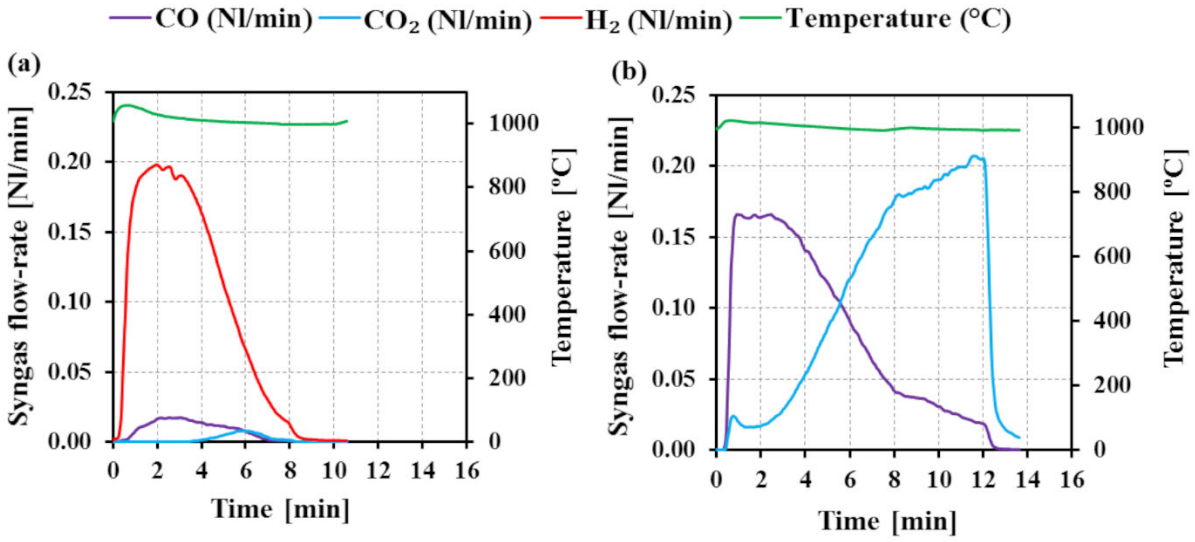

Figure 2-23. CO, CO_2 and H_2 evolution rates along with nominal reactor temperature during reduced ceria oxidation with (a) H_2O (H_2O flow-rate of 200 mg/min, inlet mole fraction of 55%) and (b) CO_2 (CO_2 flow-rate of 0.2 Nl/min, inlet mole fraction of 50%) at 1000 °C (total Ar flow of 2.2 Nl/min).

Table 2-1. Comparison of the syngas yields obtained during reduced ceria oxidation with H_2O and with CO_2 at 1000 °C.

Oxidizing agent	Total syngas yield during oxidation step (mmol/g_{CeO_2})			H_2 yield from $CeO_{2-\delta}+H_2O$ (mmol/g_{CeO_2})	CO yield from $CeO_{2-\delta}+CO_2$ (mmol/g_{CeO_2})	δ_{red}	δ_{ox}
	H_2	CO	CO_2				
H_2O (200 mg/min)	2.305	0.178	0.042	2.043	-	0.36 ± 0.01	0.35 ± 0.01
CO_2 (0.2 Nl/min)	-	2.504	-	-	2.064	0.36 ± 0.01	0.36 ± 0.01

2.4.7 Assessment of thermochemical stability during cycling

The cycling stability of ceria was experimentally studied. Ceria foam (18.3705 g, ST-1000) was subjected to a total of 15 cycles (Table A-1), for which 10 of them (cycles 1, 3-5 and 10-15) were operated under the same conditions in order to investigate performance stability and to confirm experimental repeatability (the other cycles were performed using different conditions of temperatures and CH_4 flow-rates and were thus not reported). For these cycles (Fig. 2-24), both reduction (CH_4 flow-rate of 0.2 Nl/min) and oxidation (H_2O flow-rate of 200 mg/min) were performed at 1000 °C (total Ar carrier gas flow-rate of 2.2 Nl/min, N_2 was used in place of Ar in cycles 13 and 14 to confirm that the type of carrier gas does not change the cycling performances).

As a result, the CO, CO_2 and H_2 yields produced from CeO_2+CH_4 reaction during reduction step were constant throughout the 10 non-consecutive cycles (Fig. 2-24a), despite a slight fluctuation in the H_2 yield associated with CH_4 cracking (0.35-1.27 mmol/g_{CeO_2}). This is simply because the amount of H_2 from methane cracking depends on the reduction step duration that was not exactly the same for each cycle (as methane is continuously injected, the injection duration, and thus the amount of H_2 produced is different). The δ_{red} values were reasonably stable in the range 0.35-0.38 and the δ_{ox} values (in the range 0.35-0.37, Fig. 2-24b) were also similar to the δ_{red} values throughout the cycles, thereby highlighting stable oxygen exchange capacity of ceria foam for relatively large changes in oxygen stoichiometry.

During oxidation (Fig. 2-24b), a stable pattern in the H_2 yield from $CeO_{2-\delta}+H_2O$ in the range of 2.04-2.17 mmol/g_{CeO_2} was evidenced while the other H_2 yields produced by the reaction of carbon with H_2O ($C+2H_2O$, $C+H_2O$) were also constant. The amounts of CO and CO_2 were in the range of 0.11-0.18 and 0.02-0.05 mmol/g_{CeO_2}, respectively. Note that the result of syngas yields in the cycle 15 was not shown because ceria was re-oxidized with CO_2.

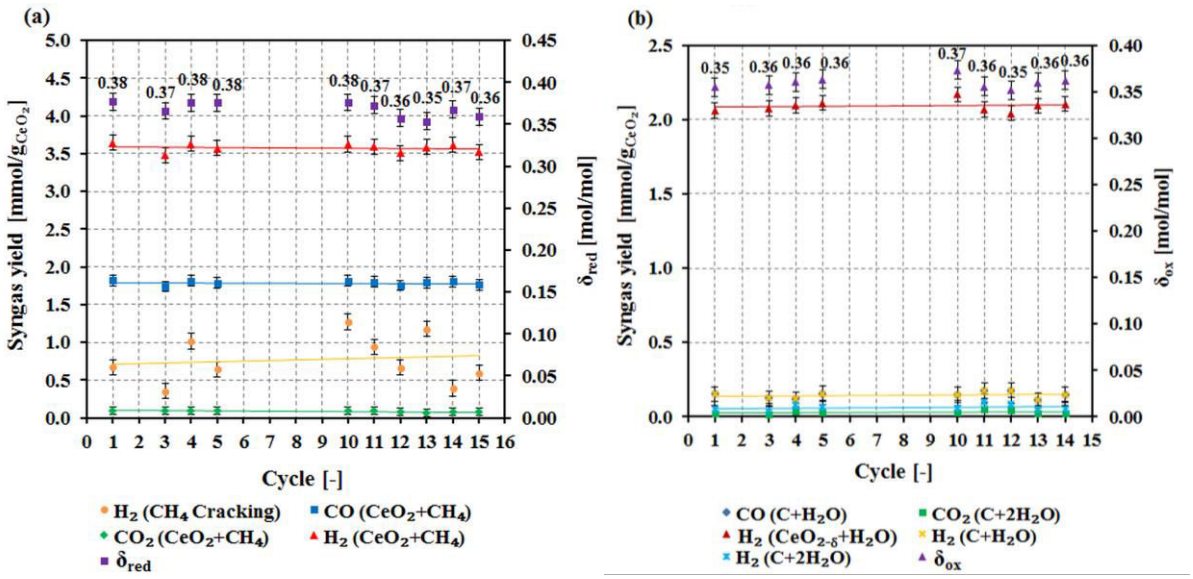

Figure 2-24. Cycling stability related to syngas yields (with associated tendency lines) and δ for both (a) reduction and (b) oxidation of ceria foam performed at 1000 °C.

The H_2 and CO production rates (cycles n° 12, 13 and 14) were plotted to demonstrate the repeatability for both reduction (Fig. 2-25a) and oxidation (Fig. 2-25b) of ceria. The H_2 profiles in the reduction step showed a slight difference (Fig. 2-25a) attributed to a variation in the H_2 produced by CH_4 cracking. Nevertheless, the CO flow-rate showed overlapping profiles. Additionally, the H_2 and CO flow-rates regarding oxidation step were also similar through cycles 12-14 (Fig. 2-25b), thereby corroborating excellent repeatability of syngas production rates.

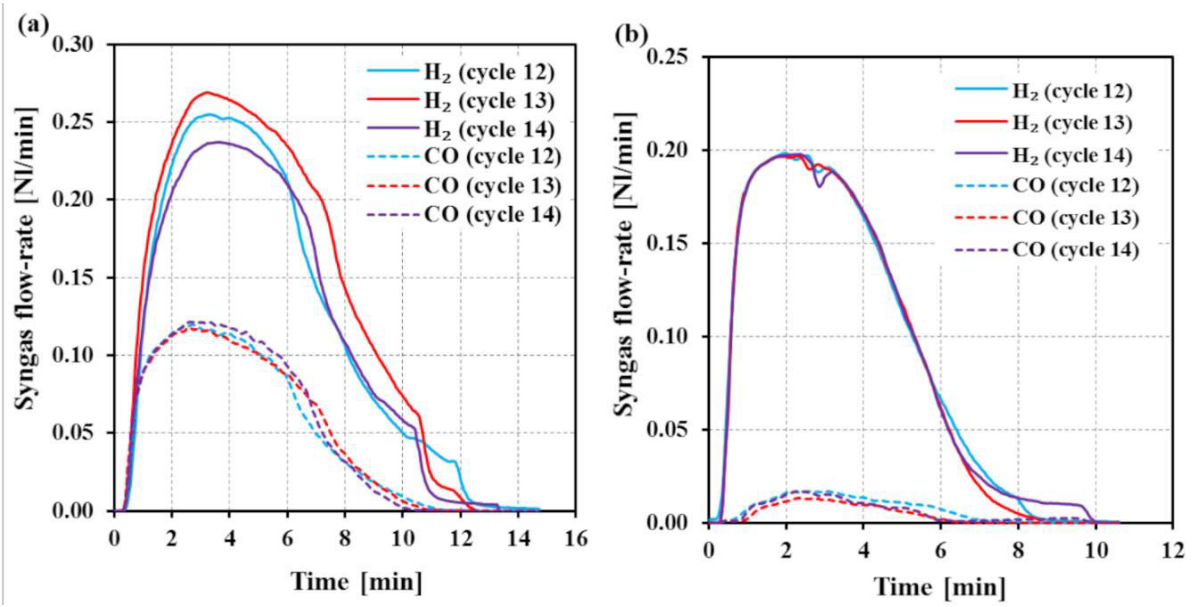

Figure 2-25. H_2 and CO evolution profiles for both reduction and oxidation of ceria foam at 1000 °C: (a) CH_4 was utilized as reducing agent and (b) H_2O was utilized as oxidizing agent.

Fig. 2-26a shows the reduction yield (X_{red}), oxidation yield (X_{ox}), methane conversion (X_{CH_4}) and solar-to-fuel energy conversion efficiency ($\eta_{solar\text{-}to\text{-}fuel}$) for the 10 non-consecutive cycles. Both X_{red} and X_{ox} fluctuated minimally in the ranges of 70.7-75.4% and 94.1-100%,

respectively, thus leading to a stable $\eta_{solar\text{-}to\text{-}fuel}$ (3.3-4.3%). Fluctuating pattern of X_{CH_4} between 47-61% was observed due to a small variation in the rate of ceria reduction with methane that directly modifies the operating duration (in the range 9.4-11.4 min). This results in a variation of the total injected methane quantity (1.35-1.63 g), thereby affecting U in the 0.99-1.07 range (Fig. 2-26b). Noticeably, the U evolution is reverse to that of X_{CH_4} since the increase of X_{CH_4} may imply an increase in the amount of carbon deposition that leads to a lowered U (e.g., cycles 5 and 10). The total H_2 and CO yields over cycling (Fig. 2-26b) were also stable (5.55-5.80 and 1.74-1.82 mmol/g_{CeO_2}, respectively), thus leading to fairly constant H_2/CO ratio (3.13-3.2) and overall syngas yield (7.55-7.89 mmol/g_{CeO_2}). Small amounts of CO_2 (0.07-0.1 mmol/g_{CeO_2}) and H_2O (0.13-0.2 mmol/g_{CeO_2}) were also detected.

The material thermal stability upon the cycling conditions was satisfactory. The foam shape and dimensions remained intact in the cavity after the cycling series, with some cracks making the structure more brittle than the original one.

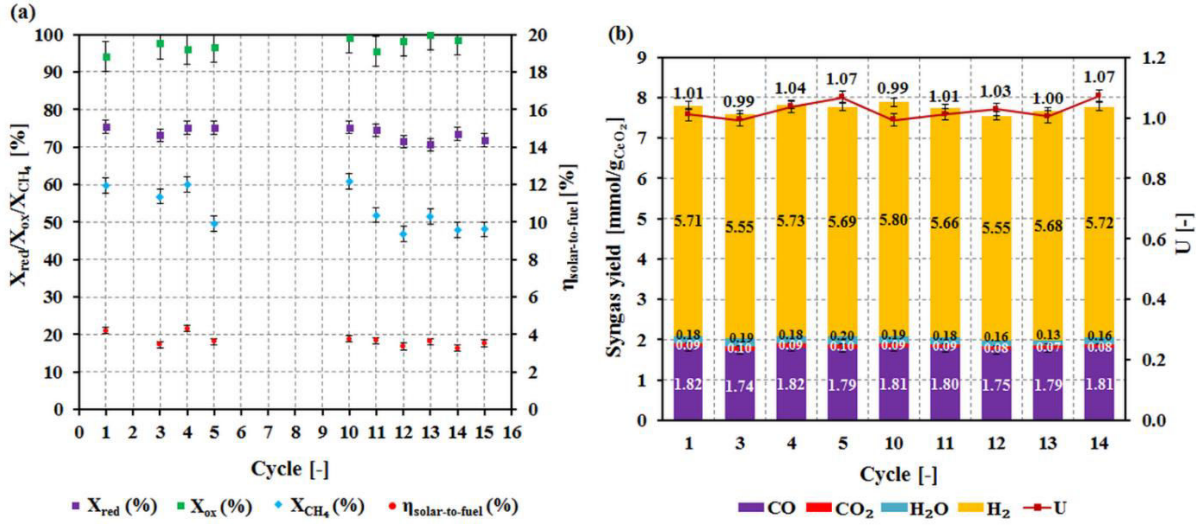

Figure 2-26. Cycling stability of ceria regarding (a) reduction yield, methane conversion, and solar-to fuel energy conversion efficiency, and (b) energy upgrade factor and total syngas yields (from both CeO_2+CH_4 and $CeO_{2-\delta}$+H_2O).

To validate the cycling stability of ceria, a pristine ceria reticulated foam (17.0152 g) sintered at 1000 °C for 6 h was used (Fig. A-15a) to experimentally investigate the cycling stability during 6 consecutive cycles at 1000 °C (CH_4 flow rate of 0.2 NL/min for reduction step and H_2O flow-rate of 200 mg/min for oxidation step). N_2 was used as a carrier gas (2.2 NL/min). Fig. 2-27 shows the syngas yields and reaction extents over six consecutive cycles during ceria reduction with methane (Fig. 2-27a) and ceria oxidation with H_2O (Fig. 2-27b). As expected, the H_2 (CeO_2+CH_4), CO, and CO_2 yields were constant over the whole cycling (ranging between 3.39-3.68 mmol/g_{CeO_2} for H_2, 1.69-1.84 mmol/g_{CeO_2} for CO, and 0.05-0.07 mmol/g_{CeO_2} for CO_2, Fig. 2-27a), thus validating ceria cycling stability. However, both small sintering and cracking lines within the sample were observed after the last cycle (Fig. A-15b), presumably due to its weakened structure associated with low sintering temperature (1000 °C). Nevertheless, the redox cycling performance of ceria was not altered as reflected by a minimal fluctuation of reduction extent (δ_{red} in the range of 0.32-0.36). The H_2 (CH_4 cracking) yield fluctuated slightly (0.64-1.16 mmol/g_{CeO_2}), except for cycle 1 (2.00 mmol/g_{CeO_2}) in which the

H_2 yield and δ_{red} were much higher due to a higher reduction temperature (1050 °C) than the other cycles (the CO and CO_2 formed in the oxidation step were thus also higher, Fig. 2-27b).

Likewise, the H_2 ($CeO_{2-\delta}+H_2O$) yield produced by Eq. 2-13 (Fig. 2-27b) was fairly stable (1.94-2.05 mmol/g_{CeO_2}) thus leading to a similar stable δ_{ox} pattern (0.33-0.35). In addition, the quantities of $H_2(C+2H_2O)$, $H_2(C+H_2O)$, $CO(C+H_2O)$, and $CO_2(C+2H_2O)$ remained similar except for cycle 1 as mentioned above. Stable patterns in X_{red}, X_{ox}, X_{CH4}, $\eta_{solar\text{-}to\text{-}fuel}$ and total syngas yield were consistently noticed (Fig. A-16). Thus, the cycling stability of ceria can fairly be validated.

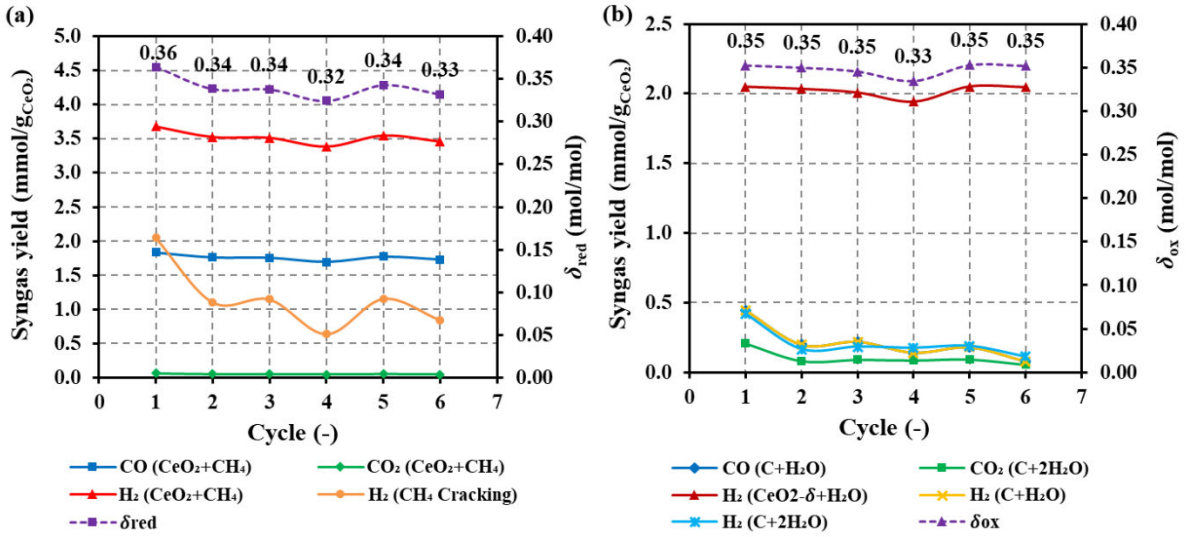

Figure 2-27. Syngas yield and δ for both (a) reduction and (b) re-oxidation of ceria during 6 consecutive redox cycles performed at 1000 °C.

2.5 Conclusions

A solar process for chemical looping reforming of methane (CLRM) using solid oxidants has been developed, with final aim of producing syngas according to the following reaction: $CH_4 + M_xO_y \rightarrow M_xO_{y-1} + CO + 2H_2$. The key advantages of such a process with respect to the conventional process are: (i) generation of a gaseous mixture suitable for methanol synthesis, (ii) utilization of a solid oxidant instead of gaseous oxygen or steam water, (iii) absence of costly catalysts, and (iv) possible production of H_2 (or CO)-rich gas in a second step enabling the regeneration of the starting oxide. This chemical looping reforming process has been fully demonstrated using CeO_2 and Fe_2O_3 as the oxygen carrier materials in the form of powders and reticulated porous foams within both fixed bed and volumetric solar reactor. Indeed, a directly irradiated 1.5 kW_{th} solar reactor has been successfully operated for solar-driven CLRM and isothermal H_2O/CO_2 splitting using different cerium and iron oxide structures as oxygen carriers, demonstrating the reliability and flexibility of the combined process towards syngas production. A parametric study was carried out focusing on the influence of sintering temperature of the ceria foam structure, CH_4 flow-rate, operating temperature, type of oxidant (H_2O or CO_2) and oxygen carrier structures on lattice oxygen transfer (n_O) and averaged oxygen non-stoichiometry (δ), CH_4 conversion, syngas production, reactor performance, and thermochemical cycling stability. The thermodynamic analysis provided insights into the theoretically possible chemical reactions and equilibrium species distribution for comparison with experimental results.

- A high sintering temperature (1400 °C) adversely affects the syngas yield, methane conversion, and reactor performance, because of both lowered solid/gas interface area and lattice oxygen mobility, thus decreasing oxygen exchange capacity.

- Increasing the CH_4 flow-rate enhances δ (maximum value up to 0.41 for ceria powder), syngas production rate, and syngas yield. However, a remarkable decrease in CH_4 conversion is concomitantly observed (minimum value as low as 43% for CeO_2 powder). High CH_4 flow rate also favors CH_4 cracking reaction and carbon deposition, since the rate of methane decomposition exceeds the rate of ceria reduction. Such carbon deposition is not detrimental for the whole process since carbon is gasified in the oxidation step.

- Increasing the temperature (between 900-1050 °C) accelerates the rate of ceria reduction, which in turn significantly enhances the methane conversion (up to 77.4% for CeO_2-Al_2O_3 blend) and syngas yield and decreases the reduction step duration. However, it comes at the expense of favoring methane cracking, especially at 1050 °C. The $\eta_{\text{solar-to-fuel}}$ is increased with both CH_4 flow-rate and temperature (values in the range 1.14%-5.60%), while the energy upgrade factor up to 1.19 is accomplished with CO_2 as oxidant.

- The shape of ceria materials (packed-bed powder, foam) does not show any significant impact on both the syngas yield and δ but rather on CH_4 conversion and efficiency. The ceria foam shows better performance in terms of volumetric solar radiation absorption and uniform heating with lower solar power consumption compared to the other structures, thereby upgrading $\eta_{\text{solar-to-fuel}}$ (maximum value up to 5.6%). This implies that the foam structure is the most suitable to achieve high specific syngas production with reduced solar energy input.

- The ceria re-oxidation step is always complete (δ_{ox} and δ_{red} are similar), which means it is not kinetically limited, and it depends only on the extent of ceria reduction achieved during the previous reduction step. Ceria reduction (δ_{red}) is strongly dependent on temperature or methane flow rate, which thus denotes kinetically-controlled reaction rate.

- Stable patterns in the ceria reduction and oxidation extents, CH_4 conversion, and syngas yields during cycles for reticulated porous foam demonstrated remarkable thermochemical cycling stability.

- Iron oxide (Fe_2O_3) in the form of powder or porous foam showed relatively low reaction rate when reacting with methane at 1000 °C, and the reduction extent strongly depended on temperature. However, increasing the temperatures (≥1100 °C) resulted in strong sintering (dense structure), lowered syngas yield, and material deactivation. In contrast, cerium oxide (CeO_2) showed faster reaction rates than iron oxide when reacting with methane at 1000 °C. Thus, utilizing iron oxide (Fe_2O_3) as oxygen carrier is not suitable for solar CLRM with respect to poor material re-oxidation capability; instead, iron oxide reduction with CH_4 could be an attractive route for producing both metallic iron and syngas via CO_2-free solar metallurgical process. For these reasons, the use of cerium oxide as oxygen carrier for solar CLRM is more appropriate than iron oxide

The solar reactor concept is expected to be flexible in processing different oxygen carrier structures with varying particle sizes or geometries. Combining concentrated solar energy and CLRM was shown to be a promising and sustainable pathway toward clean solar fuels.

Chapter 3: Solar gasification of biomass in a continuous spouted-bed solar reactor[2]

3.1 Introduction

The solar-driven gasification of carbonaceous feedstock represents a promising pathway for producing synthesis gas [31]. It also enables solar energy storage in a chemical form [26], and improves the fuel yield without CO_2 emissions compared to conventional gasification. The carbonaceous feedstock is gasified with an oxidant such as H_2O/CO_2 by utilizing concentrated solar power as an external energy source to drive the gasification reaction. In addition, the process is carbon-neutral when biomass is utilized as carbonaceous feedstock [38].

To reach greater performance, either the improvement of the solar reactor or the optimization of operating conditions is required. In this chapter, an experimental study of continuous solar gasification of biomass is investigated to convert both solid biomass and solar energy into synthesis gas and to optimize syngas production capacity as well as reactor performance through parametric investigation. A parametric study considering a variety of operating parameters with respect to different lignocellulosic biomass feedstocks (wood type), biomass feeding rates (0.6-2.7 g/min), steam/biomass molar ratios (1.6-2.8), carrier gas flow rates (2-3.3 Nl/min) and reaction temperatures (1100-1300 °C) was conducted in a 1.5 kW_{th} continuous spouted-bed solar reactor utilizing highly concentrated sunlight provided by a solar concentrating system.

3.2 Experimental set-up and methods

3.2.1 Feedstocks

Prior to the solar-driven tests, the outlet components (outlet tubes, bubbler and filters) as well as the pre-loaded biomass feedstock are precisely weighed with a digital balance (0.01 g readability) for obtaining their initial weights. Five types of biomass feedstocks consisting of beech wood (Type A and B) or a mix of pine and spruce wood (Type C, D and E) with different sizes (Fig. 3-1), compositions and properties (Table 3-1) were utilized in the solar-driven experiments for investigating the influence of both biomass type and particle size on the syngas production, gasification performance, and biomass injection stability in a continuous feeding mode of operation.

[2] Details of this chapter consist of three peer-reviewed articles:

- S. Chuayboon, S. Abanades, S. Rodat, *Chem. Eng. Process. Process Intensif.* 125 (2018) 253-265.
- S. Chuayboon, S. Abanades, S. Rodat, *Renew. Energy*. 130 (2019) 360–370.
- S. Chuayboon, S. Abanades, S. Rodat, *Fuel Process. Technol*. 182 (2018) 1–14.

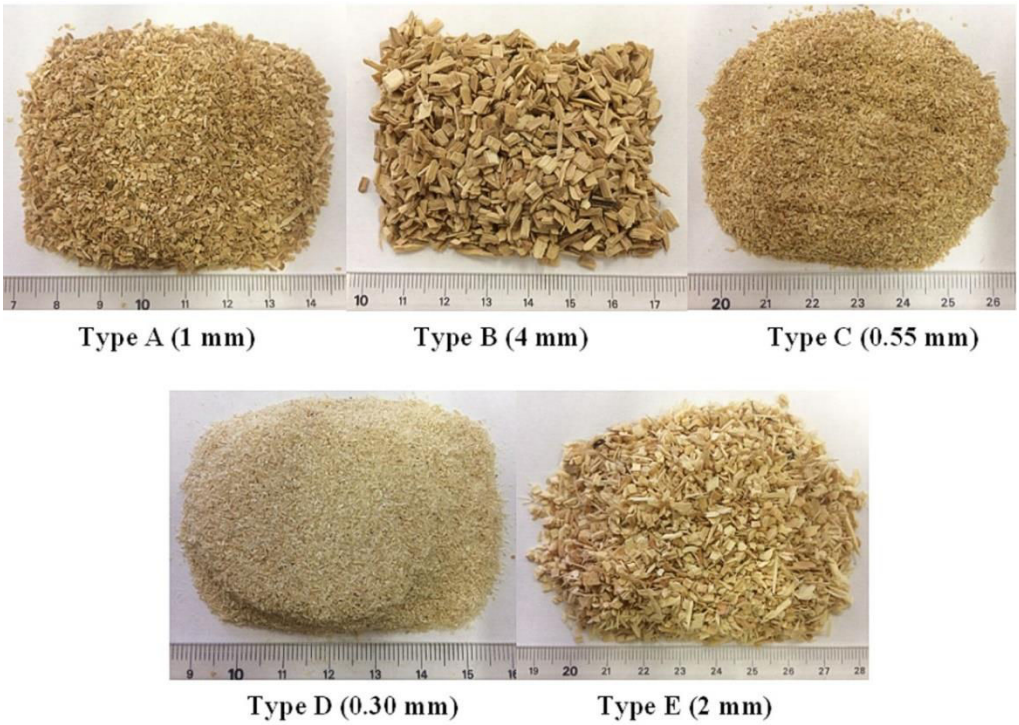

Figure 3-1. Photographs of the different biomass feedstocks. Types A and B are beech wood while types C, D and E are resinous mix wood (the unit scale on the ruler is 1 cm).

Table 3-1. Characteristics of the different biomass feedstocks (elemental composition determined via flash combustion to quantify C, H, N, S, and O by difference).

Type	Biomass specie	Low heating value (MJ/kg)	Mean particle size (mm)	Apparent density (g/cm^3)	Proximate analysis (wt %)		Ultimate analysis (wt %)				
					Moisture	Ash	C	H	O	S	N
Type A	Beech ($C_6H_9O_4$)	18.29	1	0.201	8.9	0.46	48.3	6.7	44.4	<0.1	0.11
Type B	Beech ($C_6H_9O_4$)	18.38	4	0.222	8.9	0.57	48.5	6.7	44.1	<0.1	0.11
Type C	Resinous mix ($C_6H_{11}O_4$)	17.66	0.55	0.194	7.3	0.46	49.9	7.1	42.4	<0.1	0.12
Type D	Resinous mix ($C_7H_{11}O_4$)	18.3	0.3	0.140	9.3	0.29	52.8	7.1	40.7	<0.1	0.14
Type E	Resinous mix ($C_7H_{11}O_4$)	17.4	2	0.124	9.2	0.28	52.3	7.2	40.1	<0.1	0.09

3.2.2 Solar reactor

Fig. 3-2 shows the schematic diagram of the continuously particle-fed solar biomass gasifier driven by real high-flux solar radiation. The system includes the solar gasifier coupled with an automatic feedstock delivery system, gas injection, gas cleaning, particle separation and gas analysis unit. This solar reactor was designed and tested by Bellouard et. al [143], and the main details on this solar reactor have already been described in the previous Chapter. The additional information is summarized here.

The design of the solar reactor is based on the concept of conical spouted bed reactor. This reactor is flexible and displays high solid and gas residence times and enhanced heat and mass transfer via particle-gas circulation [122]. The stainless steel water-cooled reactor shell is cylindrical. Its reaction chamber consists of an axisymmetric cylindrical cavity receiver made of FeCrAl alloy, and its bottom part features a conical shape with a 60° angle according to

Fig.3-3 left. The cavity is insulated with a 30 mm thick layer of alumino-silicate, which can withstand temperatures up to 1600 °C. The top of the cavity is covered by an alumina cap with a 20 mm-diameter aperture and then a 2 mm-thick zirconia felt to minimize heat losses. Subsequently, an additional protective graphite layer (2 mm-thick) with a 15 mm diameter aperture is positioned at the focal point above the zirconia felt to protect the alumina cap from the high-flux radiation in the case of sudden changes in focal point position. The solar reactor is closed by a hemispherical transparent glass window and heated by the high-flux solar radiation delivered by a solar concentrator (2 m diameter parabolic dish with 0.85 m focal distance and with peak flux density of ~10 MW/m^2 for a DNI of 1 kW/m^2). The maximum solar power absorbed by the cavity via the aperture is 1526 ± 30 W (for a DNI of 1 kW/m^2).

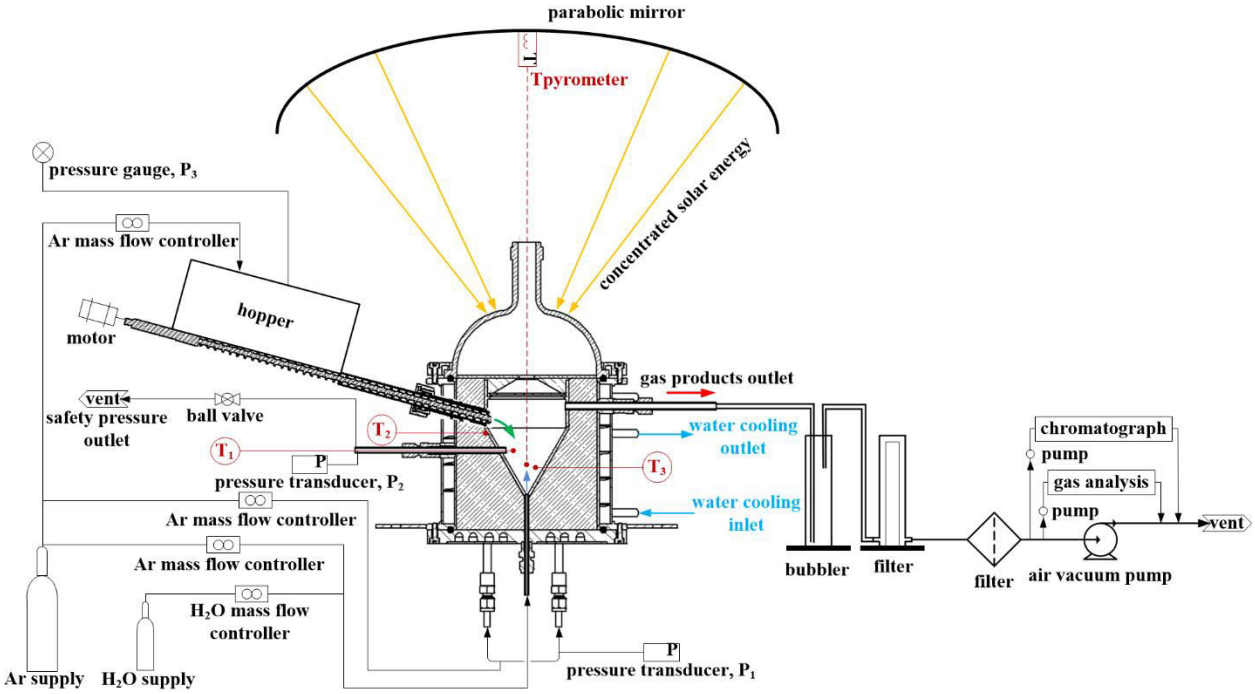

Figure 3-2. Schematic of the continuously-fed solar biomass gasifier and auxiliary components.

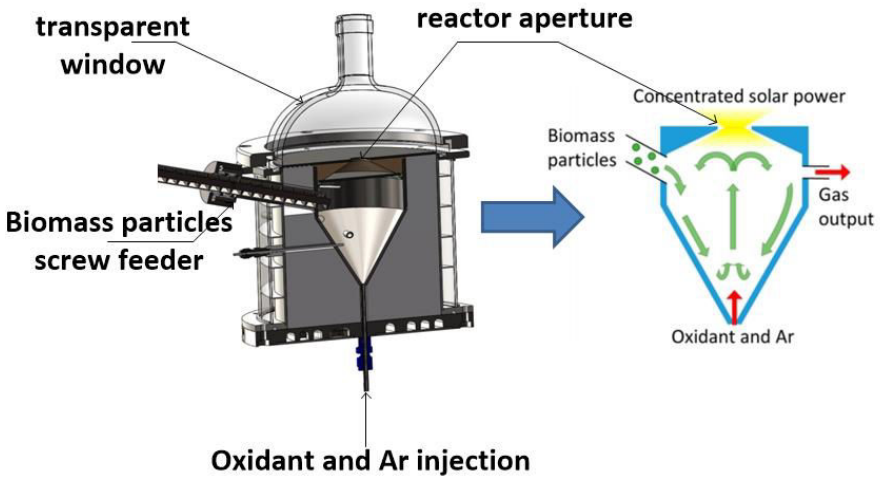

Figure 3-3. 3D cross section of the spouted bed solar reactor (left) and particle trajectory in the reactor cavity (right) [122].

The automatic biomass feeding system is composed of a hopper (1.15 L capacity) and a screw feeder (40 cm length) driven by an electrical motor. B-type thermocouples are inserted inside the conical part of the cavity for measuring the temperatures during experiments (T_1 at the cavity center, and T_3 near the bottom of the cavity in the conical region) and at the external cavity surface (T_2). Their tips are enveloped within an alumina shielding tube in order to protect them from the reacting gases. To confirm the thermocouple measurements, a "solar-blind" optical pyrometer (Impac, operating at 4.8-5.2 μm in a H_2O absorption band) placed at the center of the parabolic mirror is utilized to directly measure the temperature inside the cavity through a calcium fluoride window (installed at the top of the transparent window). Three pressure measurements are employed for monitoring the pressures in the window area (P_1), cavity (P_2), and hopper (P_3). A Venturi pump is positioned at the end of the outlet tube for controlling and maintaining the chamber pressure below 1 bar (~0.85 bar for atmospheric pressure at site elevation) throughout the tests, and a pressure safety valve is also installed.
The injected gases consist of Ar and steam flows. The Ar flows are supplied and controlled by mass flow controllers (MFC, Brooks Instruments model SLA5850S, 0-5 Nl/min ± 0.2% of full scale), while the liquid water flow is supplied by a mass flow controller (Horiba, 0-30 g/h ± 1% of full scale). Filtering and gas cleaning units comprising a bubbler and two micro filters (pore diameter: 0.1μm) are installed at the outlet tube to eliminate steam and condensed particles (char and tars) from the gas products prior to gas analysis.

The gas analysis unit consists of an on-line syngas analyzer (GEIT 3100) and a gas chromatograph (micro GC, Varian CP4900). The syngas analyzer measures continuously the syngas composition (one recording every 3 s). H_2 concentration is measured by utilizing a thermal conductivity detector, while the concentrations of CO, CO_2, and CH_4 are measured by using sensors equipped with NDIR cells. In addition, the GC is utilized for measuring the H_2, CO, CO_2, CH_4, and C_2H_m (C_2H_2, C_2H_4 and C_2H_6) concentrations after gas sampling every ~2 min. Finally, all the data derived from the mass flow controllers, thermocouples, pyrometer, and pressure transducers are recorded by an automated data acquisition system (BECKHOFF).

3.2.3 Procedures

Prior to solar-driven experiments, the particle screw feeder was calibrated at ambient temperature for the different biomass feedstocks, in order to achieve the targeted particle mass-flow rate during solar experiments. A given amount of biomass feedstock is placed into the hopper, and subsequently the feeding system is tightened to the injection port on the side of the reactor. The reactor cavity is then flushed with Ar and concomitantly sucked with the Venturi pump to remove residual air from the system. Then, the solar gasifier is progressively solar-heated (Fig. 3-4a) to the targeted temperature in the range of 1100-1300 °C.

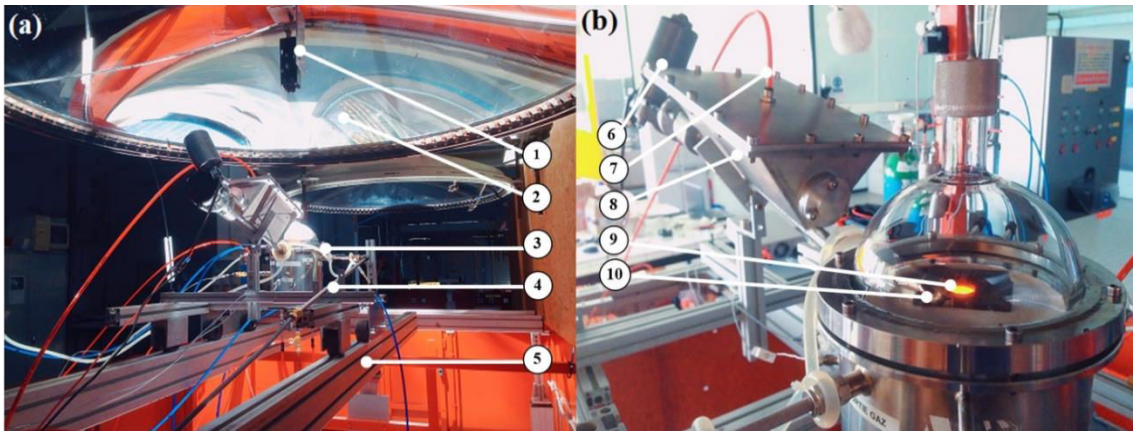

Figure 3-4. (a) On-sun experimental testing of the biomass gasifier and (b) hot reactor cavity after solar heating: (1) pyrometer; (2) 2-m diameter parabolic solar concentrator; (3) solar reactor; (4) gas product outlet tube; (5) reactor frame to adjust the reactor in upward/downward directions with respect to the focal plane; (6) electrical motor; (7) Ar inlet tube; (8) hopper; (9) reactor aperture; (10) protective graphite plate.

During solar heating, the Ar protective flow (2 Nl/min) is fed in the upward direction into the transparent window area via two stainless steel tubes, which are inserted through the insulation layer, and subsequently enters the cavity through the aperture in the downward direction, thereby preventing the hot gases as well as the particles deposition on the window surface. Another Ar protective flow (0.5 Nl/min) is also injected through the feeding system to prevent back-flow of hot gases from the cavity into the biomass injector passage. The homogeneous temperature and low gradient in the reaction zone is confirmed by a small gap between T_1 and T_3, while $T_{pyrometer}$ is lower as a result of the selected slightly over-estimated emissivity (=1) for the cavity (Fig. 3-5a).

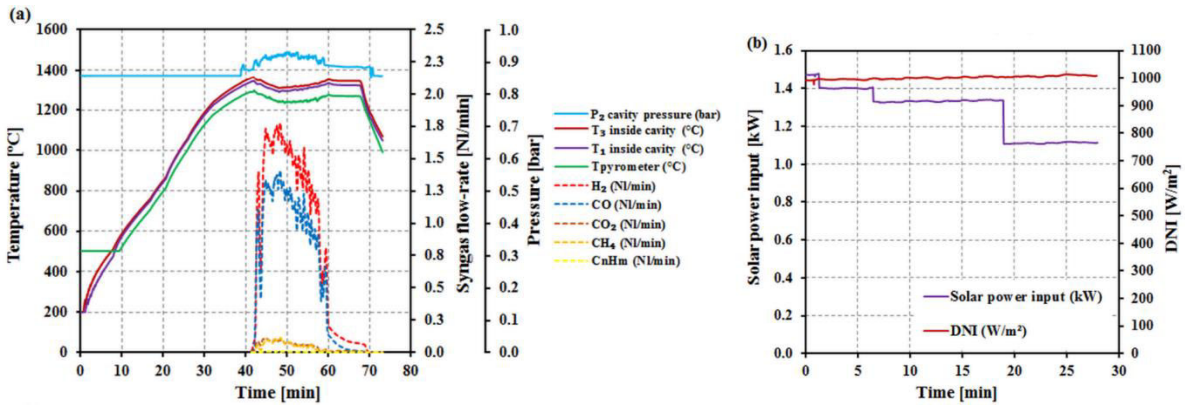

Figure 3-5. (a) Pressure, temperatures and syngas species evolution during heating phase and feedstock injection, (b) solar power input and DNI evolution during feedstock injection period (Run No.12).

Once the desired temperature is reached (40 min to reach 1300 °C in the cavity, Fig. 3-5a), the water is introduced along with Ar carrier gas (0.2 Nl/min) through a vertical alumina tube (2 mm i.d.) at the bottom of the conical cavity. Water is first vaporized before entering the cavity and then steam is entrained by the Ar flow, thereby delivering continuous steam flow inside the cavity. Subsequently, biomass feedstock is continuously fed into the hot cavity

receiver (Fig. 3-4b) until complete feedstock load injection. Therefore, the steam gasification reaction proceeds in a continuous mode. The trajectory of the biomass particles is presented schematically in Fig. 3-3b. Note that the steam/biomass ratio was kept constant at a slightly over-stoichiometric ratio (10% of excess water) by referring to Fig. 3-6.

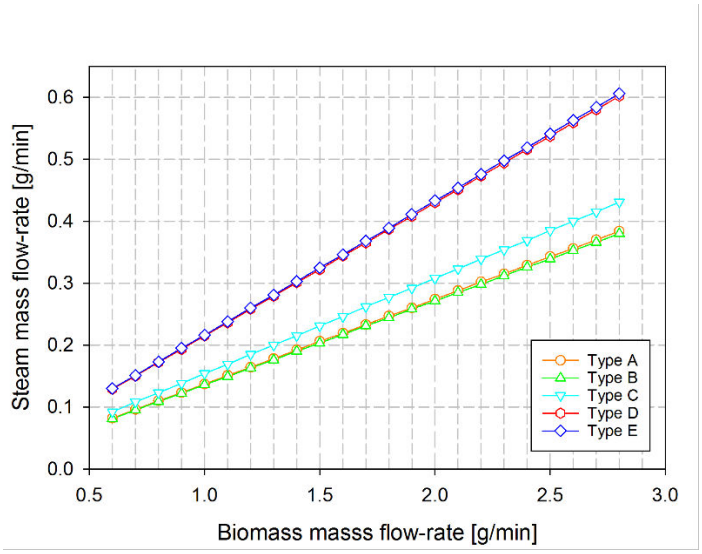

Figure 3-6. Relation between the mass flow rates of steam and biomass feedstocks for a stoichiometric ratio (H_2O/biomass molar ratios of 2 for biomass types A, B and C and 3 for biomass types D and E, including biomass moisture content in the calculation).

During feeding, the solar power input is adjusted by the means of a shutter to stabilize the operating temperature while the DNI remained stable throughout the tests (Fig.3-5b). The produced gases constantly exit the reactor and subsequently flow into the gas cleaning and filtering prior entering the gas analysis system. The gas species concentrations are continuously measured by the online-gas analyzer while the GC measurements are performed every 2 min (Fig. B-1in Appendix B). The production rates of secondary hydrocarbons (C_nH_m) measured by GC include the C_2H_2, C_2H_4, and C_2H_6 (the latter being in negligible amounts). After the test, the outlet components are weighted again for mass balance.

The time-dependent production rate of each gas species (F_i) is calculated from the known flow rate of inert gas (F_{Ar}) and the measured species mole fractions (y_i): ($F_i = F_{Ar} \cdot y_i / y_{Ar}$). Then, both the averaged syngas composition (over the experiment duration) and the syngas yields (mol/g of dry biomass) are calculated by time integration of the gas production rates. The performances of the reactor are then quantified. A representative experiment of steam gasification with continuous biomass injection and the evolutions of syngas production rates at 1300 °C are shown in Figs. B-1 and B-2.

The energy upgrade factor (U) represents the ratio of the energy content of the chemical products to the calorific value of the biomass feedstock:

$$U = \frac{LHV_{syngas} \cdot \dot{m}_{syngas}}{LHV_{feedstock} \cdot \dot{m}_{feedstock}} \quad (3\text{-}1)$$

Where LHV_{syngas} and $LHV_{feedstock}$ are the lower heating values (J/kg) of syngas products and biomass feedstock, and $\dot{m}_{syngas}$ and $\dot{m}_{feedstock}$ are the mass flow rates (kg/s) of syngas products and biomass feedstock, respectively.

The solar-to-fuel energy conversion efficiency ($\eta_{solar-to-fuel}$) represents the ratio of the chemical energy of the syngas produced to the total energy input (both solar power and calorific value of the biomass feedstock):

$$\eta_{solar-to-fuel} = \frac{(LHV_{syngas} \cdot \dot{m}_{syngas})}{\dot{Q}_{solar} + (LHV_{feedstock} \cdot \dot{m}_{feedstock})} \quad (3\text{-}2)$$

Where $\dot{Q}_{solar}$ is the solar power input (W).

The thermochemical reactor efficiency represents the ratio of solar energy absorbed by the reactor that is used to drive the chemical reaction, and to heat steam, inert gas, and solid reactant:

$$\eta_{reactor} = \frac{\dot{Q}_{heating} + \dot{Q}_{reaction}}{\dot{Q}_{solar}} \quad (3\text{-}3)$$

The mass conversion rate is defined as the ratio of net output (syngas, solid products and unconverted water) to net input (biomass and water), which indicates if the mass balance is well closed:

$$M = \frac{m_{syngas} + m_{solid\ products+water}}{m_{biomass} + m_{oxidant}} \quad (3\text{-}4)$$

The carbon conversion is defined as the ratio of the carbon yield in the syngas to the initial amount of carbon in the biomass feedstock (F_i represents the molar flow rate of species i, mol/s):

$$X_C = \frac{\int_0^t F_{CO}(t)dt + \int_0^t F_{CO_2}(t)dt + \int_0^t F_{CH_4}(t)dt + \int_0^t 2F_{C_2H_m}(t)dt}{\int_0^t xF_{C_xH_yO_z}(t)dt} \quad (3\text{-}5)$$

Note that incomplete carbon conversion is the results of some unconverted tars and char remaining after the experiments and collected in the different outlet components.

The mean gas residence time (τ) represents the average amount of time that the gases spend inside the cavity volume at the actual reactor temperature and pressure.

The solar energy storage fraction ($\eta_{solar\ fraction}$) is defined as the ratio of the solar-upgraded chemical energy of the produced syngas to the solar energy input:

$$\eta_{solar\ fraction} = \frac{LHV_{feedstock} \cdot \dot{m}_{feedstock}}{\dot{Q}_{solar}} (U - 1) \quad (3\text{-}6)$$

The whole operating conditions and experimental results for 64 solar-driven experiments using the directly-irradiated solar gasifier are summarized in Appendix B (Table B-1).

3.3 Experimental study of the solar gasification process

3.3.1 Material mass balance

Based on the initial amount of reactants fed into the solar gasifier (biomass and steam) converted into the syngas (quantified by integrating the calculated mass flow-rates of the main gas products), the solid char (recovered in the outlet components) and the unconverted water (trapped in the bubbler), the material mass balance was performed. Char was not found in the cavity after solar tests confirming complete gasification and it was only recovered in the outlet components (trapped in bubbler along with unconverted water and filters). Fig. 3-7 shows the overview of the mass balance, using the data from typical experiments regarding the highest energy upgrade factor for each biomass type at 1300 °C. The mass balances were closed beyond 99% for biomass types A, D and E (Fig. 3-7). Actually, most of them achieved values above 95%, thereby indicating that complete feedstock gasification was reached. Remarkably, the amount of solid residues remaining in the cavity after experiments was negligible (due to low ash content in the range of 0.28-0.46 wt % in the initial biomass as shown in Table 3-1).

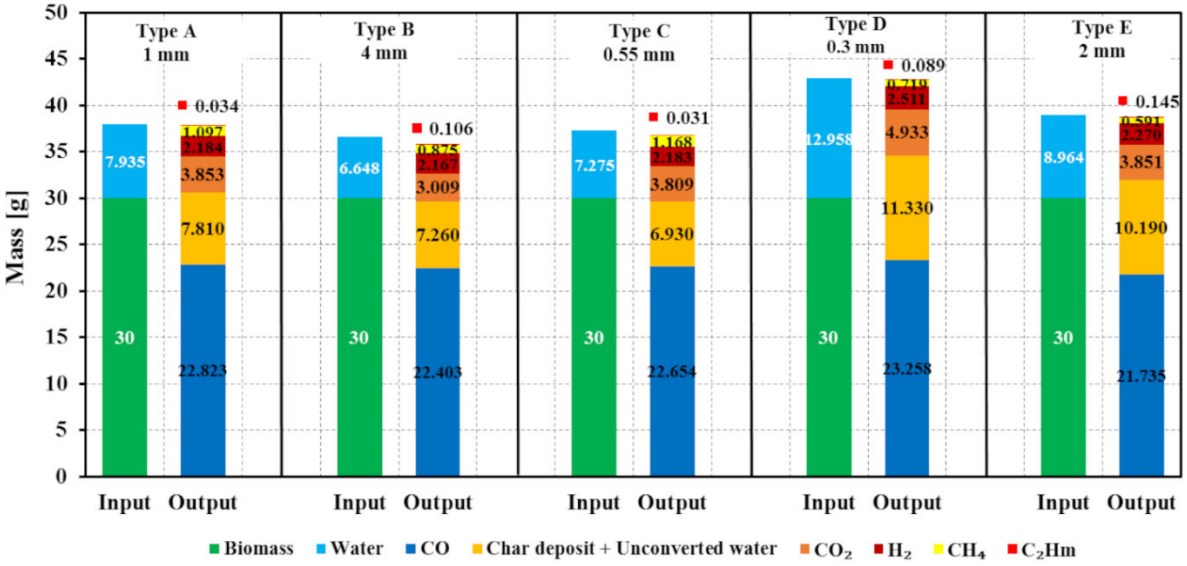

Figure 3-7. Overview of representative mass balances for biomass gasification at 1300 °C (biomass types A: Run No.17, B: Run No.32, C: Run No.42, D: Run No.54 and E: Run No.64).

3.3.2 H_2O/biomass molar ratio influence

The influence of H_2O/biomass molar ratio on the gas species molar fraction and yield (on dry matter basis) was experimentally investigated at 1200 °C for biomass type B and 1300 °C for biomass Type A. At 1200 °C, the biomass flow-rate was set at 1.2 g/min while the steam flow-rates were controlled at 163, 200, and 500 mg/min, resulting in H_2O/biomass molar ratios of 2 (stoichiometric ratio), 2.3 (slightly over-stoichiometric ratio) and 4.5 (largely over-stoichiometric ratio), respectively. At 1300 °C, the biomass feeding rate was kept constant at ~2.2 g/min while adjusting H_2O flow-rates at 200, 300 and 500 mg/min, leading to H_2O/biomass molar ratios of 1.6 (under-stoichiometric ratio), 2.1 (slightly over-stoichiometric ratio) and 2.8 (largely over-stoichiometric ratio), respectively. Note that stoichiometric ratio (based on Eq. 1-16) of both biomass type A and type B was 2 and the moisture content (8.9%

wt. in Table 3-1) contained in the biomass was taken into account for the calculation of H_2O/biomass ratio.

At 1200 °C (Fig. 3-8a and Fig.3-8b), the CO_2 and H_2 mole fractions increased when increasing H_2O/biomass ratio, then resulting in the increase of total syngas yield, from 66.1 mmol/$g_{biomass}$ at stoichiometric ratio of 2 to 69.0 mmol/$g_{biomass}$ at stoichiometric ratio of 4.5. The highest mole fractions of CO_2, H_2, and CH_4, and the lowest mole fraction of CO were found at the highest H_2O/biomass ratio. The variations of CO, H_2, and CO_2 mole fractions can be explained by the excess of water that reacts with CO and favors CO_2 and H_2 formation via the water gas shift reaction ($CO+H_2O \rightarrow CO_2+H_2$). Regarding stoichiometric ratio (H_2O/biomass =2), CO mole fraction was lower while C_2H_m and CH_4 mole fractions were higher when compared with H_2O/biomass ratio of 2.3, while the lowest CO_2 mole fraction (0.047) was noticed. The CH_4 mole fraction increased considerably either at the lowest or at the highest H_2O/biomass ratio. On the one hand, the lack of water implies that CH_4 reforming is not favored ($CH_4+H_2O \rightarrow CO+3H_2$), explaining the high CH_4 content. On the other hand, a large excess of steam injected induces an increase of the volumetric gas flow that reduces the gas residence time, which in turn results in high CH_4 content in the produced syngas. For these reasons, an indication about the optimal syngas production was found at the H_2O/biomass molar ratio of 2.3 with regard to the highest mole fraction of CO and H_2 and the lowest mole fraction of CH_4 and C_2H_m produced. Similar to the results shown in Fig. 3-8a and Fig.3-8b, the optimal syngas production at 1300 °C was found at the slightly over-stoichiometric ratio (H_2O/biomass = 2.1), regarding the highest H_2 and CO production, which results in the H_2/CO molar ratio of 1.35, according to Fig. 3-8c and Fig.3-8d). This condition also leads to the maximum energy upgrade factor (U) of 1.12 (1.17 when accounting for the amount of C_2H_m) and syngas yield (75.1 mmol/$g_{biomass}$) and the lowest amounts of C_2H_m and CH_4. Therefore, the limited excess of H_2O with respect to the stoichiometry is very necessary for favoring H_2 and CO production. In addition, the increased amount of C_2H_m at the highest and the lowest H_2O/biomass molar ratios has a positive impact on the increase of U (due to the high calorific value of C_2H_m) but a negative impact on syngas quality. Hence, the highest value of U when accounting for the C_2H_m quantity cannot point out the optimal condition of syngas production. The values of U without including the calorific value of C_2H_m are thus also specified to better reflect the parameters influence on syngas quality.

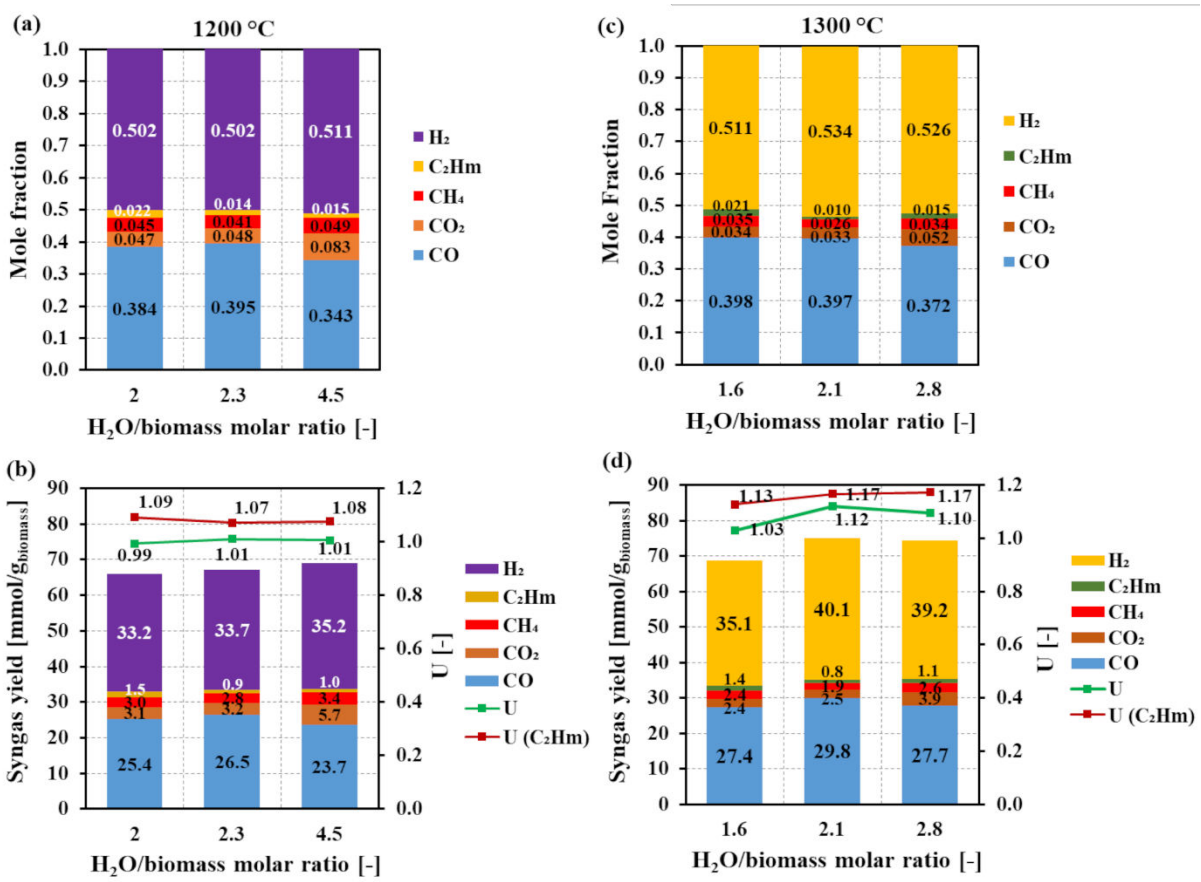

Figure 3-8. Influence of H_2O/biomass molar ratio on (a,c) average syngas composition and (b,d) syngas yield and energy upgrade factor (1200 ℃ (biomass type B) and 1300 ℃ (biomass type A)).

3.3.3 Gas residence time influence

The residence time (τ) that gases spend inside the cavity volume, where the reaction happens, was evaluated (calculated as the ratio of the cavity volume to the total output syngas volumetric flow-rate produced at the actual reactor pressure and temperature conditions). It is a crucial factor that affects the performance of a gasification process. In fact, the residence time is directly changed by adjusting the carrier gas flow rate. For this study, argon (Ar) was used as carrier gas while both biomass type A and type B were employed as carbonaceous feedstock to experimentally determine the influence of residence time on syngas production at 1200 ℃ for type B and 1300 °C for type A under a continuous biomass injection. At 1200 ℃, biomass type B (30 g) was fed at 1.2 g/min while keeping a constant steam flow at 200 mg/min (H_2O/biomass molar ratio=2.3); then, the total Ar flow-rates were varied at 2, 2.7, and 3.2 Nl/min. At 1300 ℃, biomass type A (30g) was fed at 1.5 g/min while injecting steam at 200 mg/min (H_2O/biomass molar ratio=2.1). Then experiments were carried out by changing Ar flow-rate at 2, 2.3 and 3.3 Nl/min. Although the inert gas flow rate also affects the steam partial pressure, the steam fed at the cavity bottom is well mixed with the feedstock and char gasification should not be limited by steam supply. It is however possible that the steam partial pressure modification (due to dilution with inert gas) could affect the gas-phase reactions.

Fig. 3-9a depicts the average mole fraction and quantity of syngas produced at different flow-rates of carrier gas at 1200 ℃. H_2 and CO_2 mole fractions decreased, but C_2H_m and CH_4 mole fractions increased while CO mole fraction tended to slightly increase when increasing the carrier gas flow-rate. According to Fig. 3-9b, the amounts of H_2, CO and CO_2 dropped markedly while the amounts of C_2H_m, and CH_4 increased slightly with the increase of carrier gas flow-rate, thus resulting in the reduction of the total syngas yield and energy upgrade factor. These results can be explained by the reduction of the gas residence time (from 0.87 second at 2 Nl/min to 0.67 second at 3.2 Nl/min) that directly decreases when increasing the carrier gas flow-rate. Therefore, the reaction duration in the gas phase is reduced, thus lowering the extent of gasification reactions. Hence, the higher the carrier gas flow-rate, the lower the amount of H_2 and CO and the higher the amount of C_2H_m, CH_4, and CO_2. Similar to the results shown in Fig. 3-9a and Fig. 3-9b, increasing the carrier gas flow also has adverse influence on syngas yield and energy upgrade factor at 1300 ℃, according to Fig. 3-9c and Fig. 3-9d. As a result, the carrier gas flow should be maintained as low as possible in order to increase the gas residence time; nevertheless, sufficient amounts of carrier gas flow are essential to sweep product gases as well as to protect the window at the expense of additional energy consumed for inert gas heating.

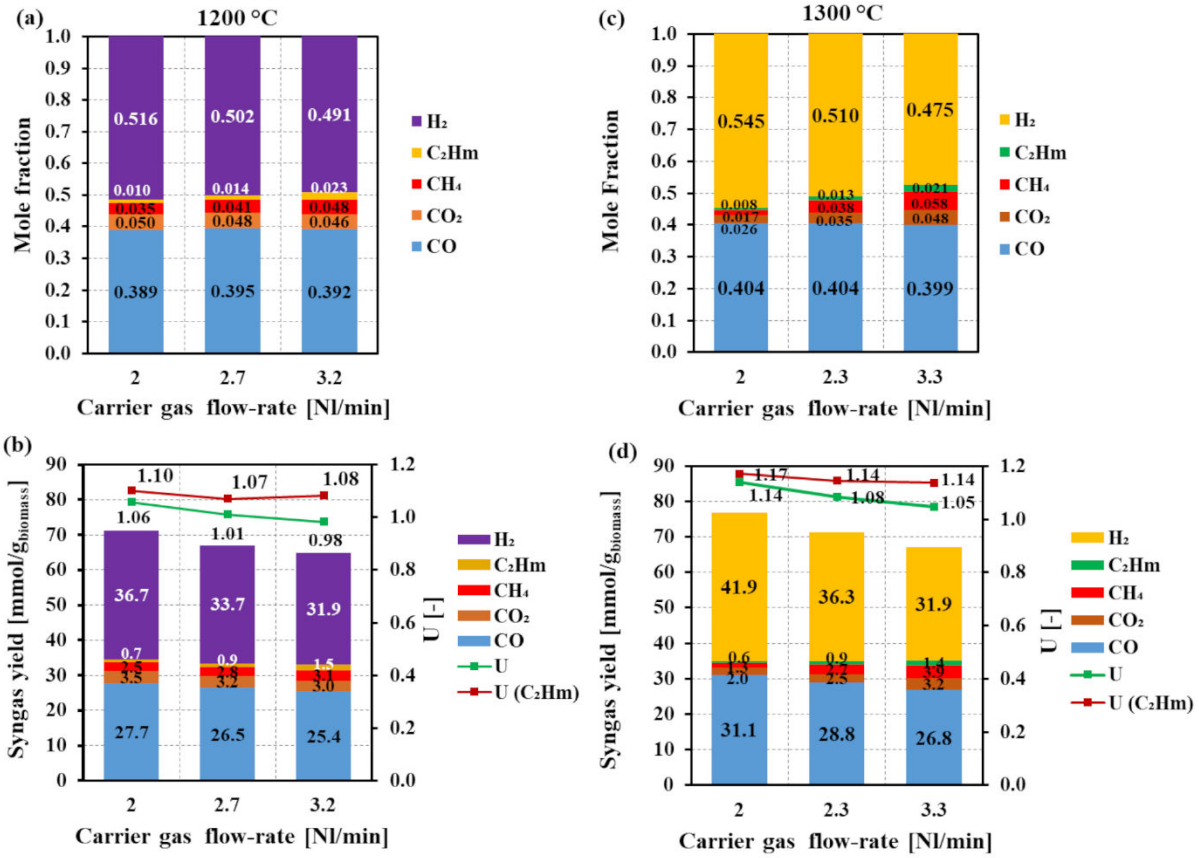

Figure 3-9. Influence of carrier gas flow-rate (residence time) on (a,c) average syngas composition and (b,d) syngas yield and energy upgrade factor (1200 ℃ (biomass type B) and 1300 ℃ (biomass type A)).

3.3.4 Temperature influence

Five different carbonaceous feedstocks were utilized for examining the influence of the temperature on syngas production from steam biomass gasification at the considered operating temperatures of 1100 ºC, 1200 ºC and 1300 ºC (T_3 is the nominal-mentioned temperature for experiments). The continuous biomass feeding rate was set at 1.2 g/min while the steam flow-rate was controlled at the slightly over-stoichiometric flow (10% of excess water) by referring Fig. 3-6 (depending on biomass type). Ar flow rates were set at 2.7 Nl/min, except at 1100 °C for biomass types A and D (3.3 Nl/min). Note that when focusing on the effect of biomass feeding rate, it is quite difficult to operate the solar reactor during long-duration biomass injection at high biomass feeding rate (>1.2 g/min) when considering low operating temperature (1100 °C). Indeed, the kinetic rate of the gasification reaction is slow, which in turn leads to the biomass accumulation in the reactor cavity (the rate of the gasification reaction is lower than the biomass feeding rate). This effect can sometimes be visually observed by the excessive presence of smoke (pyrolysis gases) in the reactor during the gasification process, dirtying the window, as depicted in Fig. B-3. For this reason, the biomass feeding rate was maintained below 1.2 g/min.

The syngas yields at different temperatures along with the evolution of energy upgrade factors (U) (either accounting for the calorific value of C_2H_m or not) during steam gasification are represented in Fig. 3-10 for each type of biomass. Additional experiments were also performed with different operating parameters (steam and biomass feeding rate) to validate the effect of temperature (Fig. B-4).

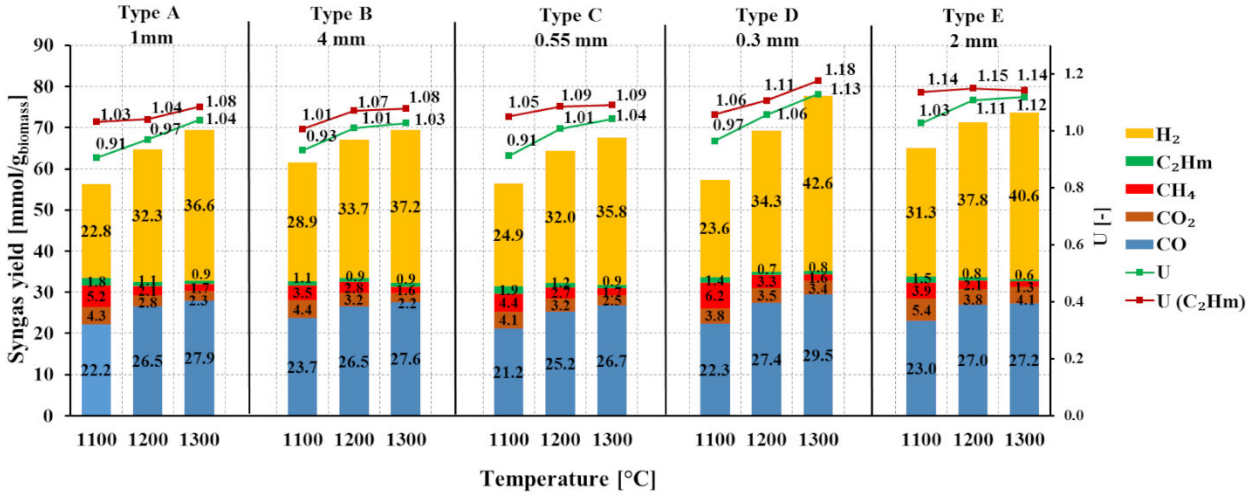

Figure 3-10. Temperature influence on syngas yields and energy upgrade factors for biomass types A- E (biomass feeding rate: 1.2 g/min).

Overall, the quantities of produced H_2 and CO increased strongly while the amounts of C_2H_m, CH_4, and CO_2 decreased significantly with temperature, independently of the biomass type and particle size. For example, the quantities of H_2 and CO for biomass type C increased (from 24.9 and 21.2 mmol/$g_{biomass}$ at 1100 °C to 35.8 and 26.7 mmol/$g_{biomass}$ at 1300 °C), while the quantities of C_2H_m, CH_4 and CO_2 decreased (from 1.9, 4.4 and 4.1 mmol/$g_{biomass}$ at 1100 °C to 0.9, 1.7 and 2.5 mmol/$g_{biomass}$ at 1300 °C, respectively). The substantial increase in the

produced H_2 and CO with the temperature induces the rise of the total syngas yield (despite the reduction of C_2H_m, CH_4 and CO_2 quantities), thus resulting in high-quality syngas. These results are chiefly explained by the significant enhancement of the kinetic rate of gasification ($C + H_2O \rightarrow CO + H_2$) and steam methane reforming ($CH_4 + H_2O \rightarrow CO + 3H_2$). Thus, the higher the temperature, the higher the reaction kinetics and the higher the syngas yield. This was confirmed by an increase of the H_2 and CO production rates with temperature according to both Fig. 3-11a and the Arrhenius equation (Fig. B-5). The maximum H_2 and CO production rates were noticed for the lowest biomass particle size (type D, 0.3 mm) with high H and C contents (Table 3-1).

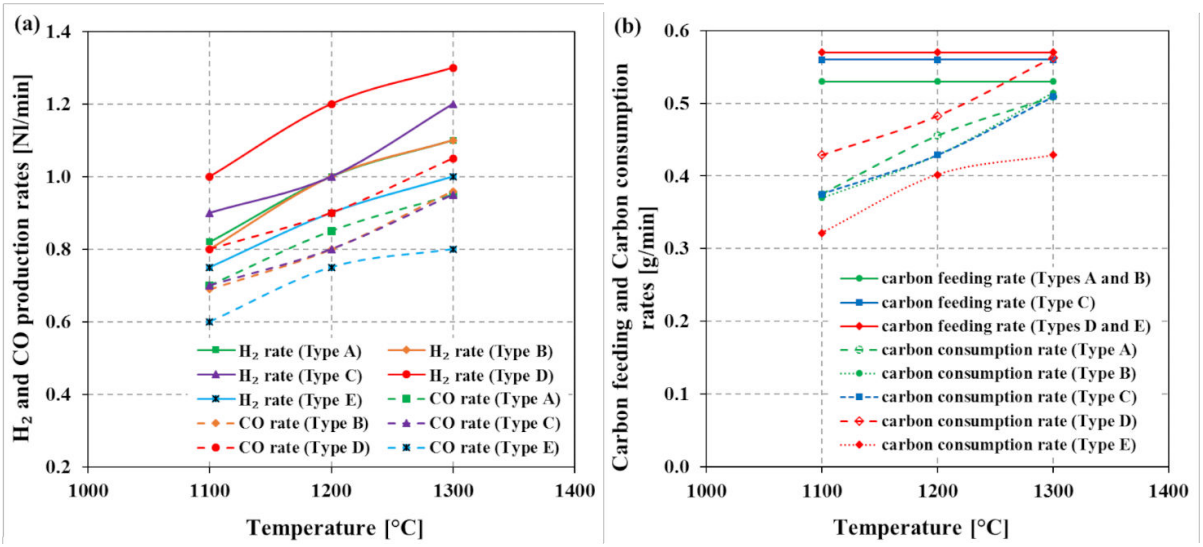

Figure 3-11. (a) Nominal H_2 and CO production rates measured at steady state and (b) carbon feeding and carbon consumption rates for each biomass type as a function of temperature (constant biomass feeding rate of 1.2 g/min for each biomass).

The obtained activation energy (Ea) of the syngas production mechanism, determined from the slope of the line in Fig. B-5, was consistent with biomass particle size (low particle sizes feature a lower Ea, thus favoring rapid gasification rates). For example, the Ea values (Table B-3) for H_2 and CO increased from ~24 kJ/mol (at 0.3 mm size for biomass type D) to ~29 kJ/mol (at 4 mm size for biomass type B). This denotes the sensitivity of the gasification rate to the particle size. Moreover, the Ea values obtained independently from H_2 and CO rates evolution were similar for any biomass type, thus indicating that the H_2 and CO production rates are mainly governed by the same global reaction mechanism (Eq. 1-16).

In addition, the carbon consumption rate was determined (Fig. 3-11b) by assuming that it is equivalent to the summation of the carbon production rates contained in the produced CO, CO_2 and CH_4. The carbon consumption rate increased significantly with temperature, while the carbon feeding rate (i.e., the carbon contained in the fed biomass) for each biomass type was kept constant. This clearly demonstrates that increasing temperature hastened the rate of biomass gasification, thus enhancing ultimately the syngas yield. The lowest carbon consumption rates were observed at the lowest temperature (1100 °C), which denotes that the gasification rate is too low to completely convert the injected biomass, as confirmed by the presence of smoke (Fig. B-3). Moreover, the biomass type D (smallest size) shows higher

carbon consumption rate than other biomass types and the carbon consumption rate matches the carbon feeding rate at 1300 °C, thus confirming complete conversion of biomass feedstock and proper reactor operation (the feeding rate must equal the consumption rate for reliable continuous operation). This also points out that small particle sizes favor the reactivity [144].

Due to very similar chemical compositions between biomass types A and B and between biomass types D and E, the effect of their particle size can be studied and compared. According to Fig. 3-10, both the syngas yields and energy upgrade factors (U) of biomass type A were not significantly different as compared to those of biomass type B (except for biomass type A at 1100 °C for which a higher amount of C_2H_m and CO and a lower amount of H_2 were observed, resulting from a higher carrier gas (Ar) flow that directly results in a drop of the residence time as described in the previous section). Concerning biomass type D compared to type E, the total syngas yields and energy upgrade factors were slightly greater at 1300 °C for biomass type D, but the inverse trend was detected at 1200 °C while their results at 1100 °C cannot be compared due to the effect of different Ar flow. Despite this issue, the effect of temperature on syngas production can clearly be observed. Regarding the particle size influence, it can be presumed that the syngas yields were not significantly affected by the considered particle size in the range of 0.3-4 mm. This means that heat and mass transfers are not limiting factors for the gasification reaction in this particle size range.

Besides, it is interesting to notice that the evolution trend of U when accounting for C_2H_m is less sensitive to temperature than without accounting for C_2H_m because the C_2H_m production is favored at lower temperature due to lower gasification kinetics. This leads to the highest C_2H_m produced at the lowest temperature, which in turn increases U because of the high calorific value of C_2H_m.

Furthermore, the presence of ashes remaining in the reactor after experiments decreased considerably with increasing temperature according to Fig. B-6. This indicates that ashes were melted when the temperature increased

Fig. 3-12 displays the influence of temperature on performance indicators (U, X_C, $\eta_{solar\text{-}to\text{-}fuel}$, $\eta_{reactor}$, solar power and solar energy inputs) for different biomass types at 1.2 g/min. According to Fig. 3-12a, U increased with temperature as a result of the increase of X_C (Fig. 3-12b). The lowest U value of 0.91 was obtained for biomass types A and C at 1100°C, while the highest U value of 1.13 was obtained for biomass type D at 1300 °C. A temperature increase improved X_C, and the highest X_C value of 80.6 % was reached at 1300 °C (biomass type A) while the dependence of X_C on biomass type was observed.

Small gaps in U between biomass types A and B and between biomass types D and E were noticed due to their similar chemical compositions, thus unveiling that the variations of U are related to their elemental composition as a characteristic of the carbonaceous feedstock [126]. However, the effect of particle size on U and X_C was not obvious. Noticeably, $\eta_{solar\text{-}to\text{-}fuel}$ (Fig. 3-12c) reached the highest values at 1200 °C (e.g., 20.4% for biomass type D). It subsequently decreased slightly at 1300 °C. This is because the required solar power input was higher at 1300 °C (above 1.2 kW according to Fig. 3-12d), which in turn results in higher heat losses. The $\eta_{solar\text{-}to\text{-}fuel}$ of biomass type D at 1200-1300°C were greater than those of other biomass types. This can be attributed to its different physical and chemical properties (smallest mean particle size and highest H and C content, Table 3-1) that favor both reaction rates [144]

and reaction extent (enhanced H_2 and CO yields) while the required solar energy input remains similar (Fig. 3-12f), thereby leading to higher $\eta_{solar\text{-}to\text{-}fuel}$. In addition, $\eta_{reactor}$ (Fig. 3-12e) followed the same trends as $\eta_{solar\text{-}to\text{-}fuel}$ with the highest $\eta_{reactor}$ values of 20.3% at 1200 °C for biomass type D. This is explained by the increased heat losses when increasing the temperature. However, a temperature increase offered significant benefits in promoting syngas yield, quality and reaction kinetics while reducing the formation of tars. For these reasons, a temperature trade-off needs to be considered to attain high syngas yield while minimizing heat losses.

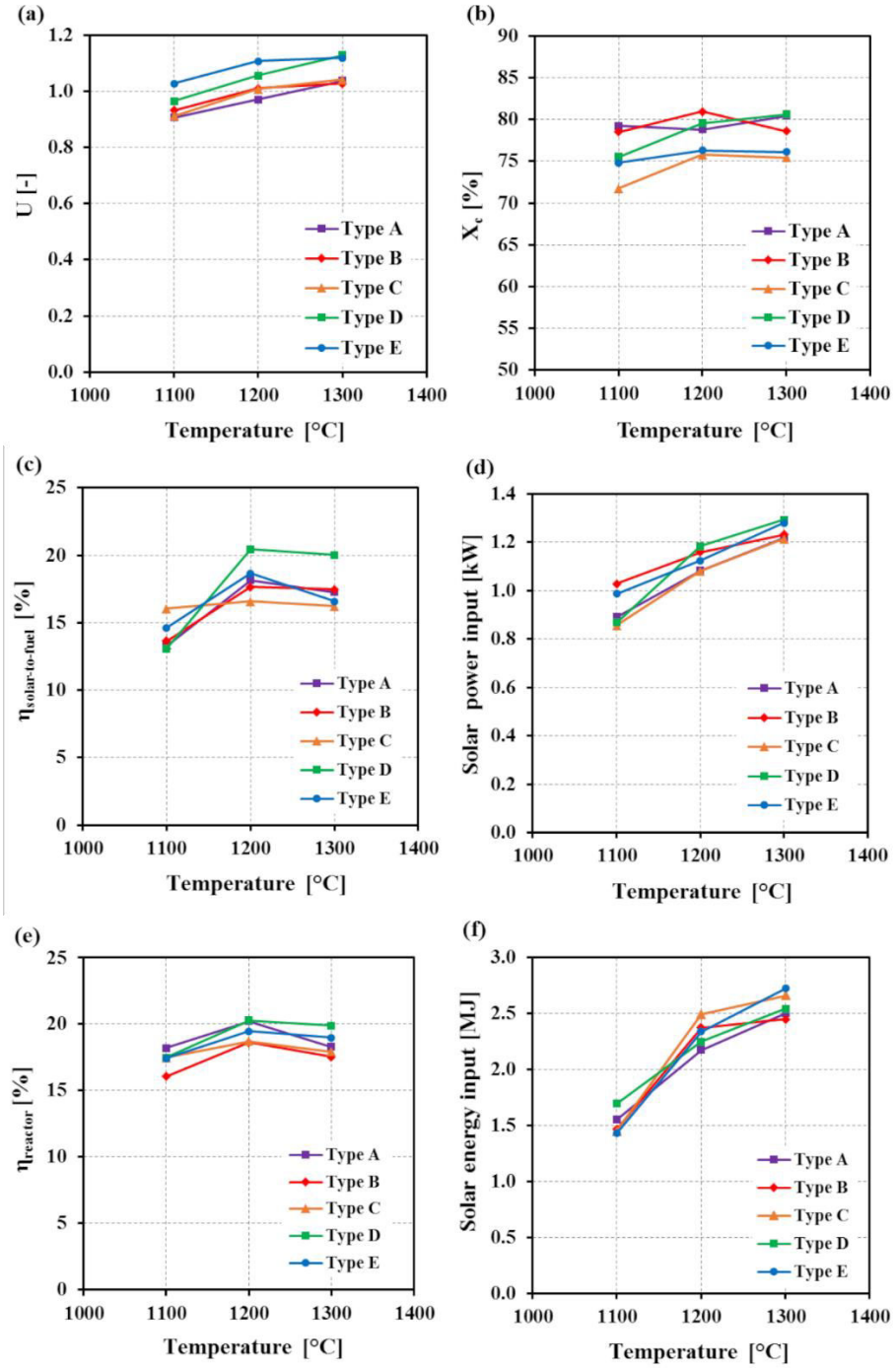

Figure 3-12. Temperature influence on (a) energy upgrade factor, (b) carbon conversion, (c) solar-to-fuel energy conversion efficiency, (d) solar power input (e) thermochemical reactor efficiency, and (f) solar energy input for different biomass feedstocks (C_2H_m not included in the calculation).

3.3.5 Effect of biomass feeding rate on syngas production yield and rate

The effect of biomass feeding rate ($\dot{m}_{feedstock}$) on both syngas production and reactor performance was investigated.

The feedstocks (total amount of 30 g) were continuously fed (feeding rates in the range of 0.8-1.5 g/min (1100 °C), 0.6-2.2 g/min (1200 °C) and 0.6-2.7 g/min (1300°C)) and subsequently steam gasified at 1100, 1200 and 1300 °C. Note that the considered ranges of biomass feeding rate for each biomass type are different due to their physical characteristics (particle size and shape). The steam/biomass ratio was kept constant (10% of excess water) at a slightly over-stoichiometric ratio (Fig. 3-6). This ratio was selected based on the study of the H_2O/biomass molar ratio influence. The stoichiometric H_2O/biomass ratio is 2 for biomass types A, B and C and 3 for biomass types D and E, according to Eq. (1-16). Finally, the total Ar flow-rate was supplied at a constant flow of 2.7 Nl/min.

Fig. 3-13 presents the syngas yields of H_2, CO, CH_4, CO_2 and C_2H_m for each biomass type as a function of biomass feeding rate at 1100, 1200, and 1300 °C (the effect of biomass feeding rate on syngas yield is detailed separately in Figs. B-7 at 1200 °C and B-8 at 1300 °C, Appendix B) .

At 1100 °C, the lowest H_2 and CO yields and the highest CO_2, CH_4, and C_2H_m yields were observed, resulting from low gasification kinetics evidenced by the presence of pyrolytic gases as mentioned before. As a result, the maximum $\dot{m}_{feedstock}$ can only reach 1.5 g/min, and no optimal $\dot{m}_{feedstock}$ could be identified at this temperature. At 1200 °C, $\dot{m}_{feedstock}$ was increased up to 2.2 g/min, and all gas yields rose with increasing $\dot{m}_{feedstock}$. When compared to 1100 °C, H_2 (Fig. 3-13a) and CO (Fig. 3-13b) yields at 1200 °C were higher while CO_2 (Fig. 3-13c), CH_4 (Fig. 3-13d) and C_2H_m (Fig. 3-13e) yields were lower as a result of the improved kinetics of gasification. At this temperature, the $\dot{m}_{feedstock}$ of biomass type C reached its optimal point at 2.2 g/min (reflected by a stable pattern in H_2, a slight decrease in CO, and a significant increase in CO_2, CH_4, and C_2H_m). At 1300 °C, the highest H_2 and CO yields and the lowest CO_2, CH_4, and C_2H_m yields were noticed, demonstrating the highest syngas quality as well as syngas yield at this temperature. Moreover, the optimal $\dot{m}_{feedstock}$ of biomass type A was highly approached, as evidenced by stable H_2 and CO yields at 2.5-2.7 g/min, while that of biomass type C and biomass type D were determined to be 2.5 and 1.8 g/min, respectively. For example, the H_2 and CO yields for biomass type C reached the maximum value of 39.2 and 29.1 mmol/$g_{biomass}$ at 2.5 g/min and then reduced to 37.6 and 27.9 mmol/$g_{biomass}$, respectively, at 2.7 g/min, while the amounts of CO_2, CH_4, and C_2H_m for biomass type C reached the maximum value of 4.0, 3.2, and 1.4 mmol/$g_{biomass}$, respectively, at 2.7 g/min, thus confirming the optimal feeding rate at 2.5 g/min. However, the optimum feeding point could not be found for the other biomass types due to the limitation of the maximum feeding rate. Trends of H_2 yield between biomass types A and B and between biomass types D and E for any temperatures were not significantly different as a result of their similar initial chemical composition (Table 3-1). The H_2 yields for biomass types D and E were considerably higher than for the other types owing to their higher initial hydrogen content (Table 3-1) while the trends of CO for each biomass were similar. In addition, smaller particle size showed a positive effect on syngas yield resulting from enhanced heat and mass transfer rates [145–147]. However, their compared trends (type A vs. type B, and type D vs. type E) remained similar. Hence, the biomass type

(composition) showed more significant influence on syngas yield than the biomass particle size in the considered size range (0.3-4 mm). In summary, increasing the $\dot{m}_{feedstock}$ enhanced syngas yield, at the expense of an increase in CO_2, CH_4, and C_2H_m yields due to a lowered gas residence time, thereby showing adverse impact on syngas quality. This issue can be tackled by increasing the temperature to hasten the reaction kinetics, which in turn increases biomass consumption and syngas quality. However, exceeding an optimal $\dot{m}_{feedstock}$ point led to a reduction in syngas yield and biomass accumulation, as evidenced by biomass type C at 2.7 g/min. The optimal biomass feeding rate was 2.2 g/min (1200 °C) and 2.5 g/min (1300 °C) for biomass type C, 1.8 g/min (1300 °C) for biomass type D, and was approached at 2.7 g/min for biomass type A. It could not be determined at 1100 °C because of pyrolytic gases generating smoke issue caused by low reaction kinetics as mentioned before.

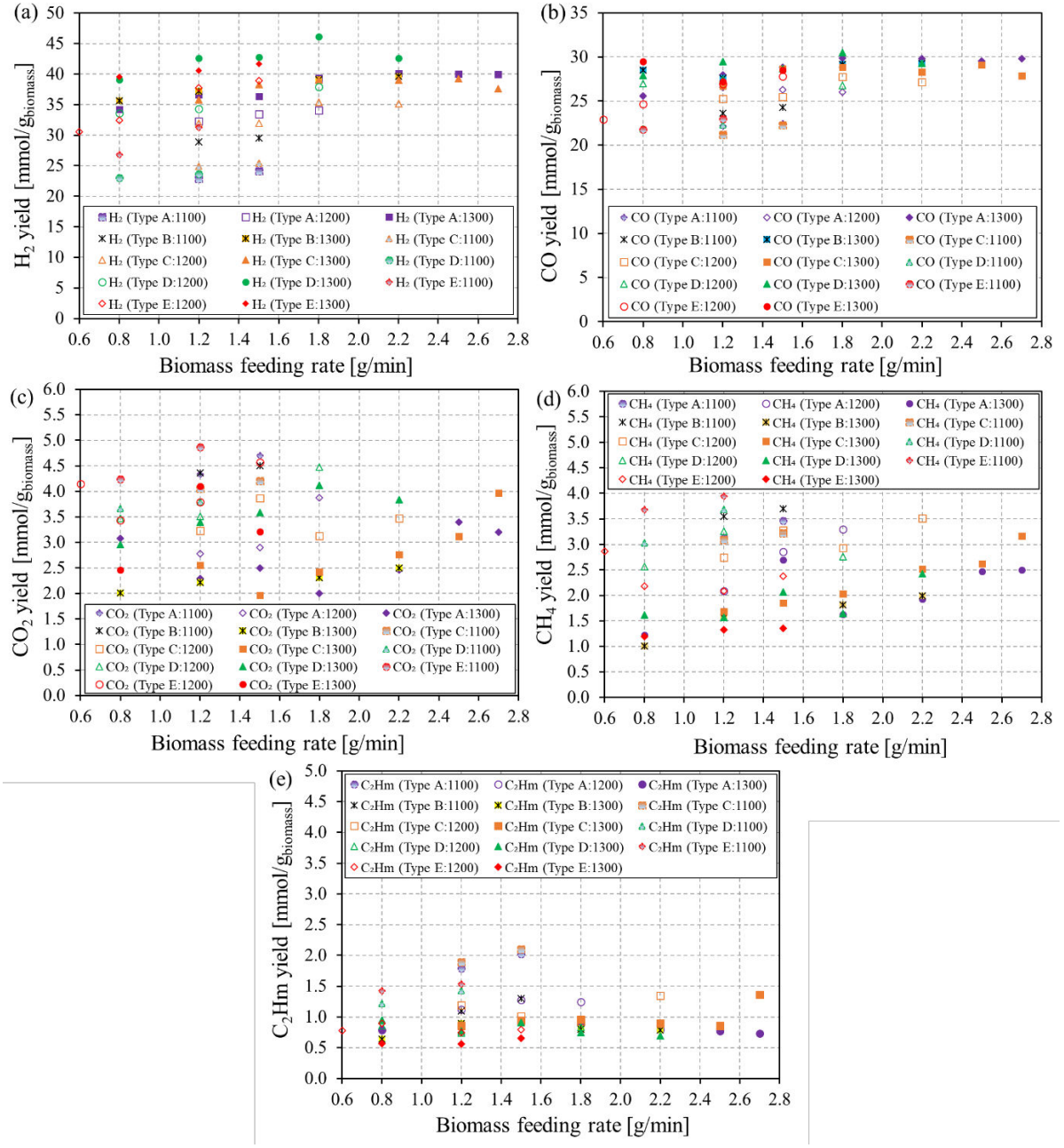

Figure 3-13. Syngas yields for different biomass feedstocks as a function of biomass feeding rate at 1100 °C, 1200 °C, and 1300 °C.

The biomass feeding rate influence on syngas production rates evolution at 1300 °C is presented in Fig 3-14 (representative biomass type A). It is clear that increasing biomass feeding rate both increased syngas production rates and decreased the operating duration time, thus improving both syngas yield and reactor performance (reduced heat losses). For instance, the biomass injection duration decreased significantly from 40-45 min at ~0.8 g/min to 11-18 min at ~2.7 g/min, while the nominal H_2 and CO production rates were 0.6 and 0.5 Nl/min at 0.8 g/min compared to 2.4 and 2 Nl/min at 2.7 g/min respectively.

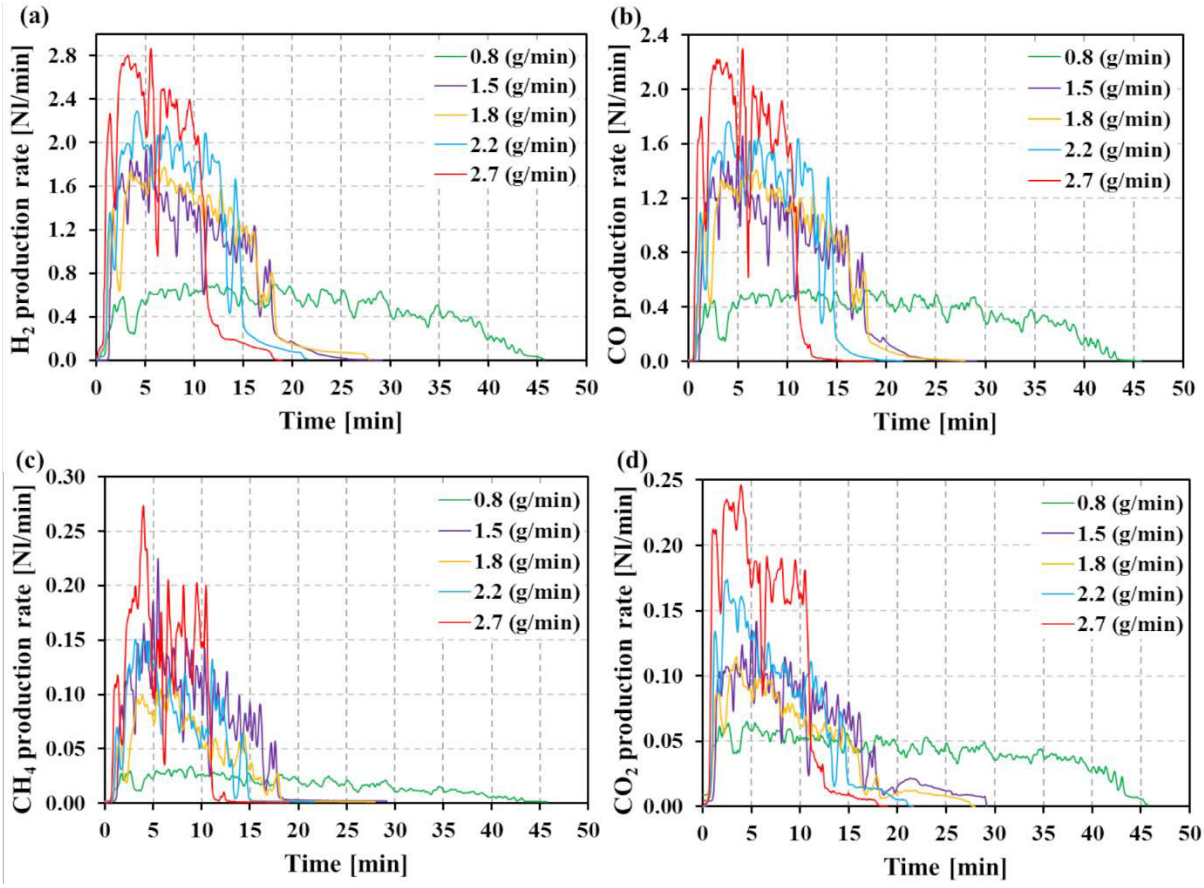

Figure 3-14. Biomass feeding rate influence on (a) H_2, (b) CO, (c) CH_4 and (d) CO_2 production rates during gasification at 1300 °C (Biomass type A).

Fig. 3-15 represents the H_2 and CO production rates as a function of biomass feeding rate at 1200 and 1300 °C. Increasing the biomass feeding rate led to a substantial rise in H_2 and CO production rates. For example, the H_2 and CO production rates for biomass type D increased from 0.9 and 0.7 Nl/min at 0.8 g/min to 2.3 and 1.8 Nl/min at 2.2 g/min, respectively. Both the H_2 and CO production rates at 1300 °C for any biomass type were obviously higher compared to those obtained at 1200 °C because the kinetic rate of gasification reaction at 1300 °C was higher. The increase of syngas production rate with biomass feeding rate (linear correlation) was demonstrated.

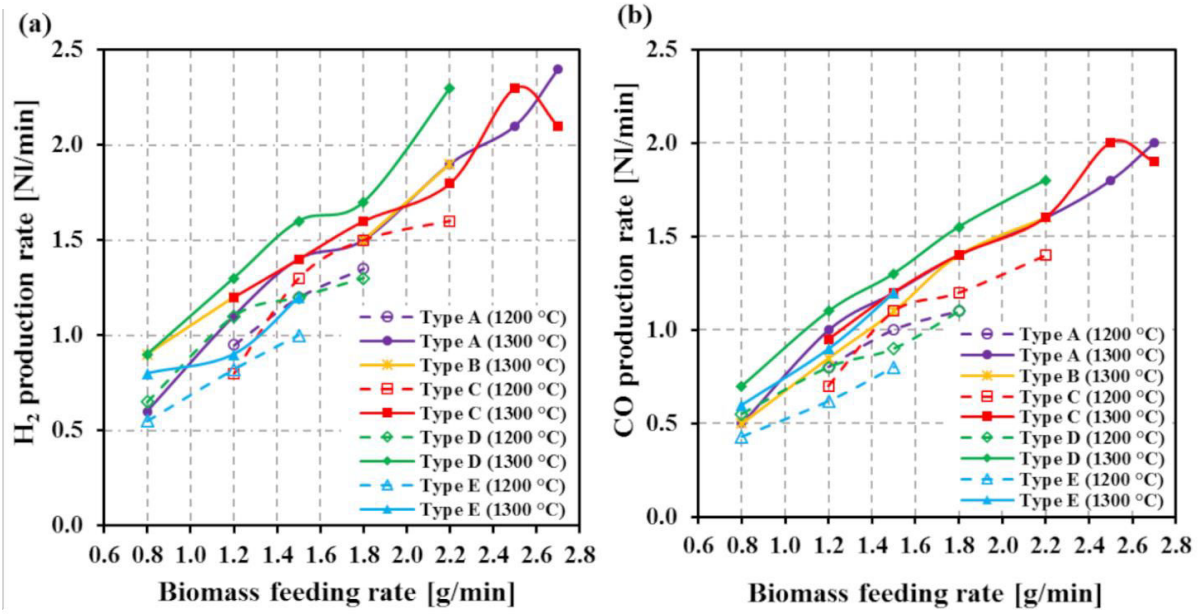

Figure 3-15. (a) H_2 and (b) CO production rates (nominal steady-state values) as a function of biomass feeding rate at 1200 and 1300 °C.

The biomass gasification rate (equivalent to the carbon consumption rate) was determined as a function of the carbon feeding rate at 1100, 1200, and 1300 °C for biomass types A, B, C, D, and E, and was further compared to the ideal carbon consumption rate for each biomass type (equal to the carbon feeding rate, i.e. the carbon contained in the fed biomass), as presented in Fig. 3-16. The carbon consumption rate is quantified by the summation of the nominal production rates of CO, CO_2, and CH_4 contained in the produced syngas (assuming that the C consumption rate and the summation of production rates of carbon-containing gas species are equivalent), and achieved during continuous biomass injection (at steady state). The carbon consumption rate increased when increasing both temperature and biomass feeding rate regardless of biomass type. Typically, at 1300 °C the carbon consumption rate closely matched the carbon feeding rate at low feeding rates (linear tendency at 0.4-0.7 g/min), which also means that the reactant feeding rate closely matched the rate of the gasification reaction. From a threshold value of carbon feeding rate, the carbon consumption rate became slightly lower than the carbon feeding rate at above 0.8 g/min (1300 °C), which means that the gasification rate was not high enough to convert totally the injected biomass. In other words, from this point, carbon accumulation in the reactor (due to incomplete biomass gasification) may occur if the feeding rate is too high with respect to the reactor capacity. An optimal value was observed for biomass type C at a carbon feeding rate of ~1.16 g/min (corresponding to 2.5 g/min of biomass feeding rate at 1300 °C). Both the carbon consumption rates and carbon feeding ranges at 1300 °C were greater and closer to the ideal carbon consumption rates for any biomass types, compared to those obtained at 1200 °C and 1100 °C. This is because the higher gasification kinetics at 1300 °C resulted in both higher carbon consumption rate and carbon feeding range. The impact of biomass feeding rate on syngas production capacity and reactor performance was thus evidenced. The carbon consumption rate at 1300°C matched closely the carbon feeding rate (provided the feeding rate was below a threshold value regardless of the biomass type). This means that 1300°C is a suitable

temperature to operate reliably the solar biomass gasifier in a stable continuous mode with a biomass conversion rate equal to the feeding rate.

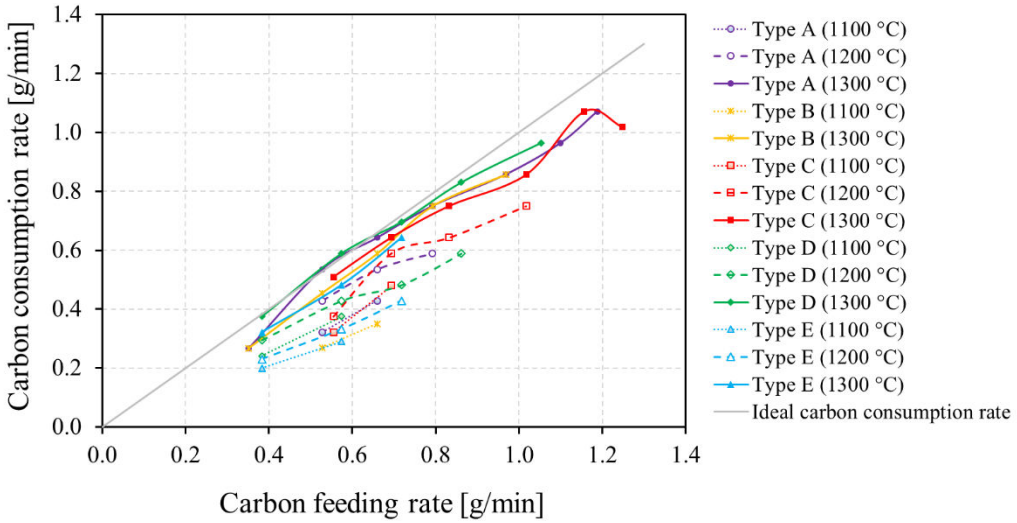

Figure 3-16. Comparison of the effect of carbon feeding rate on carbon consumption rate for each biomass type at 1100, 1200 and 1300 °C.

3.3.6 Solar reactor performance and efficiencies

The solar reactor performance at 1000 °C, 1200 °C, and 1300 °C for the representative biomass types A, C, and D was compared, according to Fig. 3-17. Note that the results of biomass types B and E were omitted as they are similar to the ones of biomass types A and D, respectively, due to similar chemical biomass composition; instead, the solar reactor performance for all biomass types at 1200 °C and 1300 °C is presented separately in Fig. B-9 and Fig. B-10, respectively. As expected, both U (Fig. 3-17a) and X_C (Fig. 3-17b) increased with $\dot{m}_{\text{feedstock}}$ regardless of temperature and biomass type. At 1300 °C, trends in U and X_C clearly leveled off at above 1.8 g/min, pointing out the optimal biomass feeding rate, and the maximum U values of 1.14, 1.10, 1.16, 1.20 and 1.15 (1.19, 1.15, 1.22, 1.24 and 1.19 when accounting for C_2H_m) were identified for biomass types A (at 2.7 g/min), B (at 2.2 g/min), C (at 2.5 g/min), D (at 1.8 g/min) and E (at 1.5 g/min), respectively. The optimal $\dot{m}_{feedstock}$ with respect to the highest U value at 1300 °C was found at 2.5 and 1.8 g/min for biomass types C and D, respectively. These types of biomass exhibit the lowest particle sizes; hence, their gasification rate is more sensitive to the feeding rate. The overlapped trends of U between biomass types A and B and between biomass types D and E were due to their similar chemical properties, indicating a negligible impact of the biomass particle size on U for the considered size range (0.3−4 mm). In addition, the evolution of U consistently followed the same trend as X_C (Fig. 3-17b). The highest and lowest X_C values of 88.6% and 72.9% (90.4% and 76.2% when accounting for C_2H_m) were obtained for biomass type A at 1300 °C (2.7 g/min) and biomass type E at 1100 °C (0.8 g/min), respectively. In comparison, both U and X_C values at 1300 °C were higher than those obtained at 1200 and 1100 °C (U and X_C in the range of 1.04-1.10 and 80.4-84.2% at 1300 °C compared to 0.91-0.95 and 77.6-79.8% at 1100 °C for biomass type A), thus confirming the enhancement of syngas yield and reaction extent at 1300 °C.

Moreover, a rise in $\dot{m}_{feedstock}$ increased $\eta_{solar\text{-}to\text{-}fuel}$ (Fig. 3-17c) because the total solar energy input (Fig. 3-17d) was lowered (due to the significant reduction in the biomass injection duration) even though the solar power input (Fig. 3-17f) was increased consistently with $\dot{m}_{feedstock}$ for maintaining the isothermal operating temperature. For example, $\eta_{solar\text{-}to\text{-}fuel}$ for biomass type A increased from 12.4% at 0.8 g/min to 26.6% at 2.7 g/min. The maximum $\eta_{solar\text{-}to\text{-}fuel}$ values of 26.6%, 25%, 27.6%, 25.3%, and 21.2% (27.8%, 26.0%, 29.0%, 26.3%, and 21.8% when accounting for C_2H_m) were achieved for biomass types A (at 2.7 g/min), B (at 2.2 g/min), C (at 2.5 g/min), D (at 2.2 g/min) and E (at 1.5 g/min), respectively. The $\eta_{solar\text{-}to\text{-}fuel}$ of biomass type C noticeably decreased at 2.7 g/min, confirming that exceeding the optimal $\dot{m}_{feedstock}$ feeding point adversely resulted in incomplete gasification, thus leading to solid reactant accumulation and temporal stop in the biomass feeding to let the accumulated reactant being gasified. In this case, the injection duration was in turn extended, leading to an increase in the solar energy input (Fig. 3-17d). In comparison, $\eta_{solar\text{-}to\text{-}fuel}$ (Fig. 3-17c) at 1200 °C was slightly higher that that at 1300 °C as both the solar energy (Fig. 3-17d) and power inputs (Fig. 3-17f) were considerably lower, while the product syngas yield was not drastically different. For example, $\eta_{solar\text{-}to\text{-}fuel}$ for biomass type A was in the range of 18.1-20.6% at 1200 °C compared to 17.3-20.8% at 1300 °C, respectively. However, $\eta_{solar\text{-}to\text{-}fuel}$ at 1100 °C was still lower than that at 1200 °C as a result of the downgraded gasification performance. Similar to $\eta_{solar\text{-}to\text{-}fuel}$, $\eta_{reactor}$ (Fig. 3-17e) rose with $\dot{m}_{feedstock}$, ranging between 15.3-25.3%, 17.3-24.2%, 17.9-27.0%, 16.1-24.0% and 15.7-21.2% for biomass types A, B, C, D and E, respectively, indicating an efficient solar energy utilization and conversion, and leading to a reduction of the heat losses. Moreover, $\eta_{reactor}$ dropped when $\dot{m}_{feedstock}$ was over its optimum point (2.5 g/min for biomass type C) as a result of biomass accumulation and extension of the reaction duration, as mentioned before. In summary, an increase in both biomass feeding rate and temperature is substantially favorable for increasing solar gasification performance because reaction kinetics and biomass consumption rates are enhanced. However, heat losses increase consistently with temperature, which adversely leads to a reduction in both $\eta_{solar\text{-}to\text{-}fuel}$ and $\eta_{reactor}$ at 1300 °C. The maximum U, X_C, $\eta_{solar\text{-}to\text{-}fuel}$, and $\eta_{reactor}$ were consistently obtained at the optimal feeding point, in agreement with maximum syngas yield and biomass gasification rate (Fig. 3-13 and 3-16).

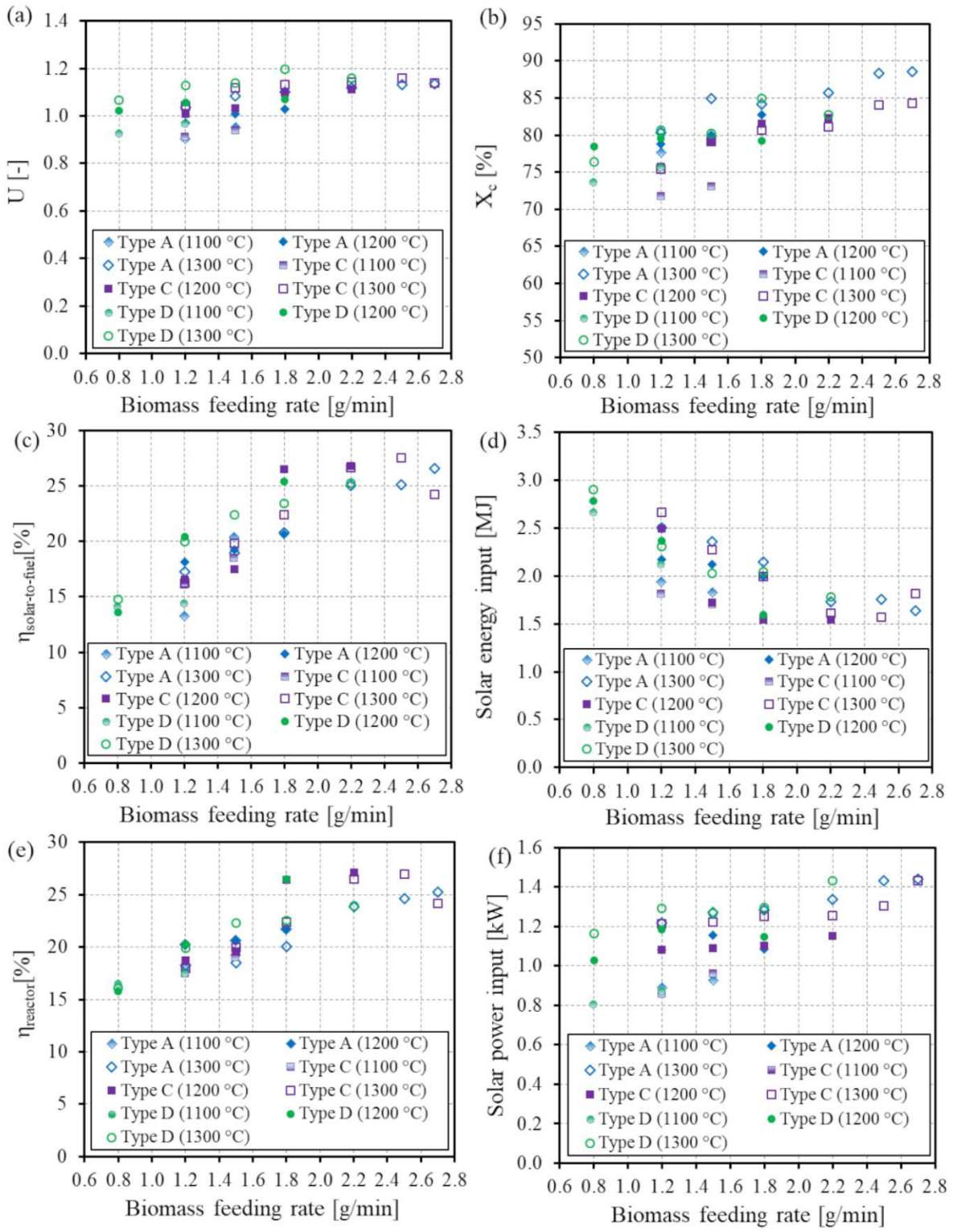

Figure 3-17. Comparison of the effect of biomass feeding rate at 1100 ℃, 1200 °C and 1300 °C on (a) energy upgrade factor, (b) carbon conversion,(c) solar-to-fuel energy conversion efficiency, (d) solar energy input, (e) thermochemical reactor efficiency and (f) solar power input (C_2H_m not included in the calculation).

3.3.7 Energy balance

Fig. 3-18 shows the distribution of the solar power consumption and energy partition of the solar reactor at different biomass feeding rates at 1300 °C (biomass type A). The solar power consumed for heating biomass ($\dot{Q}_{biomass}$) and steam ($\dot{Q}_{water}$) at 1300 °C increased consistently with $\dot{m}_{feedstock}$ (from 0.024 and 0.016 kW at 0.8 g/min to 0.058 and 0.034 kW at 2.7 g/min). The amount of solar power devoted to the chemical reaction ($\dot{Q}_{reaction}$) increased sharply with the rise of $\dot{m}_{feedstock}$ (from 0.090 kW at 0.8 g/min to 0.219 kW at 2.7 g/min) because it is utilized for providing the reaction enthalpy (ΔH° = 0.8 MJ/mol, 1.2 MJ/mol at $T_{reactor}$ (1200 °C)). The amount of solar power consumed for inert gas heating ($\dot{Q}_{Ar}$) remained the same (0.054 kW) as the inert gas flow rate was kept constant at 2.7 Nl/min over all experimental tests (dilution factor of the syngas by Ar in the range of 1.6-3.3 for the conditions displayed in Fig. 3-18). Thus, the sensible heat losses associated to the energy consumed by inert gas were significantly reduced when increasing $\dot{m}_{feedstock}$ as the processing duration was shortened. Obviously, increasing $\dot{m}_{feedstock}$ resulted in the increase of the total solar power consumption ranging from 0.185-0.364 kW at 0.8-2.7 g/min, which is accompanied by the increase of solar power input ranging from 1.20-1.44 kW. As mentioned above, the major part of the solar energy was devoted to chemical reaction, followed by inert gas, biomass, and lastly steam heating, but $\dot{Q}_{biomass}$ became higher than $\dot{Q}_{Ar}$ above 2.5 g/min.

The results from Fig. 3-18a were used to calculate the energy partition for the solar reactor given as percentage of the average solar power input over the entire experimental tests (Fig. 3-18b). The amounts of heat losses decreased considerably with $\dot{m}_{feedstock}$ (from 84.7% at 0.8 g/min to 74.7% at 2.7 g/min). Thus, increasing $\dot{m}_{feedstock}$ enhances the efficient utilization of the solar energy input leading to a reduction of the heat losses, thereby pointing out the benefits of biomass feeding rate adjustments. This asset also allows for the treatment and conversion of a higher amount of biomass with the same amount of solar energy input and determines the reactor potential.

Nevertheless, exceeding the optimal point of $\dot{m}_{feedstock}$ (2.7 g/min for biomass type C in Fig. 3-19a) resulted in a reduction of the solar power consumption because of an adverse impact of both the lowered gas residence time and the solid reactant accumulation in the reactor cavity. In this case, the injection of biomass needs to be temporarily stopped to let the residual reactants being steam gasified at the expense of the additional solar energy consumption due to the extension of injection duration, which in turn results in the increase of the heat losses (Fig. 3-19b at 2.7 g/min) in agreement with a decrease in syngas yield (Fig.3-13), biomass gasification rate (Fig. 3-15 and 3-16), and reactor performance (Fig. 3-17).

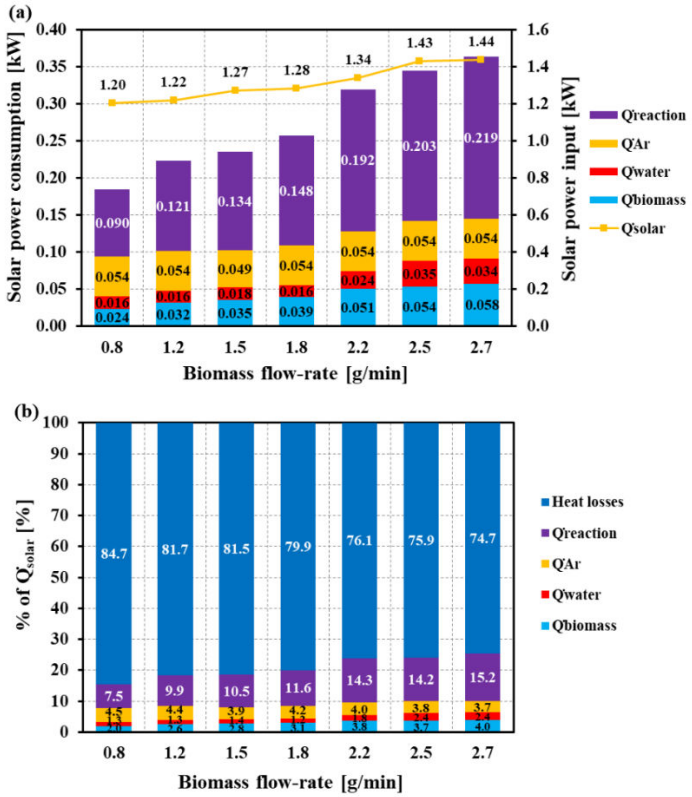

Figure 3-18. Solar power consumption for biomass type A and (b) energy partition for the solar reactor given as percentage of the total solar power input averaged over the entire experimental test at 1300 °C.

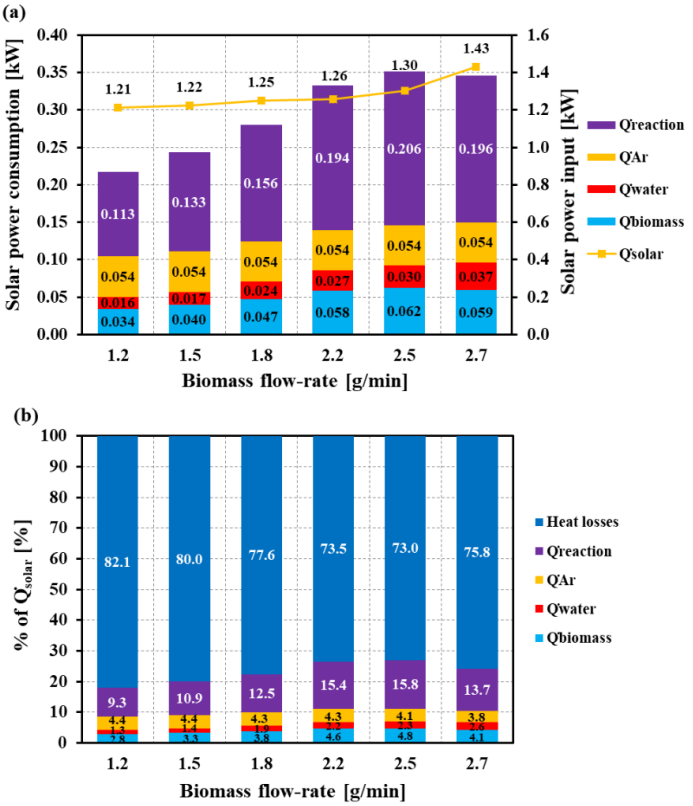

Figure 3-19. (a) Solar power consumption for biomass type C and (b) energy partition for the solar reactor given as percentage of the solar power input averaged over the entire experimental test at 1300 °C.

3.3.8 Solar energy storage fraction

The solar energy storage fraction ($\eta_{solar\ fraction}$) represents the amount of solar energy actually stored and upgraded in the form of syngas with respect to the energy content of the biomass feedstock. Fig. 3-20 shows the $\eta_{solar\ fraction}$ for biomass type C as a function of biomass feeding rate compared with the theoretical solar energy storage fraction at different values of energy upgrade factors (assuming U values from 1.05 to 1.25 in Eq. 3-6) at 1300 °C. The experimental pattern approached the theoretical solar storage fraction, which can be used to estimate the solar energy stored in the produced fuel at different $\dot{m}_{feedstock}$. The $\eta_{solar\ fraction}$ increased with $\dot{m}_{feedstock}$ and attained the optimal value of 8.3% (11.6% when accounting for C_2H_m) at 2.5 g/min for biomass type C, meaning that this portion of the solar energy input was successfully stored in the produced syngas.

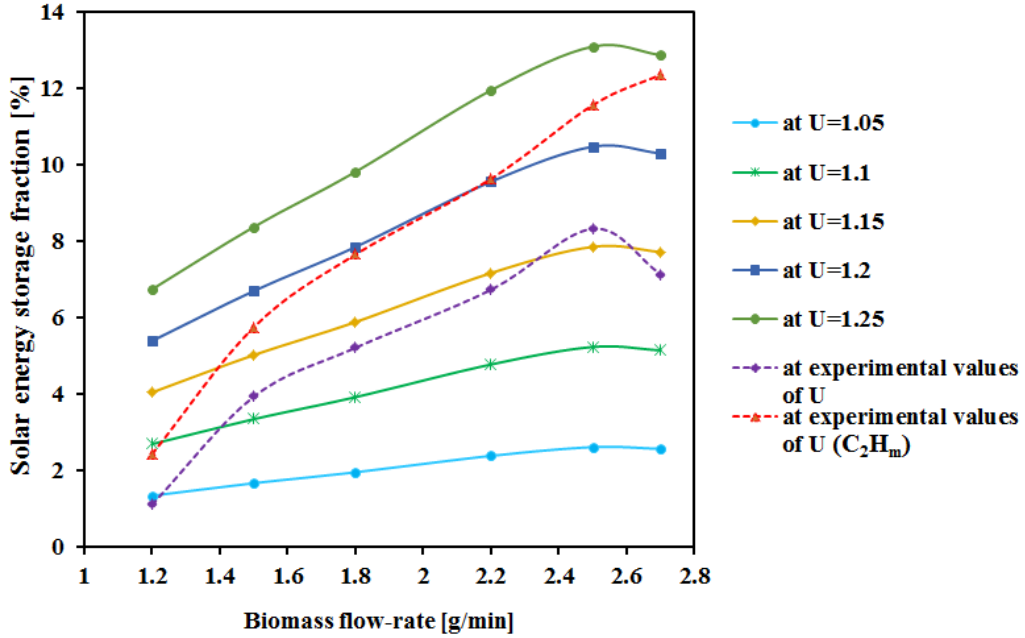

Figure 3-20. Solar energy storage fraction for biomass type C as a function of biomass feeding rate at 1300 °C (using Q_{solar} reported in Fig. 3-19a for the calculation).

3.4 Conclusion

The performance assessment of a continuous solar biomass gasifier was performed in the temperature range of 1100-1300 °C with different lignocellulosic biomass feedstocks. The influence of operational conditions considering steam flow-rate (H_2O/biomass molar ratio), gas residence time, gasification temperature, starting carbonaceous feedstocks and biomass feeding rate on syngas production and performance was emphasized during continuous biomass gasification. The solar gasifier was successfully operated at the different processing conditions under real concentrating solar flux and several key points in the performance outputs can be outlined as follows.

- Complete biomass gasification was supported by the global mass balance achieved above 95% and the carbon conversion up to 90.4%, confirming the efficient biomass feedstock conversion into syngas.

- Either a lack or an excess of water regarding the reaction stoichiometry resulted in a significant increase in the C_2H_m, CH_4 and CO_2 and a decrease in the produced CO and H_2. A

slightly over-stoichiometric amount of water was thus suited for complete gasification reaction, leading to high quality syngas with low C_2H_m, CH_4 and CO_2 content and high syngas yield (CO and H_2).

- A decrease in the gas residence time (adjusted via the inert carrier gas flow rate) showed a negative effect on syngas composition and yield in terms of both a considerable increase of the C_2H_m, CH_4 and CO_2 contents and a reduction of the CO and H_2 quantities.

- Substantial improvement of syngas production rates, yields and quality through the increase of temperature was highlighted. However, a temperature increase enhanced the heat losses, thereby adversely altering both $\eta_{solar\text{-}to\text{-}fuel}$ and $\eta_{reactor}$.

- A smaller particle size led to higher gasification rates and syngas yields, due to higher particle reactivity (as denoted by the lower activation energy). However, the biomass type (composition) showed more significant impact than the biomass particle size in the considered range (0.3-4 mm).

-An increase in biomass feeding rate significantly promoted syngas yield and reactor performance; however, exceeding the optimal biomass feeding point showed an adverse effect on produced syngas. Indeed, H_2 and CO yields decreased at the expense of a growth in C_2H_m, CH_4, and CO_2 due to a reduction of the gas residence time, and eventually biomass accumulation issues and pyrolytic gases emissions may occur. Increasing temperature (1100-1300°C) significantly enhanced reaction extent, and reaction kinetics, which in turn increased biomass consumption rates matching biomass feeding rate. At 1300 °C, the biomass feeding rate reached its optimum point at up to 2.5 g/min for biomass type C (1.8 g/min for biomass type D) and approached the optimal biomass feeding rate of biomass type A at 2.7 g/min, whereas at 1200 °C the optimal biomass feeding point was found at 2.2 g/min (biomass type C) corresponding to the nominal feeding rate for this 1.5 kW_{th} solar reactor. However, heat losses rose consistently with temperature, which adversely led to a reduction in both $\eta_{solar\text{-}to\text{-}fuel}$ and $\eta_{reactor}$ at 1300 °C. Moreover, increasing temperature and biomass feeding rate enhanced biomass gasification rate (carbon consumption rate). At 1300 °C, the carbon consumption rates were greater than those obtained at 1200 and 1100 °C, and their values were closer to the ideal maximum carbon consumption rate for any biomass type. The energy upgrade factor, reaction extent (carbon conversion), solar-to-fuel energy conversion efficiency, and thermochemical reactor efficiency increased with biomass feeding rate because the total solar energy input during processing was decreased, resulting from a shortened biomass injection duration (maximum achieved values (accounting for C_2H_m) up to 1.24, 90.4%, 29.0%, and 27.0%, respectively). Optimizing the biomass feeding rate consistently with operating temperature is beneficial for continuous solar biomass gasification. It aims to enhance biomass consumption rate, reaction kinetics, as well as reaction extent (carbon conversion) for maximizing syngas yield and quality and minimizing heat losses. Although increasing the heat losses, the temperature of 1300 °C is appropriate to operate reliably the solar biomass gasifier in a stable continuous mode with a biomass conversion rate matching well the feeding rate.

The measured efficiencies reported here for a 1.5 kW_{th} solar gasifier could possibly be upgraded by scaling-up for enhancing syngas production capacity. Automated control of the biomass feeding rate could be used as a suitable dynamic control tool of continuous solar gasifiers under variable or intermittent solar conditions.

Chapter 4: Solar carbothermal reduction of ZnO and MgO[3]

4.1 Introduction

The solar chemical looping reforming of methane (CLRM) and continuous solar gasification of biomass was presented in Chaps. 2 and 3, respectively, providing insights into how gaseous (methane) and solid carbonaceous feedstock (biomass) can be converted into syngas via promising solar thermochemical processes. In this Chapter, the solid carbonaceous feedstock was utilized as reducing agents to both lower the thermodynamic barrier and extract oxygen from ZnO and MgO to produce Zn and Mg via solar carbothermal reduction (CTR).

This work focuses on the experimental study of solar CTR of ZnO and MgO in a new prototype solar reactor operated on-sun. Experiments were conducted with different reducing agents including pure carbons and beech wood biomass in batch and continuous operation modes under vacuum and atmospheric pressures to demonstrate flexibility, reliability, and robustness of this scalable metallurgical process for Zn and Mg production. In addition, a parametric study of CTR of ZnO and MgO regarding the influence of pressure, carbonaceous feedstocks (different solid carbon types), and C/MgO or C/ZnO molar ratio on CO production rate, products yield (CO and Mg/Zn), and reactor performance was conducted .

4.2 Thermodynamic analysis

4.2.1 ZnO

The overall solar carbothermal reduction (CTR) of ZnO with solid carbon is represented as:

$$ZnO(s)+C(s)\rightarrow Zn(g)+CO(g) \quad (4\text{-}1)$$

If employing wood biomass as a reducing agent (with molecular formula assumed to be $C_6H_9O_4$), the reaction can be written as:

$$ZnO(s)+1/2C_6H_9O_4(s)\rightarrow Zn(g)+3CO+9/4H_2(g) \quad (4\text{-}2)$$

The possible solid-gas reactions occurring during ZnO reduction with solid carbonaceous feedstock are:

$$ZnO(s)+CO(g) \leftrightarrow Zn(g)+CO_2(g) \quad (4\text{-}3)$$

$$C(s)+CO_2(g) \leftrightarrow 2CO(g) \quad (4\text{-}4)$$

[3] Details of this chapter consist of one peer-reviewed article:

- S. Chuayboon, S. Abanades, *J. Clean. Prod*. 32 (2019) 784-795.

According to Eq. 4-3, ZnO can be reduced by CO produced from Eq.4-1 to Zn and CO_2 (global reaction: $2ZnO+C \rightarrow 2Zn+CO_2$), and the produced CO_2 is subsequently reduced by carbon according to the Boudouard reaction (Eq. 4-4).

Fig. 4-1 displays the variations of Gibbs free energy change ($\Delta G°$) with temperature for the possible reduction reactions of ZnO with or without carbonaceous materials at 1 bar. Overall, all the considered reduction reactions of ZnO are thermodynamically favorable when increasing the temperature ($\Delta G°<0$). The direct thermal dissociation of ZnO proceeds at above ~2000 °C. In contrast, the required temperature decreases significantly to 950 and 850 °C when ZnO is reduced with C and CH_4, respectively. The formation of CO_2 can be obtained from ZnO+CO, 2ZnO+C, and Boudouard reactions at above 1300, 1050, and 700 °C, respectively (H_2O can theoretically be formed from the $ZnO+H_2$ reaction at above ~1200 °C).

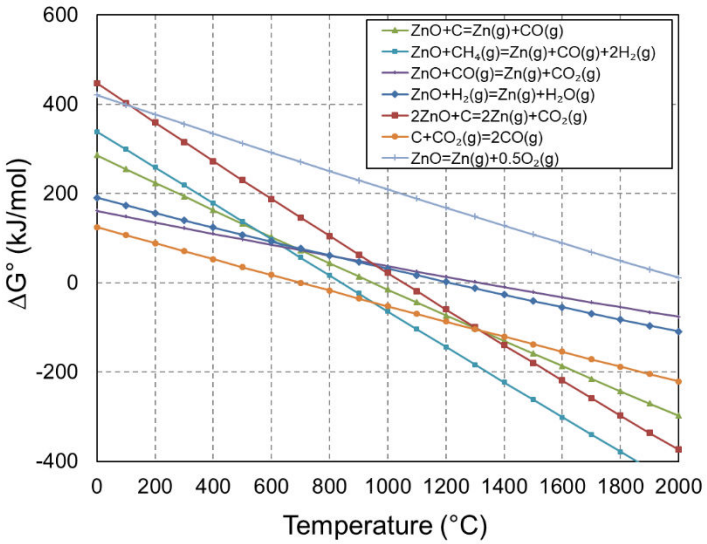

Figure 4-1. Variation of $\Delta G°$ for various ZnO reduction reactions as a function of temperature at 1 bar.

Fig. 4-2 shows thermodynamic equilibrium products distribution for CTR of ZnO calculated by HSC Chemistry software. At 1 bar (Fig. 4-2a), the CTR reaction of ZnO with pure carbon theoretically begins at 600 °C and reaches completion above 800 °C, yielding an equimolar gas mixture of Zn(g) and CO(g) (formation of CO_2 is predicted below 800 °C). When decreasing the pressure to 0.1 bar, the starting reaction temperature becomes 500 °C, and the reaction reaches completion at above 700 °C, thus shifting the chemical equilibrium to lower temperature. In addition, the reaction requires lower pressures when decreasing the temperature to reach completion (e.g. below 0.4 bar at 750°C vs. below 0.2 bar at 700°C, according to Fig. 4-2b).

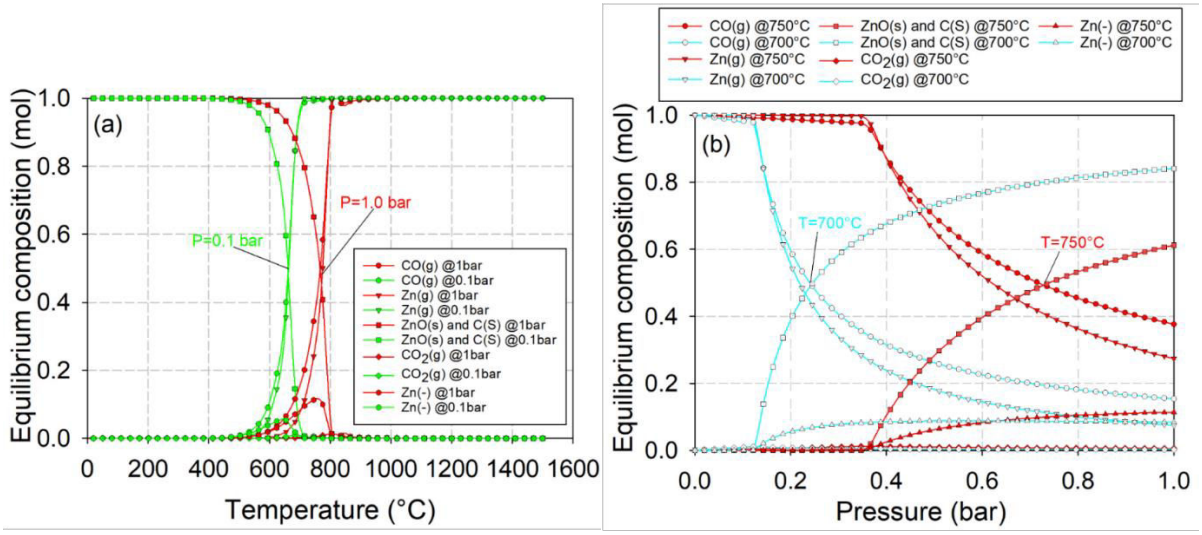

Figure 4-2. Thermodynamic equilibrium products distribution of ZnO carbothermal reduction as a function of (a) temperature (at 0.1 and 1.0 bar) and (b) pressure (at 700 and 750 °C).

The equilibrium products distribution of ZnO carbothermal reduction is plotted as a function of C/ZnO molar ratio at 800 °C and 1 bar (Fig. 4-3). At C/ZnO molar ratios above 1, the ZnO+C reaction yields almost 1 mol of CO (CO_2 is negligible), along with the formation of Zn in both gas and liquid states, thus confirming that excess carbon is required to achieve ZnO reduction completion.

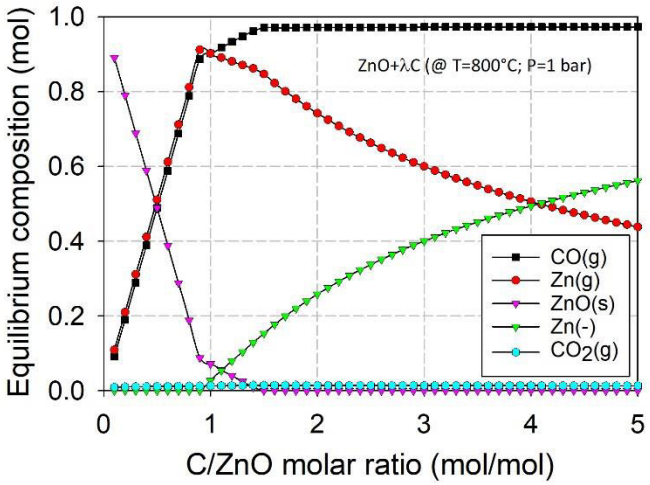

Figure 4-3. Thermodynamic equilibrium products distribution of ZnO carbothermal reduction as a function of C/ZnO molar ratio.

4.2.2 MgO

The carbothermal reduction reaction of MgO is written as:

$$MgO + C \rightarrow Mg + CO \tag{4-5}$$

Possible side reactions may also occur during MgO reduction with carbon according to Eq. 4-4.

The thermodynamic stability domain of chemical species for various MgO reduction reactions either with or without carbonaceous materials is represented by the Gibbs free energy change (ΔG°) in Fig. 4-4. According to the ΔG° variations, the thermodynamically favorable reactions are MgO+C, and C+CO_2 that proceed at above 1800, and 700 °C, respectively. In contrast, the other reactions (in particular, MgO+H_2 and MgO+CO) are not able to produce Mg below 2000 °C, according to thermodynamics. Direct thermal reduction of MgO to Mg(g) and O_2(g) would require temperature in excess of 3430 °C, thus making the process not feasible in practice. Note that the formation of CO_2 can only be obtained from Boudouard equilibrium (CO disproportionation is favored below 700°C, Eq. 4-4), since the reaction of MgO with CO is not favorable.

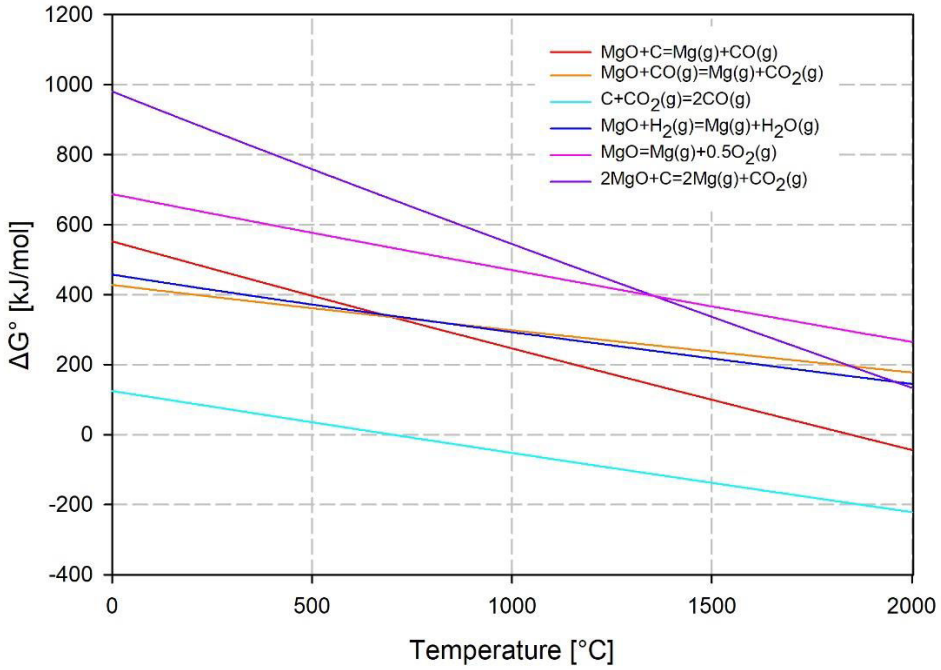

Figure 4-4. Variations of ΔG° for various MgO reduction reactions as a function of temperature.

In addition, thermochemical equilibrium compositions were calculated for MgO/C. The calculated equilibrium compositions of MgO carbothermal reduction as a function of temperature and pressure are shown in Fig. 4-5. At 1 bar, the MgO+C reaction (Fig. 4-5a) starts at 1200 °C and reaches completion at 1600 °C, thereby yielding an equimolar gas mixture of Mg(g) and CO(g). For a pressure decreased to 0.1 bar, the MgO+C reaction starts at 1000 °C, and reaches completion at 1400 °C, confirming that reduced pressure can theoretically shift the chemical equilibrium to lower temperature. Fig. 4-5b further validates that lower temperatures require larger pressure reduction to reach Mg formation (below 0.4 bar at 1500°C vs. below 0.1 bar at 1400°C).

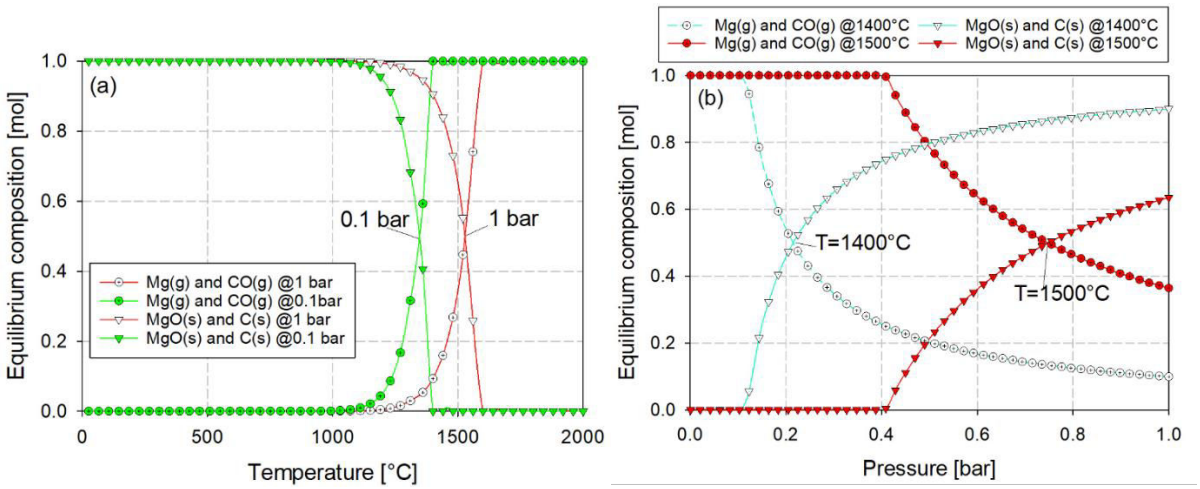

Figure 4-5. Thermodynamic equilibrium composition of MgO carbothermal reduction as a function of (a) temperature (at 0.1 and 1 bar) and (b) pressure (at 1400 and 1500 °C).

4.3 Experimental set-up and methods

4.3.1 Materials

Different solid carbonaceous feedstocks were considered for ZnO and MgO carbothermal reduction according to Table C-1 in Appendix C. Pure solid carbon powders (activated charcoal (AC),carbon black (CB), and graphite) and beech wood biomass ($C_6H_9O_4$) with ~1 mm particle size were employed as reducing agents. For reactant powder preparation, ZnO (99.8% purity, 1-5 µm, PROLABO) and MgO (particle size: 1-2 µm, 99.8% purity, Alfa Aesar) powders were well grinded with a mortar and then mechanically mixed with AC (99.9% purity, <149µm),CB (99.9% purity, 15.10^{-3}µm), or graphite (99.9% purity, <20 µm) with C/MO molar ratios (λ) of 1.5 (50% excess of carbon with respect to stoichiometry) for ZnO and 1.5 and 2 for MgO carbothermal reduction experiments. For reactant pellets, well mixed ZnO+CB powder (CB/ZnO molar ratio = 1.5) and ZnO+$C_6H_9O_4$ powder ($C_6H_9O_4$/ZnO molar ratio = 0.75, 50% excess of reducer with respect to stoichiometry) were prepared. Then the pellets (volume: 0.471 cm^3/pellet, 10 mm diameter) were obtained with manual hydraulic press at a pressure of ~75 kg/cm^2 for 2 min/pellet (Fig. C-1 in Appendix C).

4.3.2 Reactor prototype

A new 1.5 kW_{th} prototype solar vacuum reactor was designed and constructed, based on the concept of directly-irradiated cavity-type solar reactor (Fig. 4-6). This reactor can be operated in either batch or continuous modes under vacuum pressure conditions at high reduction temperatures up to ~1650 °C. The reactor is composed of an inner cylindrical cavity receiver made of alumina surrounded by a layer of porous ceramic insulation (Fig. C-2), thereby enabling rapid solar heating to the desired temperature. The bottom of the cavity is sealed with a circle alumina plate pierced at its center so that a small alumina tube can be inserted for the injection of nitrogen (N_2) carrier gas to the cavity receiver. N_2 protective gas is also directly injected into the window area and then subsequently enters downwardly the cavity through the aperture before exiting with the product gases through the outlet port, thereby protecting the transparent window from products deposition. A packed bed of inert alumina particles (2 mm diameter) is placed at the bottom of the cavity receiver above a layer of alumina

wool to support the reacting powder at the cavity center. The top of the cavity receiver is closed by an alumina cap with a 17 mm-diameter aperture where concentrated solar radiation enters, and a protective graphite plate (2 mm-thick) with a 15 mm-diameter aperture is then placed on top of the alumina cap to protect it (Fig. C-2). A hemispherical transparent glass window is lastly attached to the front flange edge of the reactor shell to operate under controlled atmosphere.

During reactor operation, the temperature within the cavity receiver (in the center of the packed bed) was measured with a type-B thermocouple (T_1), and the uppermost sample surface temperature was measured with a solar-blind optical pyrometer (operating at 4.8-5.2 µm in a H_2O absorption band). The cavity pressure (P) was measured by a pressure transducer while N_2 and CH_4 flow-rates (purity of 99.999%) were regulated by electronic Mass Flow Controllers (MFC, Brooks Instruments model SLA5850S, range 0-5 Nl/min ±0.2% of full scale).

In case of continuous operation (Fig. C-3), the reactor was equipped with an automatic particle delivery system consisting of a hopper and a screw feeder driven by an electrical motor for reactant powder injection. Alternatively, it was equipped with the alumina feeding tube with a pushing rod for reactant pellets injection. All the product gases including N_2 carrier gas exit the reactor through a single outlet port (20 mm in-diameter alumina tube) at the upper cylindrical sidewall of the cavity and subsequently flow into a ceramic filter where the main solid products (Mg or Zn) are deposited. Indeed, the Mg or Zn formed at the reaction temperature are gaseous, vapors are thus entrained by the carrier gas out of the reactor and subsequently condense as small particles upon gas cooling. Solid particles are thus collected in the outlet deposits on the inner tube walls (zone A) and in the filter (zone B).

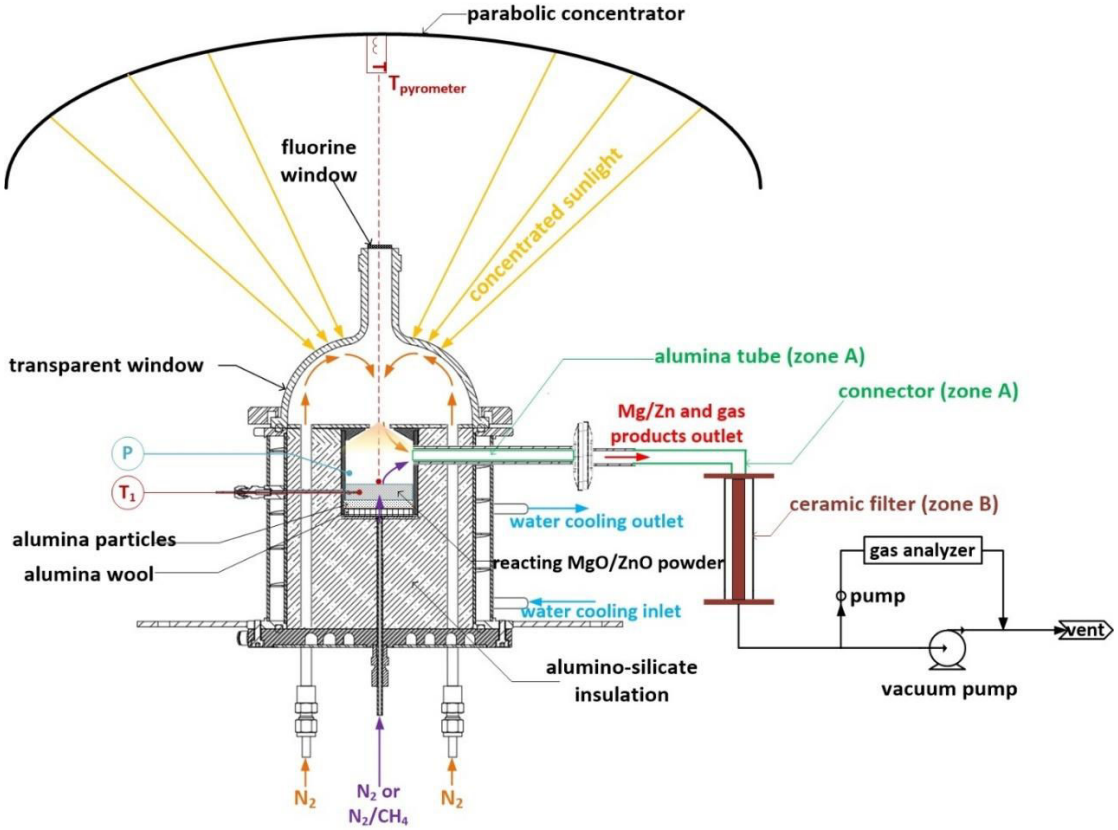

Figure 4-6. Schematic diagram of the 1.5 kW_{th} directly irradiated prototype solar reactor and external components.

4.3.3 Procedure

The solar vacuum reactor is positioned at the focus of a vertical axis parabolic dish solar concentrator with a solar concentration ratio up to 10,551 suns (2 m diameter, 0.85 m focal distance, peak flux density of ~10.5 MW/m^2 for a DNI of 1 kW/m^2) at CNRS-PROMES, Odeillo (France). The incident concentrated solar power is controlled manually by opening a shutter placed above the sun-tracking heliostat that vertically reflects incident solar radiation toward the facing down concentrator. Prior to the on-sun tests, homogeneous reacting samples are positioned in either the cavity receiver (batch test, Fig. 4-7a), hopper (continuous reactant powder injection, Fig.4-7b), or alumina feeding tube (continuous reactant pellets injection, Fig. 4-7c and Fig. 4-7d). The solar reactor is primarily flushed by a N_2 flow and concomitantly sucked by a Venturi pump to purge residual air from the system and then heated by highly concentrated sunlight. During solar heating, both N_2 carrier gas (via the cavity bottom and the screw feeder) and N_2 protective gas are supplied to the cavity receiver and window area, respectively.

Regarding vacuum and non-isothermal operation (Fig. 4-7a), once reaching the temperatures of ~650 °C (for CTR of ZnO) and 900 °C (for CTR of MgO), the reactor is evacuated with a rotary vane vacuum pump (Alcatel) to the targeted pressure (0.11-0.40 bar). Reduction reaction occurs from ~750 °C (ZnO) and ~1000-1200 °C (MgO depending on total pressure) during temperature rising as reflected by CO and CO_2 formation detected from an online gas analyzer. Solar heat supply rate is kept constant (~50 % shutter opening for CTR of ZnO and 100% shutter opening for CTR of MgO). Otherwise, it can be varied (by adjusting the shutter opening) to stabilize the targeted temperature for isothermal experiments (continuous operation with reactant injection). In addition, DNI remained stable throughout the on-sun tests. The product gas species (CO, CO_2, and Zn or Mg) exit the reactor from the single outlet port (20 mm in-diameter alumina tube) and then flow through a ceramic filter to separate and recover the condensed Zn or Mg particles from the gas. A small stream of product gases is then sampled by a secondary membrane pump to an on-line syngas analyzer for continuous gas analysis (using infrared detectors for CO, CO_2, CH_4 and thermal conductivity detector for H_2, uncertainty <0.5% of full scale). All the measured data are continuously recorded by an automated data acquisition system. Finally, the condensed products contained in the removable outlet components (zone A and zone B) are collected and then analyzed by calibrated X-ray diffraction (XRD) for phase identification (Philips PW 1820 diffractometer) with the Cu Kα radiation (αCu = 1.5418 Å, angular range = 20–100° in 2-Theta, step size of 0.02°, recording time = 2 s). Particle morphology analysis was carried out using a field emission scanning electron microscope (FESEM, Hitachi S4800) and Zn/Mg powders reactivity was assessed via thermogravimetric analysis (TGA, Netzsch STA449).

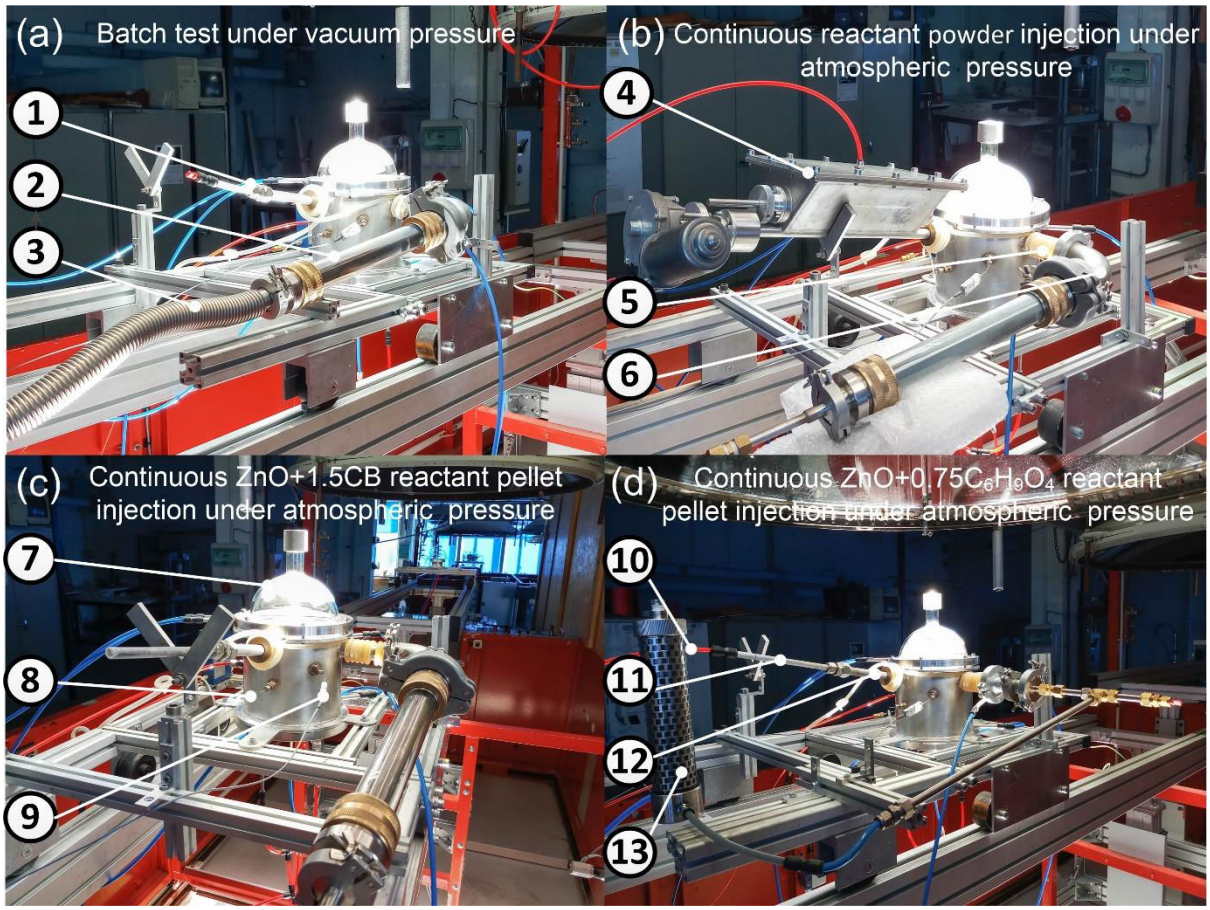

Figure 4-7. On-sun testing of ZnO carbothermal reduction in the different configurations of the prototype solar reactor: (1) alumina tube plug; (2) ceramic filter (zone B); (3) filter outlet where a vacuum pump is connected; (4) reactant powder feeding system; (5) outlet tube (zone A); (6) connector (zone A); (7) transparent window; (8) cylindrical reactor shell; (9) Type-B thermocouple; (10) N_2 inlet tube; (11) pushing rod; (12) alumina feeding tube for pellets; (13) cartridge filter.

To assess how well the reactant feedstock is converted into the products, the global mass balance (M) is estimated:

$$M = \frac{m_{gas\ products} + m_{solid\ products}}{m_{MO} + m_{carbonaceous\ feedstock}} \tag{4-6}$$

where $m_{gas\ products}$, $m_{solid\ products}$, m_{MO}, and $m_{carbonaceous\ feedstock}$ are the amounts (g) of gas product, solid product, metal oxide, and solid carbonaceous feedstock, respectively.

The ZnO or MgO conversion (X_{ZnO} or X_{MgO}) represents the net fraction of ZnO or MgO converted to Zn or Mg (also corresponding to Zn or Mg yield). It was calculated based on gas analysis using an oxygen mass balance:

$$X_{ZnO}(X_{MgO}) = \frac{n_{CO} + 2n_{CO_2}}{n_{ZnO}(n_{MgO})} \tag{4-7}$$

where n_{CO} and n_{CO2} denote the mole amounts of produced CO and CO_2 obtained by time integration of their production rates over the experiment duration.

The energy upgrade factor (U) is defined as the ratio of energy content of the chemical products to the calorific value of the carbonaceous feedstock:

$$U = \frac{(LHV_{gas\ products} \cdot \dot{m}_{gas\ products}) + (\dot{m}_M \cdot \Delta H_{M+0.5O_2 \rightarrow MO})}{LHV_{carbonaceous\ feedstock} \cdot \dot{m}_{carbonaceous\ feedstock}} \quad (4\text{-}8)$$

where LHV, $\dot{m}$, and ΔH represent the Lower Heating Value (J/kg), mass flow rate (kg/s), and standard enthalpy change (J/kg), respectively.

The solar-to-fuel energy conversion efficiency ($\eta_{solar\text{-}to\text{-}fuel}$) represents the ratio of the chemical energy of the products to the total energy input (solar power and calorific value of the carbonaceous feedstock):

$$\eta_{solar-to-fuel} = \frac{(LHV_{gas\ products} \cdot \dot{m}_{gasproducts}) + (\dot{m}_M \cdot \Delta H_{M+0.5O_2 \rightarrow MO})}{\dot{Q}_{solar} + (LHV_{carbonaceous\ feedstock} \cdot \dot{m}_{carbonaceous\ feedstock})} \quad (4\text{-}9)$$

where $\dot{Q}_{solar}$ is the solar power input (W) during reaction

The carbon conversion (X_C) represents the ratio of the carbon yield in the form of gas products to the initial carbon in the carbonaceous feedstock:

$$X_C = \frac{\int_0^t F_{CO}(t)dt + \int_0^t F_{CO_2}(t)dt + \int_0^t F_{CH_4}(t)dt + \int_0^t 2F_{C_2H_m}(t)dt}{\int_0^t xF_{C_xH_yO_z}(t)dt} \quad (4\text{-}10)$$

where F_i are the molar flow rates of species i, mol/s

4.4 Experimental results

4.4.1 Carbothermal reduction of ZnO

4.4.4.1 Solar reactor performance assessment

The operating conditions and experimental results for 17 solar runs of CTR of ZnO with different carbon types and shapes in batch or continuous operation are summarized in Table 4-1. On-sun experiments were conducted with the following range of parameters: initial reactant mass = 2.44-12.21 g, carbon types = AC, CB, and $C_6H_9O_4$, P = 0.15-0.90 bar, $\dot{m}_{N2}$=2.2-3.84 NL/min, T_1=950-1350 °C, and $\dot{Q}_{solar}$ = 0.73-1.19 kW_{th}.

M was in the ranges of 71.2-87.6% for packed-powder, 63.9-66.6% for continuous powder injection, and 75.2-97.2% for continuous pellet injection. Thus, the continuous powder injection process exhibited the lowest values of M, presumably resulting from sticky reactant deposition on the screw path or diffusion/interaction within the reactor and insulation materials [41], which cannot be quantified. Actually, the ZnO conversion in the reaction zone was total as no ZnO remained in the cavity (only carbon remained because in excess). However, a part of ZnO was recovered at the outlet due to partial Zn recombination or ZnO particle entrainment, thus somewhat lowering the net fraction of ZnO converted to Zn. X_{ZnO} was found in the ranges of 66.8-78.2% for batch runs and 44.3-73.2% for continuous runs, thus pointing out that batch operation results in higher reaction extent due to lower products recombination and particle entrainment. Most of U values were above one and approached the theoretical U (1.61 for ZnO+C according to Eq. 4-1 and 1.31 for ZnO+$C_6H_9O_4$ according to Eq. 4-2), thereby

efficiently storing solar energy into chemical fuels. However, the obtained *U* values related to continuous powder injection (Run. No. 7-9) were below one as a result of low ZnO conversion (44.3-47.1%). $\eta_{solar\text{-}to\text{-}fuel}$ was in the ranges of 1.1-1.6% for batch runs and 2.6-5.9% for continuous runs, indicating that continuous operation outperforms batch operation due to lower heat losses, reduced power consumption and better utilization of solar power input thanks to isothermal operation. X_C was in the ranges of 40.8-52.1% for (ZnO+C) packed-powder, 25.8-27.8% for continuous (ZnO+C) powder injection, 42.5-50.7% for continuous (ZnO+C) pellet injection, and 56.5-84.6% for continuous (ZnO+$C_6H_9O_4$) pellet injection. This clearly reveals that X_C from batch tests were significantly higher than those obtained from continuous tests with powder, due to higher reaction extent. However, X_C values in continuous mode were improved markedly by increasing temperatures (1100-1350 °C, pellet reactants). In addition, the maximum X_C range was achieved with continuous (ZnO+$C_6H_9O_4$) pellet injection. This is because the excess of biomass was pyrolyzed to form additional gas species, thus enhancing X_C.

Table 4-1. Operating conditions and solar reactor performance assessment

Run No.	initial reactant (g)	C/ZnO	C type	shape	Operating mode	P (bar)	$\dot{m}_{N2}$ (NL/min)	T_1 (°C)	$\dot{Q}_{solar}$ (kW)	CO yield (mmol/g$_{ZnO}$)(±2%)	CO_2 yield (mmol/g$_{ZnO}$)(±2%)	M (%)	X_{ZnO} (±2%)	U (±2%)	$\eta_{solar\text{-}to\text{-}fuel}$ (±2%)	X_C (±2%)	S_{CO}
1	2.44	1.50	AC	powder	batch	0.15	2.20	1167*	0.82	4.22	2.59	73.4	76.5	1.2	1.1	49.1	0.62
2**	2.44	1.50	AC	powder	batch	0.40	2.20	974*	0.90	4.52	1.85	71.2	66.8	1.0	1.2	40.8	0.71
3	2.45	1.50	AC	powder	batch	0.90	2.20	1139*	0.88	6.10	1.50	80.3	74.0	1.2	1.6	50.5	0.80
4**	2.44	1.50	CB	powder	batch	0.15	2.20	1106*	1.05	4.07	2.43	80.5	72.6	1.1	1.2	42.5	0.63
5	2.44	1.50	CB	powder	batch	0.40	2.20	1248*	0.98	5.48	2.07	87.6	78.2	1.2	1.2	49.1	0.73
6	2.44	1.50	CB	powder	batch	0.90	2.20	1233*	0.81	5.96	1.71	86.9	76.2	1.2	1.4	52.1	0.78
7	12.21	1.50	CB	powder	Continuous (0.5 g/min)	0.90	4.20	950	0.80	2.08	1.68	63.9	44.3	0.9	3.3	25.8	0.55
8	12.20	1.50	CB	powder	Continuous (0.5 g/min)	0.90	4.20	950	0.73	2.25	1.77	64.3	47.1	0.9	3.2	27.8	0.56
9	12.00	1.50	AC	powder	Continuous (1.0 g/min)	0.90	4.20	950	0.78	2.43	1.67	66.6	47.0	0.9	4.6	26.6	0.59
10	6.34	1.50	CB	pellet	continuous	0.90	3.64	1100	0.81	5.33	1.53	82.5	68.3	1.0	2.8	42.5	0.78
11	6.24	1.50	CB	pellet	continuous	0.90	3.64	1200	1.01	6.68	1.00	80.3	70.7	1.1	2.6	48.5	0.87
12	5.10	1.50	CB	pellet	continuous	0.90	3.64	1300	1.04	7.57	0.65	82.9	72.2	1.1	2.7	50.4	0.92
13	5.03	1.50	CB	pellet	continuous	0.90	3.64	1350	1.19	7.86	0.57	75.2	73.2	1.1	2.7	50.7	0.93
14**	4.16	0.75	$C_6H_9O_4$	pellet	continuous	0.90	3.64	1100	0.96	20.43	3.16	89.1	-	0.7	3.1	56.5	0.87
15	5.02	0.75	$C_6H_9O_4$	pellet	continuous	0.90	3.84	1200	1.04	32.32	4.63	96.9	-	1.0	5.9	81.8	0.87
16	4.99	0.75	$C_6H_9O_4$	pellet	continuous	0.90	3.84	1300	1.12	33.96	3.88	94.9	-	1.0	5.6	84.6	0.90
17	5.01	0.75	$C_6H_9O_4$	pellet	continuous	0.90	3.84	1350	1.14	34.80	3.36	97.2	-	1.0	5.6	84.6	0.91

*T_{max} ** DNI fluctuation

4.4.4.2 Parametric study

- **Influence of carbon type and pressure in batch tests**

ZnO carbothermal reduction was experimentally studied in batch mode at different pressures (0.15, 0.40, and 0.90 bar). ZnO/C blend powders (2g of ZnO with 0.44g of either AC or CB, resulting in a constant C/ZnO molar ratio of 1.5) were prepared by mechanical mixing and placed in the cavity receiver for batch tests under non-isothermal condition.

The evolution of species production rates (CO and CO_2) are plotted in Fig. 4-8. According to Fig. 4-8, the reaction started at ~750 °C with the formation of CO_2 occurring before CO regardless of the pressures and reducing agents, thus indicating negligible impact of the considered pressure range on the temperature of reaction start. When decreasing the pressure from 0.90 to 0.15 bar, the kinetic rate of reduction reaction increased, as reflected by the increase in the slope of CO production rates and reaction duration decrease (especially for CB), in agreement with thermodynamics and previous experimental study [58]. However, the peak CO production rates remained similar while those of CO_2 increased significantly: for example, the peak CO and CO_2 production rates were 13.4 and 2.8 mL min^{-1} g_{ZnO}^{-1} at 0.90 bar (Fig. 4-8d) compared to 13.4 and 8.7 mL min^{-1} g_{ZnO}^{-1} at 0.15 bar (Fig. 4-8f). The presence of CO_2 is detrimental as it favors the re-oxidation of Zn products into ZnO and CO at the reactor outlet (when temperature decreases), thus adversely affecting the Zn production yield but increasing the CO yield. Hence, atmospheric pressure operation is preferable to lower the amount of CO_2 and increase the Zn yield. Small variations in CO and CO_2 trends (Figs. 4-8b and 4-8f) were because of DNI variations (direct normal irradiance) caused by clouds passage, leading to unstable temperature, which directly modified the ZnO reduction rate. Fig. 4-9 confirms that reducing pressure did not significantly influence the starting reaction temperature (~750 °C) but had a beneficial effect on the kinetic rate of CTR [70], particularly at 0.15 bar.

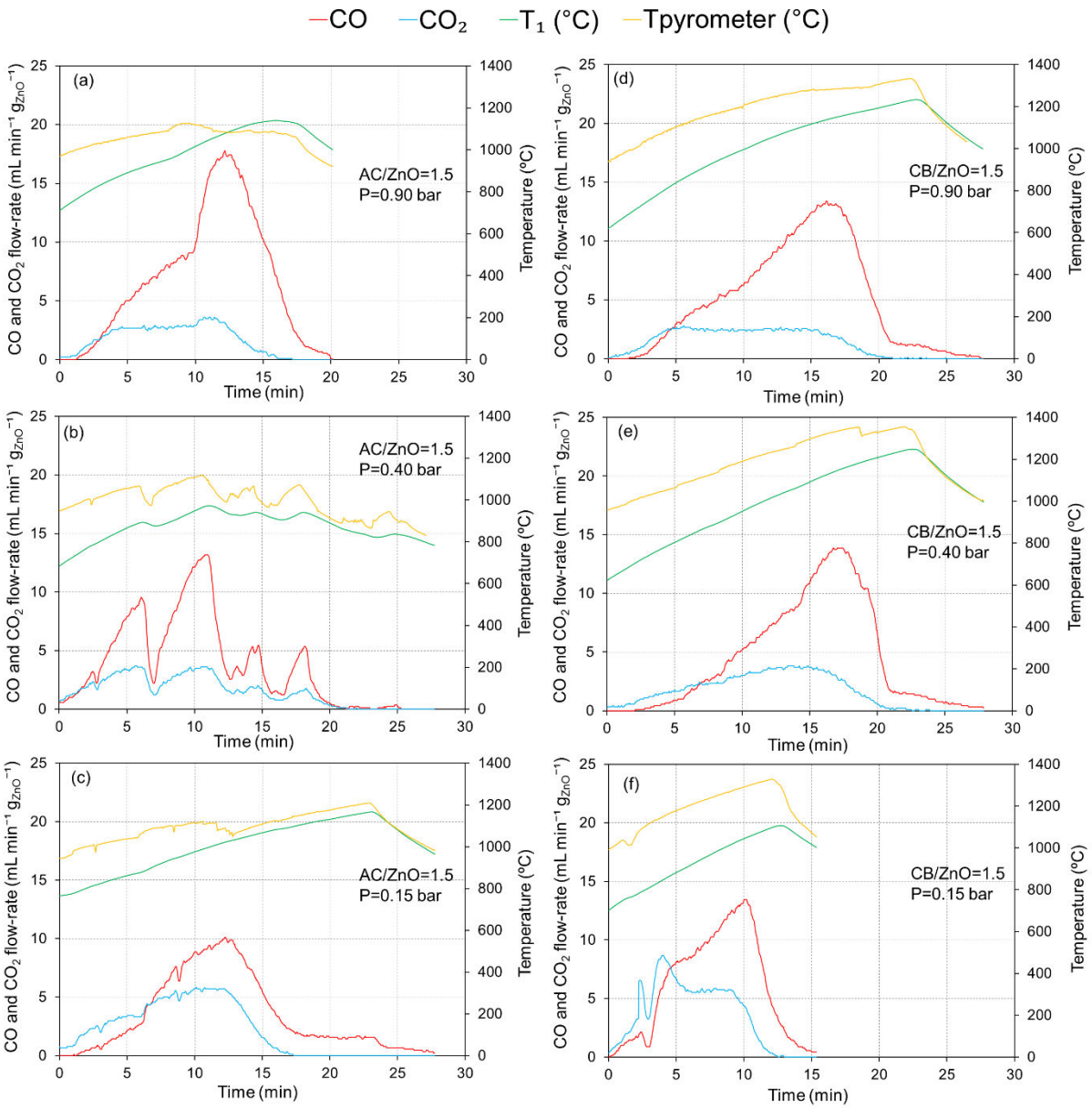

Figure 4-8. CO and CO_2 production rates along with reactor temperatures for ZnO carbothermal reduction over AC and CB at different total pressures (C/ZnO=1.5).

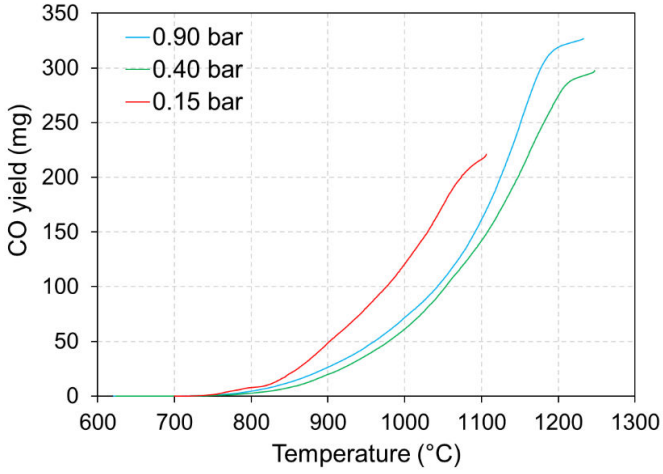

Figure 4-9. CO yield as a function of temperature for different total pressures (CB/ZnO=1.5).

Fig. 4-10 reports the global CO and CO_2 yields over the entire reaction duration along with ZnO conversion (X_{ZnO}) as a function of total pressure for AC and CB. As expected, the CO yield dropped when decreasing pressure at the expense of CO_2 increase, (CO selectivity, $S_{CO}= n_{CO}/(n_{CO} + n_{CO_2})$, thus declined from 0.80 at 0.90 bar to 0.62 at 0.15 bar for AC). For instance, the CO and CO_2 yields for AC were 6.12 and 1.50 mmol/g_{ZnO} at 0.90 bar compared to 4.22 and 2.59 mmol/g_{ZnO} at 0.15 bar, respectively. The reaction mechanism is expected to proceed via two solid-gas reactions in which ZnO is first reduced by CO to Zn and CO_2 (Eq. 4-3), and the produced CO_2 is then reduced by C (Eq. 4-4). Because the gas residence time is decreased with pressure decrease, the CO_2 reduction with C may be kinetically limited, thereby leading to the CO_2 increase. X_{ZnO} remained quite stable with decreasing pressure (e.g. 74.2% at 0.90 bar vs. 76.5% at 0.15 bar for AC) although the ZnO reduction rate was enhanced [58]. Differences in CO and CO_2 yields between AC and CB were not significant, which thus suggests that the different carbon types and properties do not affect the reaction extent. In the following tests, atmospheric pressure was selected to keep the amount of CO_2 evolved at the minimum.

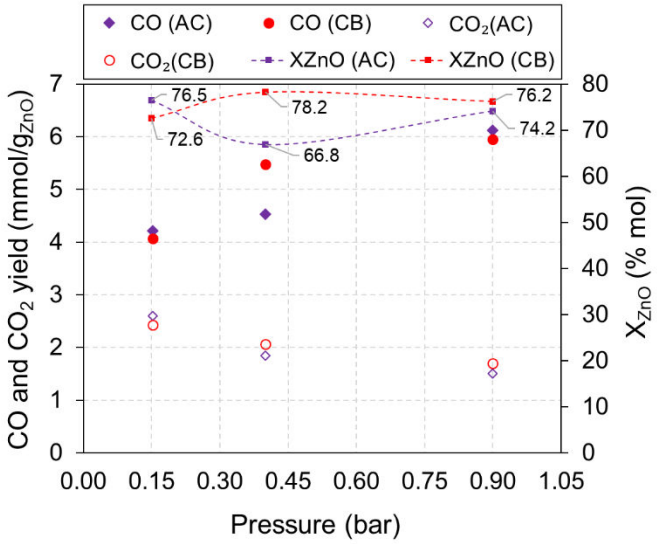

Figure 4-10. CO and CO_2 yields along with ZnO conversion (X_{ZnO}) for ZnO carbothermal reduction with AC and CB in batch mode as a function of total pressure (C/ZnO=1.5).

4.4.4.3 Continuous isothermal tests

- **Influence of carbon type and feeding rate during reactant powder injection**

The same carbon reducers (AC and CB) were employed for CTR of ZnO with continuous reactant powder injection. The screw feeder was first calibrated for the blend powders (ZnO mixed with either AC or CB) to control the reactant powder mass feeding rate. A homogenous mixture of reactant powder (12.2g in total with a fixed C/ZnO molar ratio of 1.5) was fed into the cavity receiver operated under atmospheric pressure and isothermal condition (Fig. 4-7b). The feeding rate was kept constant at 0.5 g/min, and the operating temperature (T_1) was fixed at 950 °C in order to keep the steel screw feeder tip below its melting point, as it was directly inserted in the cavity receiver area. The gas yields were calculated from the measured CO and CO_2 production rates (Fig. C-4).

Fig. 4-11 shows that higher CO yield is achieved with AC while CO_2 yield remains similar (total gas yield is 4.10 mmol/g_{ZnO} for AC vs. 3.76 mmol/g_{ZnO} for CB), thereby enhancing X_{ZnO} (47.0% for AC vs. 44.3% for CB). The higher available surface area of AC compared to CB (Table C-1) promotes contact between ZnO and AC and favors the solid-solid reaction.

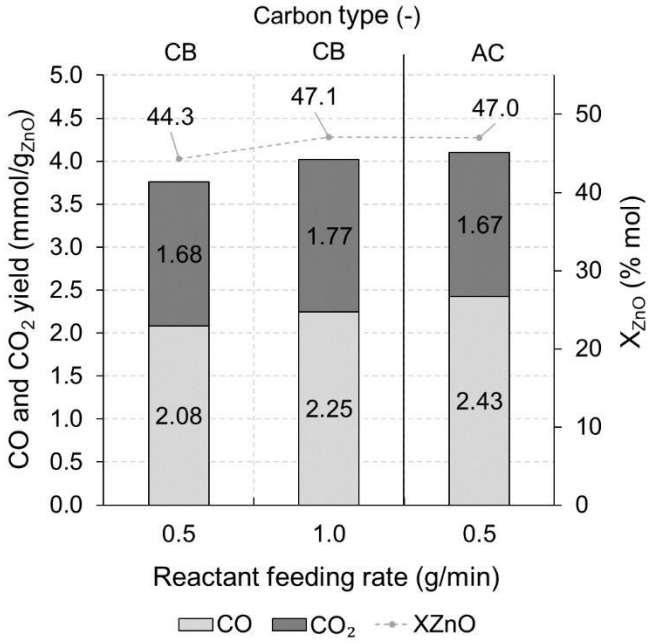

Figure 4-11. CO and CO_2 yields along with ZnO conversion (X_{ZnO}) for ZnO carbothermal reduction with AC and CB (C/ZnO=1.5) during continuous powder injection.

The influence of reactant powder feeding rate was then studied by increasing the feeding rate to 1 g/min for ZnO+CB while the other operating parameters were the same (~12g in total, CB/ZnO=1.5, T=950 °C, P=0.9 bar, Run. No.8, Fig. C-5). The CO and CO_2 yields increased slightly to 2.25 and 1.17 mmol/g_{ZnO} at 1.0 g/min, yielding X_{ZnO}=47.1% (Fig. 4-11). Low feeding rate thus results in low gas production whereas high feeding rate may lead to reactant accumulation due to kinetic limitation inducing incomplete reaction. Indeed, the reactant feeding rate must match the ZnO reduction reaction rate during continuous reactant injection. In comparison, X_{ZnO} values obtained in continuous tests (44.3-47.1%) were much lower than those obtained in batch tests (66.8-78.2%). This is due to lower reaction kinetics during isothermal operation (at 950 °C) whereas the temperature was increased constantly over 950°C (up to ~1200°C) until reaction completion for batch tests. In addition, a particle entrainment issue may also occur during continuous powder injection, and some particles can be entrained by the carrier gas before reaction occurring. To overcome these issues, the reactants were then continuously injected as pressed pellets under isothermal conditions at higher temperatures to enhance the reaction kinetics.

- **Continuous reactant pellets injection**

The continuous Zn production from CTR of ZnO was investigated at higher temperatures (1100, 1200, 1300, and 1350 °C) with reactant pellets injection. This method

aimed to alleviate the particle entrainment issue. Two types of reducers including pure carbon (CB) and beech wood biomass ($C_6H_9O_4$) were selected. CB was selected in place of AC since it also acts as a cohesive binder during the pellets making process.

The pellets with 10 mm diameter (~0.7 g/pellet for ZnO+CB and 0.35 g/pellet for ZnO+$C_6H_9O_4$) were prepared with 50% of excess carbon reducer content (C/ZnO and $C_6H_9O_4$/ZnO molar ratios of 1.5 and 0.75, respectively). The pellets (10 pellets/run for ZnO+CB and 15 pellets/run for ZnO+$C_6H_9O_4$, Fig. C-1) were loaded into the alumina feeding tube equipped with a pushing rod and the delivery system was then installed at the injection port of the reactor (Fig. 4-7c and 4-7d). On-sun continuous tests were performed isothermally in the temperature range 1100-1350 °C under atmospheric pressure (0.9 bar). Each pellet was injected once the gas production rates (mainly CO) tended to drop, as observed by gas analysis.

The evolution of gas species production rates and reactor temperatures are presented in Fig. 4-12 (ZnO+1.5CB) and Fig. 4-13 (ZnO+0.75$C_6H_9O_4$). According to Fig. 4-12, the CO and CO_2 production rates increased and the total reaction duration decreased noticeably when increasing the temperature. For instance, the peak CO and CO_2 production rates were 11.40 and 4.76 mL min^{-1} g_{ZnO}^{-1} at 1100 °C (27 min duration) compared to 34.69 and 3.53 mL min^{-1} g_{ZnO}^{-1} at 1350 °C (17 min duration), demonstrating the beneficial impact of temperature on gas production rates and reaction kinetics. Fig. 4-14a confirms that the increase of temperature remarkably enhanced CO selectivity and decreased CO_2 yield (5.33 and 1.53 mmol/g_{ZnO} at 1100 °C compared to 7.86 and 0.57 mmol/g_{ZnO} at 1350 °C for CO and CO_2, respectively). These variations also resulted in the rise of total gas yield (6.4 to 8.2 mmol/g_{ZnO} approaching the maximum theoretical yield of 12.29 mmol/g_{ZnO}), and X_{ZnO} reached up to 73.2% at 1300 °C.

Regarding the ZnO+0.75$C_6H_9O_4$ reaction (Fig. 4-13), the increase of the temperature enhanced the CO and H_2 production rates, whereas CO_2 and CH_4 production rates tended to decline, and the total experimental duration was also reduced. For example, the peak CO, H_2, CO_2, and CH_4 production rates were 303.53, 236.30, 62.24, and 49.85 mL min^{-1} g_{ZnO}^{-1} at 1100 °C (~10 min duration) compared to 532.26, 402.17, 55.29, and 26.68 mL min^{-1} g_{ZnO}^{-1} at 1350 °C (~5 min duration). In contrast to the reaction with pure carbon producing only CO and CO_2 (Fig. 4-12), H_2 and CH_4 were also formed with biomass ($C_6H_9O_4$) because of the pyrolysis process producing mainly incondensable gases and char at the elevated reactor temperature (the amount of tar was negligible). Meanwhile, ZnO can be thus reduced with the pyrolysis products such as char, CH_4, CO, and H_2 according to the possible reactions shown in Fig. 4-1, then producing Zn and syngas. Fig. 4-14b clearly emphasizes that increasing temperature from 1000 to 1350 °C substantially increased H_2 and CO yields and decreased CO_2 and CH_4 yields. Moreover, the measured syngas yield was compared with theoretical maximum syngas yield calculated from Eq. 4-2. The syngas yields experimentally obtained at 1200, 1300, and 1350 °C were higher, which can be simply explained by the pyrolysis of the biomass excess (1/4$C_6H_9O_4$→char(carbon)+CO+CO_2+H_2+CH_4+tars), thereby leading to higher experimental syngas yield than theoretical one. As a conclusion, combining ZnO reduction and biomass gasification represents an attractive option to produce both metallic Zn and high-quality syngas in a single process.

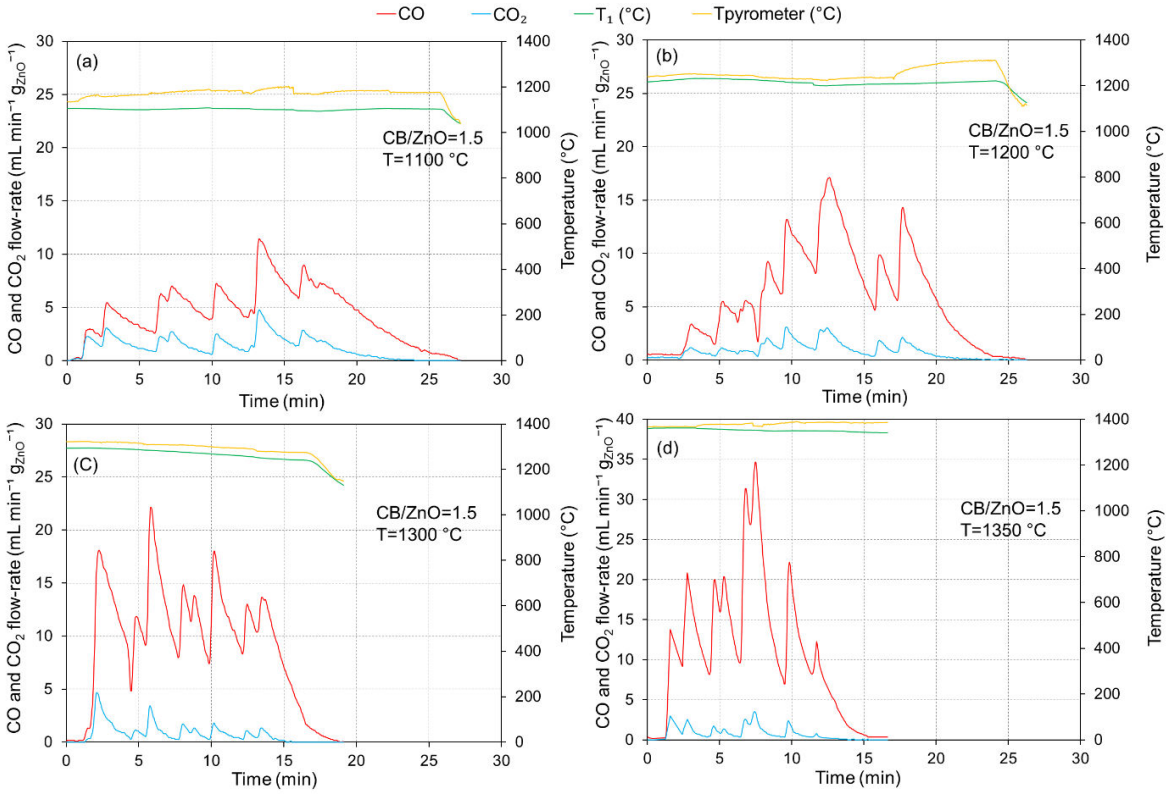

Figure 4-12. CO and CO_2 production rates along with reactor temperatures for ZnO carbothermal reduction with CB during continuous pellet reactant injection at (a) 1100, (b) 1200, (c) 1300, and (d) 1350 ℃.

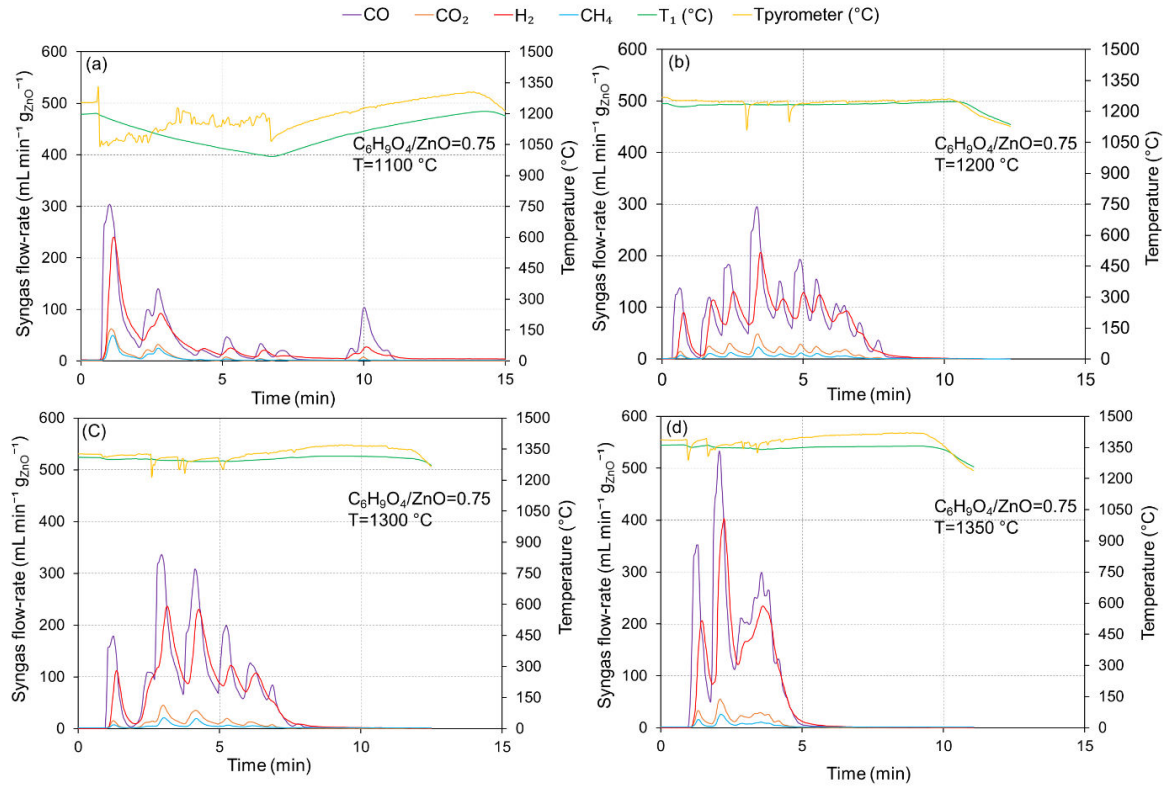

Figure 4-13. H_2, CO, CO_2, and CH_4 production rates along with reactor temperatures for ZnO carbothermal reduction with beech wood biomass ($C_6H_9O_4$) during continuous pellet reactant injection at (a) 1100, (b) 1200, (c) 1300, and (d) 1350 ℃.

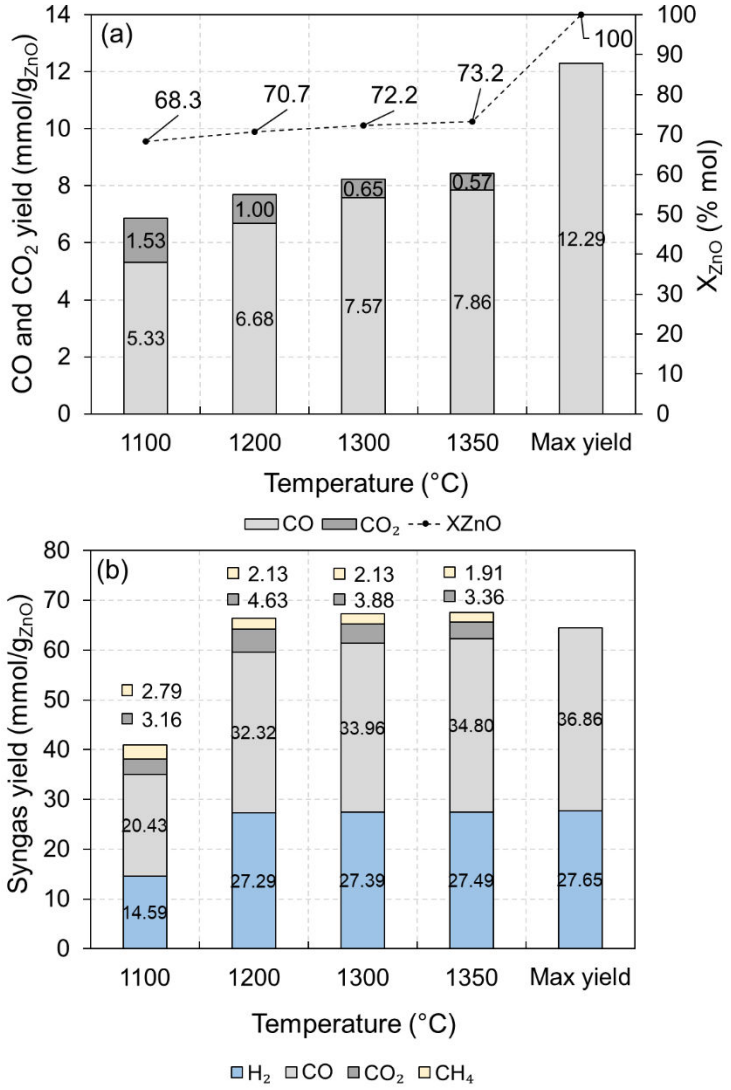

Figure 4-14. (a) CO and CO_2 yields along with ZnO conversion (X_{ZnO}) for ZnO carbothermal reduction with CB and (b) syngas yield for ZnO carbothermal reduction with beech wood biomass ($C_6H_9O_4$).

4.4.4.4 Characterization of Zn products

Solid products, mainly Zn particles, were deposited in the removable outlet components including: (1) alumina tube and connector (zone A) and (2) ceramic filter (zone B), as shown in Fig. 4-6 and Fig. 4-7. Their amounts were quantified by weighing the outlet components with a digital balance (0.01g readability) before and after experiments and then sampled for FESEM and XRD analysis. A few samples of the unreacted excess carbon remaining in the cavity receiver (Fig. C-6) were also analyzed.

Fig. 4-15 shows the XRD patterns of the collected solid products in both zone A and zone B for CTR of ZnO with AC (Fig. 4-15a) and CB (Fig. 4-15b) in batch mode at 0.15, 0.40, and 0.90 bar, compared to the commercial pure Zn reference pattern. Overall, the products were very well crystallized and mainly composed of Zn regardless of the pressure and solid carbon type. This confirms that high-purity Zn production was achieved, in agreement with the high X_{ZnO} up to 78.2% (Fig. 4-10). However, partial Zn recombination (most probably with CO_2) localized only at the outlet tip where the crystallized gray chunks occur was presumed (Fig. C-

7). This recombination occurs at a given location corresponding to the condensation zone of Zn vapor. The formed chunks in the first cm of zone A were indeed mainly composed of ZnO, thus confirming partial products recombination and explaining incomplete global ZnO conversion ($X_{ZnO} < 100\%$). Downstream this zone, the condensed Zn particles were carried by the gas, and the temperature was low enough to avoid recombination, thus recovering pure Zn powder in both the outlet tube and the filter.

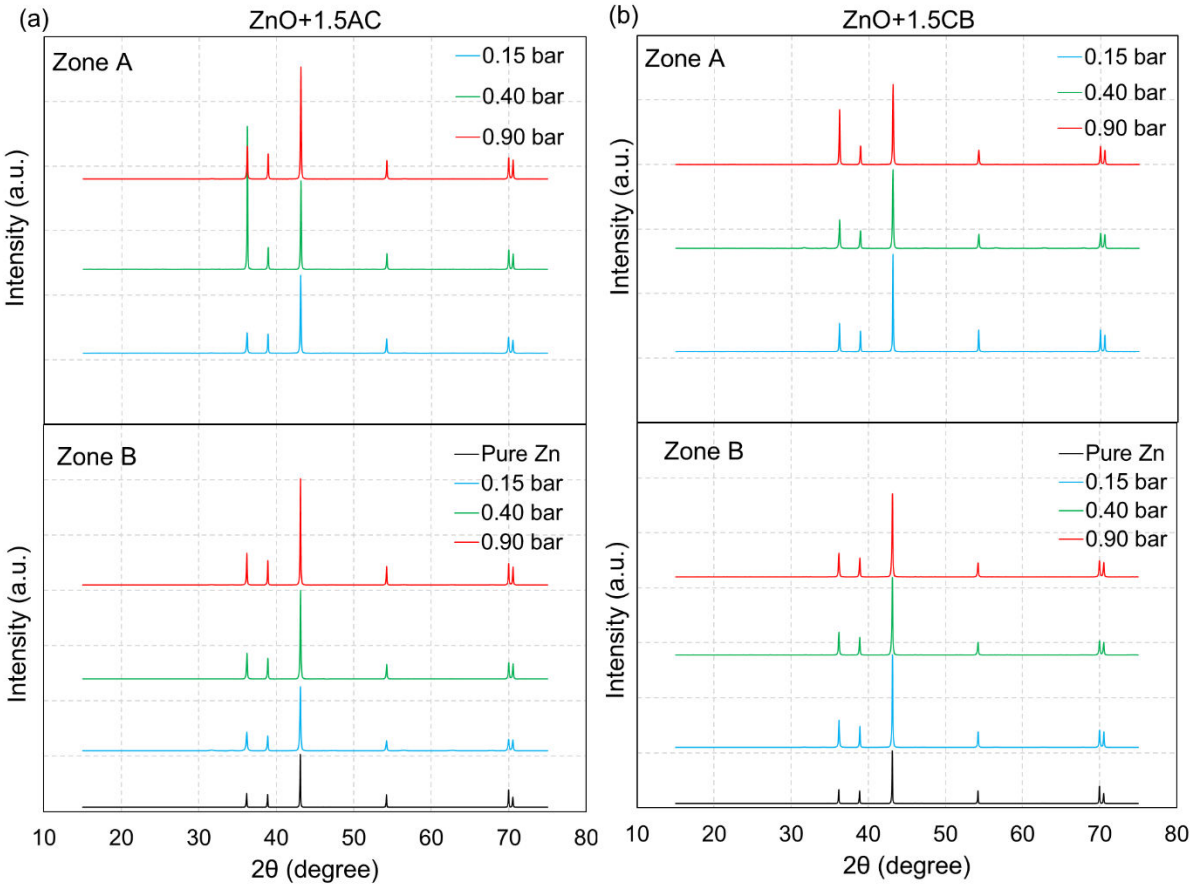

Figure 4-15. XRD patterns of the collected solid products in zone A and zone B for the reduction of ZnO with AC and CB during batch tests (AC/ZnO and CB/ZnO molar ratio of 1.5).

Fig. 4-16 shows the XRD patterns of solid products collected in zone A and zone B for continuous reactant powder injection at feeding rates of 0.5 and 1 g/min. In this case, small traces of ZnO are detected for both zones whatever the feeding rates and carbon types (ZnO peaks intensity appears more obvious in zone A). This presence of ZnO traces in continuous tests (not detected in batch tests) comes from the weak fine particles entrainment by carrier gas as mentioned before, which also agrees with the lower ZnO conversion (Fig. 4-11) when compared with batch operation (Fig. 4-10). Nonetheless, Zn contents were found to be above 90%wt for both zone A and zone B (Table. C-2).

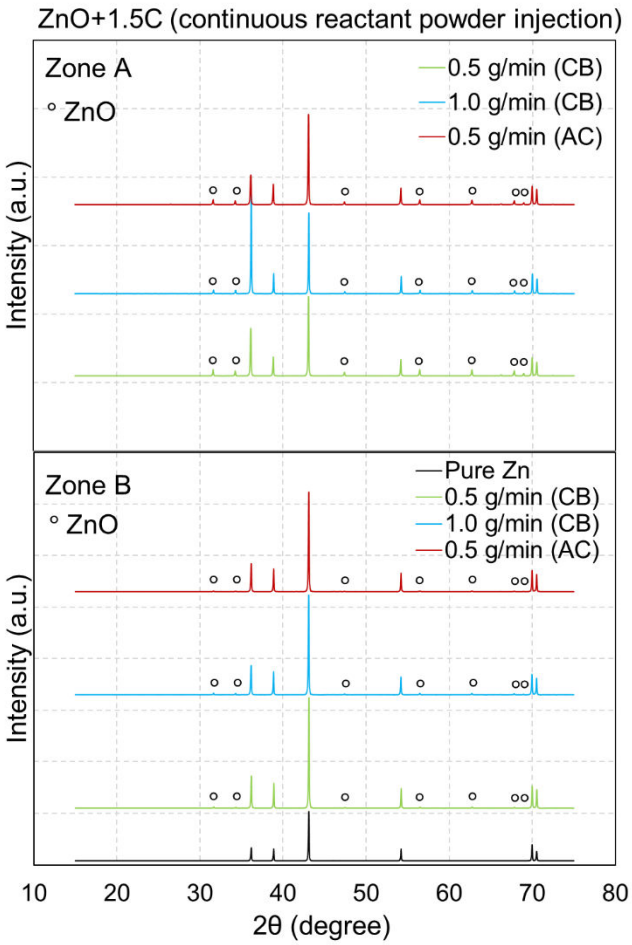

Figure 4-16. XRD patterns of the collected solid products in zone A and zone B for the reduction of ZnO with AC and CB during continuous powder injection tests at 0.5 and 1 g/min.

Regarding continuous pellets injection (Fig. 4-17), XRD patterns of solid products collected in zone A and zone B for the ZnO reduction with CB (Fig. 4-17a) and $C_6H_9O_4$ (Fig. 4-17b) also reveal small peaks ascribed to ZnO mainly found in zone A for any temperatures. However, high Zn content exceeding 90%wt was determined (Table C-2), demonstrating high-purity Zn production. At zone B, most collected products were composed of pure Zn with only the occurrence of ZnO traces at 1350 °C (ZnO+1.5CB) and at 1200 °C (ZnO+0.75$C_6H_9O_4$). In addition, no trace of ZnO was evidenced from the carbon residue collected in the cavity receiver, thus confirming complete ZnO conversion in the reaction zone.

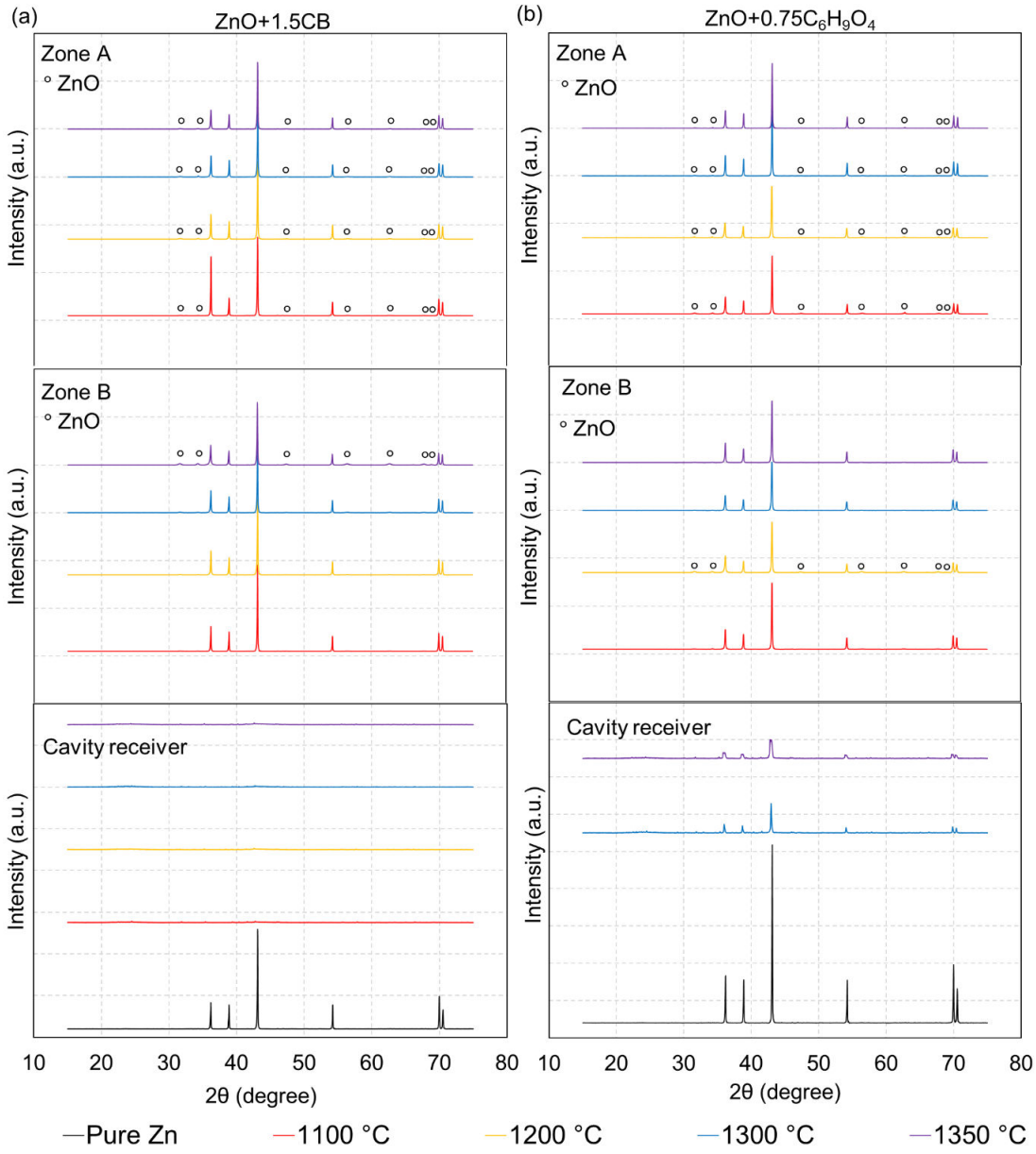

Figure 4-17. XRD patterns of the collected solid products in zone A and zone B for reduction of ZnO with (a) CB and (b) $C_6H_9O_4$ during continuous pellets injection at 1100, 1200, 1300, and 1350 ℃.

The morphology of solid products collected in the outlet (zone A) and filter (zone B) for continuous tests (powder and pellet) was analyzed by SEM (Fig. 4-18 and Fig. C-9). Overall, the condensed Zn product was formed as micrometer size particles, with clear crystal hexagonal structure, and the presence of fine particles of solid carbon was also observed in both zone A and zone B (Fig. 4-18b). The collected Zn products from the reduction of ZnO with CB (Fig. 4-18a and 4-18b) revealed clearer morphology regarding large scattered droplets of condensed Zn vapor with hexagonal shape when compared to those obtained from the reduction of ZnO with $C_6H_9O_4$ (Fig. 4-18c and 4-18d), the latter being wrapped by the deposition of fine char particles. Besides, smaller particle sizes (0.2-0.5 µm) of the condensed Zn were evidenced when employing $C_6H_9O_4$ as reducing agent (Fig. 4-18c and 4-18d).

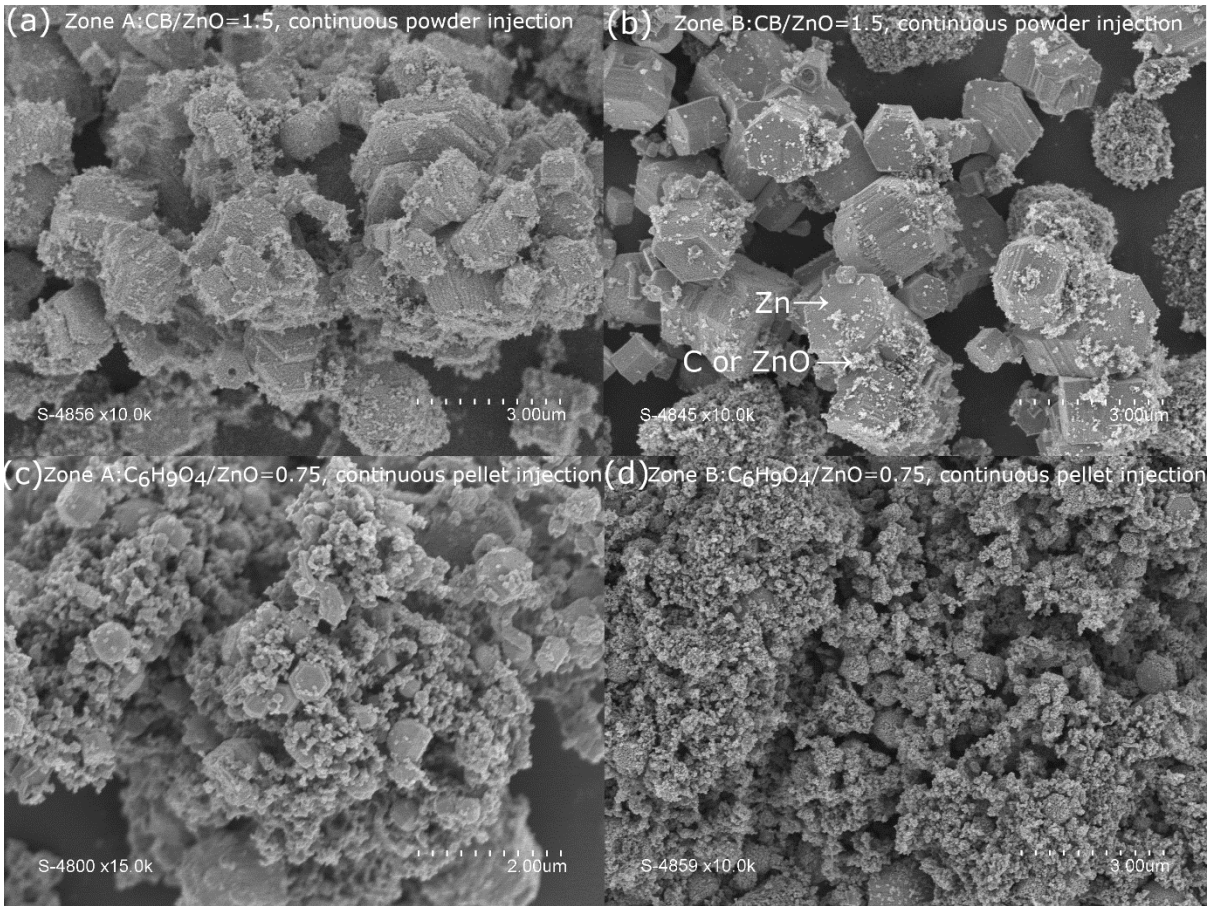

Figure 4-18. Representative SEM micrographs of solid products from the outlet tube (zone A) and filter (zone B) during (a,b) Run No. 8 and (c,d) Run No. 16.

The reactivity of the produced Zn powder during oxidation with CO_2 was investigated both to evidence its recombination ability at the reactor outlet and to highlight its potential to produce solar fuel in a second oxidation step (CO_2-splitting step). TGA confirmed the high reactivity of produced Zn with CO_2, and the complete Zn conversion (Fig. C-10). This further points out that the pure Zn produced from solar carbothermal ZnO reduction is highly reactive, which contrasts with previous studies reporting the superior oxidation reactivity of Zn in presence of ZnO as reaction promoter [148,149]. The produced pure Zn can thus be used to generate additional CO (or H_2) and solid ZnO that can be recycled to the solar step for closing the cycle.

4.4.2 Carbothermal reduction of MgO

4.4.2.1 Solar reactor performance assessment

Table 4-2 summarizes both the operating conditions and experimental results for the tests of the prototype vacuum solar reactor for producing Mg and CO. For this study, experiments were carried out to evaluate the solar reactor performance under the following range of parameters: P = 0.11-0.90 bar, $\dot{m}_{N2}$=1.2-2.2 Nl/min, $\dot{Q}_{solar}$ = 1.25-1.47 kW_{th}, reducing agents including different solid carbon (AC, CB, and graphite), and C/MgO molar ratio = 1.5-2. The ranges of maximum temperatures were 1437-1668 °C for T_1 and 1464-1622 °C for $T_{Pyrometer}$, confirming homogeneous temperature inside the cavity receiver. The global material

mass balance was also performed to quantify the amount of reactant actually converted into the products, which are syngas productions, Mg deposits and solid residues (details are given in Appendix C, Tables C-3 and Table C-4). As a result, the carbon conversion (X_C) was found in the range 60.9-73.1% for C/MgO=1.5 and 47.2-55.5% for C/MgO=2. This clearly indicates that a lower C/MgO molar ratio resulted in an enhanced X_C because a higher C/MgO excess ratio means a higher amount of unreacted carbon remaining inside the cavity (Run. No 5-8 in Table C-5). However, an excess of carbon with respect to stoichiometry (C/MgO = 1) is necessary to both favor CO yield and completely convert MgO to Mg. The MgO conversion was found in the range 68.6-99.9%, and the CO selectivity was in the range 0.98-1.00 (the amount of CO_2 stemming from CO disproportionation was negligible). U values were in the range 1.1-1.9, demonstrating successful solar energy storage in the chemical products. The highest U value (1.9), which approaches the maximal theoretical U (2.25) calculated from Eq. 4-5, was found with the following conditions: P=0.11 bar (the lowest pressure) and C/MgO=1.5 (Run. No.1), demonstrating a significant beneficial influence of pressure decrease and C/MgO molar ratio on U. The $\eta_{solar\text{-}to\text{-}fuel}$ for batch tests was found in the range of 1.1-1.8%, implying high heat losses due to a long non-isothermal period. This issue can be tackled by operating the process in an isothermal continuous mode, which directly lowers the processing duration and heat losses, thereby improving $\eta_{solar\text{-}to\text{-}fuel}$ (7.8% for a continuous test).

Table 4-2. Operating conditions and solar reactor performance assessment.

Run No.	C/MgO	P (bar)	C type	$\dot{m}_{N2}$ (Nl/min)	T_1 (°C)	Tpyrometer (°C)	$\dot{Q}_{solar}$ (kW)	CO yield (mmol/g_{MgO} ±2%)	CO_2 yield (mmol/g_{MgO} ±2%)	Global mass balance (%)	U (±2%)	$\eta_{solar\text{-}to\text{-}fuel}$ (±2%)	X_C (±2%)	X_{MgO} (±2%)	CO selectivity
1	1.5	0.11	AC	1.2	1551	1517	1.32	23.80	0.23	84.2	1.9	1.7	73.1	97.8	0.99
2	1.5	0.16	AC	2.2	1546	1464	1.25	20.21	0.22	78.3	1.7	1.8	64.3	83.2	0.99
3	1.5	0.90	AC	2.2	1668	1622	1.47	20.10	0.12	67.5	1.6	1.1	62.4	82.0	0.99
4*	1.5	0.11	CB	1.2	1437	1576	1.26	20.76	0.04	81.6	1.5	1.2	60.9	84.0	1.00
5*	2	0.11	CB	1.2	1534	1508	1.29	21.16	0.02	82.7	1.1	1.2	47.9	85.5	1.00
6	2	0.11	AC	1.2	1538	1528	1.32	24.59	0.10	85.6	1.4	1.5	55.5	99.9	1.00
7*	2	0.16	AC	2.2	1568	1538	1.39	21.21	0.17	52.5	1.3	1.6	52.1	86.8	0.99
8	2	0.16	Graphite	2.2	1581	1545	1.39	16.53	0.25	64.5	1.4	1.2	47.2	68.6	0.99
9**	1.5	0.11	AC	1.4	1501	1551	1.47	21.11	0.39	84.8	1.4	7.8	59.5	88.2	0.98

*Auto-combustion with air occurred, **continuous test

4.4.2.2 Parametric study of MgO carbothermal reduction

- **Influence of pressure**

The influence of total pressure on CO and CO_2 production rates and yields for the MgO carbothermal reduction with solid carbon was experimentally investigated in a batch mode (the MgO/C mixture was thus preloaded in the reactor before heating). Activated charcoal (AC) was employed as reducing agent with fixed AC/MgO molar ratios of 1.5 and 2. The total pressures varied from slightly over-atmospheric (0.9 bar) to rough vacuum pressures (0.16 and 0.11 bar), while the MgO reduction occurred during non-isothermal heating (heating rate controlled by adjusting the shutter opening).

The transient CO and CO_2 production rates for carbothermal reduction of MgO over AC are plotted in Fig. 4-19 (AC/MgO=1.5) and in Fig. 4-20 (AC/MgO=2). The effect of pressure was obvious with respect to the peak rates of CO production and CO evolution durations. For example, the peak CO production rate was 20 mL min^{-1} g_{MgO}^{-1} (50 min duration) at 0.9 bar compared to 26 mL min^{-1} g_{MgO}^{-1} (40 min duration) at 0.11 bar. Therefore, the kinetic rate of MgO carbothermal reduction reaction was enhanced by decreasing the total pressure, in agreement with thermodynamic analysis. The peak rate of CO production was observed before reaching the maximal temperature (below 1600°C) at reduced pressure (0.16 and 0.11 bar), whereas the reaction required temperatures above 1600 °C at atmospheric pressure to reach completion.

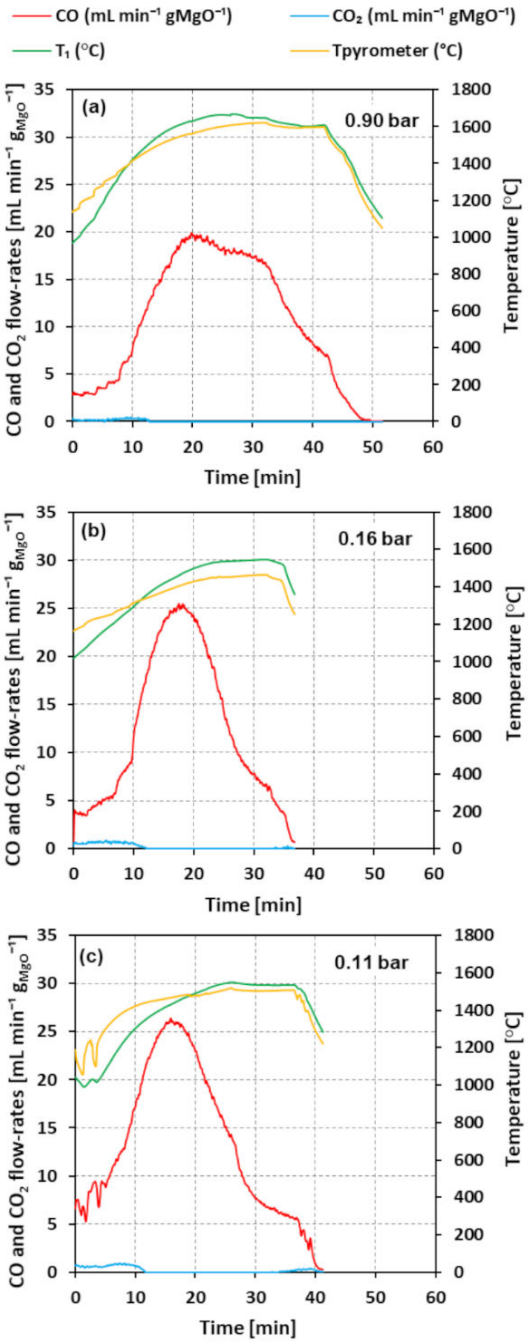

Figure 4-19. CO and CO_2 production rates along with reactor temperatures for the carbothermal reduction of MgO over AC at different total pressures (AC/MgO=1.5).

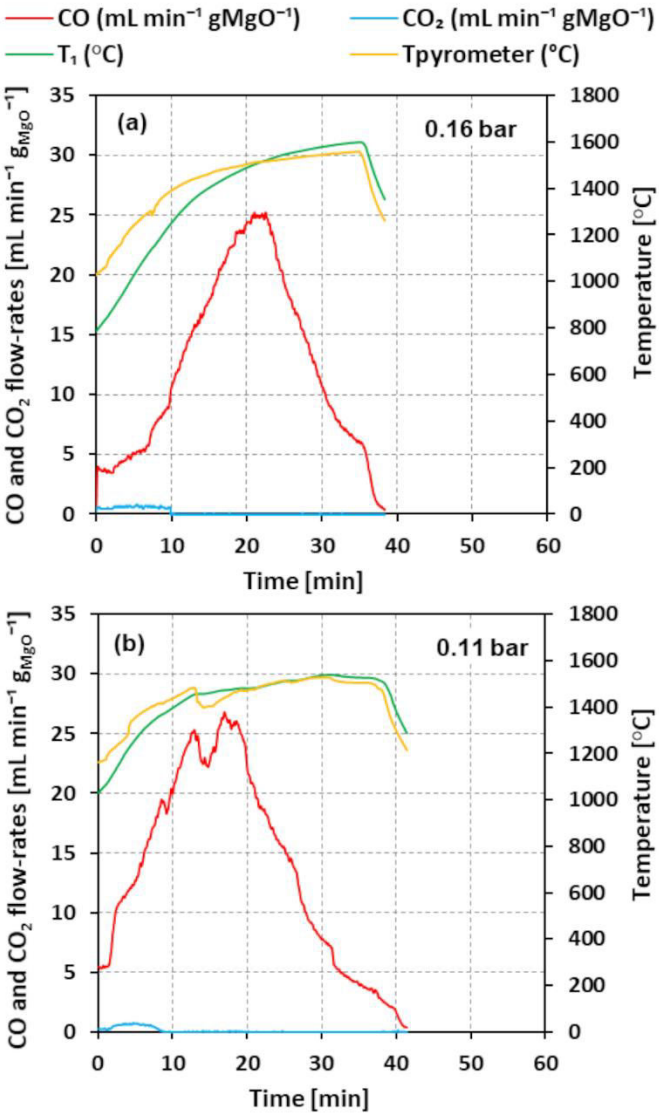

Figure 4-20. CO and CO_2 production rates along with reactor temperatures for the carbothermal reduction of MgO over AC at different total pressures (AC/MgO=2).

Fig. 4-21 shows the CO and CO_2 yields calculated by integrating the measured CO and CO_2 flow rates (Figs. 4-19 and 4-20) over the entire reaction duration as a function of total pressure for different carbon types and C/MgO molar ratios (1.5 and 2). As expected, the CO yield at both AC/MgO molar ratios increased considerably with decreasing total pressure. For example, the CO yield increased from 21.21 mmol/g_{MgO} at 0.16 bar to 24.59 mmol/g_{MgO} at 0.11 bar (AC/MgO molar ratio of 2), thus reaching 99.1% of the theoretical maximal CO yield (24.81 mmol/g_{MgO}) (1 mol CO per mol MgO according to Eq. 4-5). The enhanced CO yield means that the recombination of Mg and CO was lowered when decreasing the pressure (according to Le Châtelier's principle). In addition, CO_2 yields were found in a negligible amount (e.g. 0.10-0.17 mmol/g_{MgO} for a AC/MgO molar ratio of 2) and the selectivity to CO was thus above 99%. This low CO_2 production may presumably occur from the Boudouard equilibrium (Eq. 4-4), since the solid–gas reaction between MgO and CO

($MgO+CO \rightarrow Mg+CO_2$) is not thermodynamically favorable (Fig. 4-4). Thus, the MgO reduction reaction chiefly occurs via the solid–solid reaction (Eq. 4-5).

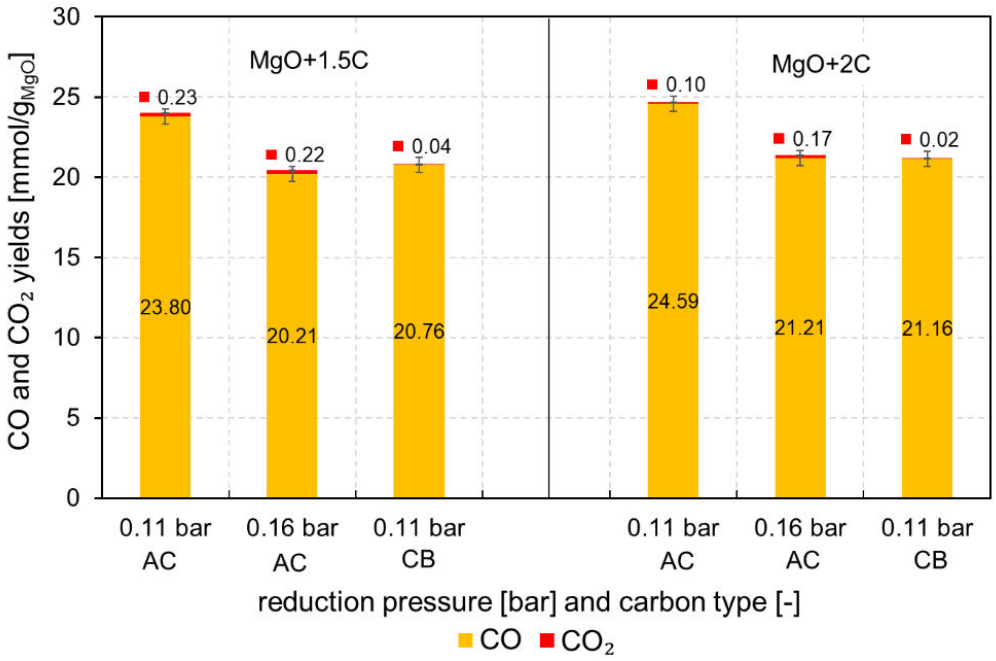

Figure 4-21. CO and CO_2 yields for MgO carbothermal reduction with AC and CB as a function of total pressure at C/MgO molar ratios of 1.5 and 2.

- **Influence of solid carbon type**

The influence of solid carbon type (AC, CB, and graphite) was experimentally investigated at C/MgO molar ratios of 1.5 and 2, while total pressure was kept constant at 0.11 bar. The progress of CO and CO_2 production rates for AC and CB are shown in Fig. C-11 (C/MgO=1.5) and Fig. C-12 (C/MgO=2). The highest reaction rates were found for AC at both C/MgO molar ratios, as evidenced by the higher peak of CO production rate for AC compared to that of CB, while the reaction duration for AC seemed to be lower than for CB, demonstrating faster reduction rate.

Fig. 4-21 also confirms that utilizing AC as reducing agent led to the highest CO and CO_2 yields at both C/MgO molar ratios when compared to CB. This can be explained by the significantly higher available surface area accessible for particle contact between MgO and AC, favoring the solid-solid reaction and thereby leading to higher CO yield. Note that the same result was also observed in the case of ZnO.

To further confirm the effect of carbon type, the carbothermal reduction of MgO with graphite was also tested and compared with that of AC. As expected, remarkable higher reaction rates were obtained for AC (Fig. C-13). The peak CO production rate was 25 mL min^{-1} g_{MgO}^{-1} for AC compared to 10 mL min^{-1} g_{MgO}^{-1} for graphite at 0.16 bar (C/MgO=2). Additionally, the higher reaction rates when using AC led to a substantially higher CO yield (21.21 mmol/g_{MgO} for AC compared to 16.53 mmol/g_{MgO} for graphite, Fig. C-14), in agreement with TGA experiments [54]. The use of AC as solid reducing agent is thus the most suitable option for solid-to-solid contact between MgO and AC, which promotes reaction rate and extent, thereby leading to higher CO and Mg yields.

- **Influence of C/MgO molar ratio**

The influence of C/MgO molar ratios was investigated with different solid carbon types (AC and CB) and total pressures (0.11 and 0.16 bar). The transient CO and CO_2 production rates are plotted for C/MgO molar ratios of 1.5 and 2 in Fig. C-15 (AC, 0.11 bar), Fig. C-16 (CB, 0.11 bar), and Fig. C-17 (AC, 0.16 bar). The influence of C/MgO molar ratios was nearly unnoticeable as evidenced by both similar peak CO production rates that occurred at the same temperatures and similar durations for both AC and CB.

As expected, similar CO and CO_2 yields (Fig. 4-21) between the C/MgO molar ratios of 1.5 and 2 were noticed for both solid carbon types, even though the CO yields at C/MgO=2 were slightly higher. Thus, increasing C/MgO molar ratio in excess from 1.5 to 2 did not significantly influence the CO and CO_2 yields.

4.4.2.3 Characterization of Mg products

The solid products were collected after each experiment in the removable outlet components of the solar reactor where solid products are condensed and deposited (detailed information are provided in Appendix C in the section of solid products analysis, Figs. C-18, C-19, C-20, and C-21 and Tables C-5,C-6). Mg was recovered in the outlet products as a pyrophoric fine powder having strong reactivity with air. All the samples were inevitably exposed to ambient air prior their analysis. Fig. 4-22 shows the XRD patterns of the collected solid products in zones A (outlet tube) and B (filter) after experiments at (a) AC/MgO=1.5 and (b) AC/MgO=2. The products were well crystallized with low contamination of carbon. Phases ascribed to Mg and MgO were identified in both zones, suggesting partial Mg recombination at the outlet (with CO) or oxidation after sample collection (with air). Indeed, the condensed Mg can be oxidized during its inevitable exposure to air when opening the reactor or transferring the powder for analysis, leading to a subsequent artificial increase of MgO content in the solid products after their collection from the reactor (auto-ignition observed at room temperature). Nevertheless, the high MgO conversion (99.9%, Table 4-2) was ascertained from the measured CO production, which confirmed that a high Mg yield was achieved in the reactor. The influence of pressure on Mg yield is noticeable at both AC/MgO molar ratios, especially in zone B (filter). The amount of Mg phase is higher when decreasing pressure, consistently with the higher CO yield in Fig. 4-21, thereby confirming that decreasing pressure favored CO and Mg production.

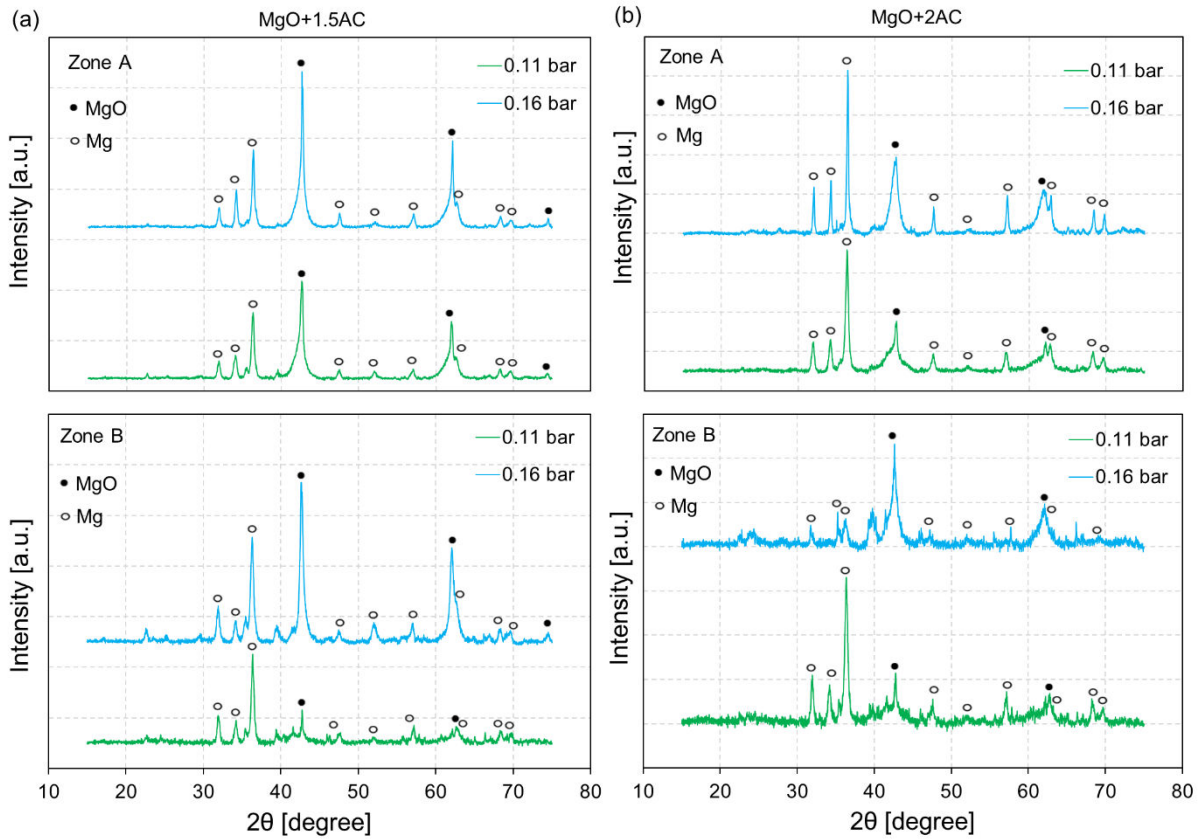

Figure 4-22. XRD patterns of the collected solid products in zone A and zone B for the reduction of MgO with AC at (a) AC/MgO=1.5 and (b) AC/MgO=2.

Regarding the influence of solid carbon type, the XRD patterns of the solid products collected in each zone at both molar ratios were not significantly different between AC and CB (Fig. C-22). However, higher Mg intensity was observed in zone B when compared with zone A. In contrast, very small Mg intensities of the XRD peaks were observed when employing graphite as reducing agent (Fig. C-23), due to the weak reaction rate, in agreement with the low CO yield (Fig. C-14). The XRD patterns between C/MgO=1.5 and C/MgO=2 for both solid carbon types were similar (Figs. C-24 and C-25), denoting that MgO and carbon were sufficiently in contact and confirming the low influence of the C/MgO ratio.

The particle morphology was analyzed by FESEM (Fig. 4-23 at nanoscale and Fig. C-26 at microscale) regarding the condensed solid products in the outlet (zone A) and filter (zone B) for two pressures (0.11 and 0.9 bar) and two solid carbon types (AC and CB). Overall, the condensed Mg was produced as nanoparticles (60−300 nm, Fig. 4-23), with morphology exhibiting spherical shapes arising from the droplet condensation during cooling (Mg melting point: 650°C). The size of condensed Mg from zone A appeared larger than zone B (e.g. Fig. 4-23e compared to Fig. 4-23f). The presence of condensed Mg in zone A was less obvious than in zone B (Fig. 4-23a) because of the oxidation with air issue. The presence of solid carbon and MgO product was also observed in the filter (Fig. 4-23d). Besides, a noticeable increase of the condensed Mg was observed when decreasing pressure to 0.11 bar (Fig. 4-23b compared to Fig. 4-23d). Employing CB as reducing agent resulted in smaller sizes of the produced Mg (Fig. 4-23f).

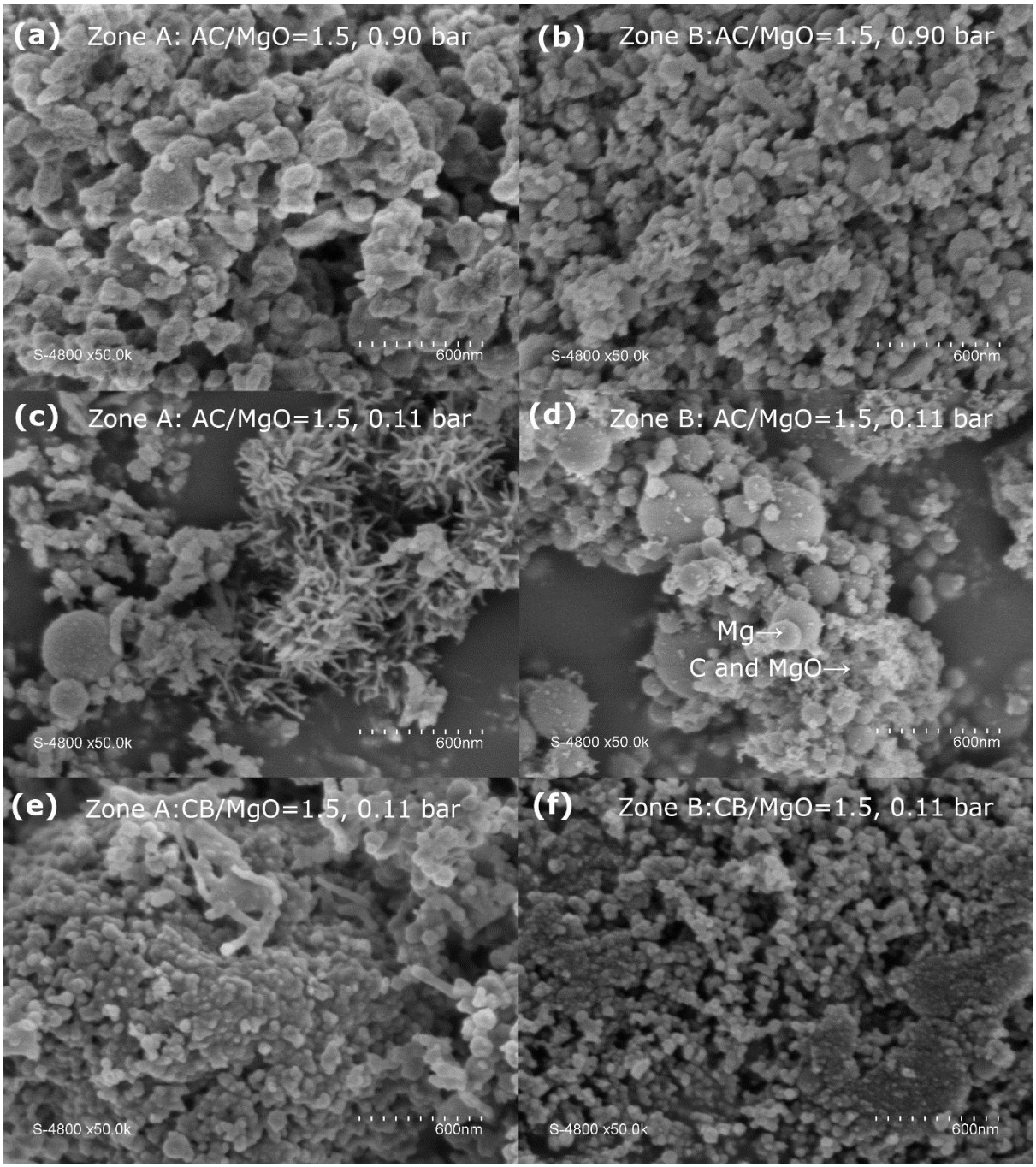

Figure 4-23. SEM micrographs of solid products from the outlet tube (zone A) and filter (zone B) during (a,b) Run No. 3, (c,d) Run No. 1, and (e,f) Run No. 4.

Furthermore, the high reactivity of solar Mg powders with CO_2 was evidenced by TGA, thus demonstrating their high oxidation capability for cycle closure (Figs. C-27 and C-28). The reaction was composed of a fast initial step (about 70% Mg conversion reached after the first 5 min period) followed by a slower reaction regime due to diffusion limitation in the packed powder layer, and complete Mg conversion was achieved at 380°C regardless of the starting Mg material, thus producing additional CO and solid MgO that can be recycled to the solar step.

4.4.2.4 Continuous process demonstration

A proof-of-concept MgO carbothermal reduction experiment was performed to demonstrate the feasibility of solar reactor operation with continuous reactant injection under vacuum and isothermal conditions. A homogeneous mixture of MgO (10 g) and AC (4.5 g) resulting in a C/MgO molar ratio of 1.5 was prepared and then placed into the hopper equipped with a screw feeder (Fig. C-3). The reacting powder was injected through the inlet path exiting into the reactor cavity with a constant feeding-rate of ~0.7 g/min (21 min injection duration) at a constant temperature of 1500 °C, while the pressure was maintained at ~0.11 bar over the entire run. Overall, product gases were produced continuously until finishing injection under isothermal and vacuum conditions (Fig. 4-24). A narrow gap of the stable temperature between T_1 and $T_{pyrometer}$ throughout the test was identified, indicating homogenous reactor cavity temperature and isothermal condition. However, a fluctuating pattern in the CO production rate was observed. This can be attributed to slight particle feeding rate instabilities and to reactant accumulation during injection occurring when the reactant feeding rate was higher than the rate of MgO carbothermal reduction. Noticeably, the experimental duration (25 min) was slightly higher than the expected duration (21 min), thereby confirming the reactant accumulation issue. The CO and CO_2 production rates decreased progressively until reaching zero at the end of reaction, in close agreement with batch tests. After experiment, the amount of unreacted carbon remaining inside the cavity receiver (~1.3 g) corresponded roughly to the excess of fed carbon, and the presence of MgO particles was not observed in the cavity. The CO and CO_2 yields (Run No.9) were compared with those obtained from a batch test (Run No.1) under the same pressure (0.11 bar) and C/MgO molar ratio (1.5), according to Table 4-2. The CO yield was somewhat lower in comparison with a batch test, presumably because of a weak particle entrainment by the gas flow before reacting inside the cavity, thus explaining the slightly lower global MgO conversion. The feasibility of continuous solar Mg production with high yields was evidenced. The energy content of the feedstock (MgO and C) was upgraded by the solar power input in the form of both CO and Mg and a solar-to-fuel energy conversion efficiency of ~8% was achieved with continuous solid reactants injection. The $\eta_{solar\text{-}to\text{-}fuel}$ increased during continuous isothermal operation when compared to batch tests, due to enhanced MgO reduction rate and more efficient utilization of solar energy input. This study is the first solar process demonstration with continuous reactant injection in a high-temperature solar reactor under vacuum operation.

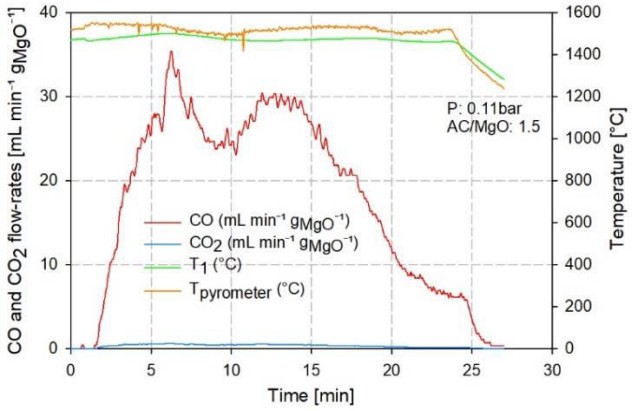

Figure 4-24. CO and CO_2 production rates along with reactor temperatures for MgO reduction with AC with continuous reactant injection under vacuum pressure (P=0.11 bar).

4.5 Conclusion

Solar carbothermal reduction of ZnO and MgO has been performed in a prototype solar reactor with different reducing agents including pure carbons and beech wood biomass in batch and continuous operation modes under vacuum and atmospheric pressures, thus demonstrating flexibility, reliability, and robustness of this scalable metallurgical process for high-purity Zn and Mg production. Gas species production rates, gas yields, metal oxides (ZnO and MgO) conversion, Zn and Mg production yield, and reactor performance have been experimentally evaluated.

Concerning ZnO reduction, batch tests showed that a pressure decrease promoted both the ZnO reduction rate and conversion up to 76.5% at 0.15 bar, thus enhancing Zn production, but CO selectivity was decreased at the expense of higher CO_2 due to the reduction of residence time. Regarding continuous reactant powder injection tests, increasing reactant feeding rate hastened ZnO consumption (ZnO conversion of 47.1% of at 1 g/min and 950 °C). In comparison, batch tests achieved significantly higher reaction extents than continuous tests, with maximum ZnO conversion exceeding 78% and energy upgrade factor up to 1.2. Nevertheless, non-isothermal operation induced higher heat losses, thus downgrading solar-to-fuel conversion efficiency (1.1-1.6%). The ZnO conversion was higher for AC exhibiting larger specific surface area than CB, thus favoring solid-solid reaction. The continuous injection of reactant pellets was considered to alleviate particle entrainment and offer continuous ZnO reduction process at higher temperatures (up to 1350 °C). This approach was proved to be effective to produce high-purity solar-driven metallic Zn whether using pure carbon or biomass as reducing agent. Through the temperature increase in the range of 1100-1350 °C, a remarkable enhancement of gas production rates, yields, ZnO conversion, and CO selectivity with solar-to-fuel energy conversion efficiency up to ~6% was highlighted. Utilizing wood biomass as a reducing agent is an attractive option to produce both metallic Zn and high-quality syngas in a single process. High-purity Zn content exceeding 90%wt with well crystallized structure and micrometric particle size was also achieved. This solar carbothermal metallurgical process can thus be used to produce both metal Zn and high-value syngas by combining biomass gasification with ZnO reduction, thus representing a new promising path towards sustainable solar fuels.

Regarding MgO reduction, solar carbothermal MgO reduction was investigated at temperature up to 1650 °C. Mg production was successfully achieved using different solid and gaseous reducing agents and operating parameters (pressure and C/MgO molar ratio) in continuous and batch modes under atmospheric or vacuum conditions (0.1-0.9 bar). The feasibility of vacuum MgO carbothermal reduction with continuous reactant injection was demonstrated for the first time. Decreasing pressure significantly enhanced the rate of MgO carbothermal reduction, MgO conversion, and CO yield, in agreement with thermodynamics. The highest CO yield (24.59 mmol/g_{MgO}) obtained for activated charcoal at the lowest pressure closely approached the theoretical yield (24.81 mmol/g_{MgO}), demonstrating nearly complete MgO conversion. MgO conversion up to 99.9% was achieved (at P=0.11 bar). High energy upgrade factor (up to 1.9) revealed efficient storage of solar energy into chemical fuels. Utilizing activated charcoal as reducing agent showed the best MgO conversion due to effective solid-to-solid contact (similar to ZnO). No significant impact of excess C/MgO molar ratios

(between 1.5 and 2) on MgO conversion was noticed. Mg product was produced as condensed nanosized particles, which highly favors their reactivity and oxidation when exposed to air (auto-ignition observed at room temperature). The new prototype vacuum reactor is expected to be flexible in processing different carbonaceous feedstocks for both MgO and ZnO reduction in both batch and continuous modes under vacuum condition.

Chapter 5: Solar gasification of biomass combined with carbothermal reduction of ZnO[4]

5.1 Introduction

The possibility of solar carbothermal reduction of ZnO combined with gasification of biomass was presented in Chapter 4. The beech wood served as reducing agent of ZnO, producing high-purity Zn and high-quality syngas. The obtained results motivated interest in combining gasification of biomass with carbothermal reduction of ZnO. In this Chapter, the aim is thus to prove the concept of the combined biomass pyro-gasification and carbo-thermal reduction of ZnO under continuous process operation for co-production of syngas and metallic Zn in a single process. The overall endothermic chemical reaction consisting of combined ZnO carbo-thermal reduction and biomass gasification (with molecular formula assumed as $C_6H_9O_4$) is shown according to Eq. 4-2. The stoichiometric molar ratio of biomass to ZnO is thus 0.5, and the reaction releases not only syngas composed of H_2 and CO, but also lower-valence metal species (Zn). On-sun experiments were carried out in a continuously-fed spouted-bed solar reactor (1.5 kW_{th}). The feasibility of syngas and Zn particles co-production in continuous operation and the influence of temperature and reactant molar ratio on reactor performance are demonstrated.

5.2 Materials and methods

5.2.1 Materials

Two types of beech wood biomass feedstocks with respect to biomass type A ($C_6H_9O_4$) and biomass type D ($C_7H_{11}O_4$) were used as reducing agents for both carbo-thermal ZnO reduction and pyrolysis/gasification experiments (the mass concentration of the main elements in lignocellulosic biomass is shown in Table 3-1 for both types of biomass). ZnO was purchased from PROLABO (chemical purity 99%, particle size 1-5 µm).

5.2.2 Apparatus and procedures

The experimental set-up was previously presented in Chapter 3. The additional details of this reactor for this study are reported here. Reacting samples were prepared by mechanical mixing of ZnO and wood biomass particles with fixed reactant molar ratios (Table D-1 in Appendix D) and were then placed in the hopper. The ZnO particles were homogeneously spread and dispersed at the surface of the biomass particles (as ZnO particle size is much

[4] Details of this chapter consist of one peer-reviewed article:

- S. Chuayboon, S. Abanades, S. Rodat, *Fuel*. 215 (2018) 66–79.

smaller in comparison with biomass), thereby warranting optimal surface-to-surface contact between ZnO and biomass particles. Given the very large discrepancy of particles sizes, the ZnO particles spread and coat uniformly the surface of the wood particles (the dispersion of ZnO at the wood particle surface is simply achieved by mechanical mixing of the powders mixture). Additional experiments consisting of wood biomass pyrolysis (without any oxidant) were carried out to compare with the combined process (with the use of ZnO as an oxidizing agent). Ar was fed into both the window area and the hopper so that residual oxygen was purged. Furthermore, this gas flow protects the glass window from deposits as it carries the ascending products in the downward direction toward the reactor exit. At the same time, the reactor was sucked by the air Venturi pump to remove the oxygen and to control the total pressure in the cavity just above atmospheric pressure (~0.87 bar). Then, the reactor was solar-heated up to the targeted temperature under Ar flow using concentrated sunlight.

Fig. D-1 (in Appendix) represents the temporal evolution of temperatures and cavity pressure in the solar reactor during the heating phase. The temperature started to increase continuously from the ambient temperature to the targeted temperature, while the cavity pressure first remained constant and then increased slightly during the reactant injection. In order to reach the high temperature smoothly and to avoid thermal shocks, a shutter (4 m^2) settled between the heliostat and the reactor was periodically and gradually opened. The desired steady-state temperature was reached after about 45 minutes, and the solid reactants were subsequently injected into the cavity in a continuous mode (at a biomass injection rate of ~2 g/min) for 10 minutes. Because of the required energy to heat reactants and to carry out the endothermic reaction, the temperature decreased slightly (30-50ºC) after the start of injection. Therefore, the shutter opening was increased slightly to balance the energy consumption by the reaction and to hold in the operating temperature. As a result, the temperature rose rapidly in a few minutes and was then stable again throughout the experiment. T_3 was slightly affected by some of the particles falling on it during injection, but isothermal experiments were fairly achieved. The homogeneous temperature inside the cavity was confirmed by a narrow gap between T_1 and T_3, which was also confirmed by the pyrometer measurement. Syngas products exited the reactor along with Zn particles and then flowed into the filter.

After completing the reactant injection, all the temperatures decreased rapidly due to the shutter being closed. Next, the solid residues collected in the different parts of the outlet system (composed of an alumina tube (deposit A), a long-steel tube (deposit B), and a filter (deposit C), Fig. D-2) were weighted for mass balance and then analyzed by X-ray diffraction (XRD) for phase identification and quantification.

5.3 Experimental results

5.3.1 Influence of temperature and type of biomass

The effect of temperature on syngas composition during combined gasification of biomass and carbo-thermal reduction of ZnO was studied and compared with the pyrolysis process. The temperatures (referred by T_3) of 1050ºC, 1100ºC, 1150ºC, 1200ºC, 1250°C and 1300ºC were considered for the biomass/ZnO molar ratio of 1 and the temperatures of 1100°C, 1200ºC, 1300°C and 1350ºC for the pyrolysis process, according to Table D-1 and Fig. 5-1. The syngas

flow-rate evolution is dependent on the temperature. The total amount of gas produced during each run was obtained from time integration of the gas flow-rates. The averaged mole fraction of the produced syngas over the entire duration of each experiment is represented in Fig. 5-2. In order to check the reproducibility of the results, pyrolysis was completed twice at 1300ºC using the same condition (Run No. 10 and 11).

Both the H_2 and CO flow-rates increased when increasing the temperature for both the combined gasification/carbo-thermal reduction (biomass/ZnO) and the pyrolysis (biomass only), but the H_2 and CO flow-rates were significantly lowered for pyrolysis when compared with combined gasification/carbo-thermal reduction. The flow-rates of CO_2 and CH_4 decreased markedly when increasing the temperature. Moreover, the CO_2 and CH_4 flow rates for pyrolysis were lower than for combined gasification/carbo-thermal reduction.

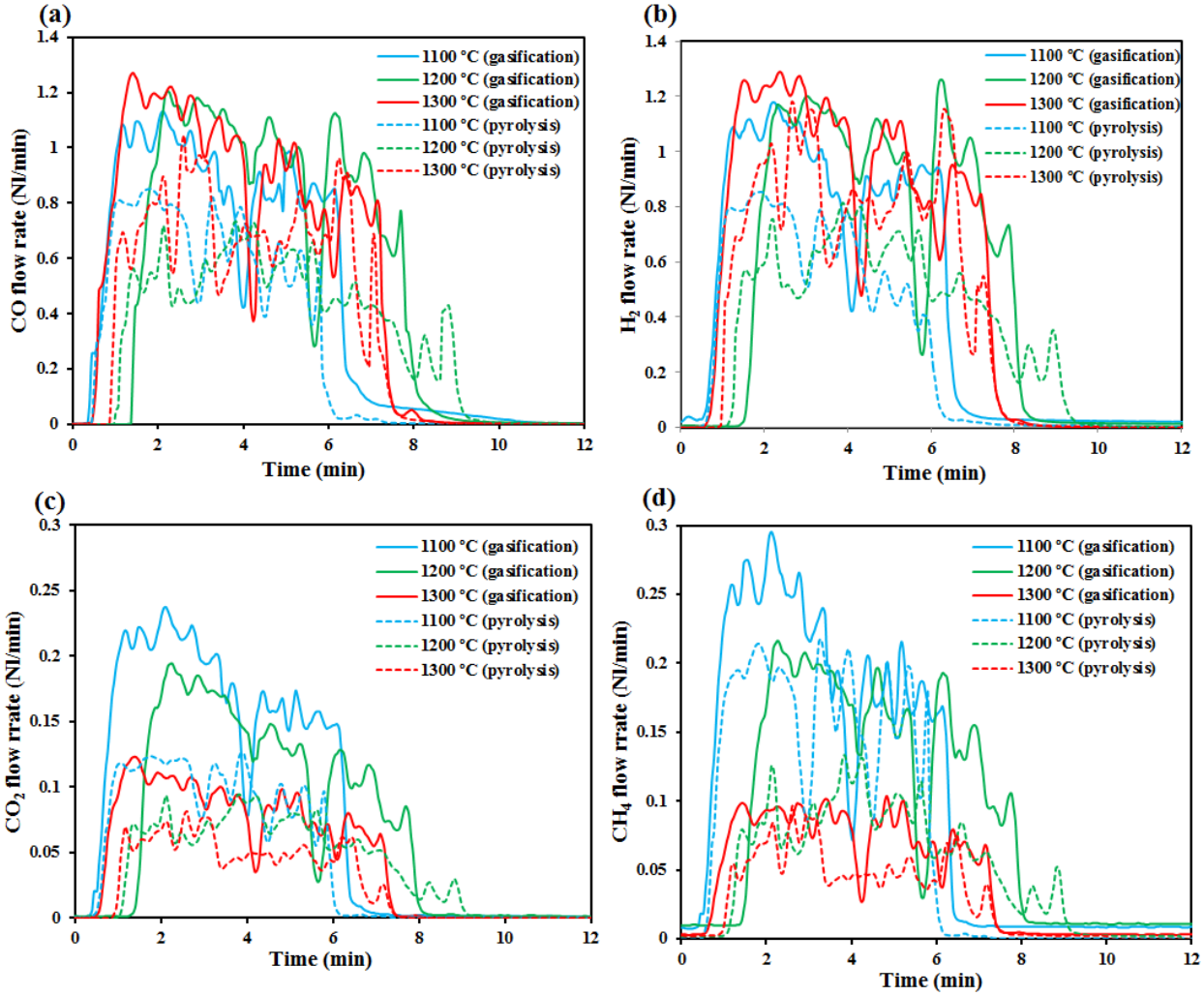

Figure 5-1. Temperature influence on (a) CO, (b) H2, (c) CO2, and (d) CH4 flow rates for combined gasification/carbo-thermal reduction (biomass/ZnO molar ratio of 1) and pyrolysis process.

Fig. 5-2 shows that the global mole fraction of H_2 in the produced syngas increased significantly when increasing the temperature, while the mole fraction of CO_2 and CH_4 decreased moderately. CO mole fraction increased slightly between 1050°C and 1300°C.

Concerning the pyrolysis process, a significant increase of the H_2 mole fraction was noticed when increasing the temperature, whereas a slight decrease of CO_2 and CH_4 was observed. The temperature influence on CO was not clear because its proportion remained quite stable from 1100ºC (Run No.8) to 1350ºC (Run No.13).

The decrease in the amount of CH_4 when increasing the temperature for both the gasification/ carbo- thermal reduction and pyrolysis can be evidenced by equilibrium gas composition. According to thermodynamics, CH_4 formation is not favored when increasing temperature [14]. Noticeably, the syngas composition produced at the highest temperature is near of the thermodynamic equilibrium.

In comparison with pyrolysis at 1100 ºC (Run No.2 and 8), the CO and CH_4 mole fraction produced by combined gasification/ carbo- thermal reduction was quite similar, CO_2 was moderately higher, while the H_2 mole fraction was slightly lower. Conversely, the mole fraction of CH_4, CO, and CO_2 produced by combined gasification/ carbo- thermal reduction compared to pyrolysis at 1200ºC (Run No. 4 and 9) and 1300ºC (Run No. 7 and 10) was moderately higher, whereas the H_2 mole fraction was considerably lower. The lower H_2 mole fraction can be attributed to its possible partial consumption by the reaction with ZnO ($ZnO+H_2 \rightarrow Zn+H_2O$). Concomitantly, H_2, CO, and CH_4 formation potentially favored the reduction of ZnO, but H_2 was shown to be the most consumed specie during ZnO reduction as its amount was reduced when compared with the pyrolysis process.

Regarding the effect of different types of biomass, the syngas mole fraction was different in the case of the combined gasification/carbo-thermal reduction (Run No. 4 and No. 5 at 1200°C) because of the different size of biomass particles. Syngas production was thus sensitive to initial biomass particle size because the biomass serves as a support for the ZnO particles. Lower initial particle size favors contact between reactants thanks to enhanced ZnO dispersion on a larger surface and promotes solid/ solid reactions, thereby increasing both H_2 and CO production. In contrast, there was a slight difference in the syngas mole fraction for pyrolysis (Run No. 11 and No. 12 at 1300°C).

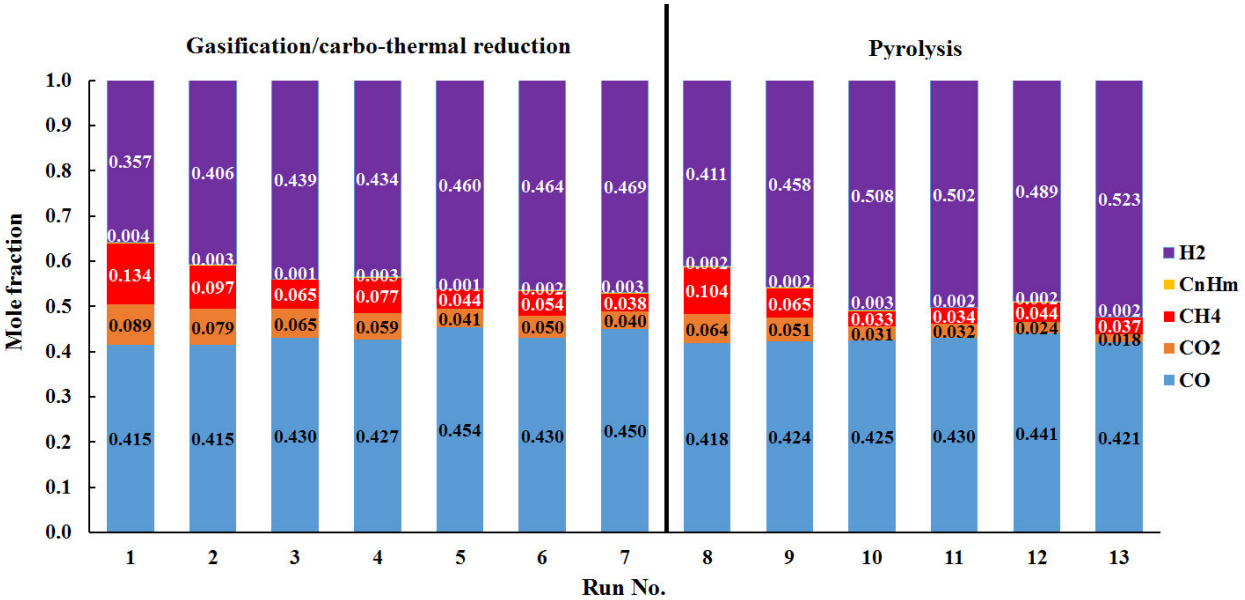

Figure 5-2. Averaged syngas composition for combined gasification/carbo-thermal reduction (biomass/ZnO molar ratio of 1) and pyrolysis as a function of temperature (Ar not included).

The total yield of syngas production ($mole_{syngas}$/ $mole_{biomass}$) for the combined gasification/carbo-thermal reduction (Run No.1-7) is not directly correlated to the temperature, although higher temperatures tend to increase the amount of H_2 and CO and to decrease the amount of CH_4 (Fig. 5-3). In contrast, the total yield of syngas produced by pyrolysis increased significantly when increasing the temperature. Nevertheless, the syngas yield of the combined gasification/carbo-thermal reduction was much higher in comparison with pyrolysis at the temperatures of 1100ºC (Run No. 2 compared to Run No 8), 1200ºC (Run No. 4 compared to Run No 9), and 1300ºC (Run No. 7 compared to Run No 10) because of the higher H_2, CO, CO_2, and CH_4 yield resulting from char gasification. Therefore, the gasification process is more advantageous as it produces more syngas output per unit of feedstock than the pyrolysis process at a given temperature.

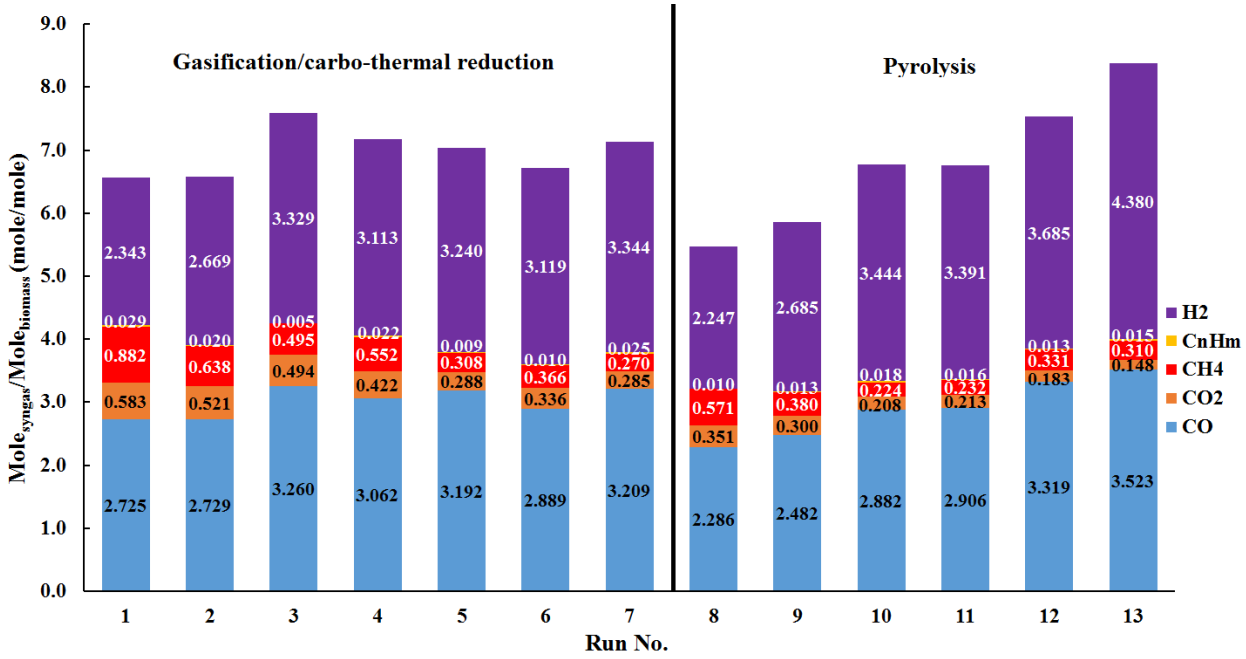

Figure 5-3. Averaged syngas yield (mole syngas/mole biomass) for combined gasification/carbo-thermal reduction (biomass/ZnO molar ratio of 1) and pyrolysis at various temperatures.

5.3.2 Influence of biomass/ZnO molar ratio

The influence of biomass/ZnO molar ratio (0.5, 0.75, and 1) on syngas production was studied at 1100ºC. Fig. 5-4 depicts the evolution of H_2, CO, CO, and CH_4 flow-rates at the various molar ratios. Indications about the optimum of syngas production was found at the biomass/ZnO molar ratio of 0.75 in regard to the highest mole fraction of H_2 and CO and the lowest mole fraction of CH_4 and CO_2, according to Fig. 5-5. For these reasons, an excess of biomass with respect to the stoichiometry (stoichiometric biomass/ZnO molar ratio is 0.5) should be necessary in order to favor syngas production (both H_2 and CO) and complete conversion of the ZnO.

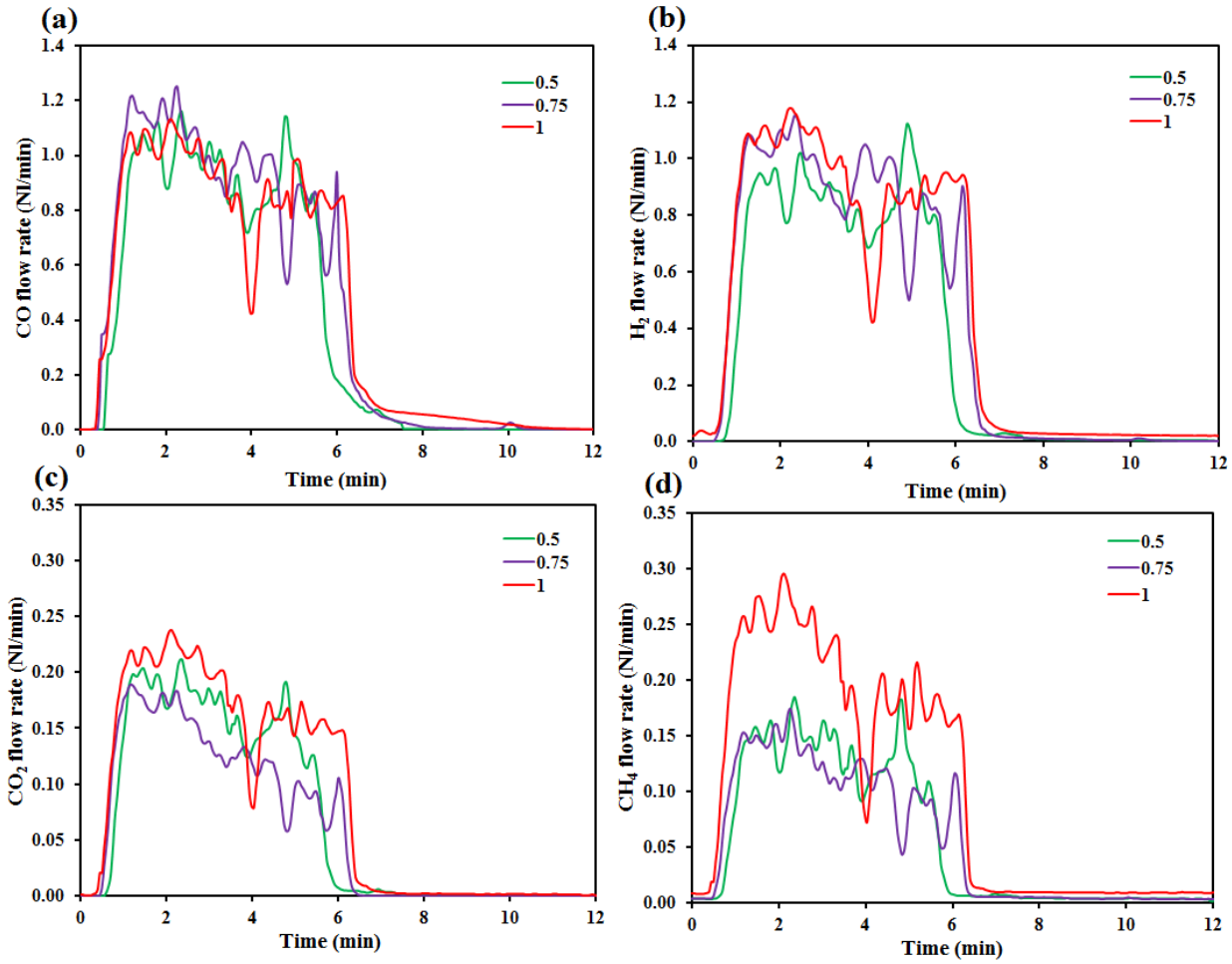

Figure 5-4. Influence of biomass/ZnO molar ratio on (a) CO, (b) H_2, (c) CO_2, and (d) CH_4 flow rates for combined gasification/carbo-thermal reduction at 1100°C.

In addition, the yield of syngas production at the biomass/ZnO molar ratio of 0.75 was also higher in comparison with the biomass/ZnO molar ratio of 1 (Fig 5-6). This trend means an optimum ratio between 0.5 and 1 exists in order to favor both complete consumption of the injected ZnO and complete conversion of the char resulting from pyrolysis. In other words, insufficient amount of biomass with respect to ZnO results in incomplete ZnO conversion, whereas insufficient amount of ZnO with respect to biomass results in lowered syngas production due to incomplete char conversion. Hence, a biomass/ZnO mole ratio of 0.75 was a good compromise to favor both complete consumption of the fed ZnO and high syngas output per unit of feedstock.

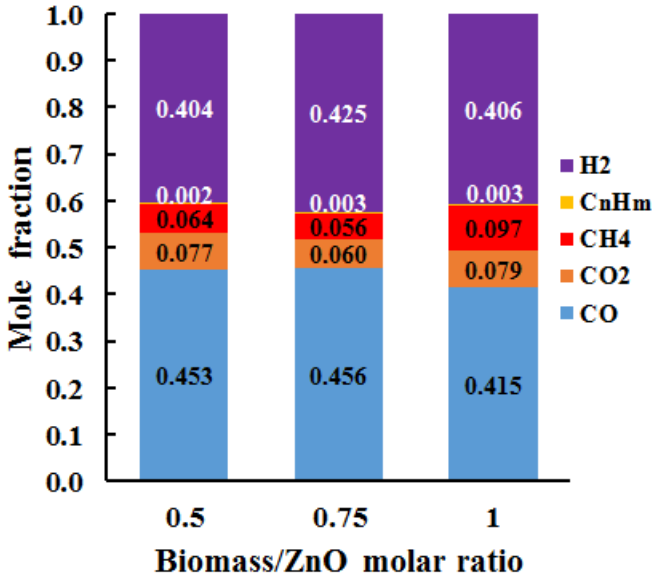

Figure 5-5. Averaged syngas composition for combined gasification/carbo-thermal reduction as a function of biomass/ZnO molar ratio at 1100°C (Ar not included).

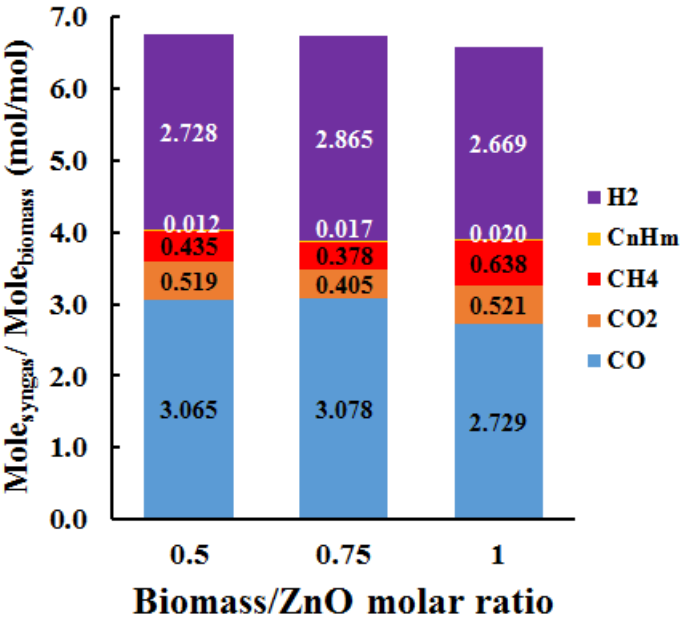

Figure 5-6. Averaged syngas yield for combined gasification/carbo-thermal reduction as a function of biomass/ZnO molar ratio at 1100°C

5.3.3 Solar reactor performance assessment

Experiments were carried out to evaluate the potential of the reactor during continuous operation. Table 5-1 summarizes the experimental results and performance indicators during continuous runs. The mass conversion rate is defined as the ratio of net output (products) to net input (reactant mixture), and the carbon conversion rate is defined as the ratio of carbon contained in the syngas products to carbon contained in fed biomass. The gas residence time represents the average duration that the gas needs to sweep the cavity volume at the actual reactor temperature.

Table 5-1. Experimental results and performance indicators of the solar reactor during continuous operation.

Run No.	Types of Biomass	Temperature (°C)	Solar input (kW)	Biomass/ZnO molar ratio	Gas residence time (s)	Mass conversion rate (%)	Carbon conversion rate (%)	U	η_{Solar} (%)
1	type A	1050	0.89	1	0.562	84.9	80.4	1.04	19.5
2	type A	1100	0.92	1	0.546	90.1	74.3	0.98	17.2
3	type A	1150	1.10	1	0.712	91.3	80.2	1.06	11.2
4	type A	1200	1.21	1	0.504	80.1	77.1	1.04	15.4
5	type D	1200	1.14	1	0.660	84.4	67.2	0.98	11.5
6	type A	1250	1.42	1	0.471	84.3	68.1	0.95	18.9
7	type A	1300	1.51	1	0.408	83.3	72.2	0.99	15.4
8	type A	1100	0.91	-	0.618	79.6	60.9	0.71	13.0
9	type A	1200	1.13	-	0.786	80.4	60.1	0.72	12.4
10	type A	1300	1.45	-	0.706	84.6	63.2	0.80	12.8
11	type A	1300	1.43	-	0.680	85.4	63.9	0.80	12.9
12	type D	1300	1.48	-	0.734	93.9	68.2	0.91	11.2
13	type A	1350	1.50	-	0.661	92.8	75.7	1.0	16.0
14	type A	1100	0.89	0.5	0.629	81.5	76.3	1.07	19.9
15	type A	1100	0.94	0.75	0.562	85.5	73.6	1.01	19.2
16	type A	1250	1.37	0.75	0.484	93.8	85.1	1.17	19.8

5.3.4 Material mass balance

The material mass balance was performed to quantify the amount of reactant actually converted into the products, which are syngas productions, Zn deposits and solid residues. The overview of the mass balance for biomass/ZnO molar ratios of 0.75 and 1 at 1250ºC is shown in Tables D-2 and D-3, respectively.

Noticeably, the solid carbon remaining in the cavity after the reaction was not fully recovered and was roughly quantified, which affects the global mass balance and explains to a large extent the lower mass output with respect to the input, as well as the incomplete carbon conversion rate. Furthermore, it must be noticed that the steam was not analyzed at the outlet and a part of the moisture initially contained in the biomass (content of ~9 wt%, Table 3-1) may exit the reactor, and it is thus omitted in the mass balance. Regarding the carbon conversion rate (Table 5-1), it is generally higher for the gasification because most of the chars are converted to syngas, in contrast to pyrolysis.

For a stoichiometric biomass/ZnO ratio (Run No. 14), the remaining solid particles inside the cavity were composed of char along with a significant amount of unreacted ZnO (Fig. D-3), because of insufficient particle mixing and incomplete ZnO conversion. This confirms that an excess of biomass with respect to stoichiometry is required to convert the whole ZnO particles. Complete ZnO conversion was achieved for biomass/ZnO molar ratio of 0.75 and 1 (excess of biomass with respect to ZnO) with only char remaining inside the cavity after the reaction. Similarly, incomplete ZnO conversion was observed for the run at the lowest temperature (Run No. 1).

5.3.5 Cold gas and energy conversion efficiencies

The cold gas efficiency (energy upgrade factor) represents the ratio of the energy content of the chemical products to the calorific value of the biomass feedstock. It quantifies the fraction of solar energy stored in the reaction products (both syngas and Zn), according to Eq.4-8. Note that the energy content of the char by-product remaining in the cavity was not taken into account in the calculation.

The energy upgrade factor is higher than 1 when the energy content of the products is higher than the energy content of the feedstock, which means that solar energy has been stored in the reaction products. The highest cold gas efficiency reached 1.17 at 1250°C for the biomass/ZnO molar ratio of 0.75 (Run No. 16), thereby approaching the theoretical cold gas efficiency (1.31) attained at the thermodynamic equilibrium according to Eq. 4-2 (theoretically reached above 1000 °C). It was generally close to or above 1 for biomass gasification with ZnO, confirming solar energy storage. In contrast, pyrolysis showed values below 1, because of the high-energy content still contained in the unconverted char product. Pyrolysis is thus not suitable to solar up-grade the calorific value of the feedstock in the form of syngas. This confirms that the addition of ZnO is energetically beneficial since it consumes part of the char by-product to produce Zn, thereby contributing to solar energy storage into solid metal products with high energy density.

In order to assess how well solar energy is used as the energy source for thermochemical processes, the solar-to-fuel energy conversion efficiency was estimated according to Eq.4-9. Solar-to-fuel energy conversion efficiencies of up to ~15-20% were estimated for the combined biomass/ZnO gasification.

The total yield of syngas was up to 8.1 $mol_{syngas}/mol_{biomass}$ (Run No.16, 43.2% CO, 44.4% H_2, 6.1% CO_2 and 6.0% CH_4, with total heating value of 186 kJ), while the theoretical yield of syngas obtained from the thermodynamic equilibrium (Eq. 4-2) was 10.5 $mol_{syngas}/mol_{biomass}$ (57.1% CO and 42.9% H_2). The evolution of syngas flow-rates for Run No. 16 leading to the best performance is depicted in Fig. D-4. Furthermore, the gas flow-rates produced during the combined gasification/carbo-thermal reduction were considerably higher in comparison to pyrolysis (Figs. 5-7, 5-8, and 5-9). These results are confirmed by the comparison of syngas yields in Fig. 5-3 (Run No. 2 compared to Run No.8, Run No. 4 compared to Run No. 9, and Run No.7 compared to Run No.10). The effect of ZnO addition as a gasifying agent promoting syngas production is thus evidenced.

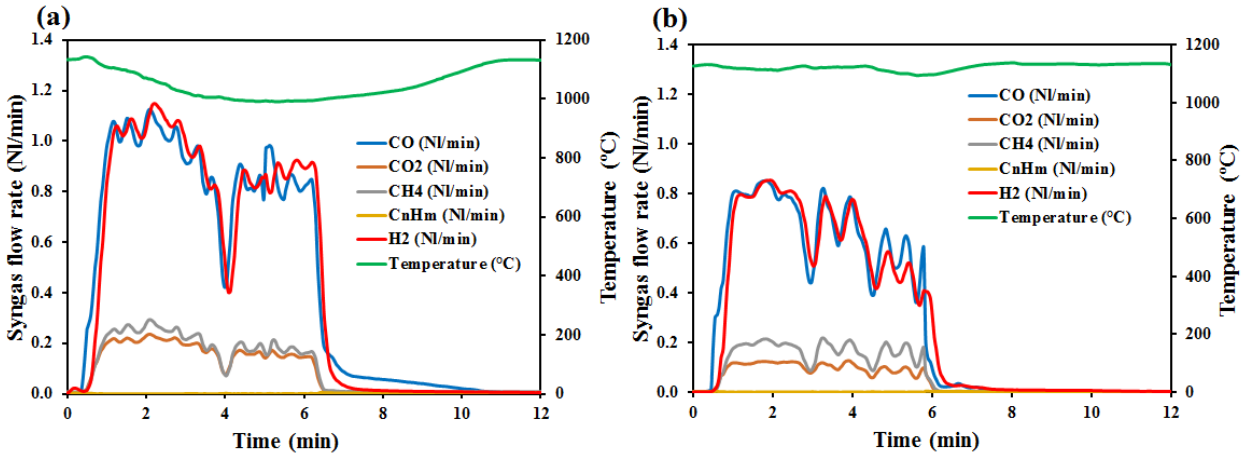

Figure 5-7. Syngas flow rates for (a) biomass/ZnO molar ratio of 1 and (b) pyrolysis during a continuous experiment at 1100°C.

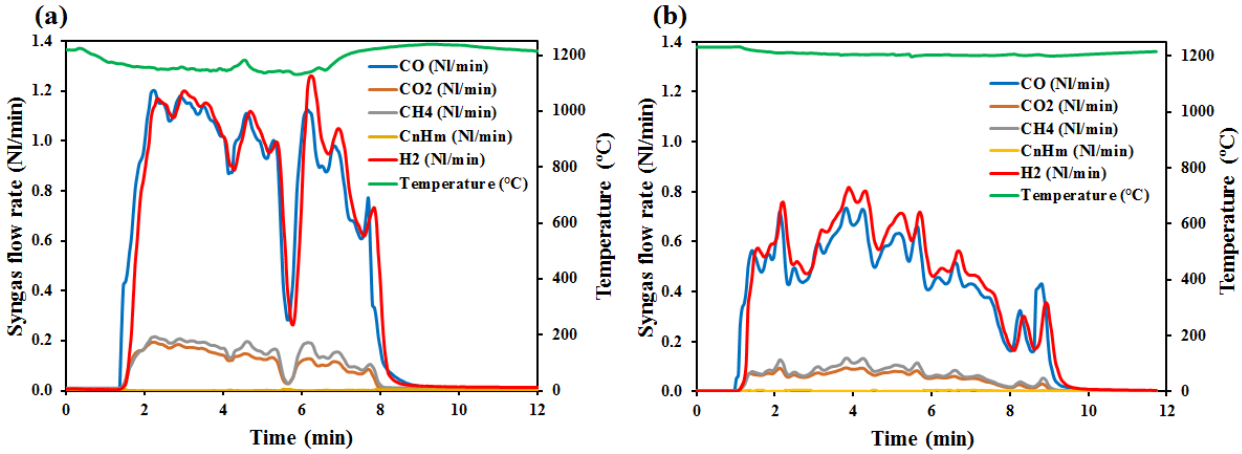

Figure 5-8. Syngas flow rates for (a) biomass/ZnO molar ratio of 1 and (b) pyrolysis during a continuous experiment at 1200°C.

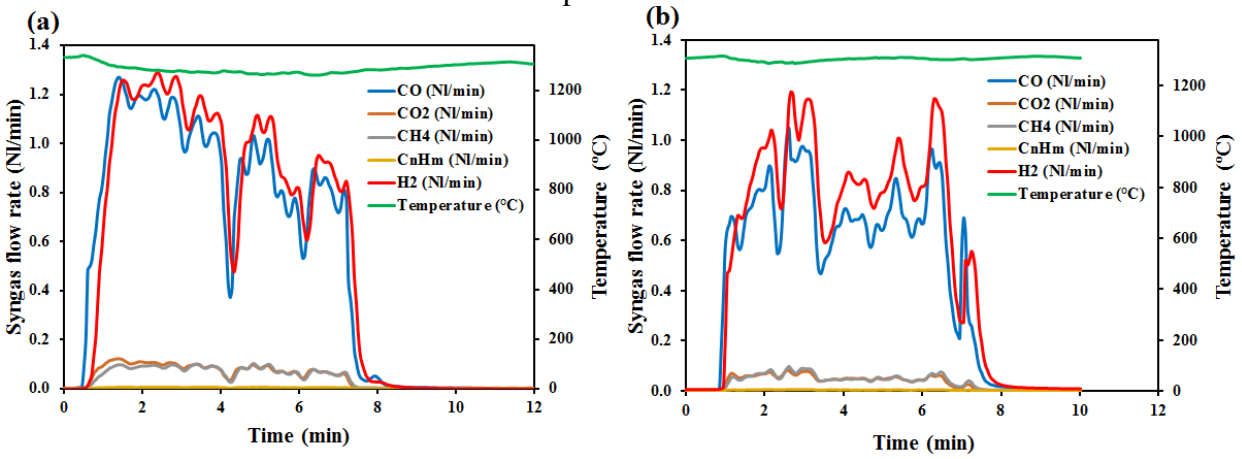

Figure 5-9. Syngas flow rates for (a) biomass/ZnO molar ratio of 1 and (b) pyrolysis during a continuous experiment at 1300°C.

5.3.6 Characterization of Zn products

Solid products were collected after each experiment. In order to analyze separately the samples, three zones of the solid products collection were defined: (i) zone A corresponds to the outlet alumina tube, (ii) zone B corresponds to the stainless-steel tube connected between the alumina tube and the filter, (iii) zone C corresponds to the filter (Fig. D-2). In addition, the remaining particles inside the cavity of the reactor consisting mainly of char and/or unreacted ZnO were also collected.

The different removable components of the reactor in which the deposits occurred were weighed before and after the experiments to quantify the amount of solid product in each component (Table 5-2).

Table 5-2. Amount of the solid deposits in each zone of the reactor.

Residue	Run No.									
	1	2	3	4	5	6	7	14	15	16
Zone A (g)	2.00	1.60	2.48	1.70	2.40	1.70	2.55	3.10	3.10	2.00
Zone B (g)	2.40	3.20	2.20	1.70	1.90	3.50	1.90	2.40	2.2	4.00
Zone C (g)	1.50	3.00	1.90	1.90	1.80	1.80	1.60	2.40	2.60	1.90
Remainder inside cavity	0.30	0.20	0.40	0.10	0.10	0.30	0.5	NA	NA	0.20
Total	6.20	8.00	6.98	5.40	6.20	7.30	6.55	7.90	7.90	8.10

After collecting Zn products from the outlet components, the Zn/ZnO composition was characterized via calibrated XRD for phase identification and quantitative analysis (Fig. C-8), and the powder morphology was investigated using scanning electron microscopy (SEM).

Fig. 5-10 shows XRD patterns for commercial Zn and the solid products collected at the biomass/ZnO molar ratio of 1 for different operating temperatures. The powder collected inside the reactor cavity is pure carbon (amorphous), except at 1100°C (Run N°2) that shows a very small amount of ZnO remaining in the collected char (Fig. 5-10a). This is consistent with the temperature influence on the reaction conversion. In addition, a biomass/ZnO molar ratio of 1 resulted in only char remaining inside the cavity (Fig. D-5).

Traces of recombined ZnO were only evidenced in zone A according to Fig. 5-10b. This low recombination is mainly located in the first part of the alumina tube where Zn condenses and possibly oxidizes with CO_2 and/or H_2O, forming a hard deposit of ZnO in a well precise zone of ~1 cm long where the clogging occurred (corresponding to the zone of the transition temperature of Zn(g)-Zn(l)). Recombined ZnO can be likely explained by the reaction of Zn with either moisture from the biomass or H_2O/CO_2 produced from gasification reactions.

Fig. 5-10c and 5-10d confirms that the samples collected from zone B and C consist of pure Zn. These results thus demonstrate that the reactor can efficiently be used for producing both Zn and syngas under continuous process operation.

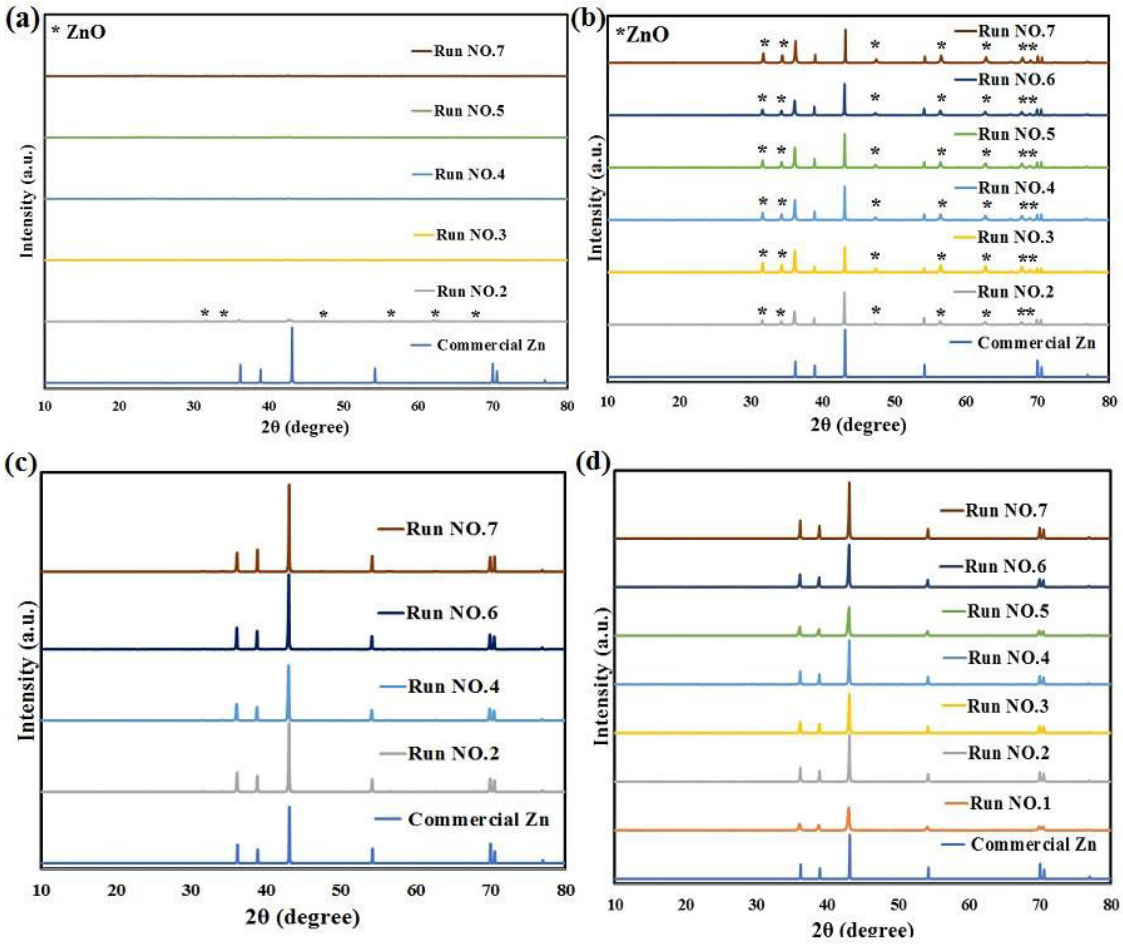

Figure 5-10. Representative XRD patterns of products collected from (a) cavity, (b) zone A, (c) zone B, and (d) zone C (biomass/ZnO molar ratio of 1).

XRD patterns regarding the influence of biomass/ZnO ratio on samples composition collected in zones A and C are showed in Fig. D-6. The lowest ZnO recombination was evidenced at biomass/ZnO molar ratio of 0.5, possibly due to an incomplete reaction (low amount of CO_2 and/or H_2O produced from gasification). The powders collected in the filter (zone C) are composed of Zn only without any trace of ZnO contamination.

XRD patterns of the solid products obtained at the optimal condition leading to the highest reactor performance are presented in Fig. D-7. The particles collected from the zones B and C were not contaminated by ZnO, while low recombination to ZnO was only found in the zone A. In spite of having recombined ZnO in this zone, the amount of solid product was lower compared with zone B and C containing pure Zn (25% of the total as seen in Table D-2). The Zn mass fractions of the powders collected in the alumina tube (zone A) were estimated by quantitative XRD analysis (Fig. 5-11). High Zn contents were evidenced supporting the low recombination to ZnO in zone A (~80% of average Zn mass fraction was achieved). As previously mentioned, pure Zn was obtained in zones B and C. In addition to Zn, the collected samples also contained a fraction of carbon that was entrained by gas flow (the carbon content was quantified precisely as described in the Table D-4).

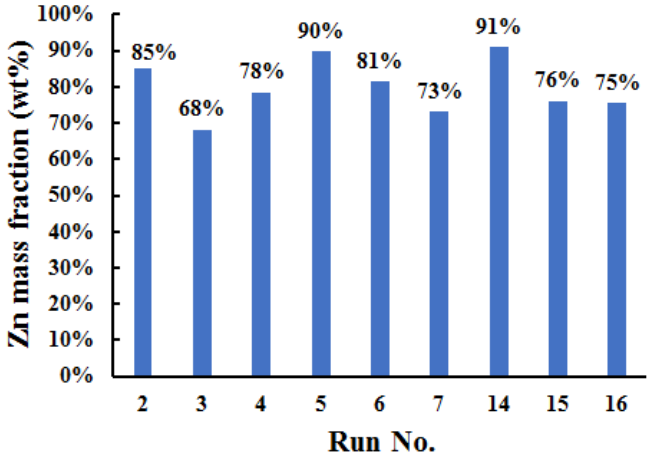

Figure 5-11. Weight fractions of Zn calculated from calibrated XRD (Fig. C-8) for the solid products collected in zone A.

The mean crystallite size of the solid products in each zone was calculated by Scherrer's equation (Fig. D-8). The largest crystallite size of Zn ranged from 120 to 160 nm and was found in zone A where products exited from the reactor. The crystallite size decreased in the range 85 to 121 nm in zone B, and 43 to 100 nm in zone C, while the size of ZnO crystallites in zone A ranged from 57 to 67 nm. Besides, most of the crystallite sizes (zones A, B, and C) are closely consistent with the SEM observations.

Fig. 5-12a and 5-12b shows SEM images of carbon remaining inside the cavity. The products collected from the alumina tube (Fig. 5-12c and 5-12d) mainly consisted of small dispersed spherical nanoparticles of Zn as well as recombined ZnO. In Fig. 5-12e and 5-12f, the powders collected from the stainless tube are composed of pure Zn nanoparticles (as confirmed by XRD), including also some carbon contamination. Likewise, the morphology of the powder collected from the filter is similar (Fig.5-12g and 5-12h), denoting the presence of agglomerates of condensed Zn nanoparticles contaminated by a small amount of carbon product.

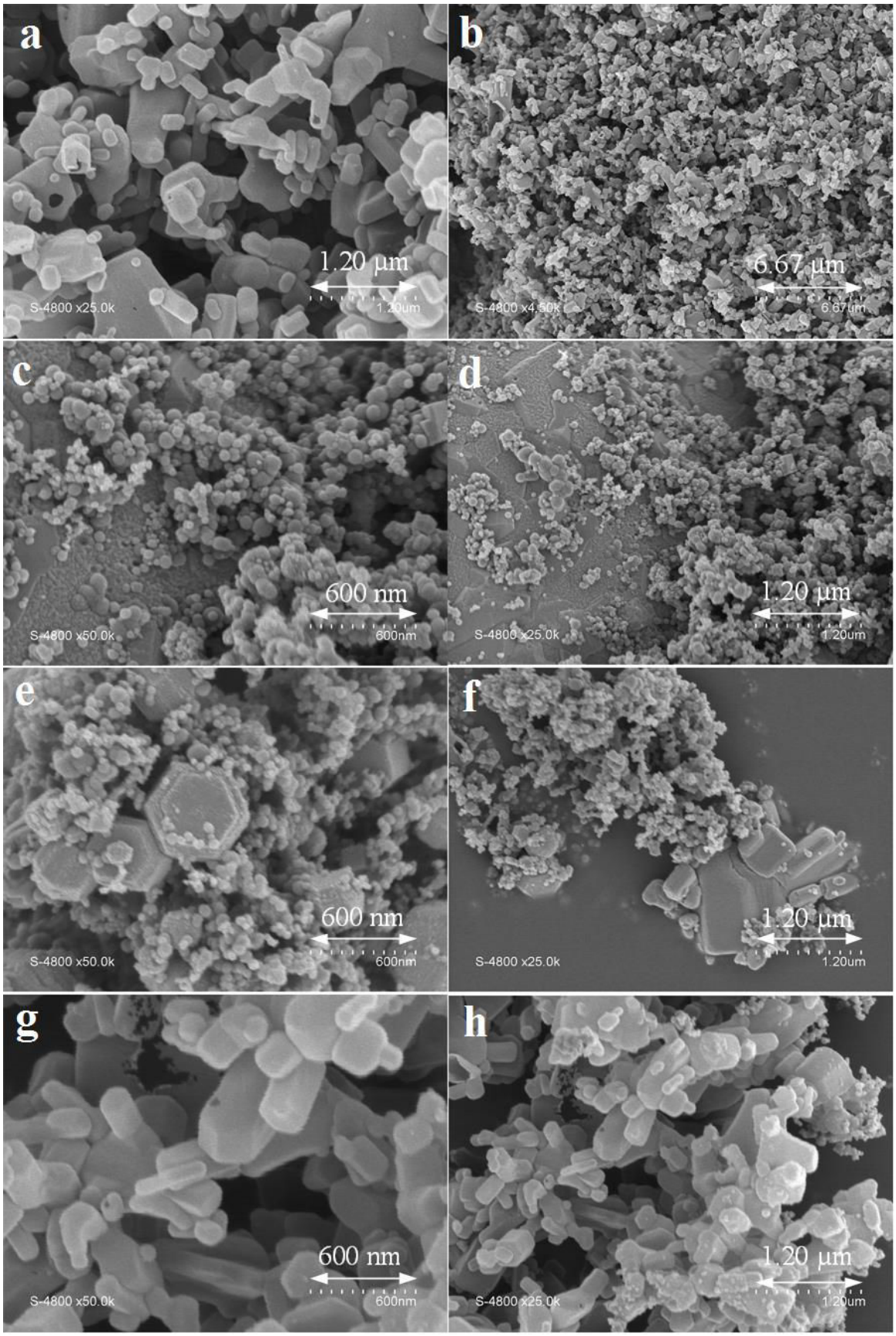

Figure 5-12. SEM micrographs of (a, b) powder in the cavity, (c, d) products in the alumina tube (zone A), (e, f) products in the stainless tube (zone B), and (g, h) products in the filter (zone C).

5.4 Conclusion

The feasibility of gasification of biomass with the ZnO/Zn redox system in a continuously-fed solar reactor was successfully demonstrated for the first time. The solar process produced both synthesis gas and Zn from the combined biomass gasification/carbo-thermal reduction of ZnO. These reactions proceeded endothermically at moderate temperatures from 1050°C to 1300°C, which can be reasonably achieved in large-scale solar concentrating systems. The temperature of Zn production was thus much reduced when compared with that required for ZnO thermal dissociation. Moreover, efficient solar energy storage into the reaction products (both syngas and Zn) was evidenced from the energy upgrade factor estimation. The influence of temperature, type of biomass and biomass/ZnO molar ratios, on the reactor performance was also investigated, and the benefits of the combined gasification/carbo-thermal reduction process over a pyrolysis process (without any oxidant) were emphasized. Such pyrolysis process was shown to be not energetically efficient for up-grading the solar power input into syngas because of the unconverted remaining char. The efficient conversion of biomass to syngas using ZnO as a gasifying agent was evidenced by global mass balance and carbon conversion rate assessment. An excess of biomass with respect to reaction stoichiometry is necessary to warrant complete ZnO conversion. A suitable biomass/ZnO molar ratio of 0.75 was highlighted, yielding maximum syngas production and energy conversion efficiencies at 1250°C, while production of pure Zn was achieved. The produced Zn particles can be further processed in a subsequent H_2O/CO_2 splitting step in order to form additional H_2/CO and ZnO that is recycled to the first step, thus closing the chemical looping process. The developed continuous solar reactor could be scaled-up in a next step and further applied to the novel combined process presented here, consisting of solar gasification of carbonaceous feedstock using various types of solid metal oxides.

General conclusion and perspectives

Solar thermochemical processes offer environmentally friendly and attractive avenues to convert gaseous and solid carbonaceous feedstocks to synthesis gas (syngas) and to further produce metals products from their corresponding metal oxides. The produced syngas can be catalytically converted to gaseous or liquid hydrocarbon fuels such as H_2 (via water-gas shift reaction) and diesel/kerosene (via Fischer-Tropsch synthesis), while the produced metals can be used as metal commodities. This work focused on the experimental investigation of three key solar thermochemical approaches with respect to gasification of biomass, chemical looping reforming of methane (CLRM), and carbothermal reduction (CTR) of metal oxides (ZnO and MgO). Gasification and CLRM were applied to convert solid and gaseous carbonaceous feedstocks (wood biomass and methane) into syngas, while CTR was applied to produce metals from ZnO and MgO. The influence of controlling parameters of the considered pathways on the reaction mechanism, conversion, yields, process performance, and on-sun testing behavior was experimentally investigated and evaluated. The experimental study was performed in 1.5 kW_{th} prototype solar chemical reactors consisting of spouted bed and high-temperature cavity-type solar reactors, utilizing highly concentrated sunlight provided by a solar concentrating system at PROMES laboratory, Odeillo, France. The spouted bed solar reactor with continuous particle injection was used for the solar biomass gasification and combined biomass gasification/CTR of ZnO and further adapted with fixed reactive solid oxide structure for the CLRM process, while the high-temperature cavity-type solar reactor was used for the CTR of both ZnO and MgO in batch and continuous operation under vacuum and atmospheric pressures. Overall, such solar-driven processes allow for improvements of conversion yields, elimination of feedstock combustion and associated CO_2 emissions, and storage of intermittent solar energy in storable and transportable chemical fuels, thereby outperforming the conventional processes. In addition, their feasibility, reliability, and robustness in converting both gaseous and solid carbonaceous feedstocks to syngas and producing metals in solar reactors in batch and continuous modes during on-sun testing were successfully demonstrated. In summary, the experimental demonstration of each thermochemical process was addressed as follows:

The first investigated process is the solar CLRM through non-volatile oxides including ceria (CeO_2) and iron (Fe_2O_3) oxides. Fifty-five on-sun cycling conditions were carried out via two-step redox cycling encompassing endothermic CeO_2 or Fe_2O_3 reduction with methane (partial oxidation of methane) and exothermic oxidation of reduced metal oxides with H_2O/CO_2 at the same operating temperature, demonstrating the capability to operate the cycle isothermally. The influence of metal oxides macrostructure (packed powder, packed powder mixed with inert Al_2O_3 particles, and reticulated porous foam), oxidants variants (H_2O and CO_2), methane flow-rates (0.1-0.4 NL/min), reduction temperatures (900-1150 °C), sintering temperatures of metal oxide structure (1000-1400 °C) on the syngas production rate, syngas yield, bed-averaged oxygen non-stoichiometry (δ), methane conversion (X_{CH4}), and solar reactor performance (energy efficiencies) was evidenced. The metal oxides cycling stability

was also demonstrated. Iron oxide reduction with methane is strongly dependent on temperature and displays relatively lower reaction rate than CeO_2. The reduced iron (Fe) is not completely re-oxidized to iron oxide (Fe_3O_4) after water-splitting step because of its low thermal stability resulting in strong sintering and agglomeration, leading to material deactivation. Employing Fe_2O_3 as oxygen carrier is thus not suitable for solar CLRM, but iron oxide reduction with methane could be an alternative option for solar metallurgy aiming at producing both metallic iron and syngas. In contrast, cerium oxide exhibits fast reaction rate and stable syngas yield with H_2/CO molar ratios approaching two over several repeated cycles, demonstrating complete ceria oxidation with either H_2O or CO_2. Successive ceria redox cycles with stable patterns in δ, syngas production yield, and reactor performance validated material stability. A decrease in sintering temperature of the ceria foam results in an increase in syngas selectivity, methane conversion, and reactor performance, at the expense of structure embrittlement. The increase of both the methane flowrate and reduction temperature promotes δ up to 0.41, in turn leading to a substantial enhancement in the syngas yields (up to 8.08 mmol/g_{CeO2}) but concomitantly favoring CH_4 cracking reaction. The ceria reticulated porous foam shows better performance in terms of effective heat transfer, due to volumetric absorption of concentrated solar radiation and uniform heating with lower solar power consumption. Using CO_2 as an oxidant results in longer oxidation duration compared to H_2O, and slower oxidation kinetics. Solar energy storage is confirmed by the maximum solar-to-fuel energy conversion efficiency of 5.60% and the energy upgrade factor up to 1.19.

The second process is solar steam gasification of wood biomass with continuous feedstock injection in a spouted solar reactor. The experimental assessment of continuous solar gasification of biomass was performed via sixty-four on-sun runs. A comprehensive parametric study considering different lignocellulosic biomass feedstocks (five wood biomass types), biomass feeding rates (0.6-2.7 g/min), steam/biomass molar ratios (1.6-2.8), carrier gas flow rates (2-3.3 NL/min), and reaction temperatures (1100-1300 °C) was conducted for optimizing the syngas production capacity, energy upgrade factor, and gasifier performance. Different wood feedstocks were continuously gasified with H_2O during on-sun testing, and syngas was continuously produced, thus successfully demonstrating the reliability of the reactor operated compatibly with different particle types, sizes, and shapes. A small excess of water with respect to stoichiometry is beneficial for biomass gasification regarding the increase of H_2 and CO and the decrease of CH_4, CO_2, and C_2H_m production. An increase in the gas residence time through the decrease of total gas carrier flow results in the improvement of the syngas yield and quality. A significant enhancement of syngas yields and production rates through the rise of operating temperature is highlighted with activation energy in the range of 24-29 kJ/mol. Increasing both biomass feeding rate and temperature improves the syngas yields, gasification rates, and syngas quality because both biomass consumption rates and reaction kinetics are enhanced, in turn improving reactor performance. However, the performance outputs are reduced, and reactants accumulation within the cavity receiver occurs when biomass feeding rate exceeds its optimal feeding point. The optimal biomass feeding rate regarding maximum syngas yield exits at 2.2 g/min at 1200 °C and 2.5 g/min at 1300 °C. The solar reactor temperature of 1300°C is recommended to operate reliably the biomass gasifier with the considered biomass particle size

range (0.3-4 mm) in a continuous feeding mode enabling complete biomass conversion, as verified by the carbon consumption rate that matches closely the carbon feeding rate. By optimizing biomass feeding rate consistently with operating temperature, the calorific value of the biomass feedstock is solar upgraded by 24% with carbon conversion extent above 90%, solar-to-fuel energy conversion efficiency up to 29%, and thermochemical reactor efficiency above 27%.

The last process is the production of Mg and Zn via the solar CTR of MgO and ZnO using solid carbonaceous feedstocks such as solid carbon or biomass as reducing agents. The reactions also produce CO or syngas, as valuable co-products. The solar CTR of ZnO and MgO was studied as a function of different reducing agents (activated charcoal, carbon black, graphite, and beech wood biomass as particles or pellets), carbon/metal oxide molar ratios (1.5-2), pressures (vacuum and atmospheric), and temperatures (950-1650 °C) in batch and continuous operation, thus demonstrating flexibility, reliability, and robustness of this scalable metallurgical process for Zn and Mg production. The equilibrium thermodynamics of the CTR of ZnO and MgO were also analyzed. ZnO and MgO conversion, reduction rate, and CO yield increased with decreasing pressure and increasing temperature, in agreement with thermodynamic analysis. High-purity Zn and Mg production was achieved with net conversion above 78% and 99%, respectively. Utilizing activated charcoal as reducing agent led to the highest MgO and ZnO conversion and CO yield. Mg recovery in the outlet products was identified as one of the most critical process challenges because of the pyrophoric property of the produced nanopowder and its strong oxidation reactivity with air. Alternatively, utilizing wood biomass as a sustainable reducer was proved to be an attractive choice to produce both metallic Zn and high-quality syngas in a single process, demonstrating the feasibility of combined gasification of biomass with the ZnO/Zn redox system in continuous operation for the first time. High conversion efficiency and solar energy storage were demonstrated with the maximum energy upgrade factor up to 1.2 and 1.9 and the maximum solar-to-fuel energy conversion efficiency up to 6% and 7.8 % for the CTR of ZnO and MgO, respectively. The produced Zn and Mg were proved to be further reactive in a second step to produce fuel via CO_2-splitting in a complete and fast reaction.

Finally, the feasibility of the combination of biomass gasification and CTR of ZnO was experimentally investigated in the particle-fed reactor using biomass feedstock as ZnO reducer, as demonstrated in the previous study. The goal was thus to prove the concept of producing syngas and metal Zn continuously in a single process. Experiments were performed in spouted bed with biomass/ZnO molar ratios of 0.5-1 at 1050-1300 °C, using beech wood biomass in continuous feeding mode. The influence of temperature and reactant molar ratio on ZnO conversion as well as syngas production was studied and additionally compared to pyrolysis tests (without any oxidant). As a result, the feasibility of continuous biomass gasification combined with pure Zn production was experimentally proved. Increasing the temperature significantly increased H_2 and slightly increased CO, while CO_2 and CH_4 decreased. The optimal biomass/ZnO molar ratio was evidenced at 0.75 yielding maximum syngas production up to ~8 $mol_{syngas}/ mol_{biomass}$ at 1250 °C. The syngas yield of the combined

gasification/carbothermal reduction was much higher in comparison with pyrolysis because of higher feedstock conversion thanks to ZnO. The energy upgrade factor of the feedstock by the solar power input and the solar-to-fuel energy conversion efficiency were 1.17 and 19.8% respectively.

Table 6-1 summarizes the temperature at which the standard ΔG° equals zero ($T@\Delta G^0=0$), enthalpy change of reaction (ΔH^0), theoretical energy upgrade factor (theoretical U), maximal achieved energy upgrade factor (Max U), percentage of achieved U compared to theoretical U (% of max value), and solar-to-fuel energy conversion efficiency obtained at Max U ($\eta_{solar-to-fuel}$) for each considered reaction. The highest energy upgrade factor (Max U) of each reaction approached their theoretical ones in the range of 74-93 %, demonstrating high conversion and solar energy storage potential into the chemical products. The theoretical U of CTR of MgO is the highest (2.25) compared to other considered reactions, as the enthalpy change of Mg formation is very high (601.1 kJ/mol), demonstrating high potential for the storage of solar energy. However, the $\eta_{solar-to-fuel}$ @ max U for CTR of ZnO and CTR of MgO is quite low as a result of high heat losses, caused by long non-isothermal duration (batch operation) and high reduction temperature (CTR of MgO), while that of CLRM with ceria was greater due to isothermal operation (reduction + oxidation steps). The maximum $\eta_{solar-to-fuel}$ @ max U was obtained for biomass gasification (27.8%), followed by biomass gasification combined with CTR of ZnO (19.8%). This is because such processes were both operated isothermally in continuous mode, thereby significantly reducing heat losses. It can be pointed out that high temperature process with respect to CTR of MgO allowed higher capacity for solar energy storage into the chemical products than low temperature process; however, at the expense of higher heat losses, leading to lower $\eta_{solar-to-fuel}$. The heat losses can be decreased by operating the process in both isothermal and continuous mode to improve the $\eta_{solar-to-fuel}$. Additionally, higher $\eta_{solar-to-fuel}$ implies a smaller solar concentrating system for the same fuel output, which directly leads to lower specific production cost, as the major costly component is attributed to the investment of the solar collecting and concentrating infrastructure.

Table 6-1. $T@\Delta G^0=0$, ΔH^0, theoretical U, Max U, % of max value, and $\eta_{solar-to-fuel}$ @ max U of each considered reaction.

Route	Reaction	$T@\Delta G^0=0$ (K)	ΔH^0 (kJ/mol)	Theoretical U	Max U	% of max value	$\eta_{solar-to-fuel}$ @ max U (%)
CLRM	$Fe_2O_3+3CH_4 \rightarrow 2Fe+6H_2+3CO$	890	715	NA	NA	NA	NA
	$3Fe+4H_2O \rightarrow Fe_3O_4+4H_2$	1285	-151				
CLRM	$CeO_2+\delta CH_4 \rightarrow CeO_{2-\delta}+\delta CO+2\delta H_2$	1058*	166*	1.26	1.15	91	5.24
	$CeO_{2-\delta}+\delta H_2O \rightarrow CeO_2+\delta H_2$	1561*	-64*				
Gasification	$C_6H_9O_4+2H_2O \rightarrow 6CO+6.5H_2$	NA	800	1.28	1.19	93	27.8
CTR	$ZnO+C \rightarrow Zn+CO$	1220	370	1.61	1.20	74	1.6
CTR	$MgO+C \rightarrow Mg+CO$	2130	638	2.25	1.9	84	1.7
Gasification+CTR	$2ZnO+C_6H_9O_4 \rightarrow 2Zn+6CO+4.5H_2$	NA	1278	1.31	1.17	89	19.8

*values given for δ=0.5

To conclude, this work provides a useful experimental database to gain understanding on the solar gasification of biomass, CLRM, and CTR of ZnO and MgO in prototype solar chemical reactors. In addition, the experimental results of each lab-scale process are very useful to support modelling as well as developing large-scale processes.

Perspectives for future research on such processes are recommended in the domains of new reactor designs, testing and optimization, modeling, as well as reactor scale up.

Concerning CLRM, the optimization of the morphological characteristics of redox materials and their integration in solar reactors should be conducted to enhance incident solar radiative flux absorption and volumetric heat transfer, reactive gas flow through cell channels, in turn improving reaction kinetics and reactor efficiency. The use of biomethane, biogas, biohythane as gaseous feedstocks instead of methane is also an alternative to produce renewable fuel. In addition, the on-sun long-term testing of materials over a large number of repeated cycles should be achieved to ensure their performance stability.

The study of solar gasification of other types of solid biomass feedstocks from agriculture plant residues such as empty fruit bunches, rice husk, sugar cane or waste feedstocks such as municipal solid wastes or solid recovered fuels is recommended. Moreover, the investigation of solar CLG of biomass with various non-volatile metal oxides in the spouted bed reactor is interesting because the oxygen carrier particles can simultaneously act as reactive heat transfer solids. Air separation unit is also avoided. Moreover, the corrosion issues attributed to H_2O oxidant may be avoided. Finally, continuous solar/autothermal hybrid gasification of biomass should be investigated to operate the process around-the-clock under intermittent or fluctuating solar power input.

Regarding metallurgical processes, the combination of biomass gasification with metal oxide reduction is a promising approach. The influence of reactant feeding rate and reducing agents (biomass types, sizes, and shapes) on the thermochemical performance of continuous ZnO reduction needs to be further investigated to identify the optimal operating conditions. In addition, the continuous CTR of MgO under vacuum operation is recommended, which requires reactor testing to demonstrate the process reliability and stability during continuous Mg production. Finally, using biomass feedstock as reducing agent for MgO is also attractive, as the required reduction temperature is high (exceeding 1400 °C), which should favor the kinetic rate of biomass gasification.

In the field of solar reactor modelling for the above solid-gas thermochemical processes, numerical reactor simulations considering a multiphase approach while coupling the fluid flow, heat and mass transfer, and chemical reactions are recommended to optimize the reactor, which can be used for reactors design and scale-up. New reactor concepts based on direct or indirect heating should be devised and developed aiming to increase residence time of reactants and solar radiative absorption. Upscaling the reactors is finally advised to improve the solid and gas residence time and reduce heat losses, which should enhance chemical conversion, products yields, and solar-to-fuel efficiency.

References

[1] Statistical Review of World Energy, 2018. https://www.bp.com/en/global/corporate/energy-economics/statistical-review-of-world-energy.html.

[2] M. Romero, A. Steinfeld, Concentrating solar thermal power and thermochemical fuels, Energy Environ. Sci. 5 (2012) 9234–9245. doi:10.1039/C2EE21275G.

[3] N. Borduas, N.M. Donahue, Chapter 3.1 - The Natural Atmosphere, in: B. Török, T.B.T.-G.C. Dransfield (Eds.), Elsevier, 2018: pp. 131–150. doi:https://doi.org/10.1016/B978-0-12-809270-5.00006-6.

[4] Global Solar Atlas, World Bank. (2017). https://globalsolaratlas.info/.

[5] P. Breeze, Chapter 13 - Solar Power, in: P.B.T.-P.G.T. (Third E. Breeze (Ed.), Newnes, 2019: pp. 293–321. doi:https://doi.org/10.1016/B978-0-08-102631-1.00013-4.

[6] P. Breeze, Chapter 4 - Parabolic Trough and Fresnel Reflector Solar Power Plants, in: P.B.T.-S.P.G. Breeze (Ed.), Academic Press, 2016: pp. 25–34. doi:https://doi.org/10.1016/B978-0-12-804004-1.00004-X.

[7] S. Qazi, Chapter 7 - Solar Thermal Electricity and Solar Insolation, in: S.B.T.-S.P. (PV) S. for D.R. and R.A. Qazi (Ed.), Elsevier, 2017: pp. 203–237. doi:https://doi.org/10.1016/B978-0-12-803022-6.00007-1.

[8] H.G. Jin, H. Hong, 12 - Hybridization of concentrating solar power (CSP) with fossil fuel power plants, in: K. Lovegrove, W.B.T.-C.S.P.T. Stein (Eds.), Woodhead Publ. Ser. Energy, Woodhead Publishing, 2012: pp. 395–420. doi:https://doi.org/10.1533/9780857096173.2.395.

[9] solar furnace, (2018). https://www.solarpaces.org/.

[10] K. Wieghardt, K.-H. Funken, G. Dibowski, B. Hoffschmidt, D. Laaber, P. Hilger, K.-P. Eßer, SynLight – the world's largest artificial sun, AIP Conf. Proc. 1734 (2016) 30038. doi:10.1063/1.4949090.

[11] A. Steinfeld, R. Palumbo, Solar Thermochemical Process Technology, in: Encycl. Phys. Sci. Technol., 2003: pp. 237–256. doi:10.1016/B0-12-227410-5/00698-0.

[12] E.A. Fletcher, R.L. Moen, Hydrogen- and Oxygen from Water, Science (80-.). 197 (1977) 1050 LP – 1056. doi:10.1126/science.197.4308.1050.

[13] T. Kodama, N. Gokon, Thermochemical Cycles for High-Temperature Solar Hydrogen Production, Am. Chem. Soc. (2007) pp 4048–4077. doi:10.1021/cr050188a.

[14] T. Kodama, High-temperature solar chemistry for converting solar heat to chemical fuels, Prog. Energy Combust. Sci. 29 (2003) 567–597. doi:http://dx.doi.org/10.1016/S0360-1285(03)00059-5.

[15] T. Nakamura, Hydrogen production from water utilizing solar heat at high temperatures, Sol. Energy. 19 (1977) 467–475. doi:http://dx.doi.org/10.1016/0038-092X(77)90102-5.

[16] M. Lundberg, Model calculations on some feasible two-step water splitting processes, Int. J. Hydrogen Energy. 18 (1993) 369–376. doi:http://dx.doi.org/10.1016/0360-3199(93)90214-U.

[17] P.T. Krenzke, J.R. Fosheim, J.H. Davidson, Solar fuels via chemical-looping reforming, Sol. Energy. 156 (2017) 48–72. doi:https://doi.org/10.1016/j.solener.2017.05.095.

[18] W.K. J., R. Julie, R. Kelvin, G. Benjamin, C. Richard, H.D. W., S.J. R., Theoretical and Experimental Investigation of Solar Methane Reforming through the Nonstoichiometric Ceria Redox Cycle, Energy Technol. 5 (2017) 2138–2149. doi:10.1002/ente.201700083.

[19] C. Wieckert, A. Steinfeld, Solar Thermal Reduction of ZnO Using CH4:ZnO and C:ZnO Molar Ratios Less Than 1, J. Sol. Energy Eng. 124 (2001) 55–62.

http://dx.doi.org/10.1115/1.1434980.
[20] T. Kodama, T. Shimizu, A. Aoki, Y. Kitayama, High-Temperature Conversion of CH4 to C2-Hydrocarbons and H2 Using a Redox System of Metal Oxide, Energy & Fuels. 11 (1997) 1257–1263. doi:10.1021/ef9700691.
[21] H.I. Villafán-Vidales, A. Stéphane, M. Moises, R. Hernando, Carbo- and Methanothermal Reduction of Tungsten Trioxide into Metallic Tungsten for Thermochemical Production of Solar Fuels, Energy Technol. 5 (2016) 692–702. doi:10.1002/ente.201600455.
[22] M. Welte, K. Warren, J.R. Scheffe, A. Steinfeld, Combined Ceria Reduction and Methane Reforming in a Solar-Driven Particle-Transport Reactor, Ind. Eng. Chem. Res. 56 (2017) 10300–10308. doi:10.1021/acs.iecr.7b02738.
[23] J.R. Scheffe, A. Steinfeld, Thermodynamic Analysis of Cerium-Based Oxides for Solar Thermochemical Fuel Production, Energy & Fuels. 26 (2012) 1928–1936. doi:10.1021/ef201875v.
[24] C. Lu, K. Li, H. Wang, X. Zhu, Y. Wei, M. Zheng, C. Zeng, Chemical looping reforming of methane using magnetite as oxygen carrier: Structure evolution and reduction kinetics, Appl. Energy. 211 (2018) 1–14. doi:https://doi.org/10.1016/j.apenergy.2017.11.049.
[25] A. Steinfeld, M. Brack, A. Meier, A. Weidenkaff, D. Wuillemin, A solar chemical reactor for co-production of zinc and synthesis gas, Energy. 23 (1998) 803–814. doi:10.1016/S0360-5442(98)00026-7.
[26] R.W. Taylor, R. Berjoan, J.P. Coutures, Solar gasification of carbonaceous materials, Sol. Energy. 30 (1983) 513–525. doi:https://doi.org/10.1016/0038-092X(83)90063-4.
[27] P. Nejat, F. Jomehzadeh, M.M. Taheri, M. Gohari, M.Z. Abd. Majid, A global review of energy consumption, CO2 emissions and policy in the residential sector (with an overview of the top ten CO2 emitting countries), Renew. Sustain. Energy Rev. 43 (2015) 843–862. doi:https://doi.org/10.1016/j.rser.2014.11.066.
[28] D.-K. Moon, D.-G. Lee, C.-H. Lee, H2 pressure swing adsorption for high pressure syngas from an integrated gasification combined cycle with a carbon capture process, Appl. Energy. 183 (2016) 760–774. doi:10.1016/j.apenergy.2016.09.038.
[29] G. Yadavalli, H. Lei, Y. Wei, L. Zhu, X. Zhang, Y. Liu, D. Yan, Carbon dioxide capture using ammonium sulfate surface modified activated biomass carbon, Biomass and Bioenergy. 98 (2017) 53–60. doi:10.1016/j.biombioe.2017.01.015.
[30] Q. Bellouard, S. Abanades, S. Rodat, N. Dupassieux, Solar thermochemical gasification of wood biomass for syngas production in a high-temperature continuously-fed tubular reactor, Int. J. Hydrogen Energy. (2016). doi:10.1016/j.ijhydene.2016.08.196.
[31] D.W. Gregg, W.R. Aiman, H.H. Otsuki, C.B. Thorsness, Solar coal gasification, Sol. Energy. 24 (1980) 313–321. doi:https://doi.org/10.1016/0038-092X(80)90489-2.
[32] H.I. Villafán-Vidales, C.A. Arancibia-Bulnes, D. Riveros-Rosas, H. Romero-Paredes, C.A. Estrada, An overview of the solar thermochemical processes for hydrogen and syngas production: Reactors, and facilities, Renew. Sustain. Energy Rev. 75 (2017) 894–908. doi:https://doi.org/10.1016/j.rser.2016.11.070.
[33] D. Baruah, D.C. Baruah, Modeling of biomass gasification: A review, Renew. Sustain. Energy Rev. 39 (2014) 806–815. doi:https://doi.org/10.1016/j.rser.2014.07.129.
[34] A.S. Al-Rahbi, P.T. Williams, Hydrogen-rich syngas production and tar removal from biomass gasification using sacrificial tyre pyrolysis char, Appl. Energy. 190 (2017) 501–509. doi:10.1016/j.apenergy.2016.12.099.
[35] S.H. Cho, J. Lee, K.H. Kim, Y.J. Jeon, E.E. Kwon, Carbon dioxide assisted co-pyrolysis of coal and ligno-cellulosic biomass, Energy Convers. Manag. 118 (2016) 243–252. doi:10.1016/j.enconman.2016.03.093.

[36] A. Meier, A. Steinfeld, Solar Thermochemical Production of Fuels, Adv. Sci. Technol. 74 (2011) 303–312. doi:10.4028/www.scientific.net/AST.74.303.
[37] A. Z'Graggen, A. Steinfeld, Heat and mass transfer analysis of a suspension of reacting particles subjected to concentrated solar radiation – Application to the steam-gasification of carbonaceous materials, Int. J. Heat Mass Transf. 52 (2009) 385–395. doi:https://doi.org/10.1016/j.ijheatmasstransfer.2008.05.023.
[38] P.G. Loutzenhiser, A.P. Muroyama, A review of the state-of-the-art in solar-driven gasification processes with carbonaceous materials, Sol. Energy. 156 (2017) 93–100. doi:https://doi.org/10.1016/j.solener.2017.05.008.
[39] B.J. Hathaway, D.B. Kittelson, J.H. Davidson, Integration of Solar Gasification With Conventional Fuel Production: The Roles of Storage and Hybridization, J. Sol. Energy Eng. 136 (2013) 10906–10910. http://dx.doi.org/10.1115/1.4025971.
[40] A.A. Kaniyal, P.J. van Eyk, G.J. Nathan, P.J. Ashman, J.J. Pincus, Polygeneration of Liquid Fuels and Electricity by the Atmospheric Pressure Hybrid Solar Gasification of Coal, Energy & Fuels. 27 (2013) 3538–3555. doi:10.1021/ef400198v.
[41] T. Osinga, U. Frommherz, A. Steinfeld, C. Wieckert, Experimental Investigation of the Solar Carbothermic Reduction of ZnO Using a Two-cavity Solar Reactor, J. Sol. Energy Eng. 126 (2004) 633–637. http://dx.doi.org/10.1115/1.1639001.
[42] S. Kräupl, U. Frommherz, C. Wieckert, Solar Carbothermic Reduction of ZnO in a Two-Cavity Reactor: Laboratory Experiments for a Reactor Scale-Up, J. Sol. Energy Eng. 128 (2005) 8–15. http://dx.doi.org/10.1115/1.2147585.
[43] M. Tsuji, Y. Wada, Y. Tamaura, A. Steinfeld, P. Kuhn, R. Palumbo, Coal Gasification Using the ZnO/Zn Redox System, Energy & Fuels. 10 (1996) 225–228. doi:10.1021/ef950121y.
[44] J. Hu, C. Li, Q. Guo, J. Dang, Q. Zhang, D.-J. Lee, Y. Yang, Syngas production by chemical-looping gasification of wheat straw with Fe-based oxygen carrier, Bioresour. Technol. 263 (2018) 273–279. doi:https://doi.org/10.1016/j.biortech.2018.02.064.
[45] S. Abanades, P. Charvin, G. Flamant, Design and simulation of a solar chemical reactor for the thermal reduction of metal oxides: Case study of zinc oxide dissociation, Chem. Eng. Sci. 62 (2007) 6323–6333. doi:http://dx.doi.org/10.1016/j.ces.2007.07.042.
[46] C. Perkins, P. Lichty, A.W. Weimer, Determination of aerosol kinetics of thermal ZnO dissociation by thermogravimetry, Chem. Eng. Sci. 62 (2007) 5952–5962. doi:https://doi.org/10.1016/j.ces.2007.06.039.
[47] S. Abanades, P. Charvin, G. Flamant, P. Neveu, Screening of water-splitting thermochemical cycles potentially attractive for hydrogen production by concentrated solar energy, Energy. 31 (2006) 2805–2822. doi:https://doi.org/10.1016/j.energy.2005.11.002.
[48] L.O. Schunk, P. Haeberling, S. Wepf, D. Wuillemin, A. Meier, A. Steinfeld, A Receiver-Reactor for the Solar Thermal Dissociation of Zinc Oxide, J. Sol. Energy Eng. 130 (2008) 21006–21009. http://dx.doi.org/10.1115/1.2840576.
[49] C. Perkins, P.R. Lichty, A.W. Weimer, Thermal ZnO dissociation in a rapid aerosol reactor as part of a solar hydrogen production cycle, Int. J. Hydrogen Energy. 33 (2008) 499–510. doi:10.1016/j.ijhydene.2007.10.021.
[50] M. Chambon, S. Abanades, G. Flamant, Thermal dissociation of compressed ZnO and SnO2 powders in a moving-front solar thermochemical reactor, AIChE J. 57 (2011) 2264–2273. doi:10.1002/aic.12432.
[51] E. Koepf, W. Villasmil, A. Meier, Pilot-scale solar reactor operation and characterization for fuel production via the Zn/ZnO thermochemical cycle, Appl. Energy. 165 (2016) 1004–1023. doi:https://doi.org/10.1016/j.apenergy.2015.12.106.
[52] J.P. Murray, A. Steinfeld, E.A. Fletcher, Metals, nitrides, and carbides via solar

carbothermal reduction of metal oxides, Energy. 20 (1995) 695–704. doi:http://dx.doi.org/10.1016/0360-5442(95)00032-C.

[53] L. Xiao, S.-Y. Wu, Y.-R. Li, Advances in solar hydrogen production via two-step water-splitting thermochemical cycles based on metal redox reactions, Renew. Energy. 41 (2012) 1–12. doi:http://dx.doi.org/10.1016/j.renene.2011.11.023.

[54] M.E. Gálvez, A. Frei, G. Albisetti, G. Lunardi, A. Steinfeld, Solar hydrogen production via a two-step thermochemical process based on MgO/Mg redox reactions—Thermodynamic and kinetic analyses, Int. J. Hydrogen Energy. 33 (2008) 2880–2890. doi:https://doi.org/10.1016/j.ijhydene.2008.04.007.

[55] T. Kodama, T. Shimizu, T. Satoh, M. Nakata, K.-I. Shimizu, Stepwise production of CO-rich syngas and hydrogen via solar methane reforming by using a Ni(II)–ferrite redox system, Sol. Energy. 73 (2002) 363–374. doi:https://doi.org/10.1016/S0038-092X(02)00112-3.

[56] J.R. Fosheim, B.J. Hathaway, J.H. Davidson, High efficiency solar chemical-looping methane reforming with ceria in a fixed-bed reactor, Energy. 169 (2019) 597–612. doi:https://doi.org/10.1016/j.energy.2018.12.037.

[57] A. Demont, S. Abanades, High redox activity of Sr-substituted lanthanum manganite perovskites for two-step thermochemical dissociation of CO2, RSC Adv. 4 (2014) 54885–54891. doi:10.1039/C4RA10578H.

[58] G. Levêque, S. Abanades, Investigation of thermal and carbothermal reduction of volatile oxides (ZnO, SnO2, GeO2, and MgO) via solar-driven vacuum thermogravimetry for thermochemical production of solar fuels, Thermochim. Acta. 605 (2015) 86–94. doi:10.1016/j.tca.2015.02.015.

[59] E.E. Koepf, S.G. Advani, A.K. Prasad, A. Steinfeld, Eeperimental investigation of the carbothermal reduction of ZnO using a beam-down, gravity-fed solar reactor, Ind. Eng. Chem. Res. (2015) 8319–8332.

[60] C. Agrafiotis, M. Roeb, C. Sattler, A review on solar thermal syngas production via redox pair-based water/carbon dioxide splitting thermochemical cycles, 2015. doi:http://dx.doi.org/10.1016/j.rser.2014.09.039.

[61] P. Haueter, S. Moeller, R. Palumbo, A. Steinfeld, The production of zinc by thermal dissociation of zinc oxide—solar chemical reactor design, Sol. Energy. 67 (1999) 161–167. doi:https://doi.org/10.1016/S0038-092X(00)00037-2.

[62] A. Steinfeld, I. Spiewak, Economic evaluation of the solar thermalco-production of zinc and synthesis gas, Energy Convers. Manag. 39 (1998) 1513–1518. doi:https://doi.org/10.1016/S0196-8904(98)00102-2.

[63] A. Steinfeld, A. Frei, P. Kuhn, D. Wuillemin, Solar thermal production of zinc and syngas via combined ZnO-reduction and CH4-reforming processes, Int. J. Hydrogen Energy. 20 (1995) 793–804. doi:http://dx.doi.org/10.1016/0360-3199(95)00016-7.

[64] A. Steinfeld, R. Palumbo, Solar thermochemical process technology, Encycl. Phys. Sci. Technol. 15 (2001) 237–256.

[65] C. Wieckert, U. Frommherz, S. Kräupl, E. Guillot, G. Olalde, M. Epstein, S. Santén, T. Osinga, A. Steinfeld, A 300kW Solar Chemical Pilot Plant for the Carbothermic Production of Zinc, J. Sol. Energy Eng. 129 (2006) 190–196. http://dx.doi.org/10.1115/1.2711471.

[66] A. Steinfeld, High-temperature solar thermochemistry for CO2 mitigation in the extractive metallurgical industry, Energy. 22 (1997) 311–316. doi:https://doi.org/10.1016/S0360-5442(96)00103-X.

[67] S. Kräupl, A. Steinfeld, Experimental Investigation of a Vortex-Flow Solar Chemical Reactor for the Combined ZnO-Reduction and CH4-Reforming*, J. Sol. Energy Eng. 123 (2001) 237–243. http://dx.doi.org/10.1115/1.1384569.

[68] A. Steinfeld, C. Larson, R. Palumbo, M. Foley, Thermodynamic analysis of the co-production of zinc and synthesis gas using solar process heat, Energy. 21 (1996) 205–222. doi:http://dx.doi.org/10.1016/0360-5442(95)00125-5.
[69] S. Kräupl, A. Steinfeld, Pulsed Gas Feeding for Stoichiometric Operation of a Gas-Solid Vortex Flow Solar Chemical Reactor, J. Sol. Energy Eng. 123 (2000) 133–137. http://dx.doi.org/10.1115/1.1351172.
[70] M. Brkic, E. Koepf, A. Meier, Solar carbothermal reduction of aerosolized ZnO particles under vacuum: Modeling, experimentation, and characterization of a drop-tube reactor, Chem. Eng. J. 313 (2017) 435–449. doi:https://doi.org/10.1016/j.cej.2016.12.057.
[71] M. Halmann, A. Frei, A. Steinfeld, Vacuum Carbothermic Reduction of Al2O3, BeO, MgO-CaO, TiO2, ZrO2, HfO2 + ZrO2, SiO2, SiO2 + Fe2O3, and GeO2 to the Metals. A Thermodynamic Study, Miner. Process. Extr. Metall. Rev. 32, (2011) 247–266.
[72] M.E. Alam, S. Han, Q.B. Nguyen, A.M. Salem Hamouda, M. Gupta, Development of new magnesium based alloys and their nanocomposites, J. Alloys Compd. 509 (2011) 8522–8529. doi:https://doi.org/10.1016/j.jallcom.2011.06.020.
[73] B.L. Mordike, T. Ebert, Magnesium: Properties — applications — potential, Mater. Sci. Eng. A. 302 (2001) 37–45. doi:https://doi.org/10.1016/S0921-5093(00)01351-4.
[74] T. Abu-Hamed, J. Karni, M. Epstein, The use of boron for thermochemical storage and distribution of solar energy, Sol. Energy. 81 (2007) 93–101. doi:https://doi.org/10.1016/j.solener.2006.06.012.
[75] B.A. Chubukov, A.W. Palumbo, S.C. Rowe, I. Hischier, A.J. Groehn, A.W. Weimer, Pressure dependent kinetics of magnesium oxide carbothermal reduction, Thermochim. Acta. 636 (2016) 23–32. doi:https://doi.org/10.1016/j.tca.2016.03.035.
[76] L. Hong, H.Y. Sohn, M. Sano, Kinetics of carbothermic reduction of magnesia and zinc oxide by thermogravimetric analysis technique, Scand. J. Metall. 32 (2003) 171–176. doi:10.1034/j.1600-0692.2003.00639.x.
[77] L. Rongti, P. Wei, M. Sano, J. Li, Kinetics of reduction of magnesia with carbon, Thermochim. Acta. 390 (2002) 145–151. doi:https://doi.org/10.1016/S0040-6031(02)00128-4.
[78] L. Rongti, P. Wei, M. Sano, Kinetics and mechanism of carbothermic reduction of magnesia, Metall. Mater. Trans. B. 34 (2003) 433–437. doi:10.1007/s11663-003-0069-y.
[79] G. Brooks, S. Trang, P. Witt, M.N.H. Khan, M. Nagle, The carbothermic route to magnesium, JOM. 58 (2006) 51–55. doi:10.1007/s11837-006-0024-x.
[80] I. Hischier, B.A. Chubukov, M.A. Wallace, R.P. Fisher, A.W. Palumbo, S.C. Rowe, A.J. Groehn, A.W. Weimer, A novel experimental method to study metal vapor condensation/oxidation: Mg in CO and CO2 at reduced pressures, Sol. Energy. 139 (2016) 389–397. doi:https://doi.org/10.1016/j.solener.2016.10.024.
[81] B.A. Chubukov, A.W. Palumbo, S.C. Rowe, M.A. Wallace, A.W. Weimer, Enhancing the Rate of Magnesium Oxide Carbothermal Reduction by Catalysis, Milling, and Vacuum Operation, Ind. Eng. Chem. Res. 56 (2017) 13602–13609. doi:10.1021/acs.iecr.7b03175.
[82] Y. Tian, B. Xu, C. Yang, B. Yang, T. Qu, H. Liu, Y. Dai, D. Liu, Analysis of Magnesia Carbothermic Reduction Process in Vacuum, Metall. Mater. Trans. B. 45 (2014) 1936–1941. doi:10.1007/s11663-014-0106-z.
[83] W. Xie, J. Chen, H. Wang, X. Zhang, X. Peng, Y. Yang, Kinetics of magnesium preparation by vacuum-assisted carbothermic reduction method, Rare Met. 35 (2016) 192–197. doi:10.1007/s12598-014-0275-6.
[84] C. Yang, Y. Tian, T. Qu, B. Yang, B. Xu, Y. Dai, Analysis of the behavior of magnesium and CO vapor in the carbothermic reduction of magnesia in a vacuum, J. Magnes. Alloy.

2 (2014) 50–58. doi:https://doi.org/10.1016/j.jma.2014.02.003.
[85] Y. Tian, B. Xu, B. Yang, C. Yang, T. Qu, D. Liu, Y. Dai, Magnesium production by carbothermic reduction in vacuum, J. Magnes. Alloy. 3 (2015) 149–154. doi:https://doi.org/10.1016/j.jma.2015.04.001.
[86] N. Xiong, Y. Tian, B. Yang, B.-Q. Xu, D.-C. Liu, Y.-N. Dai, Volatilization and condensation behaviours of Mg under vacuum, Vacuum. 156 (2018) 463–468. doi:https://doi.org/10.1016/j.vacuum.2018.08.014.
[87] W. Sheline, L. Matthews, N. Lindeke, S. Duncan, R. Palumbo, An exploratory study of the solar thermal electrolytic production of Mg from MgO, Energy. 51 (2013) 163–170. doi:https://doi.org/10.1016/j.energy.2012.11.053.
[88] M.F. Bleeker, H.J. Veringa, S.R.A. Kersten, Deactivation of iron oxide used in the steam-iron process to produce hydrogen, Appl. Catal. A Gen. 357 (2009) 5–17. doi:https://doi.org/10.1016/j.apcata.2008.12.032.
[89] A. Steinfeld, E.A. Fletcher, Theoretical and experimental investigation of the carbothermic reduction of Fe2O3 using solar energy, Energy. 16 (1991) 1011–1019. doi:http://dx.doi.org/10.1016/0360-5442(91)90061-P.
[90] A. Steinfeld, P. Kuhn, J. Karni, High-temperature solar thermochemistry: Production of iron and synthesis gas by Fe3O4-reduction with methane, Energy. 18 (1993) 239–249. doi:http://dx.doi.org/10.1016/0360-5442(93)90108-P.
[91] A. Steinfeld, A. Frei, P. Kuhn, Thermoanalysis of the combined Fe3O4-reduction and CH4-reforming processes, Metall. Mater. Trans. B. 26 (1995) 509–515. doi:10.1007/BF02653867.
[92] K.-S. Cha, B.-K. Yoo, H.-S. Kim, T.-G. Ryu, K.-S. Kang, C.-S. Park, Y.-H. Kim, A study on improving reactivity of Cu-ferrite/ZrO2 medium for syngas and hydrogen production from two-step thermochemical methane reforming, Int. J. Energy Res. 34 (2010) 422–430. doi:10.1002/er.1643.
[93] S. Takenaka, K. Nomura, N. Hanaizumi, K. Otsuka, Storage and formation of pure hydrogen mediated by the redox of modified iron oxides, Appl. Catal. A Gen. 282 (2005) 333–341. doi:https://doi.org/10.1016/j.apcata.2004.12.028.
[94] S. Takenaka, N. Hanaizumi, V.T.D. Son, K. Otsuka, Production of pure hydrogen from methane mediated by the redox of Ni- and Cr-added iron oxides, J. Catal. 228 (2004) 405–416. doi:https://doi.org/10.1016/j.jcat.2004.09.015.
[95] K.-S. Kang, C.-H. Kim, W.-C. Cho, K.-K. Bae, S.-W. Woo, C.-S. Park, Reduction characteristics of CuFe2O4 and Fe3O4 by methane; CuFe2O4 as an oxidant for two-step thermochemical methane reforming, Int. J. Hydrogen Energy. 33 (2008) 4560–4568. doi:https://doi.org/10.1016/j.ijhydene.2008.05.054.
[96] K.-S. Cha, H.-S. Kim, B.-K. Yoo, Y.-S. Lee, K.-S. Kang, C.-S. Park, Y.-H. Kim, Reaction characteristics of two-step methane reforming over a Cu-ferrite/Ce–ZrO2 medium, Int. J. Hydrogen Energy. 34 (2009) 1801–1808. doi:https://doi.org/10.1016/j.ijhydene.2008.12.063.
[97] K.-S. Kang, C.-H. Kim, K.-K. Bae, W.-C. Cho, W.-J. Kim, Y.-H. Kim, S.-H. Kim, C.-S. Park, Redox cycling of CuFe2O4 supported on ZrO2 and CeO2 for two-step methane reforming/water splitting, Int. J. Hydrogen Energy. 35 (2010) 568–576. doi:https://doi.org/10.1016/j.ijhydene.2009.10.099.
[98] P. Furler, J. Scheffe, M. Gorbar, L. Moes, U. Vogt, A. Steinfeld, Solar Thermochemical CO2 Splitting Utilizing a Reticulated Porous Ceria Redox System, Energy & Fuels. 26 (2012) 7051–7059. doi:10.1021/ef3013757.
[99] W.C. Chueh, S.M. Haile, A thermochemical study of ceria: exploiting an old material for new modes of energy conversion and CO₂ mitigation, Philos. Trans. R. Soc. A Math. Phys. Eng. Sci. 368 (2010) 3269 LP – 3294.

http://rsta.royalsocietypublishing.org/content/368/1923/3269.abstract.
[100] M.M. Nair, S. Abanades, Tailoring Hybrid Nonstoichiometric Ceria Redox Cycle for Combined Solar Methane Reforming and Thermochemical Conversion of H2O/CO2, Energy & Fuels. 30 (2016) 6050–6058. doi:10.1021/acs.energyfuels.6b01063.
[101] O.T. Sørensen, Thermodynamic studies of the phase relationships of nonstoichiometric cerium oxides at higher temperatures, J. Solid State Chem. 18 (1976) 217–233. doi:https://doi.org/10.1016/0022-4596(76)90099-2.
[102] W.C. Chueh, C. Falter, M. Abbott, D. Scipio, P. Furler, S.M. Haile, A. Steinfeld, High-Flux Solar-Driven Thermochemical Dissociation of CO2 and H2O Using Nonstoichiometric Ceria, Science (80-.). 330 (2010) 1797–1801. doi:10.1126/science.1197834.
[103] D. Marxer, P. Furler, M. Takacs, A. Steinfeld, Solar thermochemical splitting of CO2 into separate streams of CO and O2 with high selectivity{,} stability{,} conversion{,} and efficiency, Energy Environ. Sci. 10 (2017) 1142–1149. doi:10.1039/C6EE03776C.
[104] P. Furler, J.R. Scheffe, A. Steinfeld, Syngas production by simultaneous splitting of H2O and CO2via ceria redox reactions in a high-temperature solar reactor, Energy Environ. Sci. 5 (2012) 6098–6103. doi:10.1039/C1EE02620H.
[105] G.J. Yurek, J.P. Hirth, R.A. Rapp, The formation of two-phase layered scales on pure metals, Oxid. Met. 8 (1974) 265–281. doi:10.1007/BF00609944.
[106] F. He, J. Trainham, G. Parsons, J.S. Newman, F. Li, A hybrid solar-redox scheme for liquid fuel and hydrogen coproduction, Energy Environ. Sci. 7 (2014) 2033–2042. doi:10.1039/C4EE00038B.
[107] S. Abanades, G. Flamant, Thermochemical hydrogen production from a two-step solar-driven water-splitting cycle based on cerium oxides, Sol. Energy. 80 (2006) 1611–1623. doi:http://dx.doi.org/10.1016/j.solener.2005.12.005.
[108] K. Otsuka, T. Ushiyama, I. Yamanaka, Partial Oxidation of Methane Using the Redox of Cerium Oxide, Chem. Lett. 22 (1993) 1517–1520. doi:10.1246/cl.1993.1517.
[109] P.T. Krenzke, J.H. Davidson, Thermodynamic Analysis of Syngas Production via the Solar Thermochemical Cerium Oxide Redox Cycle with Methane-Driven Reduction, Energy & Fuels. 28 (2014) 4088–4095. doi:10.1021/ef500610n.
[110] K. Otsuka, E. Sunada, T. Ushiyama, I. Yamanaka, The production of synthesis gas by the redox of cerium oxide, in: M. de Pontes, R.L. Espinoza, C.P. Nicolaides, J.H. Scholtz, M.S.B.T.-S. in S.S. and C. Scurrell (Eds.), Nat. Gas Convers. IV, Elsevier, 1997: pp. 531–536. doi:https://doi.org/10.1016/S0167-2991(97)80386-2.
[111] K. Otsuka, Y. Wang, E. Sunada, I. Yamanaka, Direct Partial Oxidation of Methane to Synthesis Gas by Cerium Oxide, J. Catal. 175 (1998) 152–160. doi:https://doi.org/10.1006/jcat.1998.1985.
[112] P. Furler, J. Scheffe, D. Marxer, M. Gorbar, A. Bonk, U. Vogt, A. Steinfeld, Thermochemical CO2 splitting via redox cycling of ceria reticulated foam structures with dual-scale porosities, Phys. Chem. Chem. Phys. 16 (2014) 10503–10511. doi:10.1039/C4CP01172D.
[113] N. Siegel, R. Diver, J.E. Miller, T. Garino, S. Livers, Reactive Structures for Two-Step Thermochemical Cycles Based on Non-Volatile Metal Oxides, (2009) 431–437. http://dx.doi.org/10.1115/ES2009-90093.
[114] F.A. Costa Oliveira, M.A. Barreiros, S. Abanades, A.P.F. Caetano, R.M. Novais, R.C. Pullar, Solar thermochemical CO2 splitting using cork-templated ceria ecoceramics, J. CO2 Util. 26 (2018) 552–563. doi:https://doi.org/10.1016/j.jcou.2018.06.015.
[115] D. Arifin, A.W. Weimer, Kinetics and mechanism of solar-thermochemical H2 and CO production by oxidation of reduced CeO2, Sol. Energy. 160 (2018) 178–185. doi:https://doi.org/10.1016/j.solener.2017.11.075.

[116] M. Roeb, C. Sattler, R. Klüser, N. Monnerie, L. de Oliveira, A.G. Konstandopoulos, C. Agrafiotis, V.T. Zaspalis, L. Nalbandian, A. Steele, P. Stobbe, Solar Hydrogen Production by a Two-Step Cycle Based on Mixed Iron Oxides, J. Sol. Energy Eng. 128 (2005) 125–133. http://dx.doi.org/10.1115/1.2183804.

[117] L.J. Venstrom, N. Petkovich, S. Rudisill, A. Stein, J.H. Davidson, The Effects of Morphology on the Oxidation of Ceria by Water and Carbon Dioxide, J. Sol. Energy Eng. 134 (2011) 11005–11008. http://dx.doi.org/10.1115/1.4005119.

[118] F. Müller, P. Poživil, P.J. van Eyk, A. Villarrazo, P. Haueter, C. Wieckert, G.J. Nathan, A. Steinfeld, A pressurized high-flux solar reactor for the efficient thermochemical gasification of carbonaceous feedstock, Fuel. 193 (2017) 432–443. doi:https://doi.org/10.1016/j.fuel.2016.12.036.

[119] C. Wieckert, R. Palumbo, U. Frommherz, A two-cavity reactor for solar chemical processes: heat transfer model and application to carbothermic reduction of ZnO, Energy. 29 (2004) 771–787. doi:https://doi.org/10.1016/S0360-5442(03)00183-X.

[120] E. Koepf, S.G. Advani, A. Steinfeld, A.K. Prasad, A novel beam-down, gravity-fed, solar thermochemical receiver/reactor for direct solid particle decomposition: Design, modeling, and experimentation, Int. J. Hydrogen Energy. 37 (2012) 16871–16887. doi:https://doi.org/10.1016/j.ijhydene.2012.08.086.

[121] E.E. Koepf, S.G. Advani, A.K. Prasad, A. Steinfeld, Experimental Investigation of the Carbothermal Reduction of ZnO Using a Beam-Down, Gravity-Fed Solar Reactor, Ind. Eng. Chem. Res. 54 (2015) 8319–8332. doi:10.1021/acs.iecr.5b01249.

[122] Q. Bellouard, S. Abanades, S. Rodat, Biomass Gasification in an Innovative Spouted-Bed Solar Reactor: Experimental Proof of Concept and Parametric Study, Energy & Fuels. 31 (2017) 10933–10945. doi:10.1021/acs.energyfuels.7b01839.

[123] N. Gokon, T. Mataga, N. Kondo, T. Kodama, Thermochemical two-step water splitting by internally circulating fluidized bed of NiFe2O4 particles: Successive reaction of thermal-reduction and water-decomposition steps, Int. J. Hydrogen Energy. 36 (2011) 4757–4767. doi:https://doi.org/10.1016/j.ijhydene.2011.01.076.

[124] N. Piatkowski, C. Wieckert, A. Steinfeld, Experimental investigation of a packed-bed solar reactor for the steam-gasification of carbonaceous feedstocks, Fuel Process. Technol. 90 (2009) 360–366. doi:https://doi.org/10.1016/j.fuproc.2008.10.007.

[125] N. Piatkowski, A. Steinfeld, Solar-Driven Coal Gasification in a Thermally Irradiated Packed-Bed Reactor, Energy & Fuels. 22 (2008) 2043–2052. doi:10.1021/ef800027c.

[126] C. Wieckert, A. Obrist, P. von Zedtwitz, G. Maag, A. Steinfeld, Syngas Production by Thermochemical Gasification of Carbonaceous Waste Materials in a 150 kWth Packed-Bed Solar Reactor, Energy & Fuels. 27 (2013) 4770–4776. doi:10.1021/ef4008399.

[127] N. Gokon, T. Izawa, T. Kodama, Steam gasification of coal cokes by internally circulating fluidized-bed reactor by concentrated Xe-light radiation for solar syngas production, Energy. 79 (2015) 264–272. doi:https://doi.org/10.1016/j.energy.2014.11.012.

[128] T. Kodama, Y. Kondoh, T. Tamagawa, A. Funatoh, K.-I. Shimizu, Y. Kitayama, Fluidized Bed Coal Gasification with CO2 under Direct Irradiation with Concentrated Visible Light, Energy & Fuels. 16 (2002) 1264–1270. doi:10.1021/ef020053x.

[129] N. Gokon, R. Ono, T. Hatamachi, L. Liuyun, H.-J. Kim, T. Kodama, CO2 gasification of coal cokes using internally circulating fluidized bed reactor by concentrated Xe-light irradiation for solar gasification, Int. J. Hydrogen Energy. 37 (2012) 12128–12137. doi:https://doi.org/10.1016/j.ijhydene.2012.05.133.

[130] B.J. Hathaway, J.H. Davidson, D.B. Kittelson, Solar Gasification of Biomass: Kinetics of Pyrolysis and Steam Gasification in Molten Salt, J. Sol. Energy Eng. 133 (2011) 21011–21019. http://dx.doi.org/10.1115/1.4003680.

[131] B.J. Hathaway, J.H. Davidson, Demonstration of a prototype molten salt solar gasification reactor, Sol. Energy. 142 (2017) 224–230. doi:https://doi.org/10.1016/j.solener.2016.12.032.
[132] A.A. Ahmad, N.A. Zawawi, F.H. Kasim, A. Inayat, A. Khasri, Assessing the gasification performance of biomass: A review on biomass gasification process conditions, optimization and economic evaluation, Renew. Sustain. Energy Rev. 53 (2016) 1333–1347. doi:https://doi.org/10.1016/j.rser.2015.09.030.
[133] Q. Zheng, C. Janke, R. Farrauto, Steam reforming of sulfur-containing dodecane on a Rh–Pt catalyst: Influence of process parameters on catalyst stability and coke structure, Appl. Catal. B Environ. 160–161 (2014) 525–533. doi:https://doi.org/10.1016/j.apcatb.2014.05.044.
[134] Q. Song, R. Xiao, Y. Li, L. Shen, Catalytic Carbon Dioxide Reforming of Methane to Synthesis Gas over Activated Carbon Catalyst, Ind. Eng. Chem. Res. 47 (2008) 4349–4357. doi:10.1021/ie800117a.
[135] G. Zhang, Y. Dong, M. Feng, Y. Zhang, W. Zhao, H. Cao, CO2 reforming of CH4 in coke oven gas to syngas over coal char catalyst, Chem. Eng. J. 156 (2010) 519–523. doi:https://doi.org/10.1016/j.cej.2009.04.005.
[136] G. Zhang, A. Su, Y. Du, J. Qu, Y. Xu, Catalytic performance of activated carbon supported cobalt catalyst for CO2 reforming of CH4, J. Colloid Interface Sci. 433 (2014) 149–155. doi:https://doi.org/10.1016/j.jcis.2014.06.038.
[137] G. Zhang, Y. Du, Y. Xu, Y. Zhang, Effects of preparation methods on the properties of cobalt/carbon catalyst for methane reforming with carbon dioxide to syngas, J. Ind. Eng. Chem. 20 (2014) 1677–1683. doi:https://doi.org/10.1016/j.jiec.2013.08.016.
[138] P.T. Krenzke, J.R. Fosheim, J. Zheng, J.H. Davidson, Synthesis gas production via the solar partial oxidation of methane-ceria redox cycle: Conversion, selectivity, and efficiency, Int. J. Hydrogen Energy. 41 (2016) 12799–12811. doi:https://doi.org/10.1016/j.ijhydene.2016.06.095.
[139] D.S.A. Simakov, M.M. Wright, S. Ahmed, E.M.A. Mokheimer, Y. Román-Leshkov, Solar thermal catalytic reforming of natural gas: a review on chemistry{,} catalysis and system design, Catal. Sci. Technol. 5 (2015) 1991–2016. doi:10.1039/C4CY01333F.
[140] K.-S. Kang, C.-H. Kim, K.-K. Bae, W.-C. Cho, S.-H. Kim, C.-S. Park, Oxygen-carrier selection and thermal analysis of the chemical-looping process for hydrogen production, Int. J. Hydrogen Energy. 35 (2010) 12246–12254. doi:https://doi.org/10.1016/j.ijhydene.2010.08.043.
[141] A.C. Gladen, J.H. Davidson, The morphological stability and fuel production of commercial fibrous ceria particles for solar thermochemical redox cycling, Sol. Energy. 139 (2016) 524–532. doi:https://doi.org/10.1016/j.solener.2016.10.029.
[142] X. Zhu, K. Li, Y. Wei, H. Wang, L. Sun, Chemical-Looping Steam Methane Reforming over a CeO2–Fe2O3 Oxygen Carrier: Evolution of Its Structure and Reducibility, Energy & Fuels. 28 (2014) 754–760. doi:10.1021/ef402203a.
[143] Q. Bellouard, S. Rodat, S. Abanades, S. Ravel, P.-É. Frayssines, Design, simulation and experimental study of a directly-irradiated solar chemical reactor for hydrogen and syngas production from continuous solar-driven wood biomass gasification, Int. J. Hydrogen Energy. 44 (2019) 19193–19205. doi:https://doi.org/10.1016/j.ijhydene.2018.04.147.
[144] L. Arribas, N. Arconada, C. González-Fernández, C. Löhrl, J. González-Aguilar, M. Kaltschmitt, M. Romero, Solar-driven pyrolysis and gasification of low-grade carbonaceous materials, Int. J. Hydrogen Energy. 42 (2017) 13598–13606. doi:https://doi.org/10.1016/j.ijhydene.2017.02.026.
[145] A. Z'Graggen, P. Haueter, D. Trommer, M. Romero, J.C. de Jesus, A. Steinfeld,

Hydrogen production by steam-gasification of petroleum coke using concentrated solar power—II Reactor design, testing, and modeling, Int. J. Hydrogen Energy. 31 (2006) 797–811. doi:https://doi.org/10.1016/j.ijhydene.2005.06.011.

[146] P. Holmgren, D.R. Wagner, A. Strandberg, R. Molinder, H. Wiinikka, K. Umeki, M. Broström, Size, shape, and density changes of biomass particles during rapid devolatilization, Fuel. 206 (2017) 342–351. doi:https://doi.org/10.1016/j.fuel.2017.06.009.

[147] A. Trubetskaya, G. Beckmann, J. Wadenbäck, J.K. Holm, S.P. Velaga, R. Weber, One way of representing the size and shape of biomass particles in combustion modeling, Fuel. 206 (2017) 675–683. doi:https://doi.org/10.1016/j.fuel.2017.06.052.

[148] D. Weibel, Z.R. Jovanovic, E. Gálvez, A. Steinfeld, Mechanism of Zn Particle Oxidation by H2O and CO2 in the Presence of ZnO, Chem. Mater. 26 (2014) 6486–6495. doi:10.1021/cm503064f.

[149] S. Abanades, Thermogravimetry Analysis of CO2 and H2O Reduction from Solar Nanosized Zn Powder for Thermochemical Fuel Production, Ind. Eng. Chem. Res. 51 (2012) 741–750. doi:10.1021/ie202518k.

Appendix

Appendix A: Solar chemical looping reforming of methane through iron and ceria oxides

a. Thermodynamics

Fig. A-1 displays the equilibrium species distribution of Fe_3O_4+4CH_4 at 1 bar as a function of temperature. Similar to the results shown in Fig. 2-3, Fe_3O_4 starts reducing to FeO with the occurrence of intermediate non-stoichiometric species ($Fe_{0.945}O$, $Fe_{0.947}O$, and $FeO_{1.056}$), while H_2, C, and H_2O are simultaneously formed as main components above 400 ℃, and FeO is then reduced to Fe along with the formation of CO and CO_2 above 500 ℃. Reduction to Fe reaches completion at above 700 ℃, while C, H_2O, and CO_2 decline continuously. Above 1000 ℃, the syngas (with H_2/CO ratio approaching two) and solid Fe are the stable species.

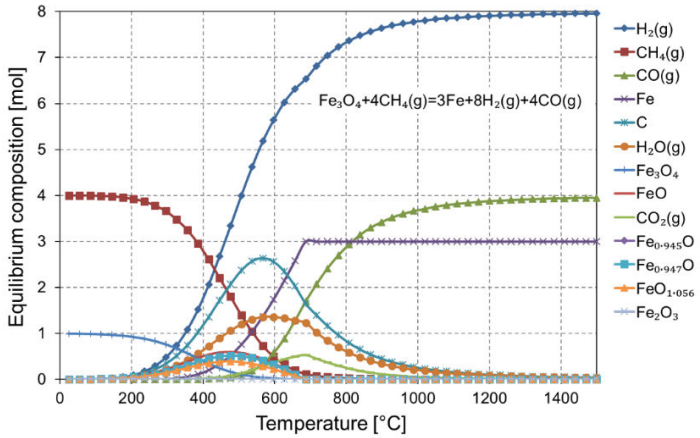

Figure A-1. Thermodynamic equilibrium composition of methane reforming over Fe_3O_4 as a function of temperature at 1 bar.

Fig. A-2 shows the equilibrium species composition of Fe_3O_4+4C at 1 bar as a function of temperature. Similar to the results in Fig. 2-4, a temperature increase leads to Fe_3O_4 reduction to FeO, followed by Fe and CO production. Above 800 ℃, complete reduction to Fe and H_2/CO ratio approaching two are obtained.

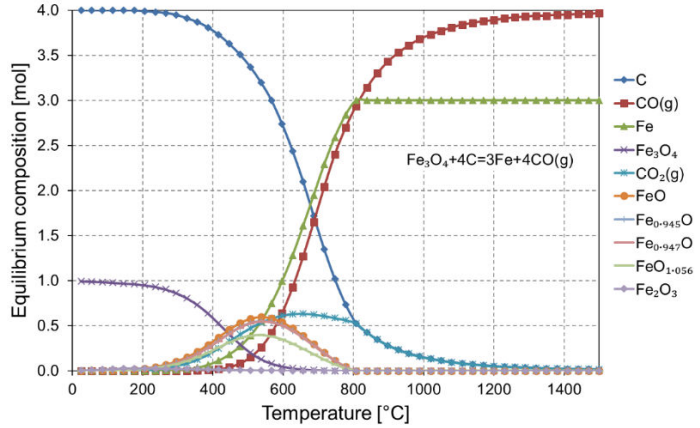

Figure A-2. Thermodynamic equilibrium composition of Fe_3O_4 carbothermal reduction as a function of temperature at 1 bar.

b. Temperature and pressure evolution in the reactor

The transient temperature and cavity pressure evolutions in the solar reactor during both heating phase and ceria powder reduction with methane, followed by ceria powder oxidation with H_2O at different cycle operating temperatures are presented for ceria foam (cycles No.: 5-10, ST-1000, 18.3705 g) according to Fig. A-3, for ceria powder (cycles No.: 3-6, 25.0052 g) according to Fig. A-4 and for ceria powder mixed with Al_2O_3 (cycles No.: 3-6, 27.0605 g of ceria powder with Al_2O_3) according to Fig. A-5.

The homogeneous temperature inside the ceria foam as well as the reactor cavity receiver was confirmed by narrow gaps between T_1 (below the foam), T_3 (inside the foam), and $T_{pyrometer}$ (upper surface of the foam) while the external cavity wall temperature (T_2) was ~150 °C lower than these temperatures (Fig. A-3). Regarding powder, during each reduction step (Fig. A-4), the temperature inside the ceria powder (T_3) was lower than that of ceria bed surface ($T_{pyrometer}$) by ~50-70 °C, while the temperature inside the alumina wool (T_1) was also lower than T_3 by 50-72 °C because the ceria powder exhibits high opacity. Therefore, incident solar thermal radiation can be mainly absorbed on the exposed surface, thereby leading to different temperature gradients across the thickness of the ceria powder bed. During each oxidation step (Fig. A-4), T_3 was conversely higher than $T_{pyrometer}$ because of the exothermic reaction. A similar temperature gradient across the particle bed layer was observed when employing ceria powder mixed with Al_2O_3 particles, but the temperature homogeneity was improved as illustrated in Fig. A-5 (smaller gaps between $T_{pyrometer}$, T_1, and T_3 compared to those for ceria powder (Fig. A-4)), presumably because of facilitated gas circulation inside the bed and enhanced heat and mass transfer. The cavity pressure for any structure was constant at ~0.9 bar during cycling.

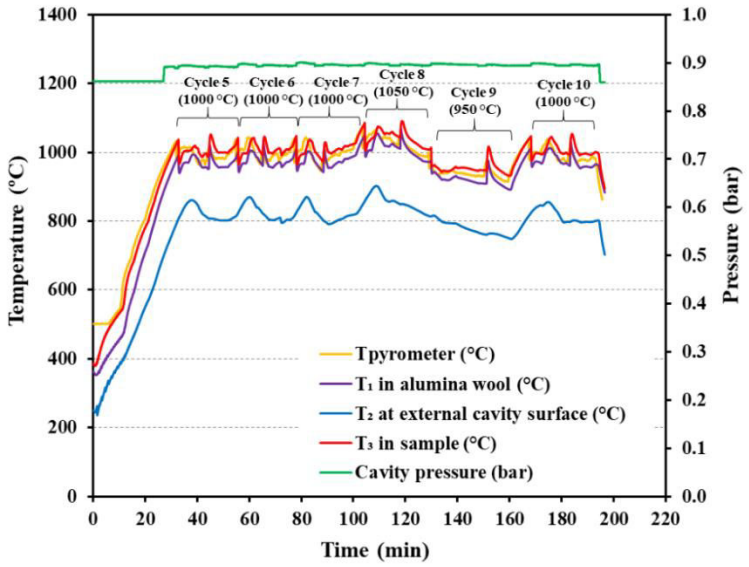

Figure A-3. Temperatures and pressure evolution in the reactor during heating phase, ceria foam reduction with methane and oxidation with H_2O (sample: ceria foam, ST-1000, 18.3705 g, cycles: 5-10 in Table 2-1).

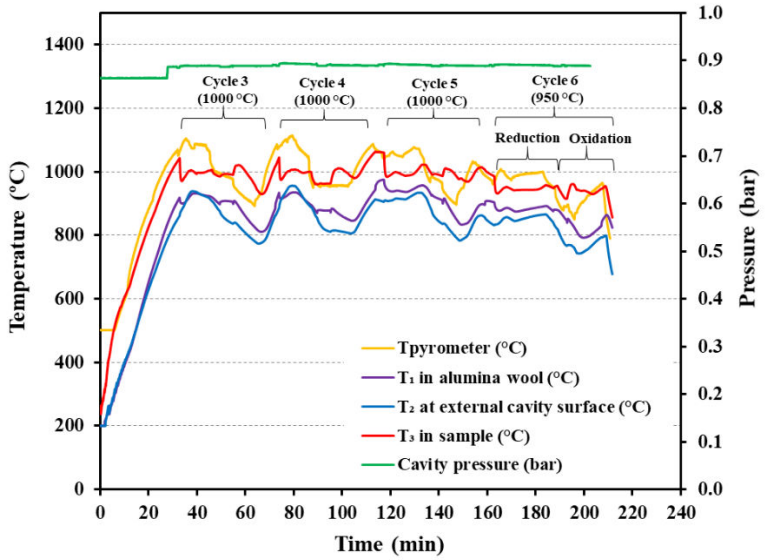

Figure A-4. Temperatures and pressure evolution in the reactor during heating phase, ceria powder reduction with methane and ceria powder oxidation with H_2O (sample: ceria powder 25.0052 g, cycles: 3-6).

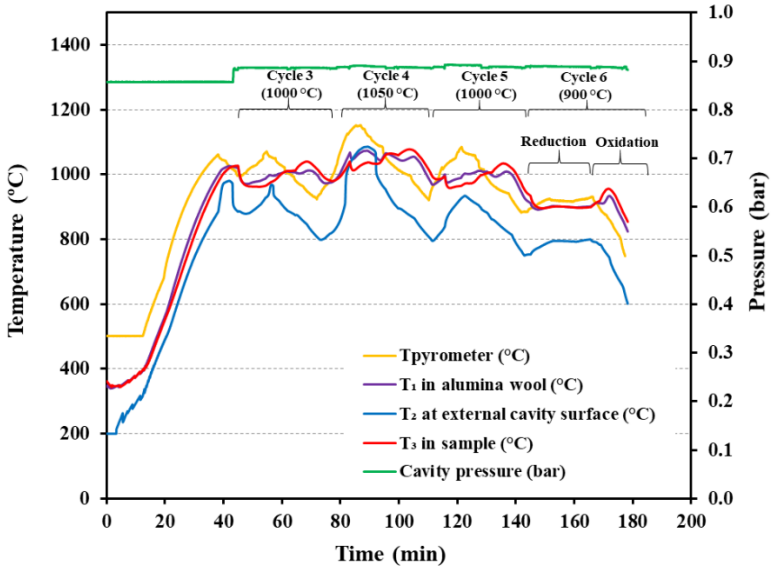

Figure A-5. Temperatures and pressure evolution in the reactor during heating phase, ceria reduction with methane and ceria oxidation with H_2O (sample: ceria powder (27.0605 g) mixed with Al_2O_3 (60 g), cycles: 3-6).

c. Experimental conditions and solar reactor performance assessment

Table A-1 summarizes the operating conditions and experimental results for 55 solar-driven experiments using the directly-irradiated solar reactor. The solar reactor was operated under the following range of operating parameters: CH_4 flow-rates (0.1–0.4 NL/min), operating cycle temperatures (900–1150 °C), steam flow-rate (200 mg/min), CO_2 flow rate (0.2 NL/min), and carrier gas flow-rates (either Ar or N_2, 2–2.2 NL/min). Each type of material was cycled several times to confirm experimental repeatability and materials stability.

For all the tests relating to Table A-1, $\dot{P}_{solar,red}$, $\dot{P}_{solar,ox}$, δ_{red}, δ_{ox}, X_{CH_4}, U, *and* $\eta_{solar\text{-}to\text{-}fuel}$ were in the ranges of 0.62-1.25 kW, 0.55-0.96 kW, 0.12–0.41, 0.12-0.40, 5.20-77.41%, 0.89-1.19 and 1.14-5.60%, respectively.

Table A-1. Operating conditions and experimental performance indicators for the solar reactor.

#	Sample structure	Initial ceria mass (g)	Cycle No.	$\dot{m}_{Ar}$ (NL/min)	$\dot{m}_{CH_4}$ (NL/min)	T_3 (°C)	$\dot{P}_{solar,red}$ (kW)	$\dot{P}_{solar,ox}$ (kW)	δ_{red}	X_{CH_4}	$\dot{m}_{H_2O}$ (mg/min)	$\dot{m}_{CO_2}$ (NL/min)	δ_{ox}	U (%)	$\eta_{solar\text{-}to\text{-}fuel}$ (%)
1	CeO_2 (Foam, ST-1400)	27.9810	1	2.2	0.2	1000	0.80	0.71	0.37	26.25	200		0.32	1.00	2.52
2			2	2.2	0.2	1000	0.83	0.72	0.35	27.32	200		0.31	1.03	2.55
3			3	2	0.4	1000	0.89	0.74	0.33	34.20	200		0.29	0.93	3.57
4			4	2.2	0.2	1000	0.82	0.66	0.34	23.00	200		0.32	1.08	2.75
5			5	2.2	0.2	900	0.62	0.65	0.12	5.20	200		0.12	1.07	1.44
6			6	2.2	0.2	1050	0.95	0.78	0.37	47.03	200		0.34	1.09	3.18
7	CeO_2 (Foam, ST-1000)	18.3705	1	2.2	0.2	1000	0.85	0.78	0.38	59.69	200		0.35	1.01	4.20
8			2	2.2	0.1	1000	0.76	0.78	0.35	68.52	200		0.35	0.97	3.12
9			3	2.2	0.2	1000	0.85	0.77	0.37	56.80	200		0.36	0.99	3.45
10			4	2.2	0.2	1000	0.85	0.69	0.38	60.00	200		0.36	1.04	4.31
11			5	2.2	0.2	1000	0.87	0.78	0.38	49.58	200		0.36	1.07	3.63
12			6	2.2	0.3	1000	0.94	0.67	0.38	60.46	200		0.36	0.97	5.10
13			7	2.2	0.4	1000	0.86	0.60	0.38	53.82	200		0.37	0.98	5.60
14			8	2.2	0.2	1050	0.76	0.87	0.38	65.91	200		0.37	1.07	4.31
15			9	2.2	0.2	950	0.67	0.55	0.33	18.59	200		0.33	1.09	3.02
16			10	2.2	0.2	1000	0.81	0.72	0.38	60.89	200		0.37	0.99	3.76
17			11	2.2	0.2	1000	0.85	0.82	0.37	51.88	200		0.36	1.01	3.67
18			12	2.2	0.2	1000	0.68	0.68	0.36	46.86	200		0.35	1.03	3.78
19			13	2.2*	0.2	1000	0.94	0.70	0.35	51.54	200		0.36	1.00	3.62
20			14	2.2*	0.2	1000	0.88	0.78	0.37	47.96	200		0.36	1.07	3.26
21			15	2.2	0.2	1000	0.81	0.68	0.36	48.08		0.2	0.36	1.10	3.52
22	CeO_2 (Foam, ST-1000)	17.0152	1	2.2*	0.2	1000	0.97	0.82	0.36	60.25	200		0.35	1.04	3.43
23			2	2.2*	0.2	1000	0.98	0.78	0.34	44.25	200		0.35	1.09	2.76
24			3	2.2*	0.2	1000	1.00	0.89	0.34	49.95	200		0.35	1.06	2.54
25			4	2.2*	0.2	1000	0.88	0.91	0.32	40.77	200		0.33	1.12	2.72
26			5	2.2*	0.2	1000	0.95	0.74	0.34	43.89	200		0.35	1.10	3.10
27			6	2.2*	0.2	1000	0.89	0.68	0.33	44.18	200		0.35	1.15	2.43
28	CeO_2+Al_2O_3 (Powder)	27.0605	1	2.2	0.2	1000	1.03	0.93	0.37	66.56	200		0.34	1.15	5.24
29			2	2.2	0.2	1000	0.98	0.67	0.39	60.19	200		0.33	1.02	4.34
30			3	2.2	0.2	1000	0.96	0.75	0.36	56.76	200		0.34	0.98	3.64
31			4	2.2	0.2	1050	1.25	0.81	0.39	77.41	200		0.36	1.06	4.01
32			5	2.2	0.4	1000	1.06	0.78	0.37	53.64	200		0.37	0.94	4.99
33			6	2.2	0.2	900	0.86	0.63	0.24	18.40	200		0.24	1.08	2.49
34	CeO_2+Al_2O_3 (Powder)	27.0892	1	2.2	0.2	1000	1.01	0.72	0.37	60.14		0.2	0.37	1.04	3.46
35			2	2.2	0.2	950	0.81	0.61	0.39	48.05	200		0.33	1.02	3.93
36			3	2.2	0.2	1000	0.91	0.77	0.38	61.00		0.2	0.39	1.11	3.67
37			4	2.2	0.2	950	0.89	0.69	0.38	37.21		0.2	0.37	1.12	2.82

38			5	2.2	0.2	1050	1.22	0.64	0.40	75.80		0.2	0.40	1.19	3.86
39	CeO_2 (Powder)	25.0052	1	2.2*	0.2	1000	0.96	0.90	0.37	44.33	200		0.36	1.09	2.97
40			2	2.2*	0.1	1000	1.06	0.57	0.37	76.35	200		0.34	1.06	3.13
41			3	2.2*	0.3	1000	0.98	0.73	0.39	50.90	200		0.35	0.89	3.45
42			4	2.2*	0.4	1000	1.14	0.96	0.41	43.00	200		0.39	0.95	3.64
43			5	2.2*	0.2	1000	0.93	0.80	0.37	39.01	200		0.36	1.13	3.07
44			6	2.2*	0.2	950	0.88	0.75	0.35	24.03	200		0.35	1.12	2.75
45	Fe_2O_3 (Powder)	20.52	1	2.2	0.2	1000	-	-	0.095**	24.7	200	-	0.012***	-	-
46			2	2.2	0.2	1100	-	-	0.068**	33.8	200	-	0.040***	-	-
47			3	2.2	0.2	950	-	-	0.000**	0.0	200	-	0.004***	-	-
48			4	2.2	0.2	1000	-	-	0.003**	0.2	200	-	-	-	-
49	Fe_2O_3 (Foam)	13.91	1	2.2	0.2	1000	-	-	0.059**	24.9	200	-	0.009***	-	-
50			2	2.2	0.2	1000	-	-	0.012**	9.3	200	-	0.011***	-	-
51			3	2.2	0.2	1000	-	-	0.009**	3.7	200	-	0.008***	-	-
52			4	2.2	0.2	1050	-	-	0.075**	27.6	200	-	0.063***	-	-
53			5	2.2	0.2	1150	-	-	0.131**	68.3	200	-	0.013***	-	-
54			6	2.2	0.2	1100	-	-	0.019**	40.3	200	-	0.011***	-	-
55			7	2.2	0.2	1000	-	-	0.008**	9.1	200	-	-	-	-

*Using N_2 as carrier and protective gases, ** $n_{O,red}$ (mol), and *** $n_{O,ox}$ (mol)

d. Iron oxide powder

Photograph of iron oxide powder after four cycles is shown in Fig. A-6.

Figure A-6. Iron oxide powder after four cycles at different temperatures.

Phase identification via XRD of the reduced iron oxide powder after the reduction step of cycle #4 is presented in Fig. A-7

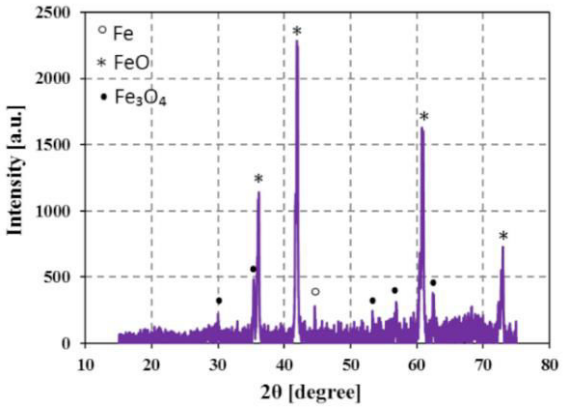

Figure A-7. Representative XRD patterns of iron oxide powder collected after the reduction step of cycle #4.

e. Iron oxide porous foam

Phase identification via XRD of the reduced iron oxide foam after the reduction step of cycle #7 is presented in Fig. A-8.

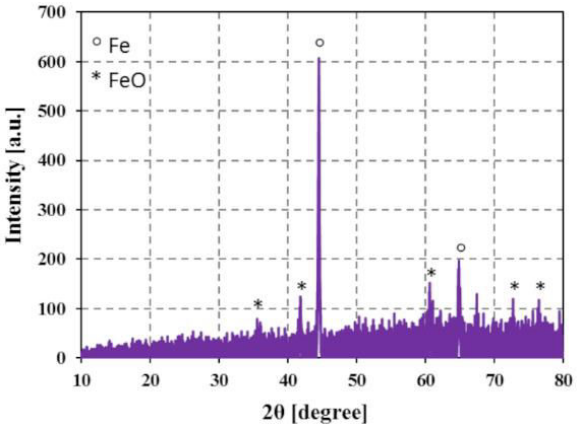

Figure A-8. Representative XRD patterns of iron oxide reticulated foam collected after the reduction step of cycle #7.

Fig. A-9 shows photographs of iron oxide porous foam before and after seven cycles. It is obvious that iron oxide exhibits strong sintering and coarsening, which results in large loss of specific surface area, thereby leading to material deactivation.

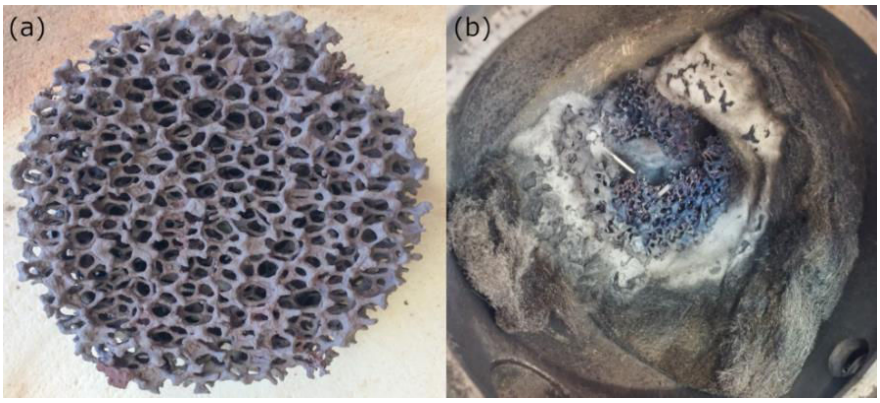

Figure A-9. Iron oxide reticulated foam (a) before the cycling test and (b) after seven isothermal cycles at different temperatures.

f. Chemical-looping methane reforming over ceria foams

The obtained sintered foams at 1000 °C (ST-1000) and 1400 °C (ST-1400) that were prepared for the solar experiments are shown in Fig. A-10.

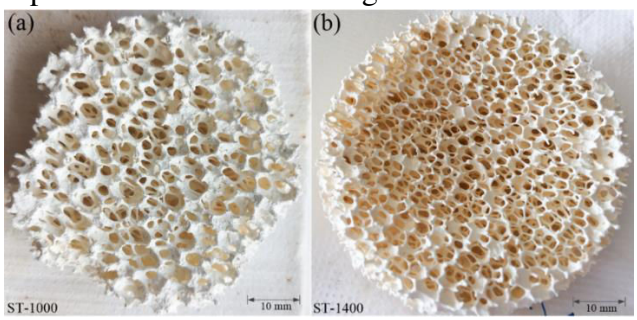

Figure A-10. Ceria reticulated foam fabricated for the solar cavity receiver: (a) after final heat treatment at 1000 °C (13 mm thickness, 55 mm diameter) and (b) after final heat treatment at 1400 °C (11 mm thickness, 60 mm diameter).

Fig. A-11 shows the syngas production rates along with nominal reactor temperature during ceria foam (ST-1400) reduction in the range 900–1050 °C (CH_4 flow-rate: 0.2 Nl/min, Ar flow rate: 0.2 Nl/min, 50% CH_4 mole fraction). It was followed by subsequent ceria oxidation with H_2O carried out at the same temperature (H_2O: 200 mg/min, Ar: 0.2 Nl/min, 55% steam mole fraction at inlet).

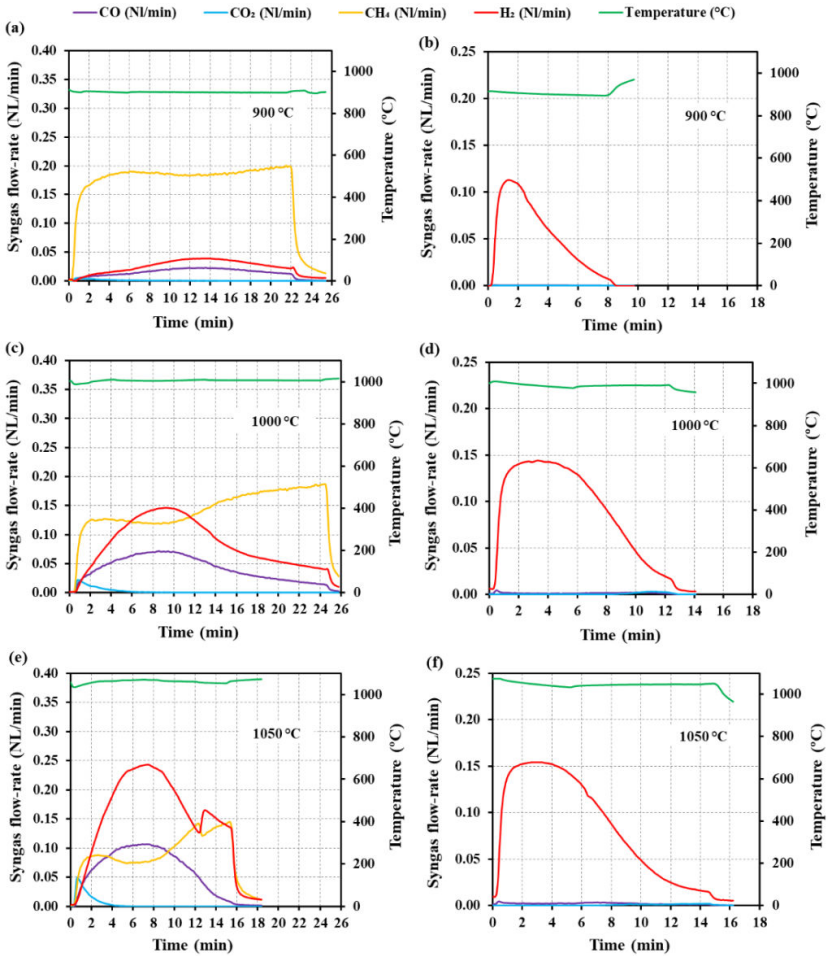

Figure A-11. Evolution of the production rates of H_2, CO, CO_2 and CH_4 in the syngas along with nominal reactor temperature for reduction (a, c, and e) and oxidation (b, d, and f) of ceria foam (ST-1400) cycled isothermally at different temperatures.

g. Carbon deposition on the filter

Fig. A-12 shows the presence of carbon deposition on the filter after 4 cycles, thereby confirming carbon particles entrainment at the reactor outlet.

Figure A-12. Carbon deposition on the filter (sample: ceria foam ST-1000, 18.3705 g, cycles: 1-4).

h. Ceria mixed with Al_2O_3 samples

The homogeneous mixture of ceria powder (mass: 27.0605 g, <5 µm particle size) with Al_2O_3 (mass: 60 g, 1.2 mm particle size) was placed in the reactor cavity receiver exposed to high-flux concentrated solar irradiation prior to solar-driven experiments (Fig. A-13a). Fig. A-13b shows the ceria powder after 6 successive experimental runs with trace of remaining carbon deposit at the surface only.

Figure A-13. Ceria powder mixed with Al_2O_3 particles as dispersion promoter for the solar cavity receiver: (a) before experiments, (b) after experiments for 6 cycles.

g. Kinetic study

In order to investigate the reaction kinetics during methane induced reduction, the Arrhenius expression was utilized to evaluate the effect of temperature on the rates of ceria reduction.

$$k = A \cdot \exp(-E_a/RT) \quad \text{(A-1)}$$

where k is the reaction rate constant, A is the pre-exponential factor, E_a is the activation energy, R is the gas constant, and T is absolute temperature.

The reaction rate constants (k) were quantified from the peak production rates of H_2 and CO for each ceria structure during reduction step at 950 °C (900 °C for CeO_2-Al_2O_3 blend), 1000 °C, and 1050 °C. The logarithm evolution of the reaction rates versus inverse temperature (Eq. A-1) was subsequently plotted (Fig. A-14) to determine the activation energy (E_a) of the ceria reduction process. A beneficial effect of the temperature increase on the H_2 and CO production rates was observed, thus confirming an improvement of the kinetics of ceria reduction with CH_4. The E_a values for different ceria structures were in the range of 92.8-114.2 kJ/mol for H_2 and 92.8-95.1 kJ/mol for CO, according to Table A-2. The E_a values related to H_2 production rates for CeO_2 foam (Fig. A-14a) and CeO_2-Al_2O_3 blend (Fig. A-14b) were slightly higher compared to those of CO as a result of the side reaction effect attributed to CH_4 cracking. However, the same E_a value between H_2 and CO production rates was noticed for CeO_2 powder (Fig. A-14c) as a result of lower methane cracking reaction impact, as evidenced by the lower methane conversion (Fig. 2-20d).

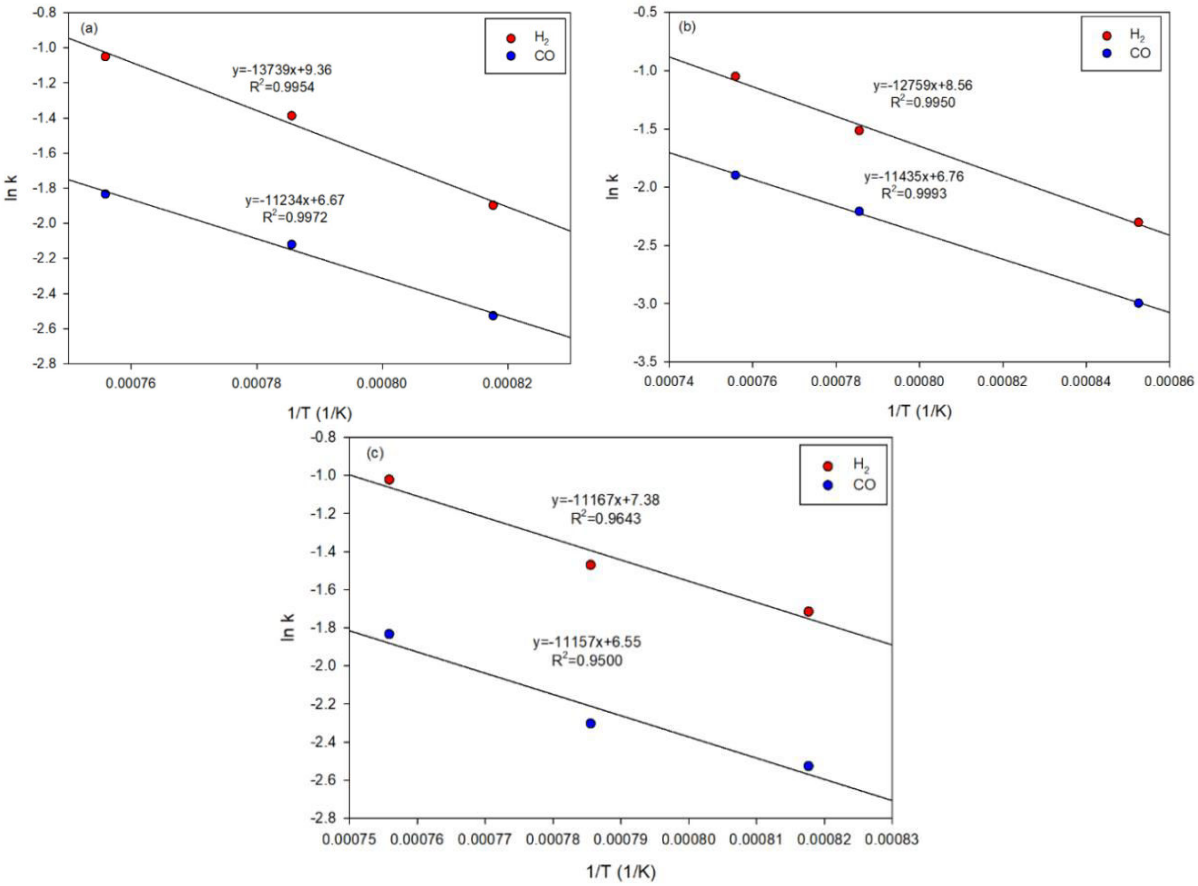

Figure A-14. Arrhenius plot for H_2 and CO production rates at 950-1050 °C for (a) ceria foam ST-1000, (b) CeO_2-Al_2O_3 blend, and (c) CeO_2 powder (CH_4 flow-rate of 0.2 NL/min).

Table A-2. Activation energy related to the H_2 and CO production rates obtained by Arrhenius plot.

Ceria structure	Gaseous Species	E_a (kJ/mol)
CeO_2 porous foam	H_2	114.2±2
	CO	93.4±2
CeO_2-Al_2O_3 powder	H_2	106.1±2
	CO	95.1±2
CeO_2 powder	H_2	92.8±3
	CO	92.8±3

h. Thermochemical cycling stability

Fig. A-15a shows a pristine ceria reticulated foam (17.0152 g) sintered at 1000 °C for 6 h that was used to investigate the cycling stability during 6 consecutive cycles at 1000 °C. Both small sintering and cracking lines within the sample were observed after the last cycle (Fig. A-15b).

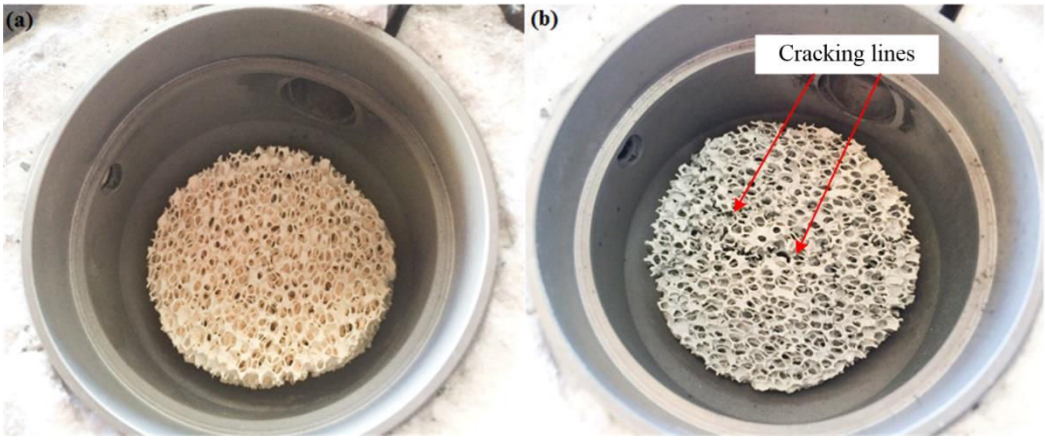

Figure A-15. Ceria reticulated foam (ST-1000) (a) before the cycling stability test and (b) after six consecutive cycles at 1000 °C.

The reduction yield (X_{red}), oxidation yield (X_{ox}), methane conversion (X_{CH_4}), and solar-to-fuel energy conversion efficiency ($\eta_{solar\text{-}to\text{-}fuel}$) for 6 consecutive cycles are presented in Fig. A-16a. Their values remained quite stable over the considered range (64.9-68.6% for X_{red}, 100% for X_{ox}, 40.8-44.2% for X_{CH_4}, and 2.4-3.1% for $\eta_{solar\text{-}to\text{-}fuel}$, for cycles 2-6 at 1000 °C), except at cycle 1 (72.8% for X_{red}, 96.8% for X_{ox}, 60.2% for X_{CH_4}, and 3.4% for $\eta_{solar\text{-}to\text{-}fuel}$) because of a higher reduction temperature (1050 °C). Similarly, the total H_2, CO, CO_2, and H_2O yields (Fig. A-16b) were stable in the range of 6.29-7.13, 1.81-1.98, 0.11-0.15, and 0.10-0.11 mmol/g_{CeO_2}, respectively, for cycles 2-6, while the yields for cycle 1 were higher (8.59, 2.29, 0.28, and 0.14 mmol/g_{CeO_2}, respectively). The energy upgrade factor (U) fluctuated slightly in accordance with the variation in the total produced syngas yield (1.04 -1.15). Thus, the cycling stability of ceria can fairly be validated.

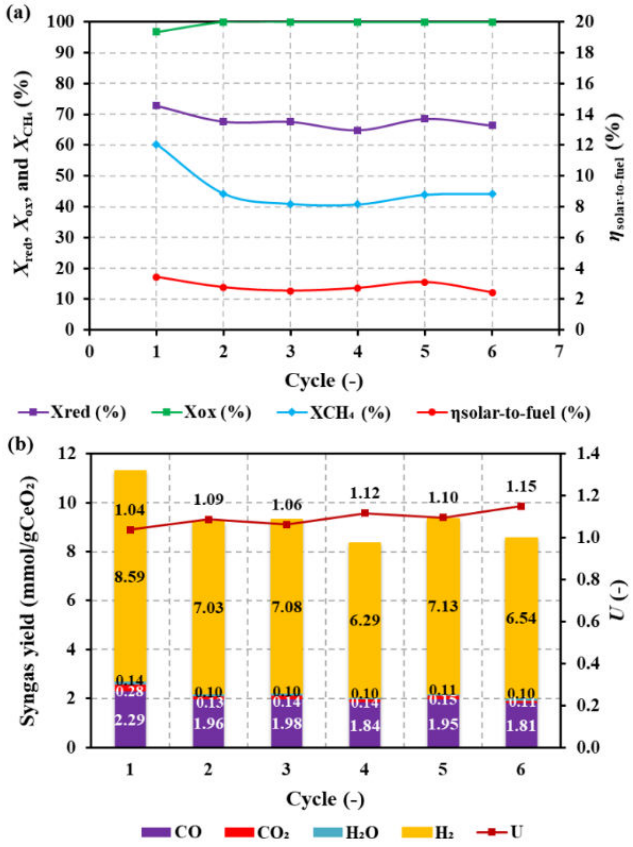

Figure A-16. Cycling stability of ceria foam (ST-1000) regarding (a) reduction (X_{red})-oxidation (X_{ox}) yields, methane conversion (X_{CH_4}), and solar-to-fuel energy conversion efficiency ($\eta_{solar\text{-}to\text{-}fuel}$), and (b) energy upgrade factor (U) and total syngas yields from both steps.

Appendix B: Solar gasification of biomass in a continuous spouted-bed solar reactor

a. Typical evolution of syngas production rates during continuous biomass injection

Fig. B-1 presents a representative experiment of steam gasification with continuous biomass injection. For this experiment, a total of 30 g of biomass type A was introduced at a biomass feeding rate of ~2.2 g/min (~15 minutes of injection time) while the steam was set at 300 mg/min throughout the test, resulting in a H_2O/biomass molar ratio of 2.1 (slightly over-stoichiometric ratio). The experiment was carried out at a temperature of 1300 °C. The GC measurements at different sampling times are also plotted (dots) to confirm and compare the consistency of experimental results obtained from the online gas analyzer. The resulting syngas production rates measured by the two techniques matched well. Stable patterns in the flow-rates of H_2 and CO were achieved during biomass injection, while CO_2 and CH_4 flow-rates were also stable throughout the experiment, thus confirming stable biomass feeding rate injection. The production rates of secondary hydrocarbons (C_nH_m) measured by GC include the C_2H_2, C_2H_4, and C_2H_6 (the latter being in negligible amounts) (Fig. B-2).

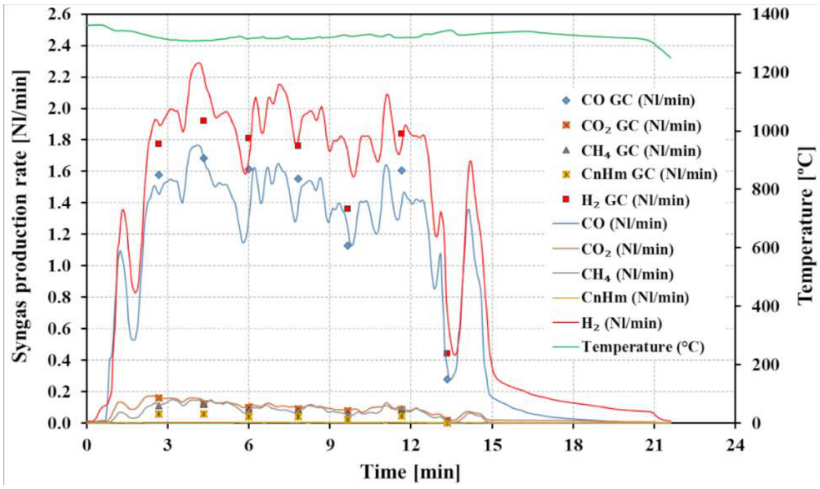

Figure B-1. Evolution of the syngas production rates of H_2, CO, CO_2, CH_4 and C_nH_m along with nominal reactor temperature during continuous steam gasification of biomass type A at ~1300 °C (Run No.14).

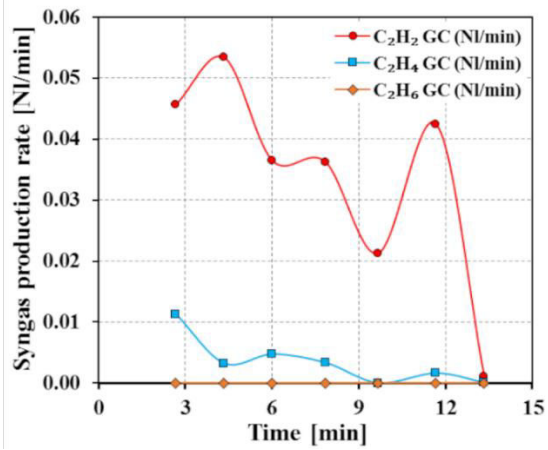

Figure B-2. Evolution of C_2H_2, C_2H_4, and C_2H_6 production rates from GC measurements during continuous steam gasification of biomass type A at 1300 °C (Run No.14).

b. Operating conditions and solar reactor performances assessment

A summary of the operating conditions and experimental results for 64 experimental runs of the continuously-fed solar reactor is shown in Table B-1. Solar-driven experiments were carried out with five biomass feedstocks in a continuous process. The solar reactor was operated under the following range of parameters: biomass feeding rates: 0.6-2.7 g/min, H_2O/biomass molar ratio: 1.6-7 (accounting for the initial moisture content in the biomass feedstocks), carrier gas flow rate: 2-3.3 Nl/min, reactor temperature: 1100-1300 °C and solar power input: 0.86-1.44 kW in order to optimize the synthesis gas production and assess the performance of the solar biomass gasifier.

In this Table, the different solar reactor performances are also highlighted related to the energy upgrade factor (U), thermochemical reactor efficiency ($\eta_{reactor}$), solar-to-fuel energy conversion efficiency ($\eta_{solar\text{-}to\text{-}fuel}$), and carbon conversion (X_C) whether or not accounting for the calorific value of C_2H_2 and C_2H_4 (total amount noted as C_2H_m) in the produced syngas obtained from GC measurements. If accounting for C_2H_m, the values of U, $\eta_{solar\text{-}to\text{-}fuel}$ and X_C are consistently increased.

Table B-1. Operating conditions and experimentally measured performance of the solar reactor during continuous operation.

Run #	Biomass type	$\dot{m}_{feedstock}$ (g/min)	$\dot{m}_{H_2O}$ (mg/min)	$\frac{H_2O}{feedstock}$	$\dot{m}_{Ar}$ (Nl/min)	T_3 (°C)	$\dot{Q}_{solar}$ (kW)	$\eta_{reactor}$ (%)	τ (sec)	Not accounting for C_2H_2 and C_2H_4			Accounting for C_2H_2 and C_2H_4		
										U	$\eta_{solar-to-fuel}$ (%)	X_c (%)	U	$\eta_{solar-to-fuel}$ (%)	X_c (%)
1	Type A	1.2	200	2.3	3.3	1100	0.89	18.2	0.83	0.91	13.3	79.2	1.03	15.1	83.7
2	Type A	1.5	200	2.1	3.3	1100	0.93	24.1	0.77	0.95	20.4	79.8	1.05	22.4	83.1
3	Type A	1.2	200	2.3	2.7	1200	1.08	20.2	0.98	0.97	18.1	78.8	1.04	19.5	81.5
4	Type A	1.5	200	2.1	2.7	1200	1.09	20.6	0.61	1.01	19.3	80.0	1.10	20.9	83.2
5	Type A	1.5	200	2.1	3.3	1200	1.16	17.9	0.85	1.01	15.7	83.8	1.11	17.3	87.4
6	Type A	1.8	300	2.3	2.7	1200	1.15	21.7	0.63	1.03	20.6	82.7	1.12	22.4	85.8
7	Type A	0.8	200	3	2.7	1300	1.20	15.3	0.96	0.94	12.4	75.0	0.99	13.0	77.0
8	Type A	1.2	200	2.3	2.7	1300	1.22	18.3	0.76	1.04	17.3	80.4	1.08	18.0	82.5
9	Type A	1.5	200	2.1	2	1300	1.22	17.3	0.95	1.14	19.4	86.2	1.17	19.9	87.7
10	Type A	1.5	200	2.1	2.3	1300	1.27	18.5	0.79	1.08	18.9	85.0	1.14	20.0	87.3
11	Type A	1.5	200	2.1	3.3	1300	1.22	17.7	0.74	1.05	15.5	84.8	1.14	16.9	88.2
12	Type A	1.8	200	1.8	2.7	1300	1.28	20.1	0.59	1.10	20.8	84.2	1.15	21.8	86.4
13	Type A	2.2	200	1.6	2.7	1300	1.25	20.1	0.59	1.03	19.4	80.3	1.13	21.2	83.9
14	Type A	2.2	300	2.1	2.7	1300	1.34	23.9	0.54	1.12	25.1	85.7	1.17	26.1	87.7
15	Type A	2.2	500	2.8	2.7	1300	1.33	24.9	0.53	1.10	24.6	85.4	1.17	26.3	88.3
16	Type A	2.5	400	2.2	2.7	1300	1.43	24.7	0.48	1.13	25.1	88.3	1.18	26.3	90.2
17	Type A	2.7	450	2.3	2.7	1300	1.44	25.3	0.47	1.14	26.6	88.6	1.19	27.8	90.4
18	Type B	1.2	200	2.3	2.7	1100	1.03	16.1	0.83	0.93	13.6	78.5	1.01	14.7	81.2
19	Type B	1.2	500	4.5	2.7	1100	1.01	23.1	0.84	0.96	18.9	80.6	1.09	21.5	85.2
20	Type B	0.8	500	6.4	2.7	1200	1.13	19.4	0.85	1.00	15.9	81.1	1.07	17.0	83.8
21	Type B	1.2	163	2	2.7	1200	1.13	18.2	0.74	0.99	16.8	78.4	1.09	18.5	82.0
22	Type B	1.2	200	2.3	2	1200	1.12	17.4	0.87	1.06	17.8	84.1	1.10	18.5	85.9
23	Type B	1.2	200	2.3	2.7	1200	1.16	18.6	0.68	1.01	17.7	81.0	1.07	18.7	83.3
24	Type B	1.2	200	2.3	3.2	1200	1.16	20.3	0.67	0.98	18.1	78.6	1.08	19.9	82.3
25	Type B	1.2	500	4.5	2.7	1200	1.18	21.0	0.74	1.01	18.1	81.3	1.08	19.4	83.8
26	Type B	1.5	500	3.8	2.7	1200	1.20	24.5	0.71	1.02	22.3	81.4	1.08	23.7	83.6
27	Type B	1.8	500	3.3	2.7	1200	1.20	24.9	0.69	1.02	22.8	81.8	1.11	24.6	84.7

28	Type B	0.8	140	2.4	2.7	1300	1.17	17.3	0.78	0.99	15.7	78.7	1.03	16.3	80.3
29	Type B	1.2	200	2.3	2.7	1300	1.23	17.5	0.67	1.03	17.5	78.6	1.08	18.3	80.8
30	Type B	1.2	500	4.5	2.7	1300	1.22	20.7	0.70	1.03	20.4	81.5	1.07	21.2	83.4
31	Type B	1.8	250	2	2.7	1300	1.24	23.6	0.58	1.09	24.0	83.1	1.1	25.0	85.1
32	Type B	2.2	300	2	2.7	1300	1.29	24.2	0.52	1.10	25.0	84.2	1.15	26.0	86.1
33	Type C	1.2	200	2.1	2.7	1100	0.86	17.5	0.85	0.91	16.1	71.7	1.05	18.5	76.3
34	Type C	1.2	200	2.1	2.7	1200	1.08	18.7	0.78	1.01	16.6	75.8	1.09	17.9	78.6
35	Type C	1.5	250	2.1	2.7	1200	1.09	19.6	0.73	1.03	17.5	79.2	1.10	18.7	81.6
36	Type C	1.8	300	2.1	2.7	1200	1.10	26.5	0.61	1.10	26.5	81.5	1.17	28.2	83.7
37	Type C	2.2	350	2.1	2.7	1200	1.15	27.1	0.55	1.11	26.8	82.3	1.21	29.2	85.6
38	Type C	1.2	200	2.1	2.7	1300	1.21	17.9	0.71	1.04	16.2	75.4	1.09	17.0	77.5
39	Type C	1.5	200	1.8	2.7	1300	1.22	20.0	0.54	1.12	19.8	79.1	1.17	20.8	81.4
40	Type C	1.8	300	2.1	2.7	1300	1.25	22.4	0.57	1.13	22.4	80.7	1.19	23.6	83.0
41	Type C	2.2	350	2.1	2.7	1300	1.26	26.5	0.54	1.14	26.7	81.1	1.20	28.1	83.3
42	Type C	2.5	450	2.2	2.7	1300	1.30	27.0	0.51	1.16	27.6	84.0	1.22	29.0	86.1
43	Type C	2.7	500	2.3	2.7	1300	1.43	24.2	0.51	1.14	24.3	84.3	1.24	26.4	87.6
44	Type D	0.8	200	3.3	2.7	1100	0.89	16.4	0.95	0.97	14.0	77.5	1.06	15.2	80.3
45	Type D	1.2	200	2.5	3.3	1100	0.87	17.5	0.76	0.97	13.1	75.5	1.06	14.3	78.9
46	Type D	0.8	200	3.3	2.7	1200	1.03	15.8	0.92	1.02	13.6	78.5	1.07	14.2	80.5
47	Type D	1.2	200	2.5	2.7	1200	1.18	20.3	0.65	1.06	20.4	79.5	1.11	21.4	81.3
48	Type D	1.2	200	2.5	3.3	1200	1.15	14.9	0.66	0.99	11.8	77.0	1.04	12.4	79.0
49	Type D	1.8	450	3.3	2.7	1200	1.15	26.5	0.64	1.07	25.4	79.2	1.13	26.8	81.2
50	Type D	0.8	200	3.3	2.7	1300	1.17	16.1	0.81	1.07	14.8	76.4	1.12	15.5	78.6
51	Type D	1.2	360	3.8	2.7	1300	1.29	19.9	0.66	1.13	20.0	80.6	1.18	20.8	82.4
52	Type D	1.2	200	2.5	3.3	1300	1.20	16.9	0.68	1.02	17.5	73.3	1.06	18.3	75.1
53	Type D	1.5	450	3.8	2.7	1300	1.27	22.3	0.61	1.14	22.4	80.3	1.20	23.6	82.4
54	Type D	1.8	500	3.6	2.7	1300	1.30	22.6	0.60	1.20	23.4	84.9	1.24	24.3	86.7
55	Type D	2.2	500	3.1	2.7	1300	1.43	24.0	0.58	1.16	25.3	82.7	1.20	26.3	84.3
56	Type E	0.8	500	7	2.7	1100	0.98	19.4	0.95	1.00	15.4	72.9	1.10	17.0	76.2
57	Type E	1.2	300	3.3	2.7	1100	0.99	17.4	0.86	1.03	14.6	74.8	1.14	16.2	78.3
58	Type E	0.6	200	4.1	2.7	1200	1.07	15.0	1.02	0.98	11.8	69.9	1.02	12.3	71.7
59	Type E	0.8	200	3.3	2.7	1200	1.08	16.0	0.88	1.00	13.7	70.6	1.05	14.4	72.6
60	Type E	1.2	300	3.3	2.7	1200	1.12	19.5	0.81	1.11	18.7	76.3	1.15	19.4	78.0
61	Type E	1.5	350	3.2	2.7	1200	1.13	20.4	0.70	1.15	20.0	80.6	1.20	20.8	82.4
62	Type E	0.8	200	3.3	2.7	1300	1.19	15.7	0.82	1.13	15.0	77.0	1.16	15.4	78.3
63	Type E	1.2	300	3.3	2.7	1300	1.28	19.0	0.80	1.12	16.6	76.1	1.14	16.9	77.4
64	Type E	1.5	350	3.2	2.7	1300	1.24	21.2	0.67	1.15	21.2	76.7	1.19	21.8	78.2

The U values were in the ranges of 0.91-1.14, 0.93-1.10, 0.91-1.16, 0.97-1.20 and 0.98-1.15 for biomass types A, B, C, D and E, respectively. When accounting for C_2H_m, the U (C_2H_m) values were in the ranges of 1-1.19, 1.01-1.15, 1.05-1.24, 1.04-1.24 and 1.02-1.20 for biomass types A, B, C, D and E, respectively. A few experiments show a value of U below one, especially at both the lowest operating temperature or at the lowest biomass feeding rates due to low reaction kinetics and low conversion rates. However, when accounting for the calorific value of C_2H_m, all of the U values are above one. On the one hand, the values of U lower than one mean that the solar energy was not stored efficiently in the chemical form and the upgrading of the calorific value of the feedstock was not successful. On the other hand, the

values of U higher than one indicate that the solar energy was successfully stored in chemical form and the calorific value of the feedstock was upgraded by the solar gasification process.

Table B-2 compares the highest energy upgrade factor at 1300 °C to the theoretical maximum values attained at the thermodynamic equilibrium reached above 1000 °C when assuming complete biomass conversion into only H_2 and CO species. Considering the U values when accounting for C_2H_m, biomass type A shows the highest percentage of U achieved as compared to equilibrium (93%).

Table B-2. Comparison of highest energy upgrade factor to theoretical one based on equilibrium.

Type	Run No.	$\dot{m}_{feedstock}$ (g/min)	T_3 (°C)	Energy upgrade factor (U)			
				Theoretical U	U	U (accounting for C_2H_m)	% of maximum achievable value
Type A	17	2.7	1300	1.28	1.14	1.19	93
Type B	32	2.2	1300	1.28	1.10	1.15	90
Type C	42	2.5*	1300	1.40	1.16	1.22	87
Type D	54	1.8*	1300	1.44	1.20	1.24	86
Type E	64	1.5	1300	1.44	1.15	1.19	83

*at optimal biomass feeding rate

Note that the conventional autothermal gasification achieves a U value of approximately 0.7 depending on feedstock [126], as a result of a significant portion of the feedstock being combusted for supplying process heat to the endothermic reaction. The calorific value of the produced syngas was solar upgraded by 15-24% with respect to the feedstock, thus highly outperforming the U obtained from conventional autothermal gasification process.

The $\eta_{solar\text{-}to\text{-}fuel}$ varies in the ranges of 12.4-26.6%, 13.6-25.0%, 16.1-27.6%, 11.8-25.4% and 11.8-21.2% for biomass types A, B, C, D and E, respectively. When accounting for C_2H_m, the values in the ranges of 13.0-27.8%, 14.7-26.0%, 17.0-29.2%, 12.4-26.8% and 12.3-21.8% were achieved. The lowest $\eta_{solar\text{-}to\text{-}fuel}$ were found at low biomass feeding rates as a result of inefficient utilization of the solar energy and limited syngas production, at the expense of higher heat losses. Obviously, increasing biomass feeding rate significantly enhanced the $\eta_{solar\text{-}to\text{-}fuel}$. Conversely, excessively high biomass feeding rate reduced the $\eta_{solar\text{-}to\text{-}fuel}$. Thus, optimal biomass feeding rate was evidenced for achieving maximum reactor performance as well as syngas production.

Likewise, the $\eta_{reactor}$ increased with biomass feeding rate ranging between 15.3-25.3 %, 16.1-24.9%, 17.5-27.1%, 14.9-26.5% and 15-21.2% for biomass types A, B, C, D and E, respectively. The lowest $\eta_{reactor}$ values were observed at the lowest biomass feeding rate, meaning that high heat losses occurred because of the extended biomass injection duration (for the same amount of feedstock injected). Increasing the biomass feeding rate inherently reduced the processing duration (for a given amount of biomass) and thus the amount of solar energy absorbed by the reactor, which in turn drastically enhanced the reactor efficiency with maximum values typically above 25%. Based on all of the experimental results, the peak values of the performance indicators achieved were: U=1.24 obtained for biomass types C and D, $\eta_{solar\text{-}to\text{-}fuel}$ = 29.2 % obtained for biomass type C, X_C= 90.4% obtained for biomass type A, $\eta_{reactor}$ = 27.1% obtained for biomass type C.

c. Window deposit due to the presence of smoke at low temperature

Fig. B-3 shows the dirt on the window as a result of smoke release during gasification process at 1100 °C.

Figure B-3. Dirt deposits on the window observed at low temperature (1100°C).

d. Effect of temperature on syngas yield and energy upgrade factor

Additional experiments (Fig. B-4) were carried out to validate the effect of temperature (1100-1300 °C) on syngas production and energy upgrade factor (U). The biomass feeding rates were 1.5 g/min for biomass type A (Fig. B-4a) and 1.2 g/min for biomass types B (Fig. B-4b) and D (Fig. B-4c). Ar and steam flow rates were fixed (3.3 Nl/min and 200 mg/min for biomass types A and D, 2.7 Nl/min and 500 g/min for biomass type B, respectively).

The results confirm that an increase in the temperature promoted total syngas yield, regardless of operating conditions and biomass types (Fig. B-4). H_2 and CO yields increased while C_2H_m, CH_4, and CO_2 yields decreased with increasing temperature. Moreover, a substantial enhancement of the syngas yield consistent with temperature led to an increase in U. It can be noticed again that a higher C_2H_m production occurred when reducing temperature, which in turn increased U(C_2H_m) because of the high calorific value of C_2H_m.

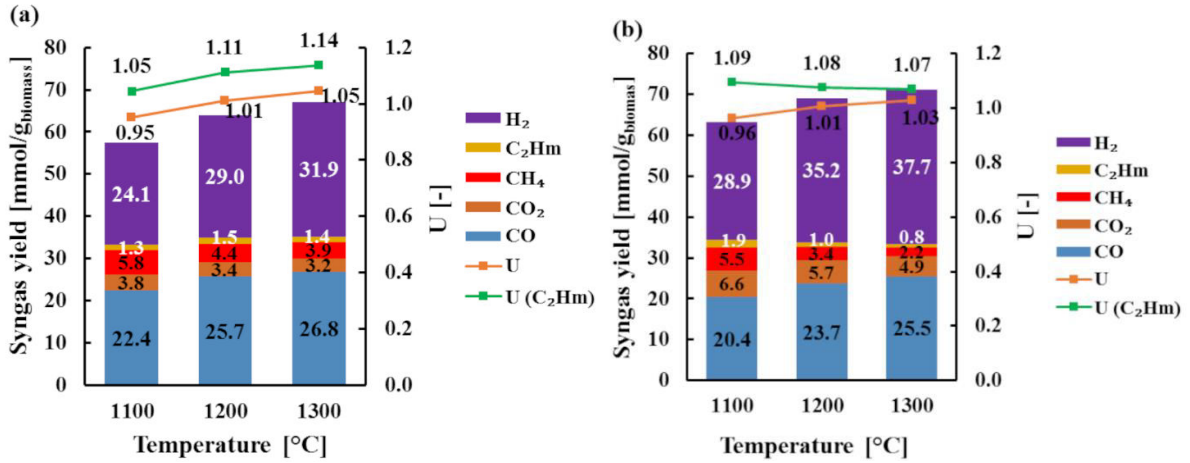

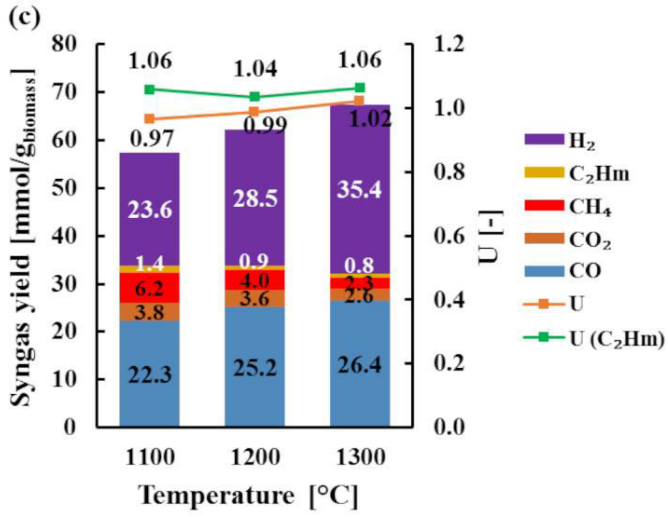

Figure B-4. Temperature influence on syngas yields and energy upgrade factors for biomass types A (a), B (b), and D (c).

e. Kinetic study

The Arrhenius kinetic rate expression is generally utilized to evaluate the influence of temperature on the rates of chemical reactions.

$$k = A \cdot \exp(-E_a/RT) \quad \text{(B-1)}$$

Where k is the reaction rate constant, A is the pre-exponential factor, E_a is the activation energy, R is the gas constant and T is the absolute temperature.

In this study, the reaction rate constants (k) were obtained for each biomass type and temperatures from the average nominal syngas production rates of H_2 and CO at steady state, which are the main gaseous species contained in the produced syngas during continuous biomass feeding. The logarithm evolution of the reaction rates versus inverse temperature (Eq. B-1) was subsequently plotted from 1100 to 1300 °C, and the values of activation energy (E_a) for each biomass type were consequently obtained as presented in Fig. B-5. A significant beneficial effect of the temperature on the production rates of H_2 and CO was observed. The obtained activation energy (E_a) of the syngas production mechanism, determined from the slope of the line in Fig. B-5, was consistent with biomass particle size (low particle sizes feature a lower E_a, thus favoring rapid gasification rates). For example, the E_a values (Table B-3) for H_2 and CO increased from ~24 kJ/mol (at 0.3 mm size for biomass type D) to ~29 kJ/mol (at 4 mm size for biomass type B). This denotes the sensitivity of the gasification rate to the particle size. Moreover, the E_a values obtained independently from H_2 and CO rates evolution were similar for any biomass types, thus indicating that the H_2 and CO production rates are mainly governed by the same global reaction mechanism (Eq. 1-16).

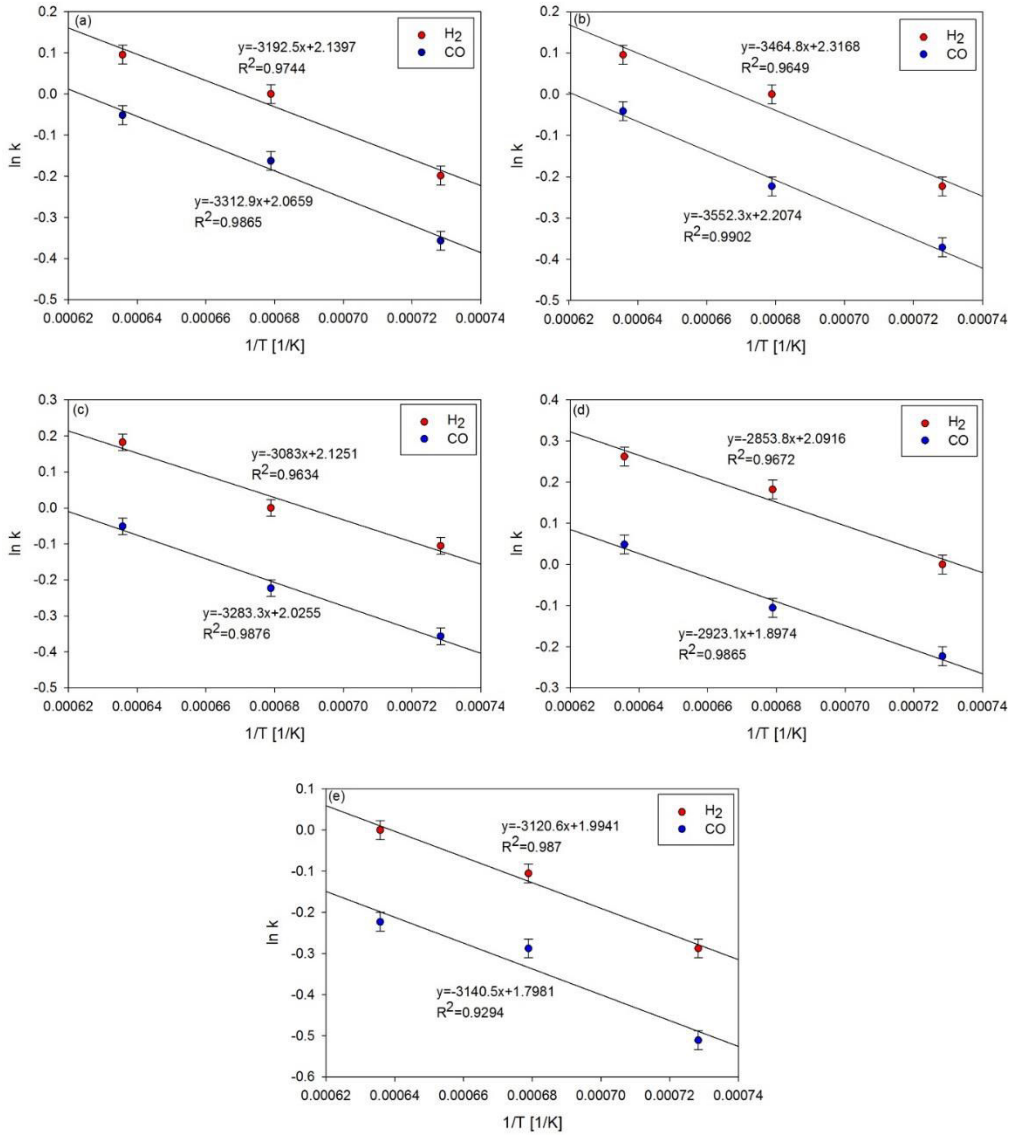

Figure B-5. Arrhenius plot based on H_2 and CO production rates for biomass types A (a), B (b), C (c), D (d) and E (e) at 1100-1300 °C (biomass feeding rate of 1.2 g/min).

Table B-3. Activation energy related to the H_2 and CO production rates obtained by Arrhenius plot.

Biomass type	Gaseous Specie	E_a (kJ/mol)
Type A (1 mm)	H_2	26.5±3
	CO	27.5±3
Type B (4 mm)	H_2	28.8±4
	CO	29.5±4
Type C (0.55 mm)	H_2	25.6±3
	CO	27.3±3
Type D (0.30 mm)	H_2	23.7±4
	CO	24.3±4
Type E (2 mm)	H_2	25.9±5
	CO	26.1±5

f. Ashes remaining in the reactor cavity

Fig. B-6 shows the presence of ashes remaining inside the reactor cavity (brown color particles covering the black SiC particles), which decreased when increasing the temperature from 1100 °C to 1300 °C. This indicates that ashes were presumably melted when the temperature increased, which may in turn favor the corrosion of the cavity walls (because of the presence of alkali metal chlorides) in accordance with the black circles on the wall surface (note that the cavity bottom was filled with SiC particles to avoid the trickling of melted ashes that may clog the gas inlet). At the lowest temperatures, non-melted ashes can be evacuated by the gas flow that is why they do not accumulate inside the reactor.

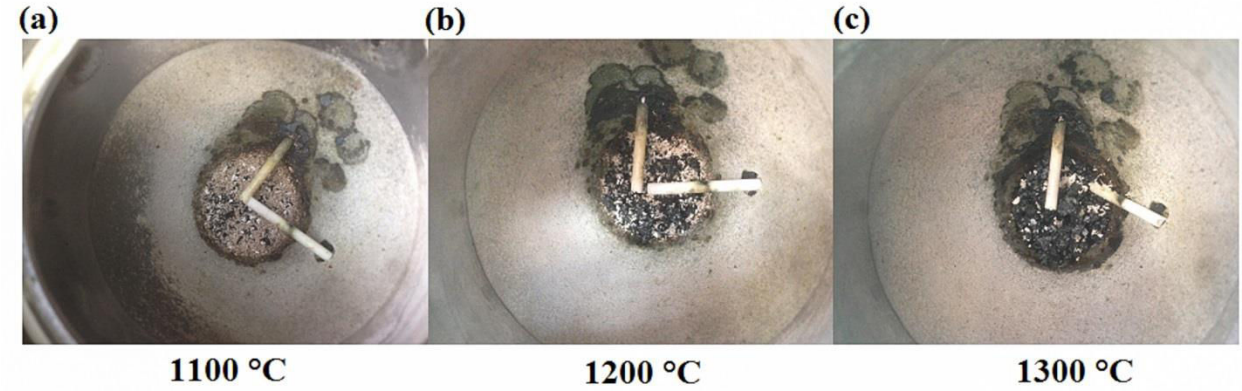

Figure B-6. Ashes remaining inside the reactor cavity for biomass type A at (a) 1100 °C, (b) 1200 °C, and (c) 1300 °C (same amount of biomass injected, 30 g).

g. Effect of biomass feeding rate on syngas yield at 1200 and 1300 °C

Fig. B-7 presents the syngas yields of H_2, CO, CH_4, CO_2 and C_2H_m for each biomass type as a function of biomass feeding rate at 1200 °C. Overall, the H_2 and CO yields increased significantly with biomass feeding rate (Figs. B-7a and B-7b). For example, the H_2 and CO quantities for biomass type E rose from 30.5 and 23 mmol/$g_{biomass}$ at 0.6 g/min to 38.9 and 27.8 mmol/$g_{biomass}$ at 1.5 g/min, respectively. The CO_2, CH_4 and C_2H_m yields first fluctuated slightly between 0.6-0.8 g/min (especially for biomass type E due to a feeding interruption issue in the biomass delivery), and then increased consistently with biomass feeding rate (Figs. B-7c and B-7d). For example, the CO_2, CH_4 and C_2H_m yields for biomass type C increased form 3.2, 2.7 and 1.2 mmol/$g_{biomass}$ at 1.2 g/min to 3.5, 3.5 and 1.3 mmol/$g_{biomass}$ at 2.2 g/min, respectively. Thus, increasing biomass feeding rate accelerated the consumption rate of biomass, which directly promoted syngas yields. Nevertheless, an increase in biomass feeding rate favored the formation of C_2H_m, CH_4 and CO_2 because of the produced gas flow-rate increase (gas expansion) and gas residence time decrease (e.g., decreasing from 0.98 s at 1.2 g/min to 0.63 s at 1.8 g/min for biomass type A).

The effect of biomass type (composition) on syngas yield was observed. For instance, biomass types E and D exhibit higher syngas yields, particularly H_2, CO and CO_2, than biomass types A and C. In contrast, the effect of particle size on syngas yield was negligible (biomass type E compared to D).

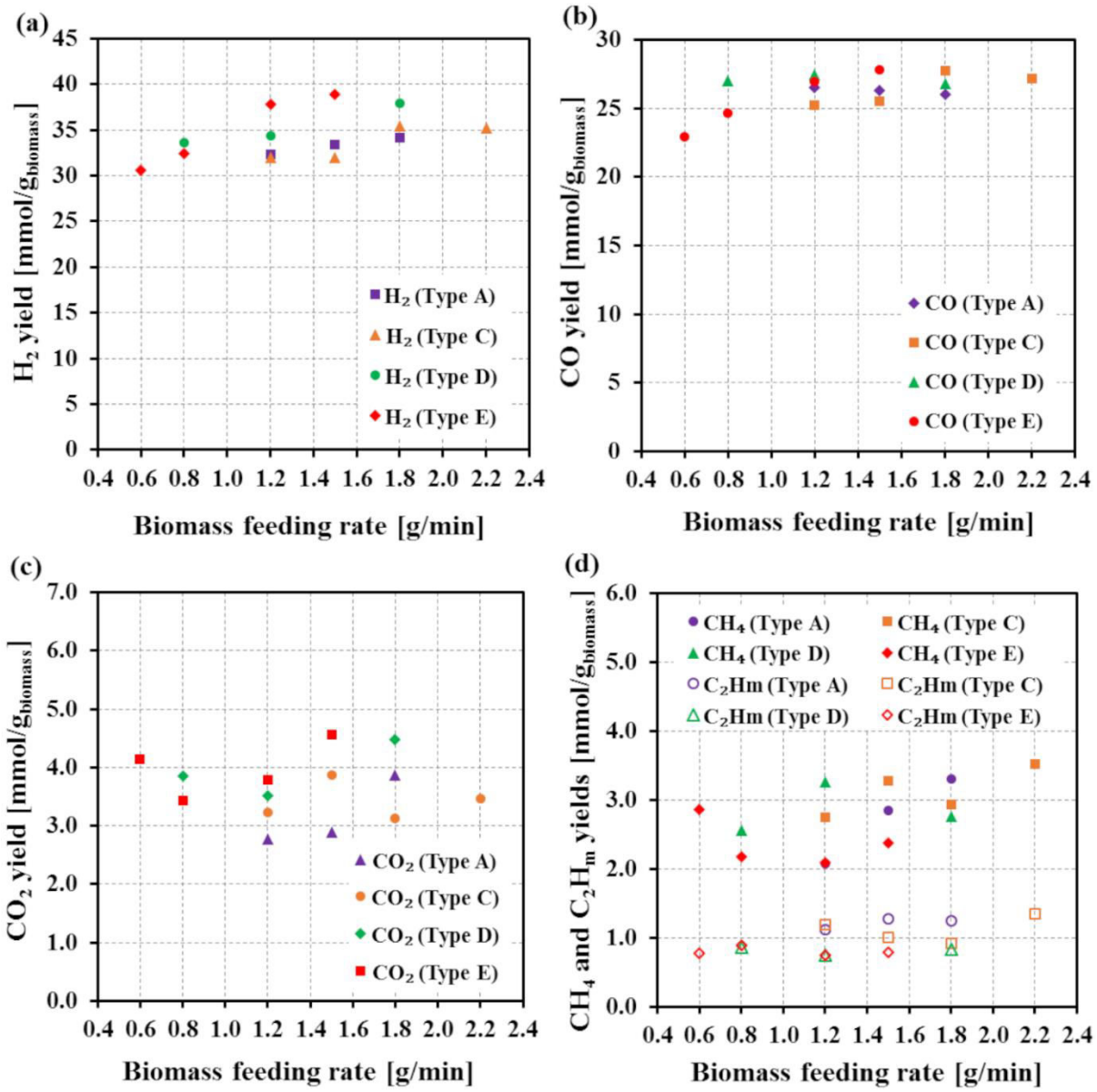

Figure B-7. Influence of biomass feeding rate on syngas yield for different biomass feedstocks at 1200 °C.

Fig. B-8 shows the H_2, CO, CO_2, CH_4 and C_2H_m yields as a function of biomass feeding rate for each biomass type at 1300 ℃. The H_2 and CO yields increased considerably with biomass feeding rate, and some of them then diminished after their optimal biomass feeding point. For example, the H_2 and CO yields for biomass type C reached the maximum value of 39.2 and 29.1 mmol/$g_{biomass}$ at 2.5 g/min and then reduced to 37.6 and 27.9 mmol/$g_{biomass}$, respectively, at 2.7 g/min. Similarly, with the increase of biomass feeding rate, the amounts of CO_2 and CH_4 for biomass type C increased in the ranges of 2.5-4.0 and 1.7-3.2 mmol/$g_{biomass}$, respectively, while the C_2H_m yields increased slightly in the range of 0.9-1.4 mmol/$g_{biomass}$. Increasing the biomass feeding rate promoted syngas yield; however, an increase in CO_2, CH_4 and C_2H_m yields due to a lowered gas residence time led to a negative impact on syngas quality. Small fluctuation in the CO_2 yields (Fig. B-8c) is attributed to temporal changes in the H_2O/biomass ratio, which influences water-gas shift reaction ($CO+H_2O \rightarrow CO_2+H_2$), because of

transient variations in feedstock delivery. Similar trends of H_2 yield between biomass types A and B and between biomass types D and E were observed thanks to their similar initial chemical composition. The H_2 yields for biomass types D and E were higher than the other types owing to their higher initial hydrogen content in the feedstock.

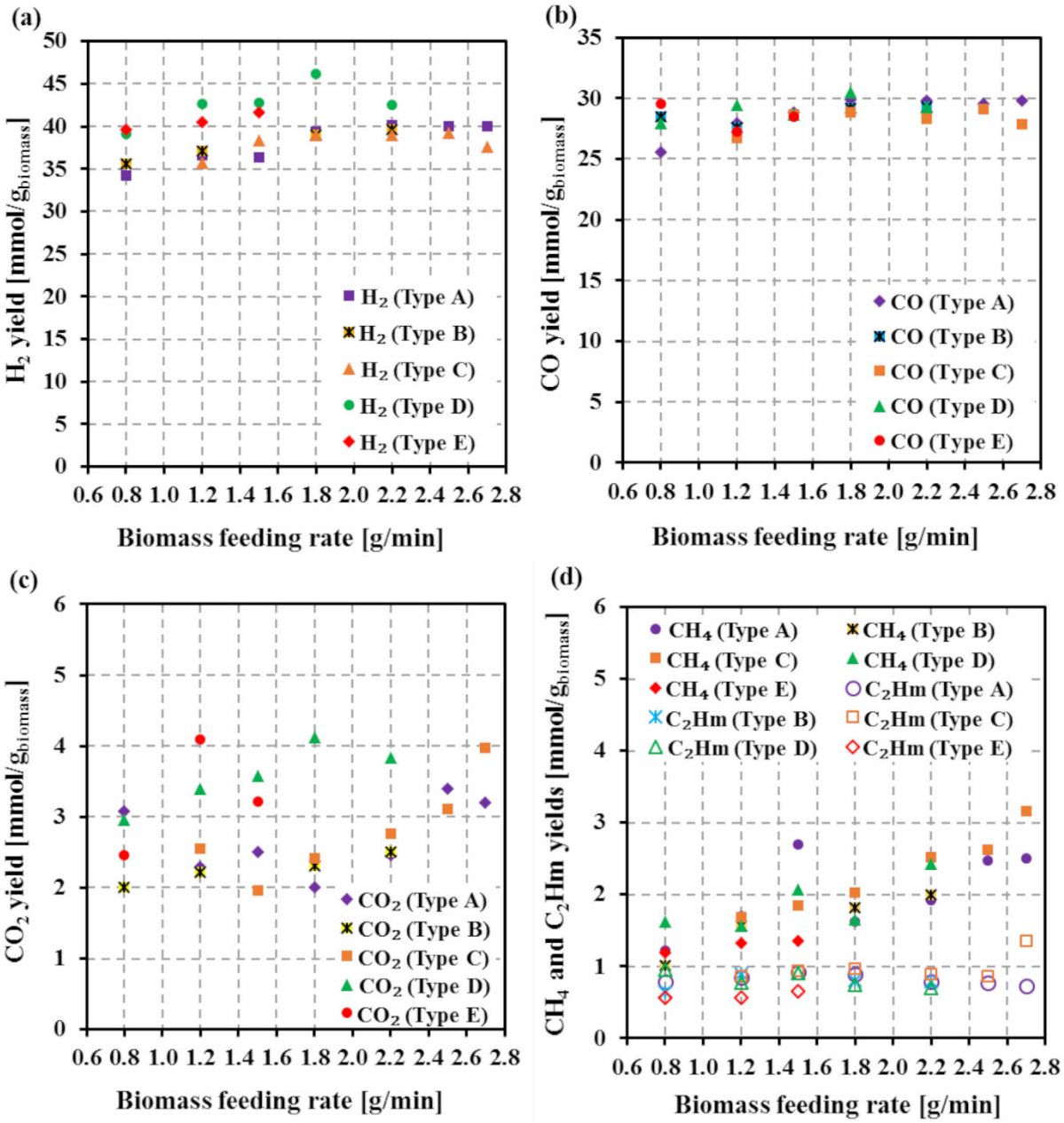

Figure B-8. Influence of biomass feeding rate on syngas yield for different biomass feedstocks at 1300 °C.

h. Effect of biomass feeding rate on reactor performance at 1200 and 1300 °C

The effect of biomass feeding rate on U, X_C, $\eta_{solar\text{-}to\text{-}fuel}$, $\eta_{reactor}$, solar power and solar energy inputs was studied at 1200 °C (Fig. B-9). As expected, U increased with biomass feeding rate (Fig. B-9a) with the maximum value of 1.15 (1.20 if accounting for C_2H_m) at the maximum biomass feeding rate for biomass type E while the U values for all the biomass types were in the range of 0.97-1.15 (1.04-1.20 if accounting for C_2H_m). Increasing biomass feeding

rate favored syngas production capacity, thus resulting in a significant improvement of X_C with a maximum value of 82.7% (85.8% if accounting for C_2H_m) at 1.8 g/min for biomass type A (Fig. B-9b) and thereby leading to an increase in U. In addition, both U and X_C tended to level off when increasing biomass feeding rate (above 1.5 g/min), especially for biomass type C, thus indicating that the optimal feeding point would be approached.

A significant beneficial enhancement of $\eta_{solar\text{-}to\text{-}fuel}$ while increasing biomass feeding rate was highlighted (Fig. B-9c). $\eta_{solar\text{-}to\text{-}fuel}$ in the range of 11.8-26.8% (12.3-29.2% if accounting for C_2H_m) was achieved (previous studies on solar gasifiers reported maximum efficiencies of 35% for a 150 kW packed-bed reactor [126], 30% for a prototype 2.2 kW molten salt reactor [131] and 20% for a continuous 3 kW vortex flow reactor [118]). In addition, increasing biomass feeding rate drastically decreased the solar energy input (Fig. B-9d), arising from the shortened biomass injection duration time, whereas the solar power input was increased (between 1.03-1.15 kW depending on the biomass type, Fig. B-9f) to stabilize the operating temperature. Otherwise, the increase of the amount of injected biomass (as well as concomitant steam flow rate increase to maintain constant the steam/biomass ratio) would result in exacerbating the temperature decrease because of the energy consumed by the reaction and the reactants heating (see the section on energy balance number 3.3.7). Furthermore, a sharp increase of $\eta_{reactor}$ with biomass feeding rate was also highlighted ($\eta_{reactor}$ ranging between 15.0 and 27.1%), regardless of the biomass types (Fig. B-9e). Increasing the biomass feeding rate inherently reduced heat losses by lowering the operating duration time, which directly decreased the required solar energy input and increased $\eta_{reactor}$. For the considered range of biomass feeding rate (0.6-2.2 g/min) at 1200 °C, it can be concluded that the higher the biomass feeding rate (within the feeder capacity range), the higher the $\eta_{solar\text{-}to\text{-}fuel}$ and the $\eta_{reactor}$, demonstrating efficient utilization of solar energy. Moreover, the additional tests with higher feeding rate for each biomass type are necessary to find their optimal feeding rate.

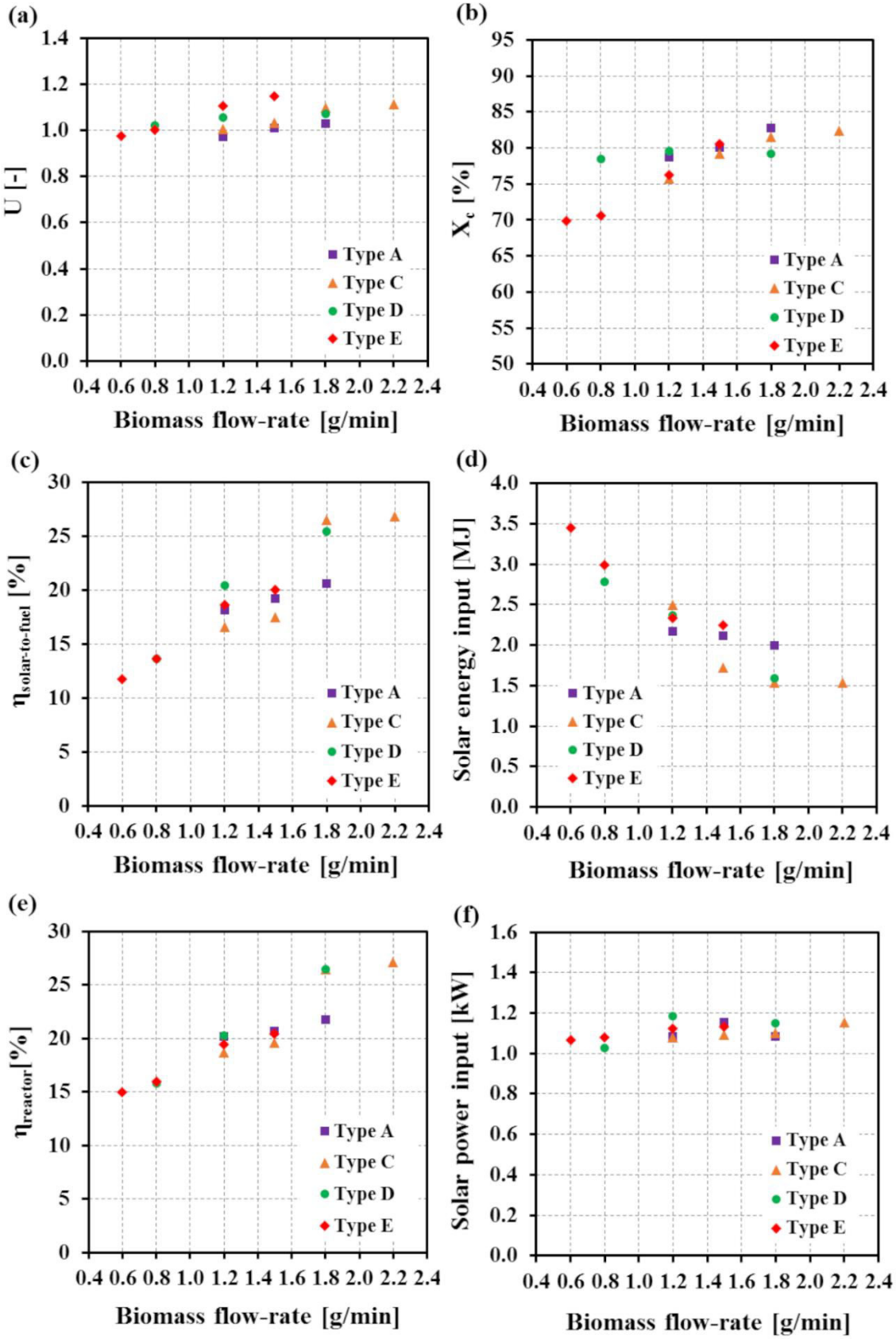

Figure B-9. Influence of biomass feeding rate on (a) energy upgrade factor, (b) carbon conversion,(c) solar-to-fuel energy conversion efficiency, (d) solar energy input, (e) themochemical reactor efficiency and (f) solar power input at 1200 °C (C_2H_m not included in the calculation).

The influence of biomass feeding rate on sola r reactor performance at 1300 ℃ is shown in Fig. B-10. The energy upgrade factor increased with $\dot{m}_{feedstock}$ and then leveled off above 1.8 g/min (Fig. B-10a), thereby pointing out the optimal biomass feeding rate. The maximum U values of 1.14, 1.10, 1.16, 1.20 and 1.15 (1.19, 1.15, 1.22, 1.24 and 1.19 when accounting for C_2H_m) were identified for biomass types A (at 2.7 g/min), B (at 2.2 g/min), C (at 2.5 g/min), D (at 1.8 g/min) and E (at 1.5 g/min), respectively. The optimal $\dot{m}_{feedstock}$ regarding the highest U value was found at 2.5 and 1.8 g/min for biomass types C and D, respectively. These biomass types exhibit the lowest particle sizes; therefore, their gasification is more sensitive to the feeding rate. In contrast, the optimum could not be found for the other biomass types due to the limitation of the maximum feeding rate offered by the delivery system. The overlapped trends for U between biomass types A and B and between biomass types D and E were observed, presumably due to their similar chemical properties, indicating a negligible impact of the biomass particle size on U for the considered size range (0.3−4 mm). In addition, the evolution of U consistently followed the same trend as X_C (Fig. B-10b). Both the highest and the lowest X_C values of 88.6 and 75.0% (90.4 and 77.0% when accounting for C_2H_m) were obtained for biomass type A at 2.7 and 0.8 g/min, respectively. With the increase of $\dot{m}_{feedstock}$, a sharp increase in the solar-to-fuel energy conversion efficiency ($\eta_{solar-to-fuel}$) was highlighted (Fig. B-10c), e.g., increasing from 12.4 % at 0.8 g/min to 26.6 % at 2.7 g/min for biomass type A. This is because the solar energy input (Fig. B-10d) dropped considerably by increasing $\dot{m}_{feedstock}$, because of a significant reduction in the biomass injection duration time although the solar power input (Fig. B-10f) was oppositely increased to stabilize the operating temperature when increasing $\dot{m}_{feedstock}$.

As illustrated in Fig. B-10c, $\eta_{solar-to-fuel}$ for biomass type C dropped noticeably at the highest biomass feeding rate because excessively high $\dot{m}_{feedstock}$ (2.7 g/min) caused the incomplete reactions of biomass gasification, which in turn results in both the solid reactants accumulation and the presence of smoke in the reactor cavity. This necessitates intermittent stops in the biomass feeder in order to let the accumulated reactants being gasified with steam. For this reason, the biomass injection time was expanded, thereby resulting in the increase of solar energy input (Fig. B-10d). The $\eta_{solar-to-fuel}$ showed the inverse trend of solar energy input, thus pointing out efficient utilization of the solar energy input with lower heat losses by the biomass feeding rate adjustment. The maximum $\eta_{solar-to-fuel}$ values of 26.6%, 25%, 27.6%, 25.3% and 21.2% (27.8%, 26.0%, 29.0%, 26.3% and 21.8% when accounting for C_2H_m) were reached for biomass types A (at 2.7 g/min), B (at 2.2 g/min), C (at 2.5 g/min), D (at 2.2 g/min) and E (at 1.5 g/min), respectively.

Fig. B-10e depicts the effect of $\dot{m}_{feedstock}$ on the thermochemical reactor efficiency ($\eta_{reactor}$), which is defined as the fraction of solar power input dedicated to the reaction (energy consumed by the endothermal reaction and the reactant heating), while the remaining energy represents the energy losses by conduction, convection and radiation. The $\eta_{reactor}$ increased with $\dot{m}_{feedstock}$, ranging between 15.3-25.3%, 17.3-24.2%, 17.9-27.0%, 16.1-24.0% and 15.7-21.2% for biomass types A, B, C, D and E, respectively. This indicates that increasing $\dot{m}_{feedstock}$ directly entails an efficient solar energy conversion, which in turn results in a reduction of the heat losses. The lowest $\eta_{reactor}$ values were observed at the lowest $\dot{m}_{feedstock}$, meaning that high heat losses occurred because of the extended biomass injection duration (for the same amount of feedstock injected).

Besides, the $\eta_{reactor}$ follows the same trend as $\eta_{solar-to-fuel}$ (Fig. B-10c). The $\eta_{reactor}$ decreased when injecting biomass at $\dot{m}_{feedstock}$ over an optimum point (2.5 g/min for biomass type C). At this point, the reactant consumption rate by the gasification reaction becomes lower than the injection rate, which leads to accumulation and extension of the reaction duration, thereby leading to higher heat losses.

According to Fig. B-10f, the solar power inputs consumed by any biomass variants were not significantly different within the range of 0.8-1.8 g/min but they tended to be significantly different at higher feeding rates. For example, biomass type D required higher solar power input than the other variants when considering $\dot{m}_{feedstock}$ in the range of 1.8-2.2 g/min, which may be attributed to its smallest particle size favoring the gasification rate, thus implying higher solar power consumption than other biomass variants.

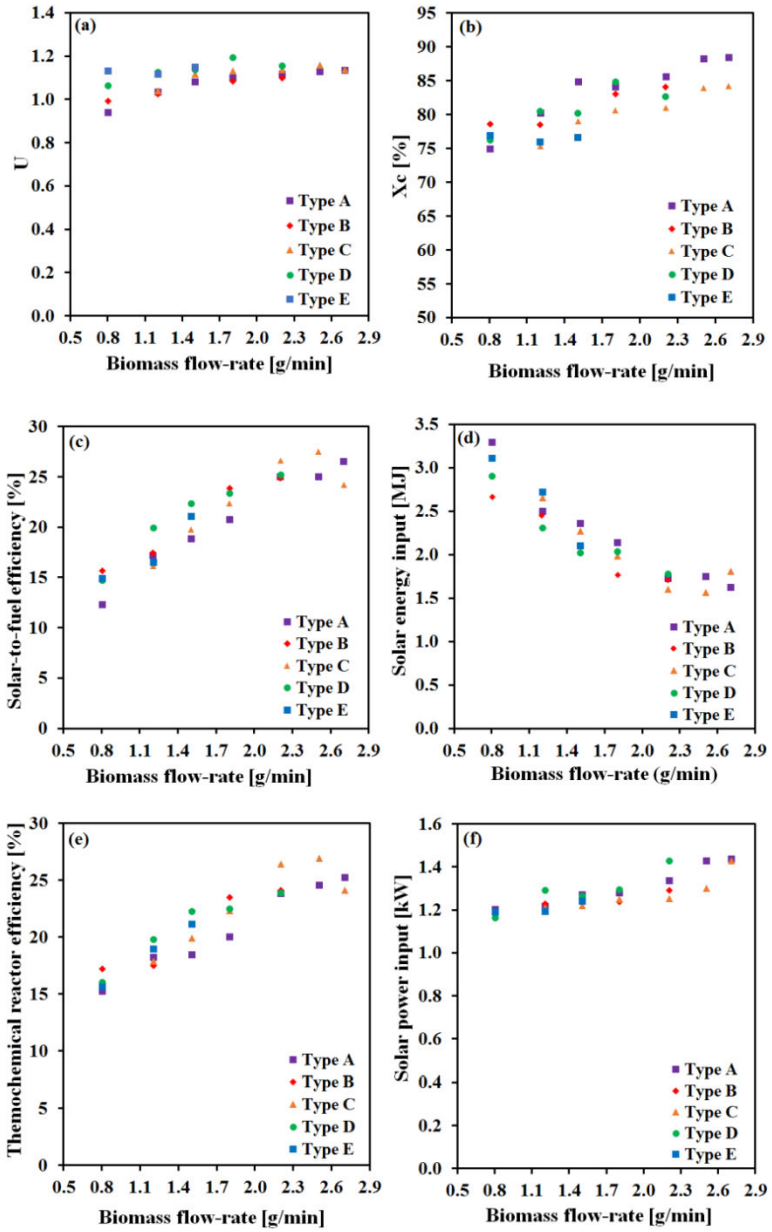

Figure B-10. Influence of biomass feeding rate on (a) energy upgrade factor, (b) carbon conversion,(c) solar-to-fuel energy conversion efficiency, (d) solar energy input, (e) themochemical reactor efficiency and (f) solar power input at 1300 °C (C_2H_m not included in the calculation).

Appendix C: Solar carbothermal reduction of ZnO and MgO

a. Carbothermal reduction of ZnO

1. Materials

Table C-1 Physical properties of solid carbonaceous materials.

Material	Supplier	Purity (%)	Average particle size (µm)	Specific surface area (m^2/g) (data sheet)	Specific surface area (m^2/g) (measured)
Activated charcoal (AC) Darco®	Sigma Aldrich	99.9	<149	732	811
Carbon black (CB), SB905 powder	Asahi Carbon (Japan)	99.9	15.10^{-3}	210	181
Graphite	Sigma Aldrich	99.9	<20	77	65
Beech wood ($C_6H_9O_4$)	Proximate analysis (wt%) moisture:8.9, ash: 0.46		Ultimate analysis (wt%) C: 48.3, H: 6.7, O: 44.4, N: 0.11, S: <0.1		

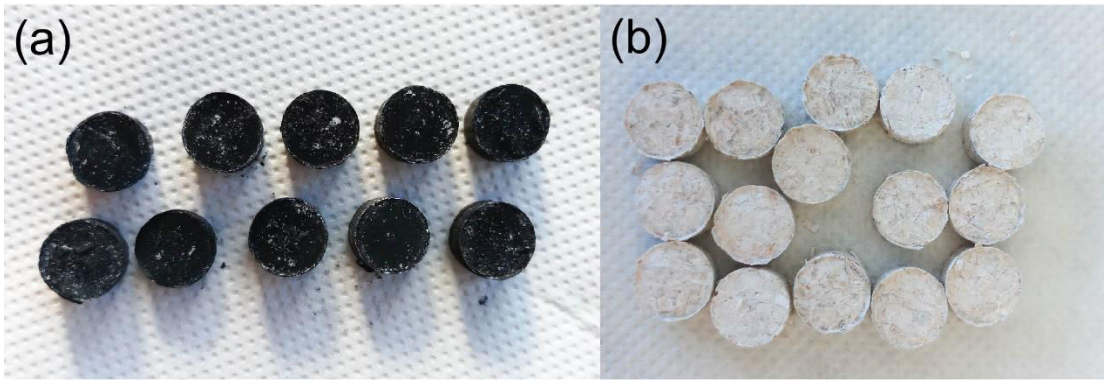

Figure C-1. Photographs of (a) ZnO+1.5CB pellets and (b) ZnO+0.75$C_6H_9O_4$ pellets.

2. Reactor prototype

The reactor is composed of an inner cylindrical cavity receiver made of alumina (Fig. C-2a) with a 0.121 L volume (47 mm ID, 56 mm OD, and 70 mm height) surrounded by a layer of porous ceramic insulation (40 mm-thick alumino-silicate layer, Fig. C-2b), thereby enabling rapid solar heating to the desired temperature. The bottom of the cavity is sealed with a circle alumina plate pierced at its center (4 mm diameter) so that a small alumina tube (4 mm O.D. and 2 mm I.D.) can be inserted for the injection of nitrogen (N_2) carrier gasto the cavity receiver. The whole cavity and insulation is vertically placed in a water-cooled cylindrical stainless-steel shell (Fig. C-2b, 170 mm O.D., 150 mm I.D., and 151 mm height, volume: 2.67 L). Two stainless-steel tubes (6 mm O.D. and 4 mm I.D.) are inserted vertically in the insulation layer exiting into the transparent window area (Fig. C-2b) to inject N_2 protective gas directly into the window area. This gas subsequently enters downwardly the cavity through the aperture before exiting with the product gases through the outlet port, thereby protecting the transparent window from products deposition. A packed bed of inert alumina particles (2 mm diameter) is placed at the bottom of the cavity receiver above a layer of alumina wool to support the reacting powders (Fig. C-2c). The top of the cavity receiver is covered by an alumina cap with a 17 mm-diameter aperture where concentrated solar radiation enters the cavity receiver (Fig. C-2d), and a protective graphite plate (2 mm-thick) with a 15 mm-diameter aperture is then placed

on top of the alumina cap to protect it (Fig. C-2e). A hemispherical transparent glass window is lastly attached to the front flange edge of the reactor shell (Fig. C-2f).

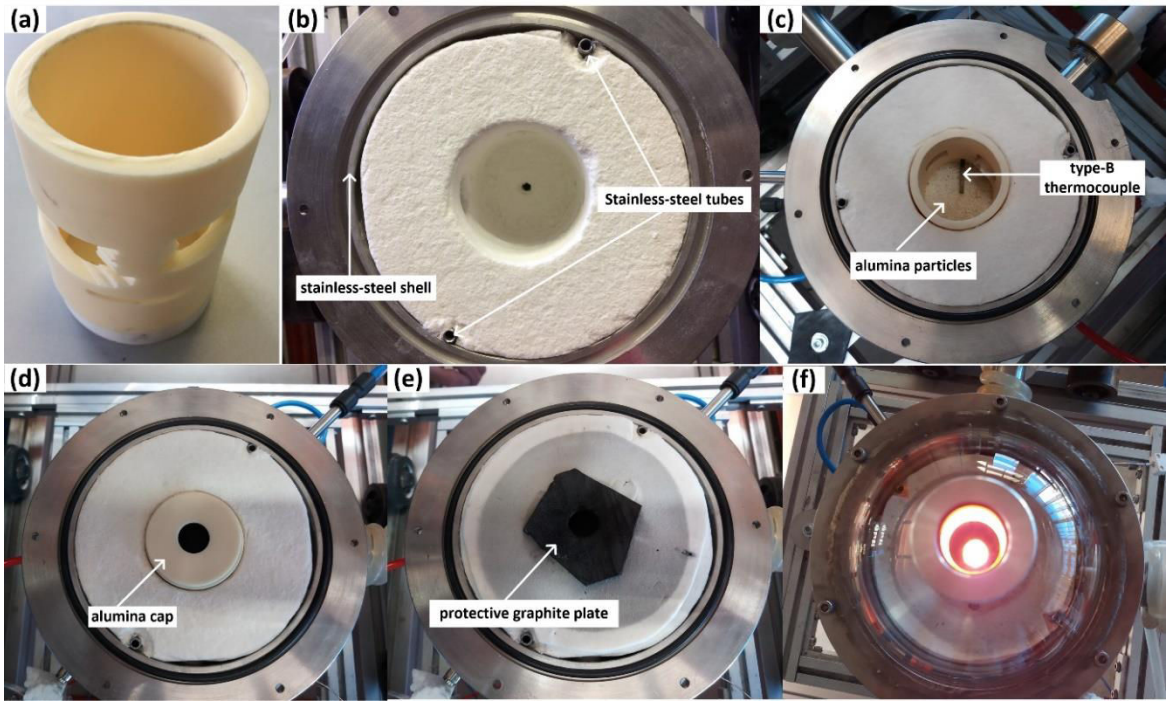

Figure C-2. Photographs of (a) reactor cavity receiver, (b) 40 mm-thick alumino-silicate insulation layer, (c) installation of cavity, insulation, thermocouple, alumina particle, inlet tube, and outlet tube, (d) alumina cap, (e) protective graphite plate, and (f) red hot cavity after a solar run at 1650 °C.

During continuous operation (Fig. C-3), the reactor was equipped with an automatic particle delivery system consisting of a hopper (1.15 L capacity) and a screw feeder (40 cm length) driven by an electrical motor, in order to directly inject the MgO particles in the reactor cavity.

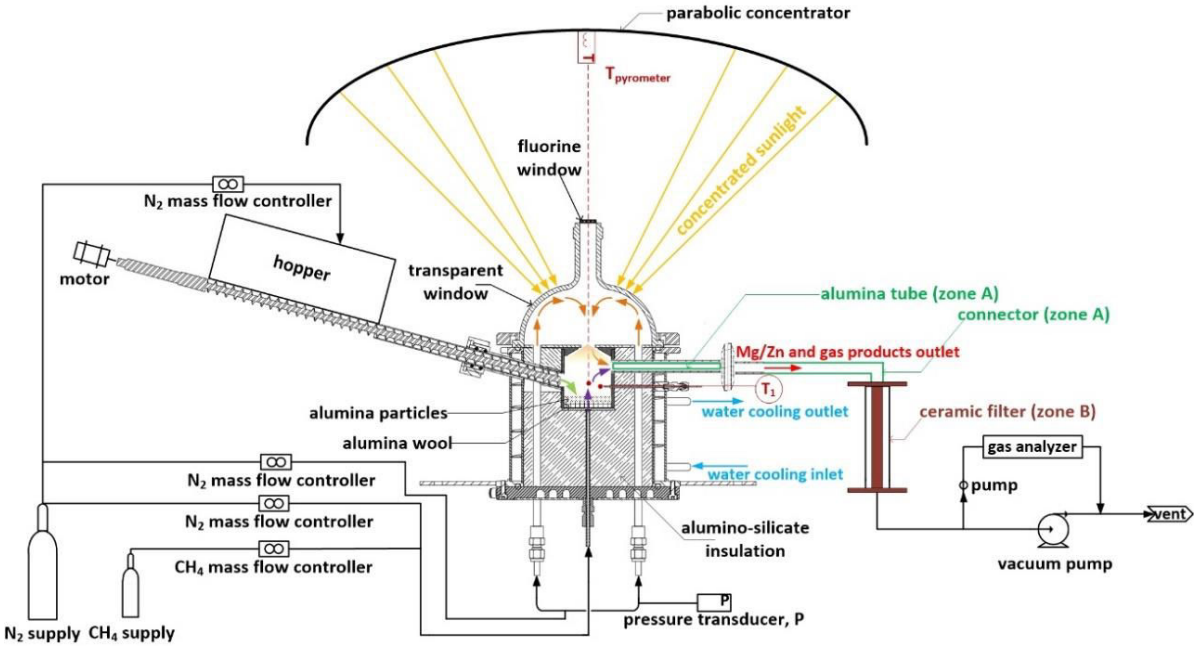

Figure C-3. Schematic diagram of the 1.5 kW_{th} prototype vacuum solar reactor equipped with an automatic particle delivery system.

3. Influence of carbon type and feeding rate during reactant powder injection

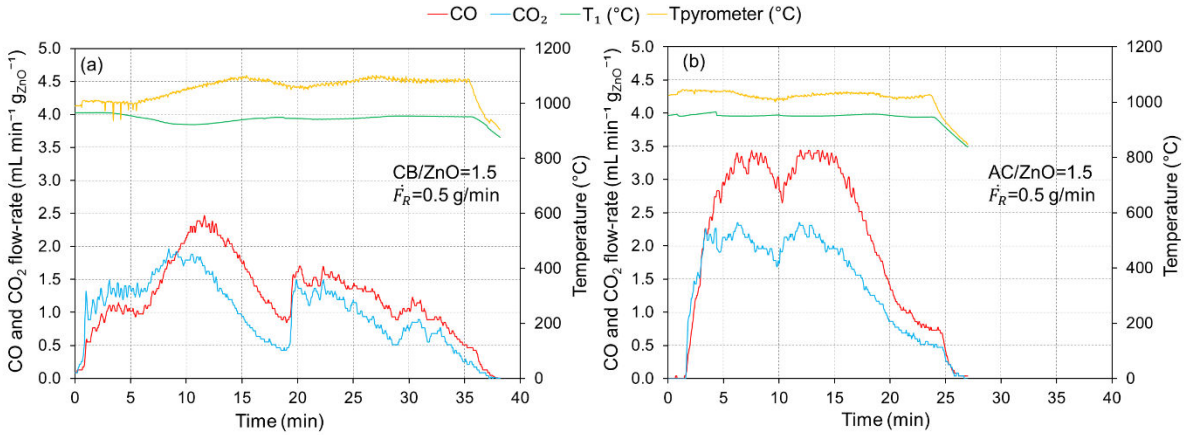

Figure C-4. CO and CO_2 production rates along with reactor temperatures for the ZnO carbothermal reduction with continuous reactant powder injection for (a) ZnO+CB and (b) ZnO+AC at a reactant feeding rate of 0.5 g/min.

The transient CO and CO_2 production rates for both feeding rates are compared (Fig. C-5). Differences between the two reactant feeding rates were not discernable at the beginning but more obvious after 25 min (higher CO peak production rate for 1 g/min than for 0.5 g/min). However, at 1 g/min, a temporal reactant blockage issue in the feeder was still noticed, evidenced by CO and CO_2 production rates decline between 17-27 min injection time. In addition, the reactant accumulation issue may occur for both feeding rates since experimental reaction durations were longer than the theoretical ones (experimental durations of 37 and 44 min compared to 24 and 12 min for theoretical durations at 0.5 and 1 g/min, respectively, for ~12g reactant). This issue occurs when the reactant feeding rate is higher than the reduction rate, and it can be overcome by increasing the temperature to accelerate the reaction kinetics.

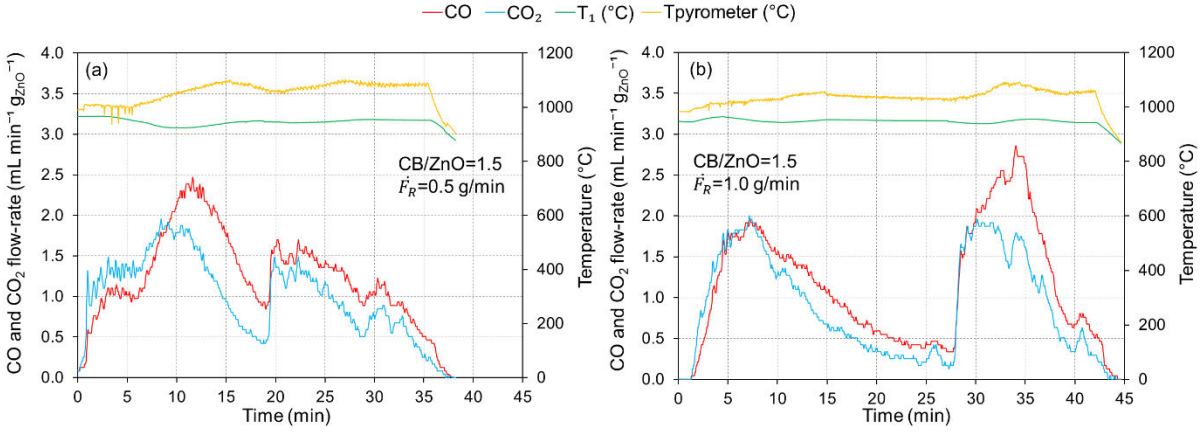

Figure C-5. CO and CO_2 production rates along with reactor temperatures for the ZnO carbothermal reduction with continuous reactant powder injection for (a) 0.5 g/min and (b) 1 g/min.

4. Solid products analysis

Fig. C-6 shows the excess carbon remaining in the cavity receiver (unreacted because in excess with respect to ZnO) after experiments for (a) batch test, (b) continuous reactant powder injection test, (c) continuous ZnO+1.5CB reactant pellet injection test, and (d) continuous ZnO+0.75$C_6H_9O_4$ reactant pellet injection test. The collected carbon from ZnO+1.5CB

reactant remained in the initial pellet shape (Fig. C-6c), as a result of compression in the pellets making process. This was not observed for ZnO+0.75$C_6H_9O_4$ pellets (Fig. C-6d) because of their lower density.

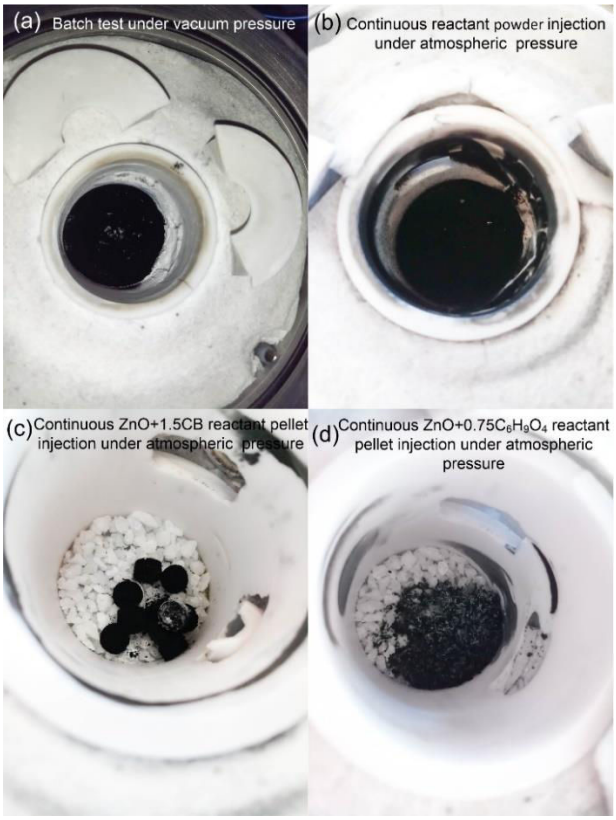

Figure C-6. Carbon remaining in the cavity receiver after experiments: (a) Run. No.1, (b) Run. No.7, (c) Run. No.12, and (d) Run.No.16.

Figure C-7. Crystallized gray chunks (recombined ZnO) located only at the tip of the alumina tube where Zn is condensed (over ~ 1 cm length).

Moreover, all the collected samples were analyzed for quantifying the Zn content utilizing a non-destructive analytical calibration method according to XRD peak intensity patterns. Standard samples were prepared by precisely mechanically mixing known amounts of commercial pure Zn and ZnO as reference with Zn mass fractions of 50%, 60%, 70%, 80%, and 90%. They were subsequently analyzed by XRD, and the intensity ratios of the main peaks of Zn (43.2°) to ZnO (31.7°) were evaluated and plotted against Zn mass fraction (wt%) in Fig. C-8.

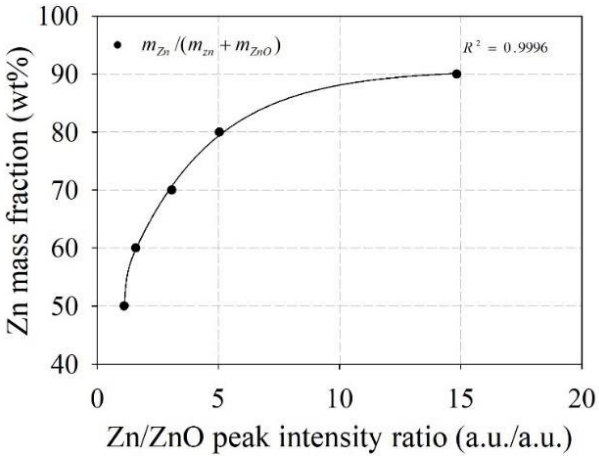

Figure C-8. Calibration curve for Zn mass fraction quantification from XRD patterns of the collected solid products.

Table C-2 lists the amounts of collected solid products (g) in zone A, zone B, and in the cavity receiver after experiments and the weight fraction of condensed Zn (wt%) in the collected solid products calculated by calibrated XRD (Fig. C-8). As a result, a large amount of condensed Zn was collected from zone A in the range 0.84-4.14 g (Table. C-2), with the occurrence of small crystallized gray chunks only at the tip of the alumina tube where the products exit (Fig. C-7). The amounts of products collected from filter (zone B) were in the range 0.21-1.91 g and they appeared to be darker in color than those of outlet (zone A) as a result of unreacted carbon deposition, especially with beech wood biomass. Furthermore, residues in the cavity receiver were found in the range 0.12-0.63 g. Zn content (continuous tests) was in the range of 90-98%wt for zone A and 92-99%wt for zone B, and pure Zn (no detection of any other species) was observed in both zones for batch tests (Run No.1-6).

Table C-2. Amounts of solid deposits and Zn content in each zone of the reactor.

Run No.	Solid product (g)				Zn content (%wt)	
	Zone A	Zone B	cavity receiver	Total	Zone A	Zone B
1	0.90	0.21	0.12	1.23	100	100
2	0.84	0.30	0.13	1.27	100	100
3	0.95	0.33	0.13	1.41	100	100
4	1.11	0.21	0.14	1.46	100	100
5	1.12	0.33	0.13	1.58	100	100
6	1.02	0.39	0.14	1.55	100	100
7	4.14	1.52	0.60	6.26	90	92
8	4.07	1.52	0.62	6.21	92	94
9	3.93	1.91	0.58	6.42	91	93
10	2.45	1.24	0.31	4.00	98	99
11	2.33	1.05	0.30	3.68	97	100
12	1.98	0.90	0.25	3.13	97	100
13	1.75	0.69	0.24	2.68	90	100
14	1.14	0.50	0.63	2.27	96	100
15	0.97	0.60	0.29	1.86	97	100
16	1.12	0.60	0.38	2.10	97	98
17	1.35	0.60	0.29	2.24	97	100

5. Particle morphology

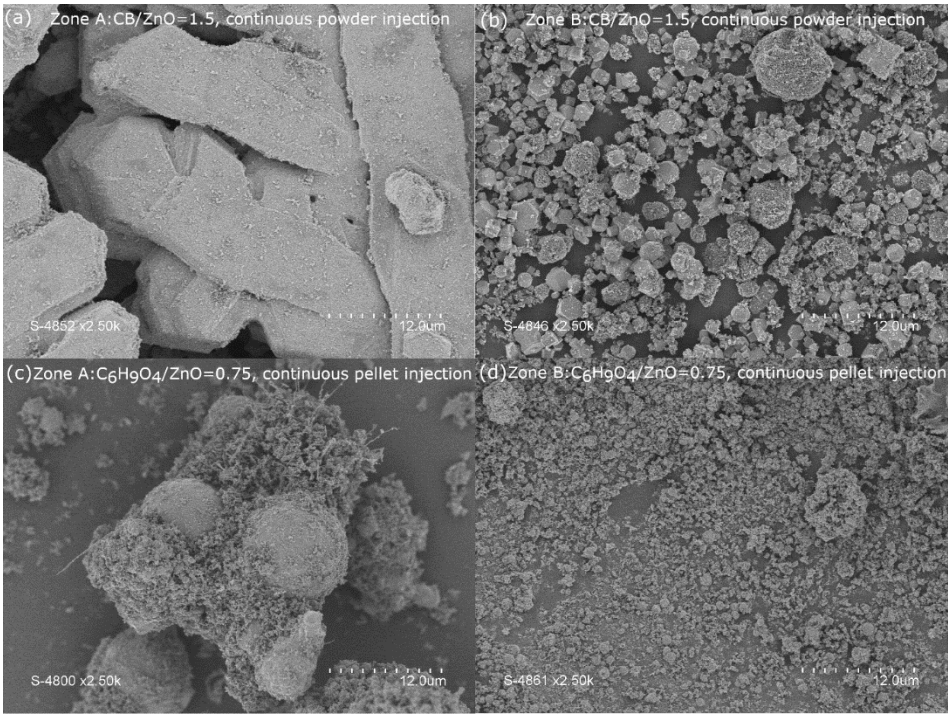

Figure C-9. SEM micrographs of solid products from the outlet tube (zone A) and filter (zone B) during (a,b) Run No. 8 and (c,d) Run No. 16.

6. Reactivity of Zn powder with CO_2

The reactivity of the solar-produced pure Zn powder (collected in the filter) was studied by thermogravimetry analysis / differential scanning calorimetry (TGA/DSC, Netzsch STA449). The Zn powder was placed as a packed-bed in an alumina crucible and heated up to 400°C in Ar (10 °C/min). When the targeted temperature was reached, CO_2 (50% in Ar) was injected under isothermal conditions during 30 min for monitoring the sample mass increase during the Zn exothermal oxidation reaction ($Zn_{(s)} + CO_2 \rightarrow ZnO_{(s)} + CO$). Complete and rapid Zn conversion was achieved, thus producing additional CO and solid ZnO that can be recycled to the solar step for closing the cycle (Fig. C-10).

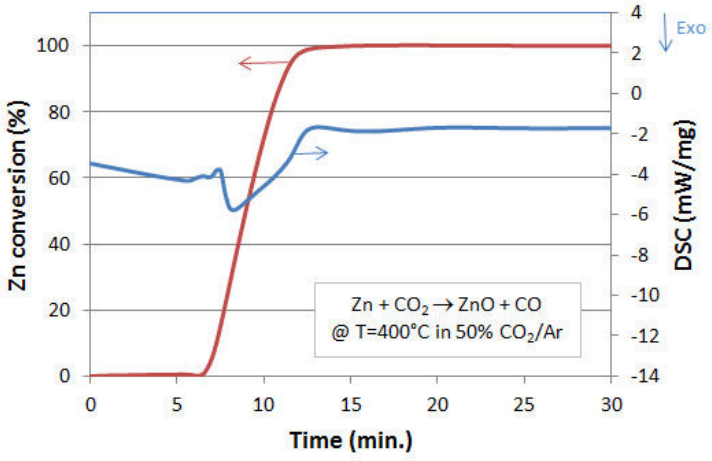

Figure C-10. Zn conversion evolution during oxidation with CO_2 (50% in Ar) at 400 °C in TGA/DSC (Netzsch STA449, solar-produced powder collected in the filter (Run No.6)).

b. Carbothermal reduction of MgO

1. Material mass balance

The material mass balance was performed to compare the amount of reactant (MgO/C) distributed between the products (CO, CO_2, and Mg) and the solid carbon residue in the cavity. The overview of the mass balance for CB/MgO=2 and AC/MgO=2 at 0.11 bar is shown in Tables C-3 and C-4, respectively.

Table C-3. Overview of the mass balance for a CB/MgO molar ratio of 2 at 0.11bar (Run No. 5).

Input		**Output**					
		Syngas		Solid deposit		rest of the reactor	
MgO	2.008 g	CO	1.190 g	Zone A	0.87 g	remainder	0.45 g
CB	1.200 g	CO_2	0.002 g	Zone B	0.14 g		
		Total gas	1.192 g	Total deposit	1.01 g	Total remainder	0.45 g
Total input 3.208 g				Total output 2.652 g			

Table C-4. Overview of the mass balance for a AC/MgO molar ratio of 2 at 0.11 bar (Run No. 6)

Input		**Output**					
		Syngas		Solid deposit		rest of the reactor	
MgO	2.005 g	CO	1.408 g	Zone A	0.72 g	remainder	0.40 g
AC	1.206 g	CO_2	0.018 g	Zone B	0.20 g		
		Total gas	1.426 g	Total deposit	0.92 g	Total remainder	0.40 g
Total input 3.211 g				Total output 2.746 g			

Overall, the mass balance was in the range 52.5-85.6% for all runs, and most values were accomplished above 70% (Table 4-2). However, because of the burning or explosion issue encountered during collecting samples (Mg-rich powders are unstable in air), the global mass balance was impaired, which thus explains to a large extent the lower mass output regarding the input.

2. Influence of solid carbon type

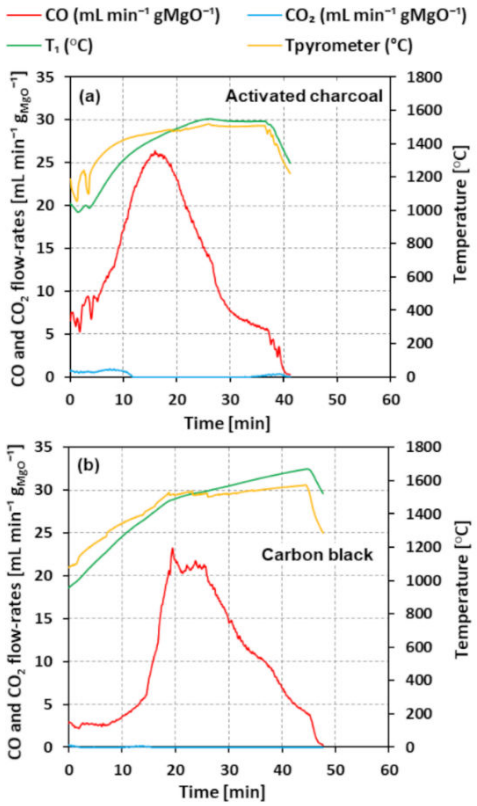

Figure C-11. CO and CO_2 production rates along with reactor temperatures for MgO carbothermal reduction with different carbon types (C/MgO=1.5, P=0.11 bar).

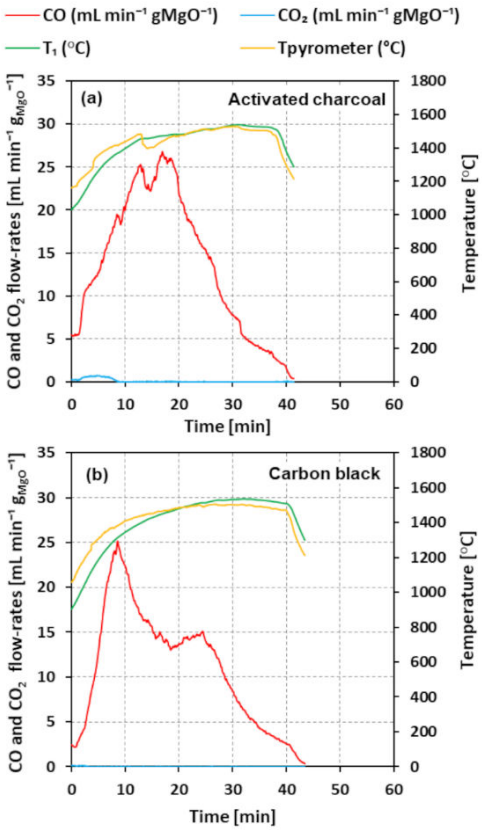

Figure C-12. CO and CO_2 production rates along with reactor temperatures for MgO carbothermal reduction with different carbon types (C/MgO=2, P=0.11 bar).

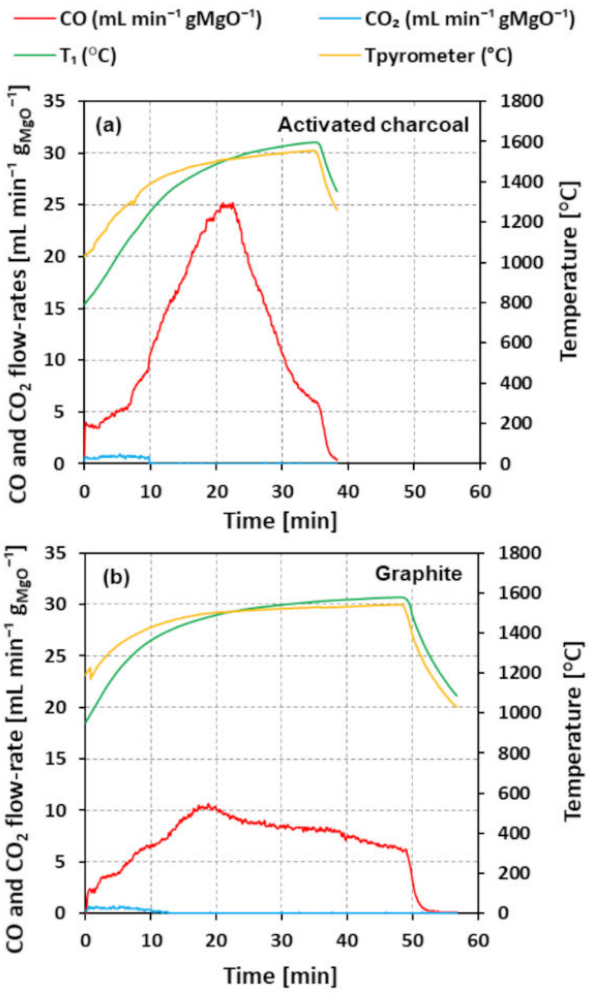

Figure C-13. CO and CO_2 production rates along with reactor temperatures for MgO carbothermal reduction with AC and graphite (C/MgO=2, P=0.16 bar).

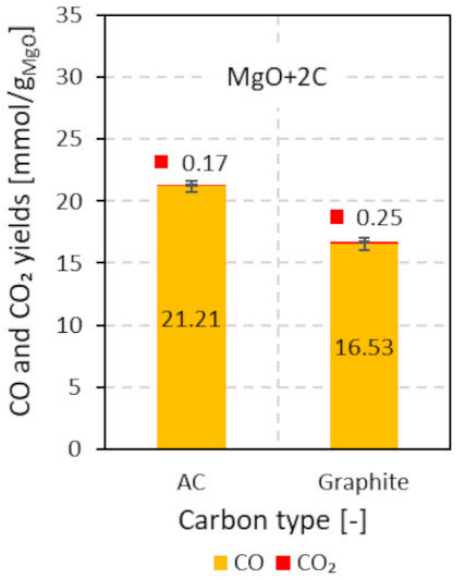

Figure C-14. CO and CO_2 yields for different carbon types (C/MgO=2, P=0.16 bar).

3. Influence of C/MgO molar ratio

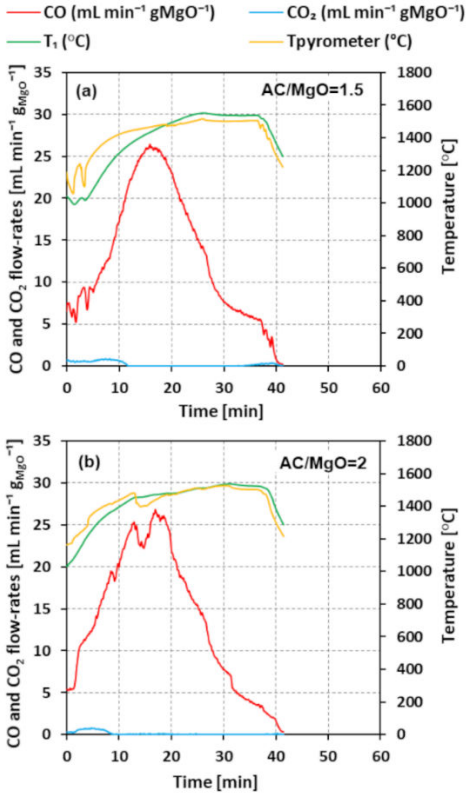

Figure C-15. CO and CO_2 production rates along with reactor temperatures for MgO carbothermal reduction with AC at different C/MgO molar ratios (P=0.11 bar).

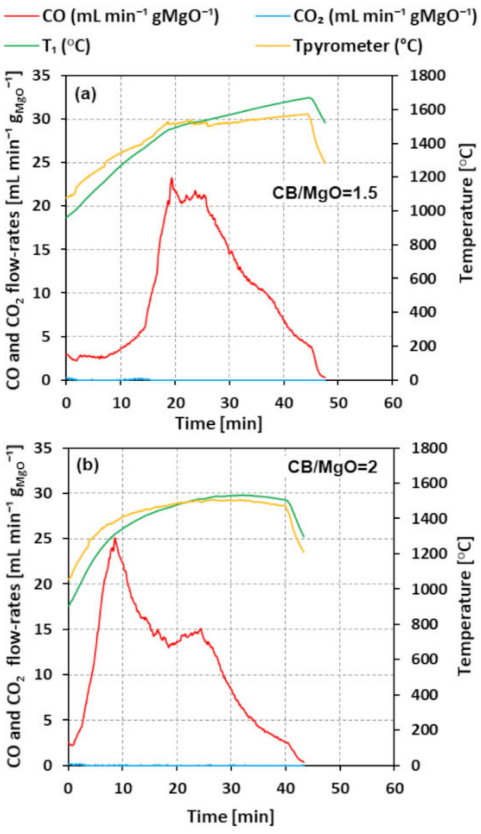

Figure C-16. CO and CO_2 production rates along with reactor temperatures for MgO carbothermal reduction with CB at different C/MgO molar ratios (P=0.11 bar).

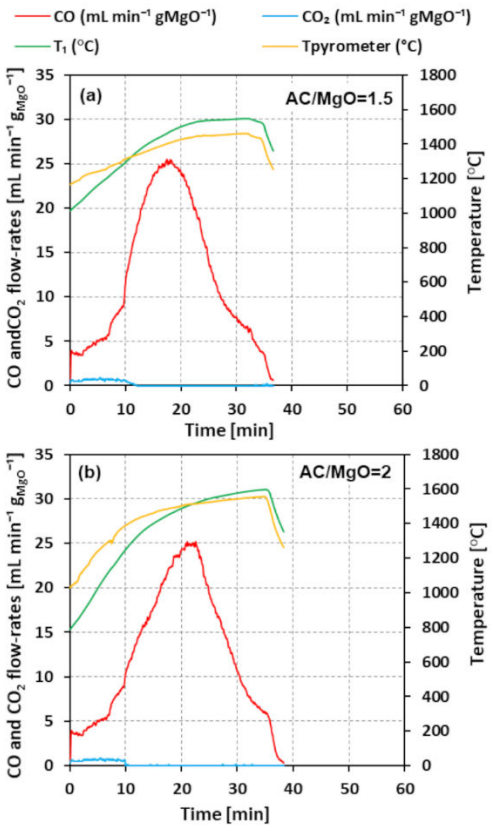

Figure C-17. CO and CO_2 production rates along with reactor temperatures for MgO carbothermal reduction with AC at different C/MgO molar ratios (P=0.16 bar).

4. Solid products analysis

The solid products were collected after each experiment in the removable outlet components of the solar reactor where solid products are condensed and deposited (zone A and zone B, Fig. C-3. In addition, the quantity of remaining unreacted carbon in the cavity receiver was also quantified (Fig. C-18).

Figure C-18. Carbon remaining in the cavity receiver after experiments (Run. No. 6).

Table C-5 provides the amounts of collected solid products in zone A, zone B (Figs. C-19 and C-20), and the cavity receiver after experiments. Notably, some parts of the solid

products were lost during their recovery from the outlet components caused by their auto-combustion at room temperature (because the produced Mg-rich powder as nanosized particles is highly flammable in air). The typical surface area of the solid product powder collected in the ceramic filter was 63.8±0.1 m^2/g (measured by N_2 sorption at 77 K). The produced powder is pyrophoric when mainly composed of Mg (auto-ignition observed at room temperature when powder exposed to air). The total amount of solid products collected from both zones A and B is in the range 0.52-1.01 g (the theoretical yield of Mg is 1.21 g converted from 2 g of MgO). The remaining carbon in the cavity was the result of an excess carbon with respect to stoichiometry. Thus, the higher the excess carbon, the higher the remainder in the cavity.

Table C-5. Amount of solid deposits collected in each zone of the reactor.

	Run No.								
Product	1	2	3	4*	5*	6	7**	8	9
Zone A (g)	0.64	0.48	0.29	0.82	0.87	0.72	NA	0.24	3.84
Zone B (g)	0.14	0.33	0.23	0.09	0.14	0.20	NA	0.42	1.02
Remainder in the cavity (g)	0.28	0.30	0.30	0.29	0.45	0.40	NA	0.45	1.30
Total (g)	1.06	1.11	0.82	1.20	1.46	1.32	NA	1.11	6.16

The solid products *partly or **entirely burned during collection before weighting

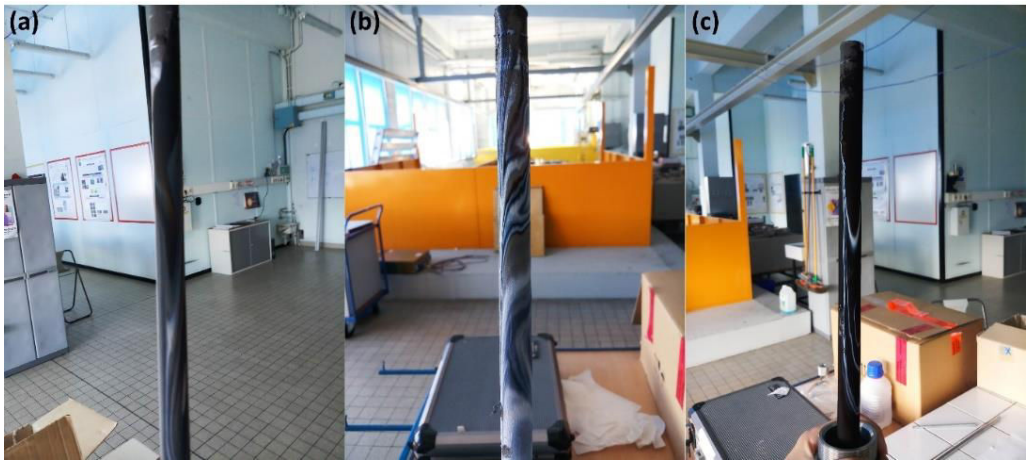

Figure C-19. Photographs of the solid products deposition on the ceramic filter: (a) Run No.2, (b) Run No.3, and (c) Run No.6.

Figure C-20. Photograph of the solid products after their collection from the ceramic filter.

To analyze the crystal structure, chemical composition, and microstructure of the produced materials, the collected solid products were characterized via powder X-ray diffraction (XRD) and particle morphology analysis using a field emission scanning electron microscope (FESEM, Hitachi S4800). Additionally, a non-destructive analytical calibration method was applied to evaluate Mg mass fraction in accordance with XRD peak intensity patterns. Standard samples were prepared by precisely mixing known amounts of commercial pure Mg and MgO as reference with Mg mass fractions of 15%, 30%, 45%, 60%, 75%, and 90%. They were then analyzed by XRD and the intensity ratios of the main peaks of Mg (36.53°) to MgO (42.71°) were calculated and plotted versus Mg mass fraction (%wt) according to Fig. C-21.

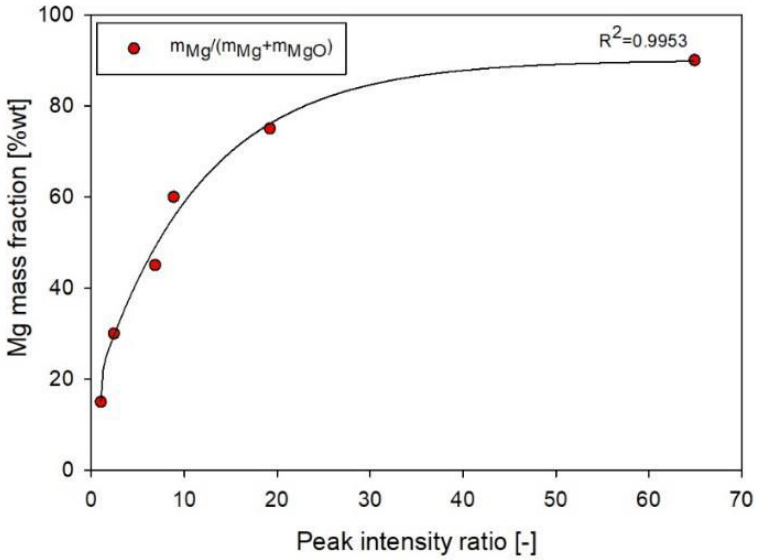

Figure C-21. Calibration curve for Mg mass fraction quantification from XRD patterns of the collected solid products.

Table C-6 shows the weight fraction of condensed Mg collected in zone A and zone B calculated with the calibrated XRD curve (Fig. C-21). The Mg fraction was in the range of 4.3-30.0% for zone A and 2.0-32.8% for zone B, thus revealing low Mg content in the solid products after their exposure to air. This is because of the strong Mg oxidation with air at room temperature (after opening the reactor). Indeed, the produced Mg-rich powder is highly flammable, especially in the form of nanoparticles. This property favors oxidation with air even at room temperature, which may lead to an auto-combustion and/or even explosion issue. This issue can be alleviated by using a hands-in-bag atmospheric chamber during collecting the solid products for safe handling of pyrophoric powders; however, the condensed Mg can still be oxidized with air while opening the reactor or transferring/preparing the powder for XRD analysis, leading to a subsequent increase of MgO content in the solid products after their collection from the reactor. Nevertheless, the high MgO conversion calculated from CO production (Table C-6) confirmed that a high Mg yield was achieved although the final Mg fraction in the solid products was low after their characterization due to their inevitable exposure to air.

Table C-6. Mg weight fraction calculated from calibrated XRD.

Run No.	reactant	X_{MgO} (%mol)	Mg weight fraction	
			Zone A (%wt)	Zone B (%wt)
1	MgO+1.5AC	97.8	8.9	30.9
2	MgO+1.5AC	83.2	6.4	8.5
3	MgO+1.5AC	82.0	9.8	5.3
4*	MgO+1.5CB	84.0	18.8	32.8
5*	MgO+2CB	85.5	6.0	20.7
6	MgO+2AC	99.9	30.0	31.9
7*	MgO+2AC	86.8	28.0	4.4
8	MgO+2Graphite	68.6	4.3	2.0
9	MgO+1.5AC	88.2	25.0	28.2

*Auto-combustion occurred

5. XRD analysis of produced powders

5.1 Influence of solid carbon type:

The XRD patterns of the solid products collected in each zone at both molar ratios were not significantly different between AC and CB (Fig. C-22). However, higher Mg intensity was observed in zone B when compared with zone A.

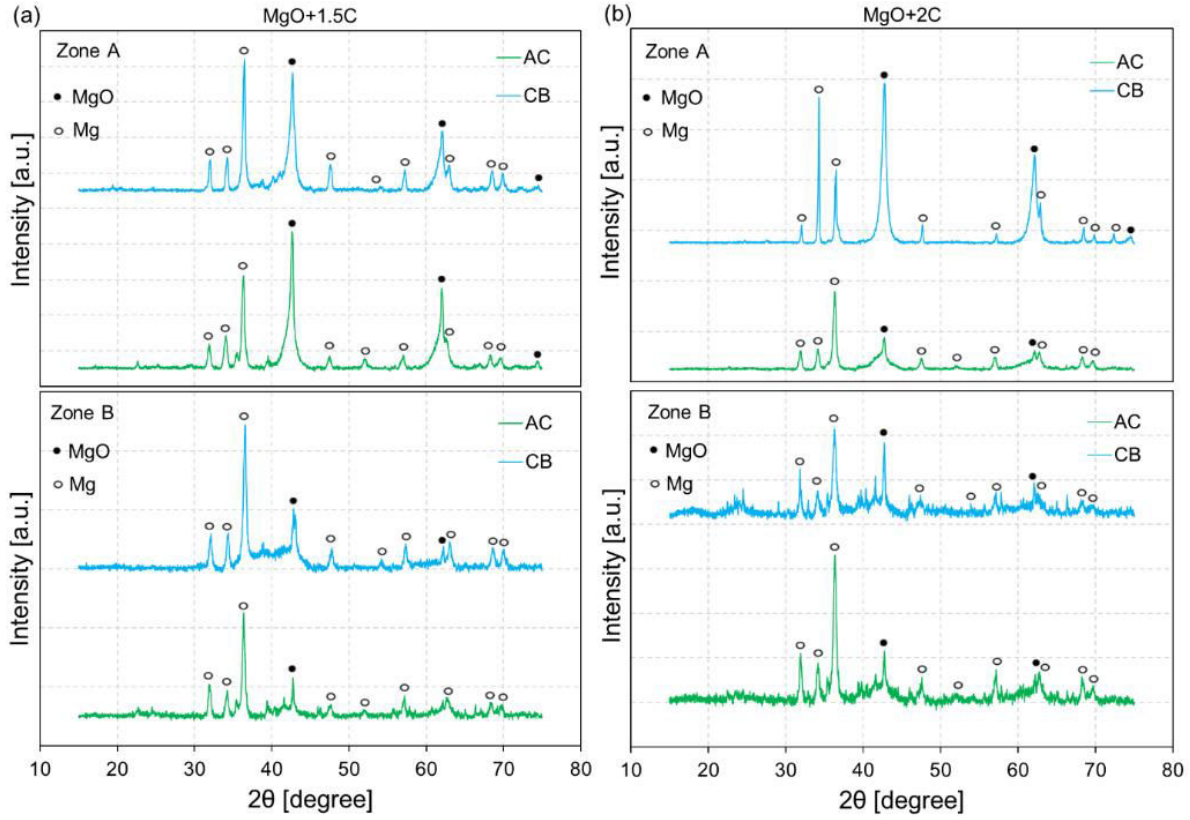

Figure C-22. XRD patterns of the collected solid products in zone A and zone B for the reduction of MgO with AC and CB at (a) C/MgO=1.5 and (b) C/MgO=2 (P=0.11 bar).

Fig. C-23 shows that very small intensities of the Mg peaks were observed when employing graphite as reducing agent, due to the weak reaction rate, in agreement with the low CO yield.

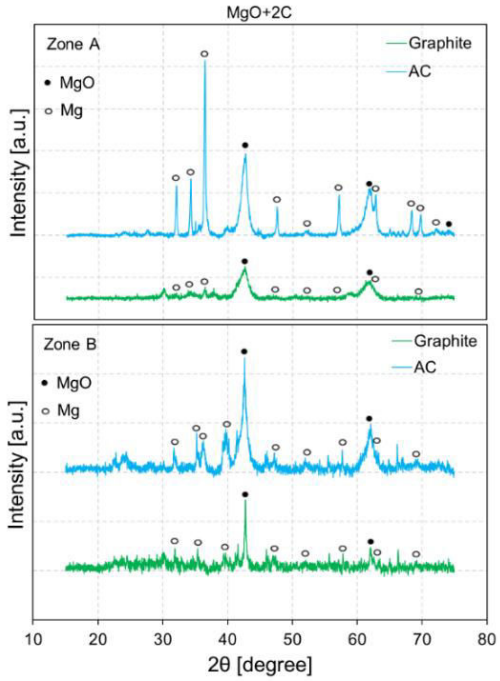

Figure C-23. XRD patterns of the collected solid products in zone A and zone B for the reduction of MgO with graphite and AC at C/MgO=2 (P=0.16 bar).

5.2 Influence of C/MgO ratio:

Fig. C-24 shows that the XRD patterns between C/MgO=1.5 and C/MgO=2 for both solid carbon types were similar, denoting that MgO and carbon were sufficiently in contact and confirming the low influence of the C/MgO ratio.

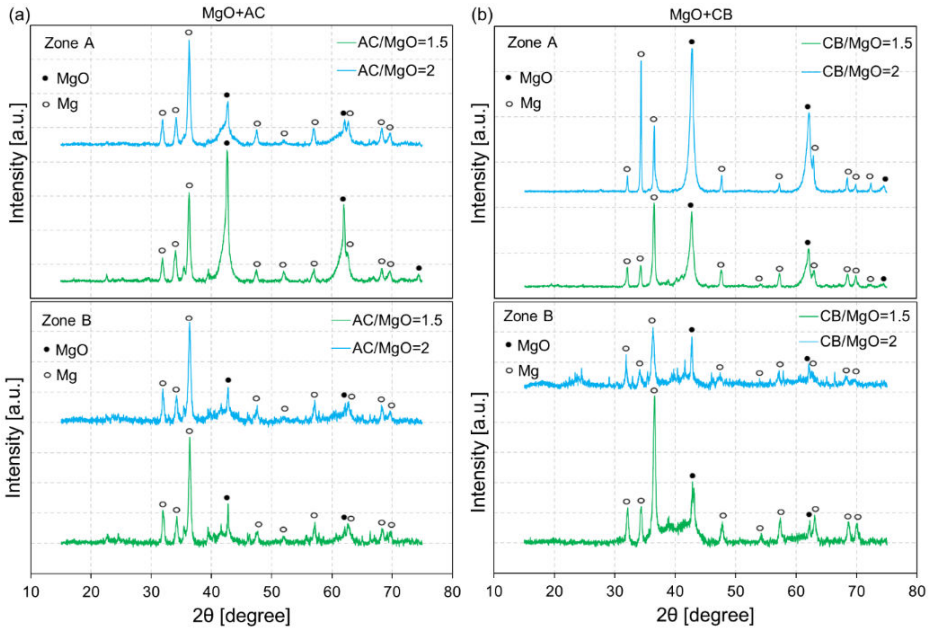

Figure C-24. XRD patterns of the collected solid products in zone A and zone B as a function of C/MgO molar ratio: (a) MgO+AC (b) MgO+CB (P=0.11 bar).

In addition, the XRD patterns of solid products as a function of C/MgO molar ratio (Fig. C-25) show that both MgO and Mg products were identified, while their differences between C/MgO=1.5 and C/MgO=2 were not obvious.

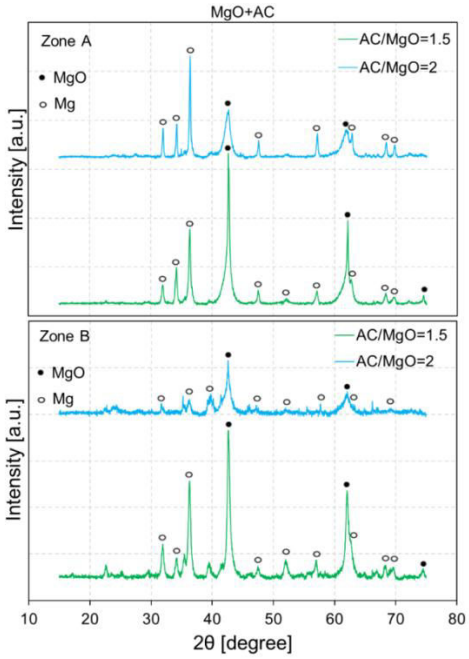

Figure C-25. XRD patterns of the collected solid products in zone A and zone B as a function of C/MgO molar ratio (P=0.16 bar).

6. Particle morphology

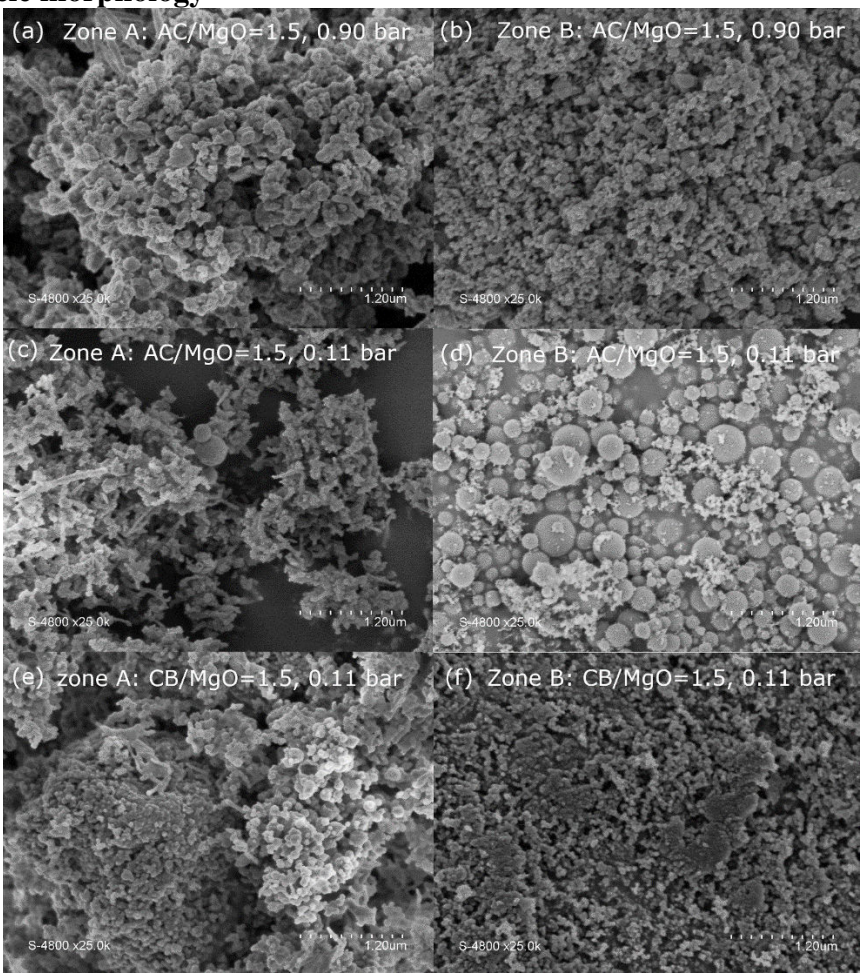

Figure C-26. SEM micrographs of solid products from the outlet tube (zone A) and filter (zone B) during (a,b) Run No. 3, (c,d) Run No. 1, and (e,f) Run No. 4.

7. Reactivity of Mg powder with CO_2

The reactivity of the solar-produced powder (collected in the filter) was studied by thermogravimetry analysis using different apparatuses (Setaram Setsys Evolution and Netzsch STA449). The powder was placed as a packed-bed in an alumina crucible and heated up to 380°C in Ar (10°C/min). When the targeted temperature was reached, CO_2 was injected under isothermal conditions during 60 min for monitoring the sample mass increase during the Mg oxidation reaction ($Mg_{(s)} + CO_2 \rightarrow MgO_{(s)} + CO$). Similar Mg oxidation patterns were observed regardless of the starting Mg material and used apparatus, with a fast initial reaction rate followed by a diffusion-limited regime arising from mass transfer limitation in the packed powder (Figs. C-27 and C-28). Complete Mg conversion was achieved, thus producing additional CO and solid MgO that can be recycled to the solar step for closing the cycle.

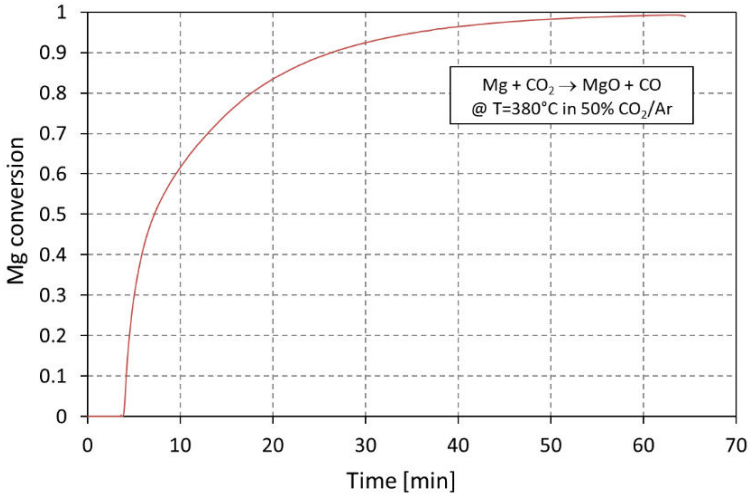

Figure C-27. Mg conversion evolution during oxidation with CO_2 (50% in Ar) at 380°C in TGA (Setaram Setsys Evolution, downward flow configuration, solar-produced powder collected in the filter and obtained from MgO+1.5AC at P=0.11 bar).

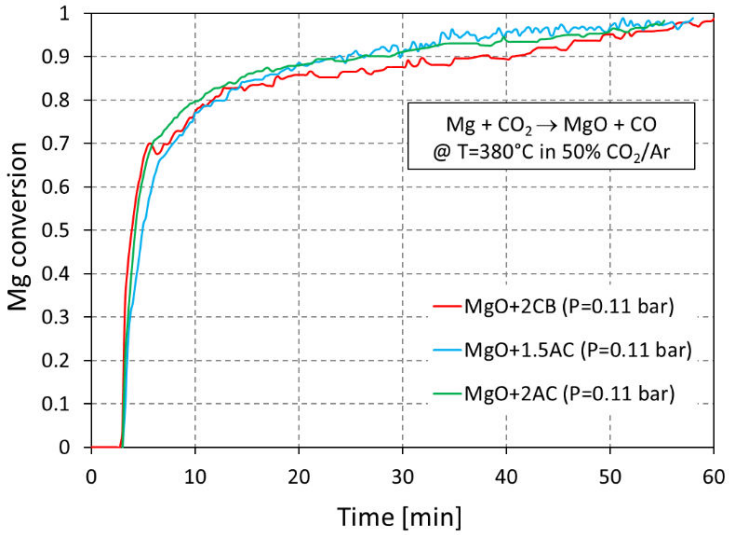

Figure C-28. Mg conversion evolution during oxidation with CO_2 (20% in Ar) at 380°C in TGA (Netzsch STA 449, upward flow configuration, solar-produced powders collected in the filter and obtained from MgO+2CB, MgO+1.5AC and MgO+2AC at P=0.11 bar).

Appendix D: Solar gasification of biomass combined with carbothermal reduction of ZnO

a. A list of experimental conditions

Table D-1. Summary of experimental conditions for combined gasification/carbo-thermal reduction and pyrolysis at different temperatures.

Run No.	Types of Biomass	Reactant	biomass/ZnO molar ratio	Initial mass (g)	Ar flow rate (NL/min)	Temperature (°C)
1	type A	ZnO+biomass	1	20	5	1050
2	type A	ZnO+biomass	1	20	5	1100
3	type A	ZnO+biomass	1	20	3.2	1150
4	type A	ZnO+biomass	1	20	3	1200
5	type D	ZnO+biomass	1	18.2	3	1200
6	type A	ZnO+biomass	1	20	5	1250
7	type A	ZnO+biomass	1	20	5	1300
8	type A	biomass	-	10	3.3	1100
9	type A	biomass	-	10	3.3	1200
10	type A	biomass	-	10	3.3	1300
11	type A	biomass	-	10	3.3	1300
12	type D	biomass	-	10	3.2	1300
13	type A	biomass	-	15.65	3	1350
14	type A	ZnO+0.5 biomass	0.5	20	5	1100
15	type A	ZnO+0.75 biomass	0.75	20	5	1100
16	type A	ZnO+0.75 biomass	0.75	20	5	1250

Temperatures and pressure evolution in the reactor during heating phase and particle injection is presented in Fig. D-1

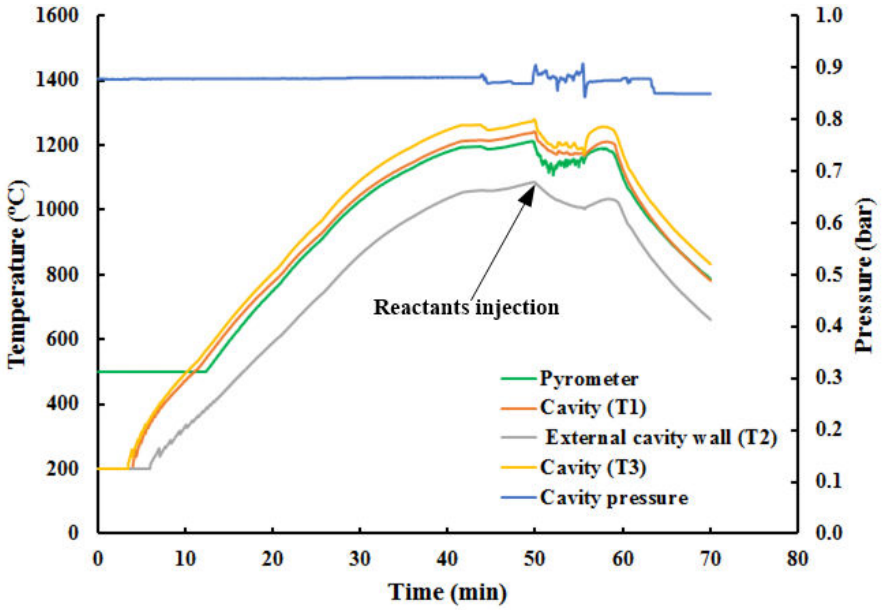

Figure D-1. Temperatures and pressure evolution in the reactor during heating phase and particle injection.

b. Mass balance

Table D-2. Overview of the mass balance for biomass/ZnO molar ratio of 0.75 at 1250ºC (Run No. 16).

Input		Output					
		Syngas		Solid deposit		rest of the reactor	
ZnO	8.56 g	CO	7.702 g	Zone A	2 g	remainder	0.2 g
Biomass	11.44 g	CO_2	1.702 g	Zone B	4 g		
		CH_4	0.616 g	Zone C	1.9 g		
		C_nH_m	0.070 g				
		H_2	0.565 g				
		Total gas	10.658 g	Total deposit	7.9 g	Total remainder	0.2 g
Total input 20 g		Total output 18.758 g					

Table D-3. Overview of the mass balance for biomass/ZnO molar ratio of 1 at 1250ºC (Run No. 6).

Input		Output					
		Syngas		Solid deposit		rest of the reactor	
ZnO	8.56 g	CO	7.102 g	Zone A	1.7 g	remainder	0.3 g
Biomass	11.44 g	CO_2	1.294 g	Zone B	3.5 g		
		CH_4	0.507 g	Zone C	1.8 g		
		C_nH_m	0.029 g				
		H_2	0.532 g				
		Total gas	9.464 g	Total deposit	7 g	Total remainder	0.3 g
Total input 20 g		Total output 16.764 g					

c. Quantification of carbon content in the samples

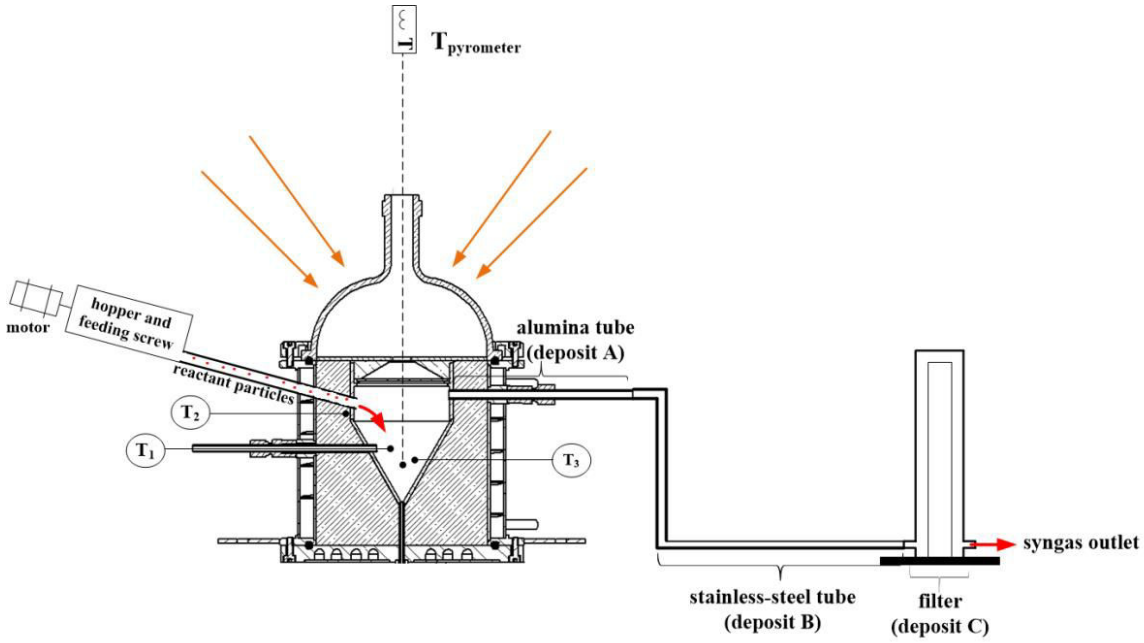

Figure D-2. Thermocouples positions and reactor output zones where the solid products are collected.

The carbon content in the collected samples from zone A, zone B, zone C, and the cavity was estimated by mass balance. Given amounts of solid product were exactly weighed and then burned at 650°C in air to remove carbon and oxidize Zn, thereby providing the amount of both carbon and Zn in the samples. After the burning process, the selected samples were precisely weighed again to determine the mass of carbon and Zn in the initial samples. The mass variation indeed corresponds to the carbon lost during the combustion minus the oxygen gained during Zn oxidation to ZnO. Table D-4 shows the carbon content of selected samples in each zone of the reactor.

The results first show that the weights of the selected samples in zone A and zone B increased slightly after the burning process because of the prevailing oxidation reaction of Zn with O_2. This means the solid products contained in zone A and zone B are minimally contaminated by carbon (17.7 wt% carbon content in zone A, and 8.8 wt% carbon content in zone B). In other words, the presence of significant carbon content was mainly evidenced in zone C (41.9 wt%) because the remaining particulate residues (char) separated from the gas stream was collected in this zone (filter). Besides, 88.5 wt% of carbon content was found in the cavity (char), while the remainder (0.16 mg) in this sample was supposed to be the deposited ashes.

Table D-4. Carbon content estimated by mass balance in each zone of the reactor.

Residue	m_{total} (before) (mg)	m_{total} (after) (mg)	Δm (mg)	m_{Zn} (mg)	m_{carbon} (mg)	Ash (mg)	Carbon content (wt%)
Zone A*	99.5	101.9	2.4	81.9	17.6	-	17.7
Zone B*	30.7	34.8	4.1	28.0	2.7	-	8.8
Zone C*	27.7	20.1	7.6	16.1	11.6	-	41.9
Remainder inside cavity**	1.4	0.2	1.2	-	1.24	0.16	88.5

*The selected samples in zone A, zone B, and zone C were collected form Run No.14.

**The selected sample in the cavity was collected from Run No.4.

Figure D-3. Char and ZnO remaining inside the cavity of the reactor for a biomass/ZnO molar ratio of 0.5 at 1100 °C.

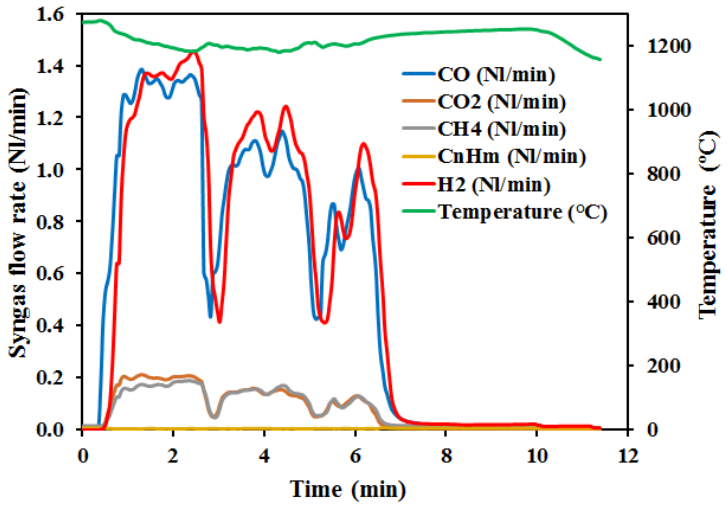

Figure D-4. Syngas flow rates during a continuous experiment for a biomass/ZnO molar ratio of 0.75 at 1250°C.

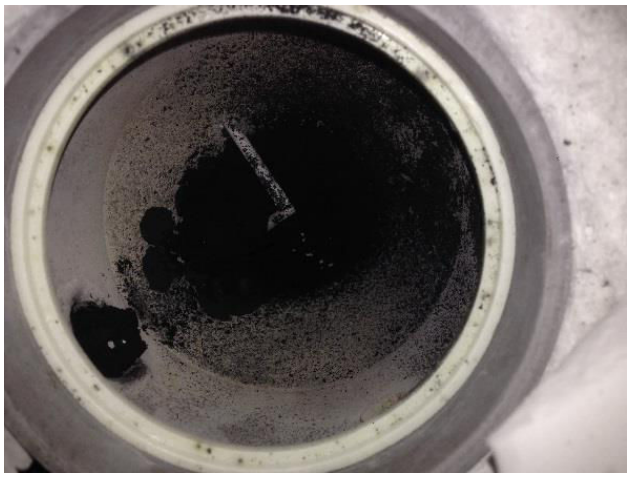

Figure D-5. Char remaining inside the cavity of the reactor for a biomass/ZnO molar ratio of 1 at 1100°C.

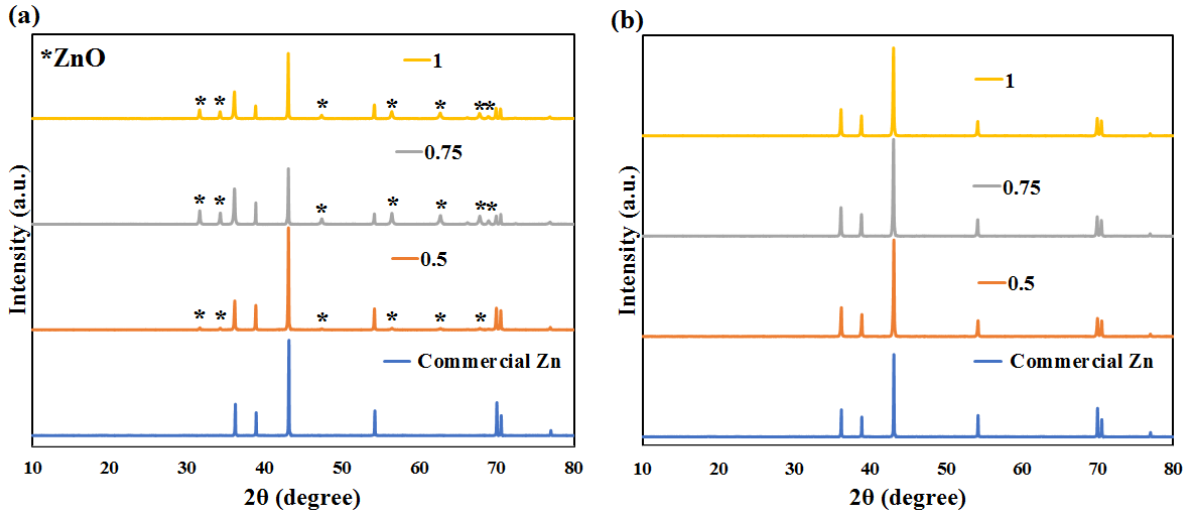

Figure D-6. Representative XRD patterns of products collected from (a) zone A, and (b) zone C at different biomass/ZnO molar ratios (1100°C).

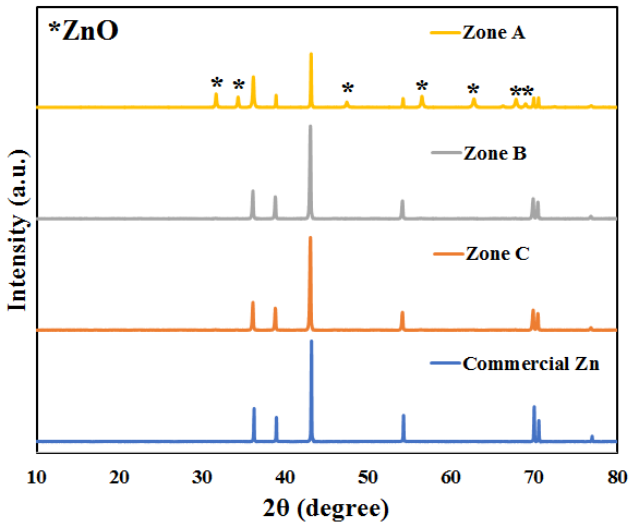

Figure D-7. Representative XRD patterns of the products collected from each zone at 1250°C (biomass/ZnO molar ratio of 0.75).

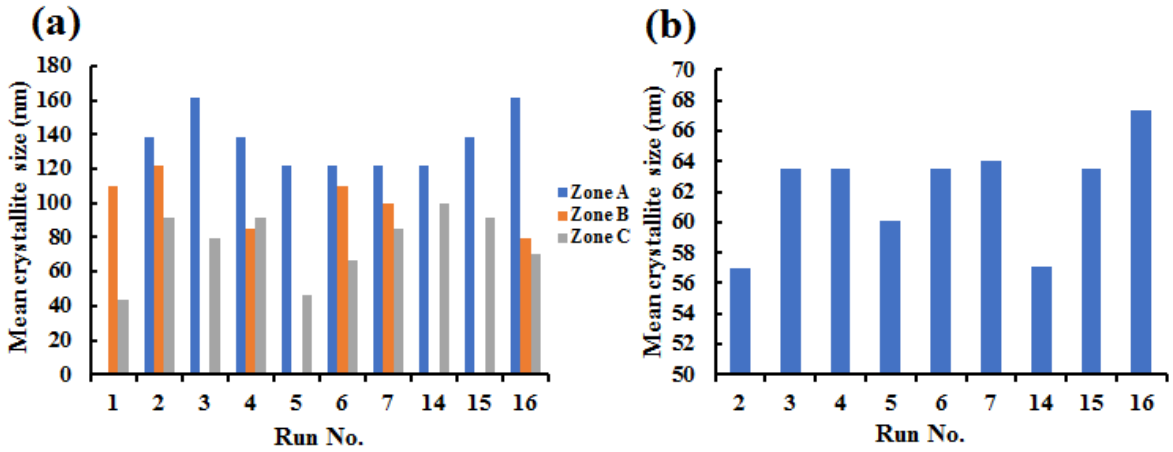

Figure D-8. Mean crystallite size of (a) Zn collected from zone A, zone B, and zone C and (b) ZnO collected from zone A.

Solar fuels production from thermochemical gasification and reforming of carbonaceous feedstocks

Abstract

The investigated solar thermochemical processes consist of the thermochemical conversion of solid and gaseous carbonaceous feedstocks into syngas as well as metal oxides reduction into metal commodities utilizing concentrated solar energy to drive endothermic chemical reactions, thereby enabling intermittent solar energy storage into solar fuels and avoiding CO_2 emissions. This work aims to experimentally investigate three key solar thermochemical conversion approaches regarding biomass gasification, chemical looping reforming of methane, and carbothermal reduction of ZnO and MgO. Solar gasification and solar chemical looping reforming allowed valorizing wood biomass and methane into syngas, while solar carbothermal reduction was applied to produce Zn and Mg from ZnO and MgO. Such solar thermochemical processes were performed in 1.5 kW_{th} prototype solar chemical reactors, utilizing highly concentrated sunlight provided by a solar concentrator at PROMES laboratory, Odeillo, France. The impact of controlling parameters of each process on the reaction mechanism, conversion, yields, and process performance, during on-sun testing was investigated and evaluated thoroughly. Such processes were proved to significantly improve the chemical conversion, syngas yields, energy efficiency, with solar energy storage into transportable fuels, thereby outperforming the conventional processes. Moreover, their feasibility, reliability, and robustness in converting both methane and biomass feedstocks to syngas as well as producing Mg and Zn metals in batch and continuous operation under vacuum and atmospheric conditions during on-sun operation were successfully demonstrated.

Keywords: gasification, chemical looping reforming, carbothermal reduction, solar reactor, concentrated solar power, syngas, solar metallurgy.

Production de combustibles solaires par voie thermochimique à partir de gazéification et reformage de ressources hydrocarbonées

Résumé

Les procédés thermochimiques solaires étudiés concernent la conversion de charges hydrocarbonées solides ou gazeuses en syngas, ainsi que la réduction d'oxydes en métaux en utilisant l'énergie solaire concentrée pour effectuer les réactions endothermiques, permettant ainsi le stockage de l'énergie solaire intermittente en carburants sans émissions de CO_2. Ce travail a pour objectif l'étude expérimentale de trois procédés solaires incluant la gazéification de biomasse, le reformage de méthane en boucle chimique, et la carboréduction de ZnO et MgO. La gazéification et le reformage permettent la valorisation de biomasse bois et de méthane en syngas, tandis que la carboréduction permet de produire Zn et Mg à partir de ZnO et MgO. Ces procédés ont été étudiés dans des réacteurs solaires de 1.5 kW_{th}, en utilisant le rayonnement concentré fourni par des systèmes à concentration du laboratoire PROMES, Odeillo, France. L'impact des paramètres opératoires de chaque procédé sur les mécanismes réactionnels, conversion, rendement, et performances énergétiques a été évalué en détail. Ces procédés ont permis d'améliorer la conversion chimique, les rendements en syngas, les efficacités énergétiques tout en permettant un stockage de l'énergie solaire en combustibles transportables, avec des performances globales supérieures aux procédés conventionnels. De plus, leur faisabilité, fiabilité et robustesse pour la conversion de méthane et biomasse en syngas et la production de Mg et Zn en fonctionnement batch ou continu sous pression réduite ou atmosphérique en conditions solaires réelles ont été démontrés.

Mots-clé: gazéification, reformage, carboréduction, réacteur solaire, énergie solaire concentrée, syngas, métallurgie solaire.